'Ezzat Abdel FATTAH

PREDICTION OF MOVING RIGID WHEEL PERFORMANCE

PREDICTION OF MOVING RIGID WHEEL PERFORMANCE AND ASSOCIATED SUBSOIL RESPONSE BEHAVIOUR

by
Ezzat Abdel Fattah

Department of Civil Engineering
and Applied Mechanics

Ph.D.

ABSTRACT

The purpose of this study is to provide a rational analytical means for predicting the performance of a moving rigid wheel and associated subsoil response behaviour.

The study:

(a) considers the effect of surface condition on wheel performance and its associated subsoil response behaviour,

(b) develops a finite element solution technique for the problem considered,

(c) evaluates the actual performance of test wheels through the use of the visioplasticity technique, and

(d) seeks verification of the validity of the application of the finite element technique developed for analysis of the moving rigid wheel on cohesive soils under plane-strain conditions through comparisons with actual test results.

The solution obtained provides detailed information on stress and deformation fields developed in the loaded soils as well as contact stresses at the wheel-soil interface for various wheel degrees of slip. This permits successful prediction of wheel performance (in energy terms) at any degree of slip.

PREDICTION DU RENDEMENT D'UNE ROUE MOBILE ET RIGIDE ET COMPORTEMENT DU SOL EN DESSOUS DE LA ROUE

par
Ezzat Abdel Fattah

RESUME

L'objet de cette étude est de fournir une méthode analytique et rationelle pour prédire le rendement d'une roue mobile et rigide, ainsi que le comportement du sol en dessous de la roue.

Cette étude (a) considére l'effet des conditions de la surface sur le rendement de la roue et sur le comportement du sol en dessous de la roue; (b) développe une solution au problème considéré, par la méthode des éléments finis; (c) évalue le rendement réel des roues d'épreuve par la méthode de visioplasticité; (d) tente de valider l'application de la méthode des éléments finis à l'analyse du mouvement d'une roue mobile et rigide sur un sol cohésif, sous des conditions de déformation plane, et ce, en comparant la théorie avec les résultats expérimentaux.

La solution fournit des renseignements détaillés sur les champs d'effort et de déformation dans les sols chargés, ainsi que sur l'effort de contact à la surface sol-roue, et ce pour des roues différentes et des degrés de glissage différents. Ceci permet la prédiction du rendement d'une roue (en termes d'énergie) à n'importe quel degré de glissage.

PREDICTION OF MOVING RIGID WHEEL PERFORMANCE AND ASSOCIATED SUBSOIL RESPONSE BEHAVIOUR

by

Ezzat Abdel Fattah

A Thesis submitted to the Faculty of Graduate Studies and Research in partial fulfillment of the requirements for the degree of Doctor of Philosophy

Department of Civil Engineering & Applied Mechanics
McGill University
Montreal, Quebec
August 1976

TABLE OF CONTENTS

APPENDICES continued

Page

PREDICTION OF MOVING RIGID WHEEL PERFORMANCE AND ASSOCIATED SUBSOIL RESPONSE BEHAVIOUR

ABSTRACT

The purpose of this study is to provide a rational analytical means for predicting the performance of a moving rigid wheel and associated subsoil response behaviour.

The study:

(a) considers the effect of surface condition on wheel performance and its associated subsoil response behaviour,

(b) develops a finite element solution technique for the problem considered,

(c) evaluates the actual performance of test wheels through the use of the visioplasticity technique, and

(d) seeks verification of the validity of the application of the finite element technique developed for analysis of the moving rigid wheel on cohesive soils under plane-strain conditions through comparisons with actual test results.

The solution obtained provides detailed information on stress and deformation fields developed in the loaded soils as well as contact stresses at the wheel-soil interface for various wheel degrees of slip. This permits successful prediction of wheel performance (in energy terms) at any degree of slip.

PREDICTION DU RENDEMENT D'UNE ROUE MOBILE ET RIGIDE ET COMPORTEMENT DU SOL EN DESSOUS DE LA ROUE

RESUME

L'objet de cette étude est de fournir une méthode analytique et rationelle pour prédire le rendement d'une roue mobile et rigide, ainsi que le comportement du sol en dessous de la roue.

Cette étude (a) considère l'effet des conditions de la surface sur le rendement de la roue et sur le comportement du sol en dessous de la roue; (b) développe une solution au problème considéré, par la méthode des éléments finis; (c) évalue le rendement réel des roues d'épreuve par la méthode de visioplasticité; (d) tente de valider l'application de la méthode des éléments finis à l'analyse du mouvement d'une roue mobile et rigide sur un sol cohésif, sous des conditions de déformation plane, et ce, en comparant la théorie avec les résultats expérimentaux.

La solution fournit des renseignements détaillés sur les champs d'effort et de déformation dans les sols chargés, ainsi que sur l'effort de contact à la surface sol-roue, et ce pour des roues différentes et des degrés de glissage différents. Ceci permet la prédiction du rendement d'une roue (en termes d'énergie) à n'importe quel degré de glissage.

ACKNOWLEDGEMENTS

The author wishes to express his most sincere and deepest appreciation to his research director, Dr. R.N. Yong, William Scott Professor of Civil Engineering and Applied Mechanics, for his guidance, inspiration, many helpful suggestions and comments throughout this investigation.

This study was performed under contract arrangement with the Department of Supply and Services and McGill University/Dr. R.N. Yong, and was administered by the Earth Science Division of the Defence Research Establishment, Ottawa, with Mr. I.S. Lindsay as Project Officer. Appreciation is expressed for the Research Assistantship provided by the contract arrangement.

The writer also wishes to thank his colleagues, Dr. A. Hanna for stimulating discussions, Messrs. A.F. Youssef and R. Lyange for assistance in experimentation, and Dr. F. Ajami for assistance in the preparation of the final manuscript.

Thanks are also due to Mr. B. Cockayne and his staff for technical help, and Miss J.M. Richards for typing this dissertation.

LIST OF FIGURES

LIST OF FIGURES (cont'd)

LIST OF FIGURES (cont'd)

LIST OF FIGURES (cont'd)

LIST OF FIGURES (cont'd)

LIST OF FIGURES (cont'd)

LIST OF TABLES

NOTATIONS

The symbols adopted in this study are defined where they first appear and the principal ones are listed below.

W	wheel load
T	input torque
P	drawbar pull
V	translational wheel velocity
ω	angular velocity of the wheel
Z	dynamic sinkage
C and ϕ	soil strength parameters
U, V	displacement or velocity components
K	element stiffness matrix
E	elastic modulus
E_o	initial elastic modulus
E_T	slope of the deviator stress $(\sigma_1 - \sigma_3)$, versus principal strain, ε_1, curve
σ	normal stress on failure plane
a, b	designate families of characteristics
$\dot{W}$	plastic work rate
I_2	strain rate invariant
ε_x, ε_y	normal strain components
γ_{xy}	shear strain
k	Von Mises yield function

$\sigma_1, \sigma_2, \sigma_3$	principal stresses
σ_x, σ_y	normal stress components
τ	tangential stress
η	viscosity parameter
J_2	second invariant of deviatoric stress tensor
$\dot{F}$	rate of interfacial energy loss
V_s	elemental slip velocity
r	wheel radius
b	wheel width
R_T	tangential reaction at wheel-soil interface
XI, YI, X, Y	coordinates
$\bar{\varepsilon}$	effective strain
ρ	specific mass
S	normal wheel slip rate

ABBREVIATIONS

ASCE	American Society of Civil Engineering
BDC	bottom dead center
DBP	drawbar pull
ft	feet
lb(s)	pound(s)
ISTVS	International Society of Terrain Vehicle Systems
min.	minute
psi	pounds per square inch
sec.	second
S.F.D.	source to film distance
SMFD	Soil Mechanics and Foundations Division
S.O.D.	source to object distance
VISIOPLS	visioplasticity method
W.E.S.	U.S. Army Waterways Experiment Station, Vicksburg, Mississippi
{ }	column vector
[ ]	matrix form

CHAPTER 1

INTRODUCTION

1.1 General

The mechanics of off-road transportation or land locomotion is concerned with the complex problems of interaction between wheeled or tracked vehicles and various types and conditions of natural terrain surfaces. The need for basic research on the ground properties which affect vehicle performance is evident from experience of land locomotion in the areas of military and civilian mobility, agriculture mechanization, timber transportation and earth-moving equipment.

The recent past has seen an increase in research efforts in the field of land locomotion mechanics to obtain a better understanding of the action of soil vehicle systems. These studies are generally directed toward the problems most frequently encountered in the field by land vehicles operating over natural ground surfaces that fall in the categories of loose or soft soil. The basic problems in these soil types are excessive wheel or track sinkage due to physical characteristics of both the soil and the vehicle, and excessive wheel or track slippage caused by insufficient traction (Goodman, 1966).

The objective of the study of track or wheel mechanics in soft or loose soil is to predict what will happen to a vehicle tractive element in given conditions. Assuming all the necessary characteristics of the tractive element (track or wheel) and the soil are known, the problem is to determine the relations among the load on the vehicle tractive element, the torque, the pull that the tractive element can develop (hence slip and sinkage), and the soil conditions.

Slip is important with respect to efficiency because, for a given tractive element speed, the vehicle reduces the distance over which the pull does work. Sinkage should be controlled, for it must remain smaller than the clearance of the vehicle. The tractive-soil parameters which control the vehicle performance are shown in Figure 1.1.

1.2 Statement of the Problem

The ability of a vehicle to move over soft or loose soil is dependent on the interaction between the vehicle running gear (wheel or track) and the supporting ground. For this study, the ground in question is soft soil. The mechanism of wheel-soil interaction consists of two parts: (a) Flotation, which deals with the ability of the ground to support the vehicle without excessive sinkage, and (b) Traction, which involves forces developed between the vehicle running gear and soil in the development of continuous vehicle motion. The characteristics of the vehicle tractive element (running gear) control its performance with respect to any specific type of soil.

Within the broad definition of the problem, there are numerous paths that can be followed for predicting tractive element performance according to emphasis and assumptions made, as shown in Figure 1.2.

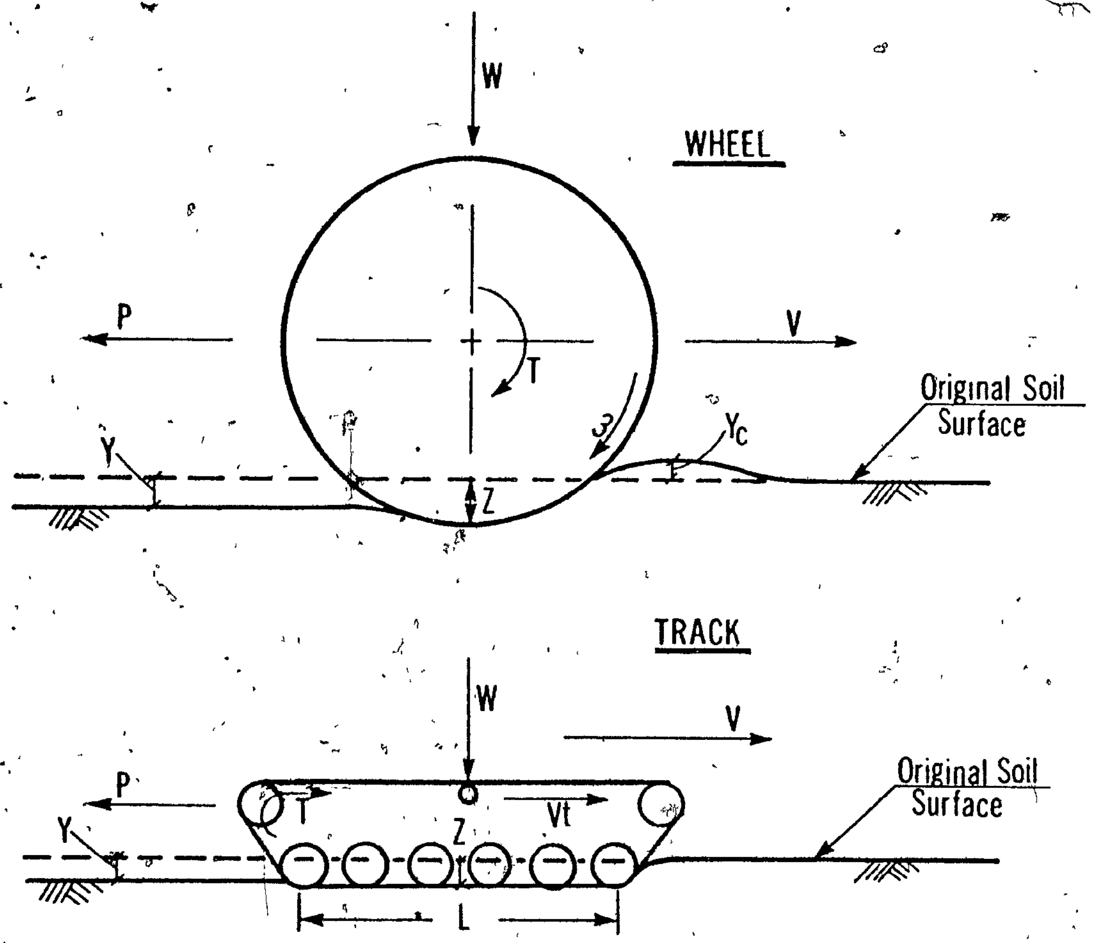

Legend:

Tractive Element Parameters

W Gear load
T Input torque
P Drawbar pull
V Translation velocity
ω Angular velocity
V_T Track speed
Z Dynamic sinkage
Y Depth of rut
Y_C Bow wave
L Soil-tractive element contact length

Soil Parameters

Plate: K_c and K_ϕ
Cone: Cone index
Vane-cone: Interfacial and deformation energies-C and ϕ
Triaxial Test: Stress-strain relations C and ϕ

Fig. 1.1 Tractive Element-Soil Parameters

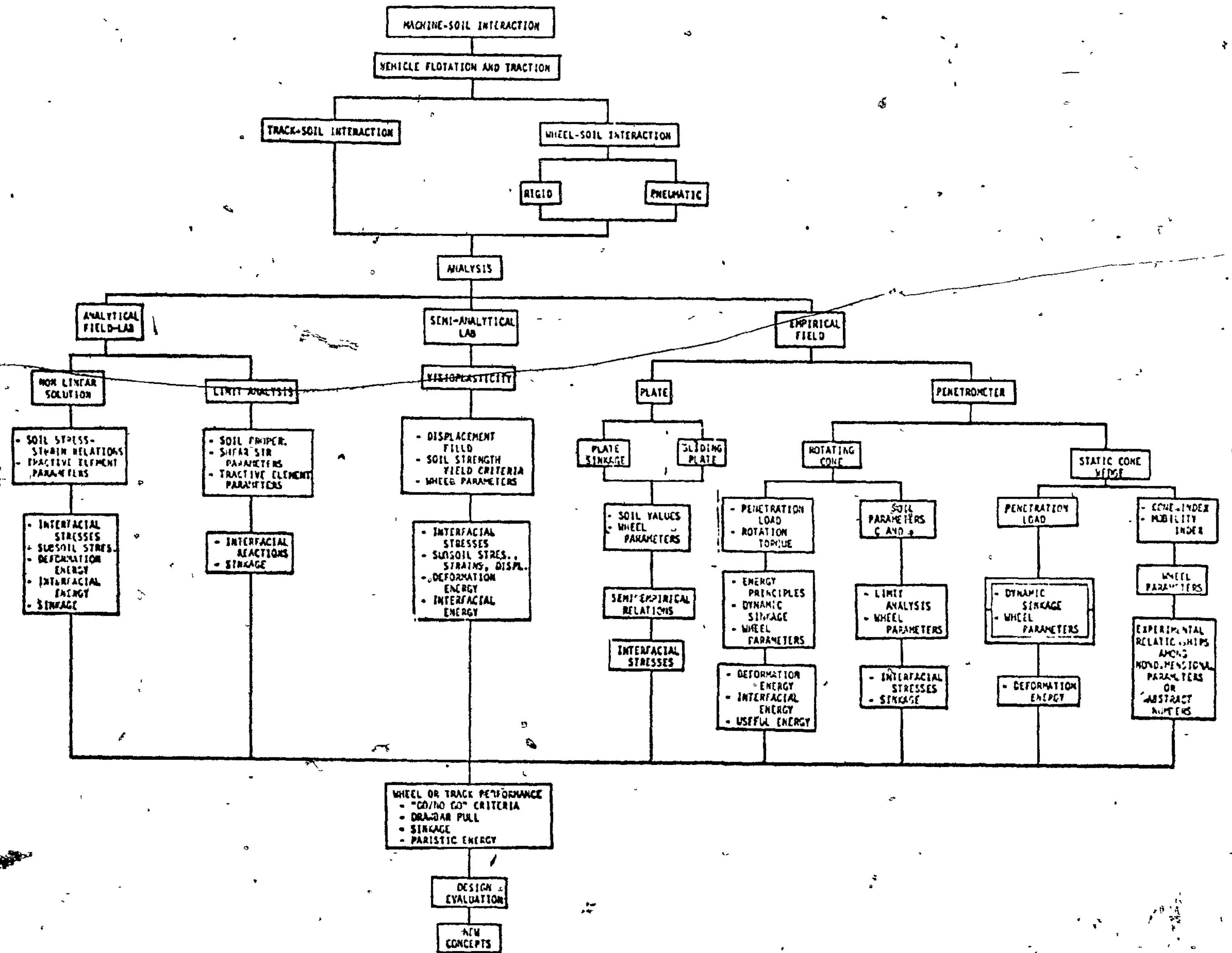

Figure 1.2 Different Techniques for Tractive Element Performance Prediction

A first approach is to attempt to predict wheel performance by determining the drawbar pull, torque, and possibly the slip and the sinkage from analyses using the relations between stresses and strain in the soil and both equilibrium conditions and the boundary conditions.

A complete theoretical solution of the wheel performance prediction problem is extremely complex because of the difficulties arising from the interdependence of such factors as:

(i)	Physical conditions:	Wheel load, wheel surface condition, wheel diameter, tire shape, tire flexibility, treads, etc.
(ii)	Soil parameters:	Strength, type, density, moisture, content, etc.
(iii)	Interaction parameters:	Translational velocity, slip, wheel type (towed or driven), etc.

Previous wheel-soil interaction theoretical considerations have utilized limit equilibrium assumptions to predict wheel-soil interfacial stresses and sinkage (Yong & Windisch, 1970; Karafiath, 1971). The assumptions adopted in the limit equilibrium analyses are described as follows:

1. The soil is an ideal rigid plastic material in a state of limit equilibrium, and is considered to obey the Mohr-Coulomb failure criteria.
2. The soil has well-defined slip surfaces at the wheel front and rear positions.

3. The angles described by the forward and rear failure zones are functions of the degree of slip and total angle of wheel-soil contact surface.

Figure 1.3 shows an idealization of the wheel-soil interaction physical model required for the limit equilibrium solution.

It is observed that in using the method of characteristics for solving limit equilibrium problems, exact solutions for the assumptions invoked are obtained. However, in the case of wheel-soil interaction problems, the assumptions utilized tend to be too restrictive and in actual fact do not realistically mirror actual physical observations.

Existing semi-empirical formulae for the prediction of wheel performance such as drawbar pull, sinkage and bulldozing resistance depend, in essence, on a prediction of the stress distribution along the soil-wheel interface from data obtained from static tests on flat plates. The plate approach previously adopted by many research workers used the idea of flotation (Bernstein, 1913; Micklethwaite, 1944; Bekker, 1956) to predict the wheel-soil interfacial stresses and sinkage from a correlation between the pressure under plate penetration test and that under the wheel. The wheel-soil tangential stresses predicted from the established relationships correlate the tangential stresses beneath skid plate (Bekker, 1969) or shear ring (Reece, 1964) to that under the wheel for the same slip velocity and radial pressure. Since (a) these relationships are based on curve-fitting procedures and (b) the flow of soil beneath a wheel and a plate are different, there is no a priori reason to believe that relationships based on such an approach would be completely successful.

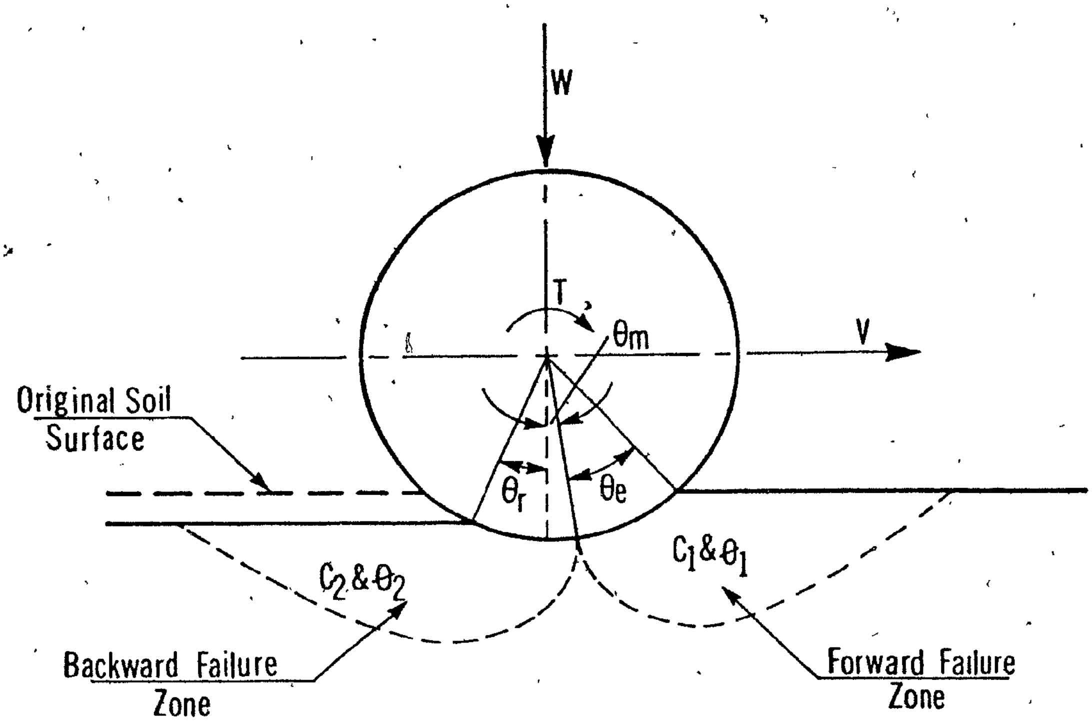

Legend:

C_1 and ϕ_1	Soil strength parameters at Forward Failure Zone
C_2 and ϕ_2	Soil strength parameters at Backward Failure Zone
θ_m	Angle of separation
θ_r	Rear angle
θ_e	Entry angle
D	Wheel diameter

Fig. 1.3 Idealization of the Physical Model for Limit Equilibrium Solution (Method of Characteristics)

The cone penetrometer, as a tool for evaluating the performance of off-road vehicles, uses graphical relationships between independent (mobility index, vehicle cone index, clay loading number, etc.) and dependent (pull number, torque number, sinkage number) dimensionless parameters, (Freitage, 1965; Rush & Temple, 1967; Kennedy & Rush, 1968). This technique lacks accuracy for the following reasons:

(a) Difference in soil behaviour under the penetrating cone and the moving wheel.

(b) Interdependence of many of the wheel-soil parameters.

(c) Difficulty in realization of dimensionless soil parameters.

A more rigorous mathematical approach for using the cone as a trafficability sampler has been adopted by Yong et al. (1971). Since the behaviour of the soil beneath the cone and the wheel is different, the approach should be dependent on scalar quantities (Yong et al., 1971). The specific deformation energy under the wheel at the self-propelled point is correlated to that under the penetrating cone. With a knowledge of the parasitic deformation energy beneath the moving wheel and of the wheel brake horsepower, a "GO/NO GO" criterion can be decided, assuming that the wheel-soil interfacial energy at the self-propelled point is negligible.

The existing problem is one which requires accurate field performance evaluation of the vehicle with respect to a specific type of ground surface. Alternatively, the design criteria for vehicle tractive elements for production of specific optimum performance needs to be rationally developed.

It is worth mentioning that the performance can be evaluated in many terms such as drawbar pull, input torque, sinkage, interfacial stresses, translational velocity, slip, soil compaction, ecological damage, subsoil behaviour or, in energy terms, as input, useful output and parasitic energies. The relative importance of the different performance terms is dependent on the type of vehicle job and the ground useful function.

This thesis is concerned with (a) the development of an analytical method for the prediction of the field performance of a moving wheel over soft soil, and (b) the application of the method to the study of the effect of simple wheel surface configurations on performance.

While much effort has been spent in evaluating wheel performance from both surficial measurements of the stress distribution at the wheel-soil interface and from rut depth measurements, very little corroboration is available relative to stress distribution and soil deformation due to a moving wheel prior to the work reported by Yong & Osler (1966), Yong & Webb (1969), and Yong & Windisch (1970). This is because consistency between surficial measurements and ground response is generally demanded. In essence, compatibility must be maintained between forcing (vehicle) and response (soil) functions.

In this study, an analytical method and a computer program are developed for evaluating and predicting wheel performance through prediction of subsoil response behaviour. The program permits:

1. Specification of a physical model which satisfies compatibility, equilibrium, boundary conditions and a stress-strain law.

2. Specification of realistic stress-strain soil relations.

3. Generation of a unique and complete solution.

4. Generation of the information necessary for the mechanics of the soil-wheel interaction problem.

1.3 Rationale for Problem Solution

Yong et al. (1975) introduced a soil strength measurement device which combined the vane shear apparatus with the cone penetrometer for use not only as a trafficability sampler but also as a tool for evaluating wheel performance. The rationale for the device was based on previous research (Yong et al., 1972; 1975) which established a correlation between the parasitic energy components of the wheel-soil interaction and the degree of slip. Figure 1.4a shows the wheel energy components and figure 1-4b shows the distribution of parasitic energy components.

The development of the understanding of the instantaneous soil response below the moving wheel and its performance required investigation of the mechanism of wheel-soil interaction and the subsoil deformation pattern. Yong & Webb (1969) used the visioplasticity technique for determining the wheel parasitic energy components and the useful output energy at any degree of slip, while Yong & Windisch (1970) used it for determining the interfacial and subsoil stresses. In this method the

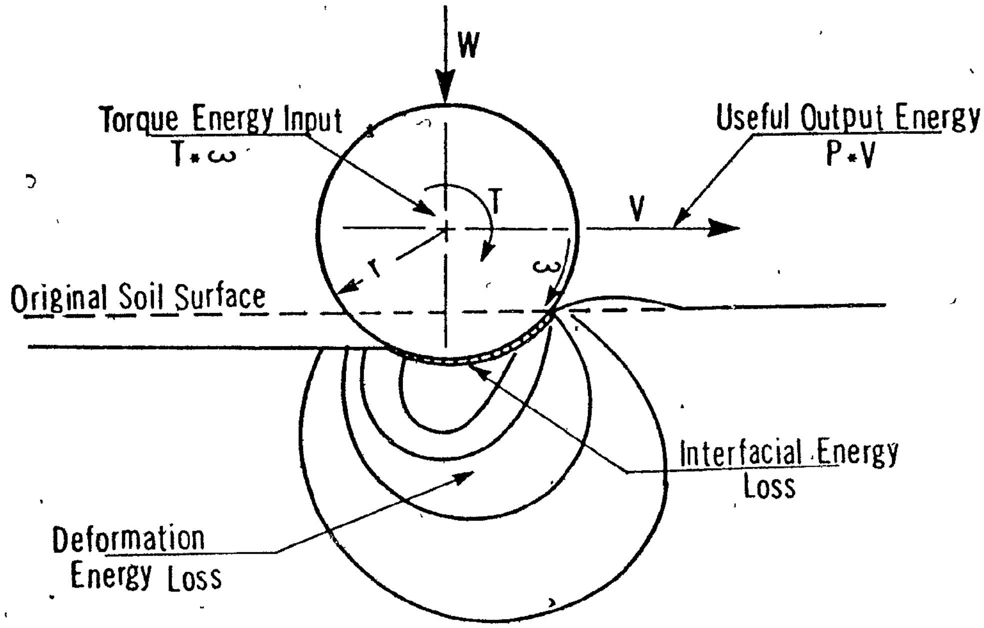

Fig. 1.4a Types of Input and Output Energy

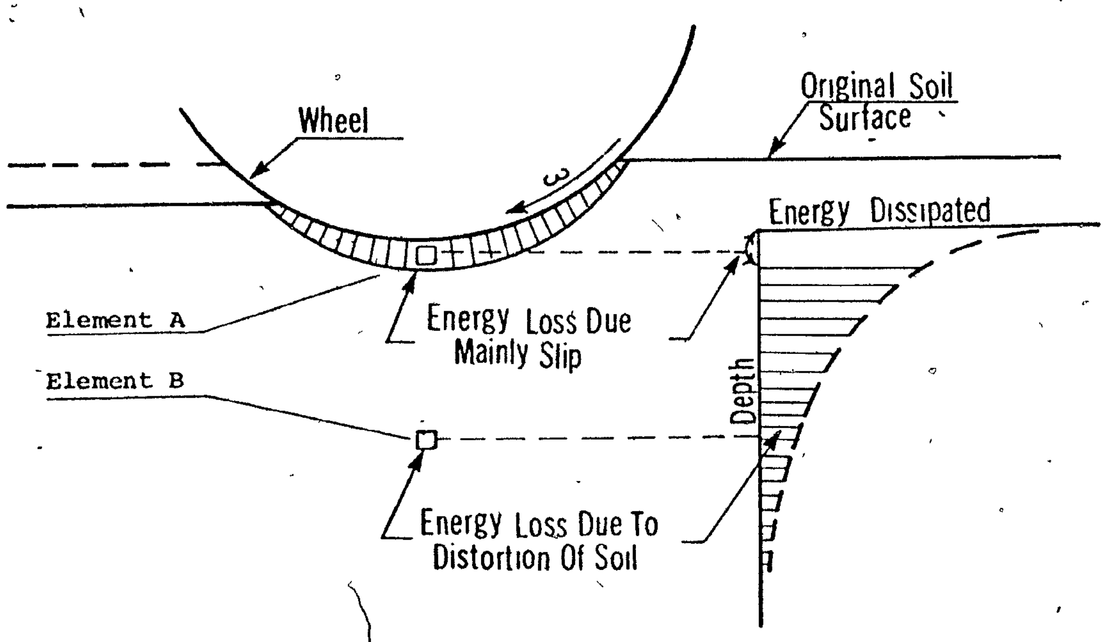

Fig. 1.4b Energy Dissipation in Substrate due to Interaction
(after Yong, 1972)

displacement field is recorded experimentally, from which a stress field is determined using a constitutive relationship. The development of this method is presently applicable to small scale testing in the laboratory (assuming steady state conditions) and cannot be readily used to predict field conditions.

It needs to be noted that research conducted to date on the problems of design or evaluation of wheel performance have adopted three basic approaches:

(a) the empirical approach - using the results of large amounts of experimental data obtained to develop methods of analysis and design.
While such approaches may have been necessary in the past, the advent of digital computers and modern methods of numerical analysis now provide the necessary tools to develop analytical solutions which can replace much of the empirical testing carried out in the past.

(b) the theoretical approach - using the limit equilibrium technique with its unrealistic ideal assumptions which do not fully satisfy the actual physical situation.

(c) a laboratory approach - which is limited to studying or evaluating the wheel performance in the laboratory.

As there is no available rational approach for evaluating both tractive element performance and soil behaviour beneath it, and since the visioplasticity method is presently restricted to laboratory application, it is apparent that a numerical method (such as the finite element method) which can predict both tractive element performance and soil response behaviour in the field would be a useful tool in soil-machine interaction studies.

1.4 Objective of the Study

The general objective of this research is to provide a rational analytical means for predicting the performance of off-road vehicle tractive elements moving on loose or soft soil, using parameters that describe the soil response due to interaction with the vehicle tractive element. It is to be appreciated that an accurate prediction of machine-soil response behaviour would provide a sound basis for the evaluation of the efficiency and economy of mobility (vehicle flotation and travel). In addition, the developed computer solution technique can be used to aid in the design of the interacting units since the various machine and soil parametric inputs to the computer code can be varied, and the resultant output evaluated. This philosophy is demonstrated in schematic form in Figure 1.5. The thrust of the argument is seen to lie in the need for a tool which would readily evaluate and assess performance of machine-soil interaction.

This study includes an analytical and an experimental approach. Analytically, a computer program based on the finite element method will be obtained. This program will provide an analytical tool that can be used by the designer, in field investigations, to evaluate automatically the

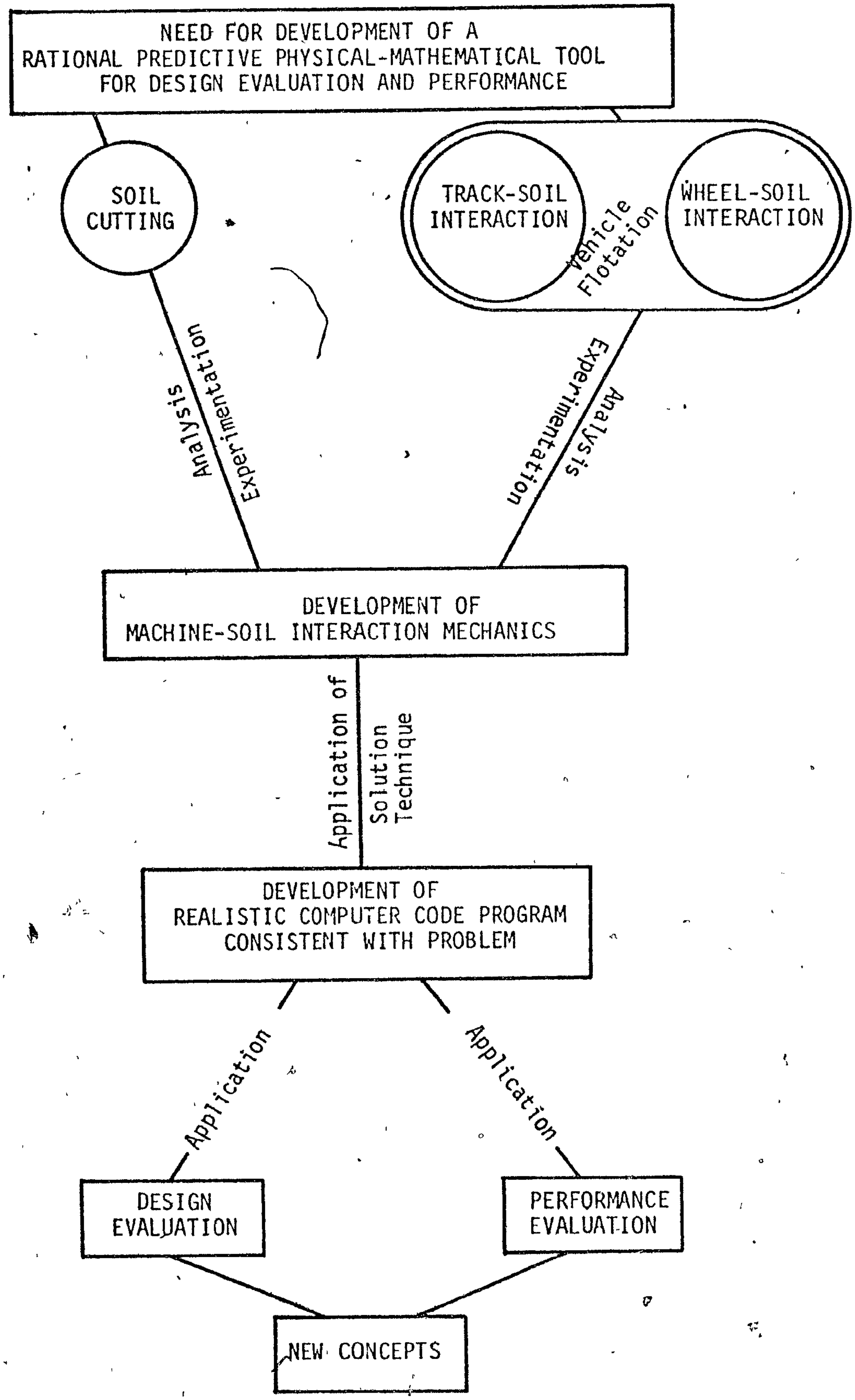

Figure 1.5 Schematic Representation of Machine-Interaction Study Purpose (Yong, Fattah and Hanna, 1972)

performance of the tractive elements of the vehicle and soil deformation behaviour beneath it, provided that a technique for measuring the interfacial stresses or particle path at wheel-soil interface is available.

Experimentally, the visioplasticity technique is used to study the effect of wheel-surface condition on its performance and subsoil behaviour beneath it and to verify the validity of the analytical model. The measurement of the surficial, above-ground paramaters,namely load, torque, drawbar pull, carriage velocity, sinkage, angular velocity as well as measurement of subsoil deformation, are also included in this part.

It is also worthy to mention that throughout this study the above aspects and considerations are presented in regard to towed and driven rigid wheels. The items of specific note are:

1. The dissipation of energy in the soil at the interface and in the subsoil as a result of soil response during the movement of the rigid wheel.
2. Prediction of wheel performance in terms of drawbar pull, sinkage, deformation energy and interfacial energy.
3. Study of the effect of controlled wheel slip on the magnitude of the interfacial and deformation energy developed.
4. Study of the effect of wheel surface condition on its performance.
5. Accountability of the effect of soil recovery at the rear of the wheel on prediction of wheel performance.

Adopting the finite element method (FEM) in the field of wheel-soil interaction studies will account for the following aspects:

(i) the non-uniform geometrical boundaries at wheel-soil interface and soil surface,

(ii) the soil nonlinear stress-strain relations,

(iii) the effect of loading and unloading of soil due to wheel travel,

(iv) any constitutive relations covering the effect of confining pressure, volume change or strain rate can be used with the method,

(v) the loading path can be followed throughout, using the particle path at wheel-soil interface as a loading boundary,

(vi) the effect of change of material coordinates due to wheel travel can be considered.

It is worthy to note that in the FEM, subsoil behaviour in terms of stresses, strains, deformations, deformation energy and interfacial energy can be predicted.

1.5 Organization of the Thesis

This thesis is presented in eight chapters and six appendices. The organization of the main body of the thesis is shown in Figure 1.6, and the outlines of each chapter and appendix are as follows.

Chapter 1 gives a definition of the problem of wheel-soil interaction together with a short review of the previous methods for evaluating the performance of off-road wheels.

Chapter 2 describes the general formulation of the governing equations of the finite element method, and the different approaches for their non-linear solutions.

Chapter 3 describes the general idealization of the non-linear behaviour of soil, the finite element idealization of the soil beneath the wheel, the boundary conditions and the incremental approach for solving the non-linear problems.

Chapter 4 describes the experimental program, the visioplasticity technique, and presents a summary of the results.

Chapter 5 discusses the results of the experimental analysis and the effect of slip on wheel performance.

Chapter 6 discusses the validity of the FEM as a technique for evaluating wheel performance. The FE results are compared with surficial and subsoil measurements. Also, the performance prediction using both visioplasticity and FEM are compared in this chapter.

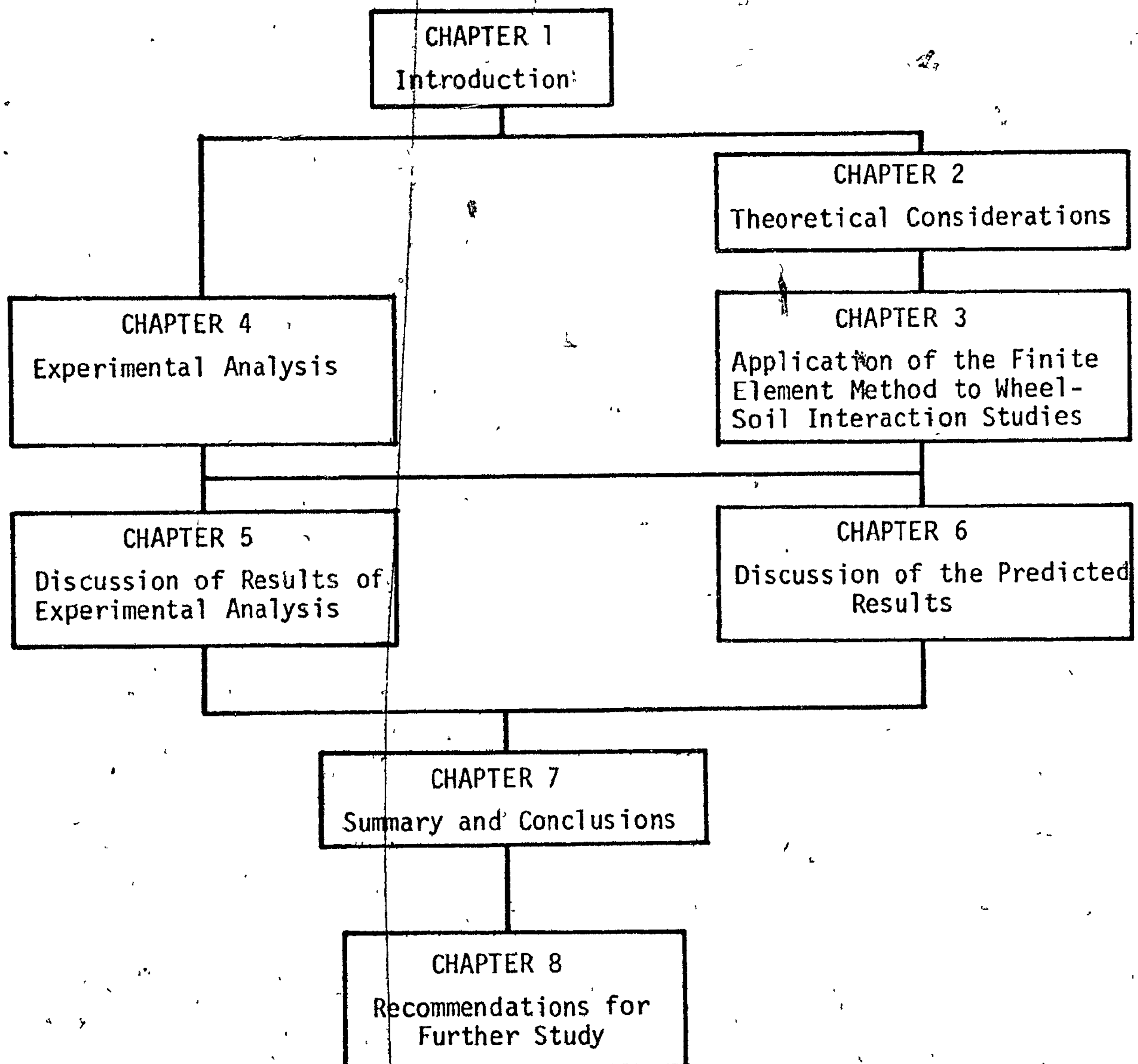

Figure 1.6 Organization of the Main Body of the Thesis

Chapter 7 contains the summary and conclusions.

Chapter 8 contains the recommendations for further study.

Appendices

Appendix A - Experimental Considerations. Describes the soil-vehicle mobility test facilities, the soil preparation and the testing procedures, and the physical, chemical and mechanical properties of the soil.

Appendix B - Data Reduction Techniques. Describes the techniques for reducing the data concerning the subsoil deformation behaviour.

Appendix C - Visioplasticity. Describes the computer program used for analysing the data concerning the subsoil deformation behaviour.

Appendix D - Constitutive Relations. Describes the different approaches used in soil-mechanics for idealizing soil stress-strain curves and constitutive relations.

Appendix E - Method of Characteristics. Describes the method of characteristics which was adopted for determining the subsoil and wheel-soil interfacial stresses.

Appendix F - Finite Element Computer Programs. Describes the different sub-routines used in the Finite Element Programme.

CHAPTER 2

THEORETICAL CONSIDERATIONS

2.1 Introduction

As stated in Chapter 1, there are different techniques for predicting (a) the performance of a moving off-road wheel, (b) the behaviour of the soil beneath the wheel, or (c) both. In this analysis the problem of a moving wheel over soft soil is studied by considering the soil as a continuum with its entire boundary being a mixed boundary on which loads and displacements take on prescribed values.

Having established a physical model for wheel-soil interaction study, an analytical model can be constructed and an exact or numerical solution for predicting the wheel performance and subsoil behaviour beneath it can be obtained. The accuracy of the predicted results is dependent on:

(a) the accuracy of the physical model in representing the problem,

(b) the accuracy of the analytical model in representing the physical model parameters,

(c) the accuracy of the mathematical solution.

The adopted mathematical solution is mainly dependent on:

(a) the assumptions made in constructing the governing equations of the analytical model,

(b) the type of the available input data,

(c) the required output results,

(d) the accuracy of the predicted results,

(e) the economy of the solution.

Many numerical techniques can be attempted in developing a solution for a particular wheel-soil interaction problem; among them are the semi-inverse approach, the finite difference, and the finite element method.

2.1.1. Semi-Inverse Approach

If certain wheel parameters (load, input torque) and soil parameters (C and ϕ) are known and certain assumptions concerning the state of the soil, the soil surface, and the physical boundaries at the wheel-soil surface are made, a semi-inverse approach can be adopted for predicting the wheel-soil interfacial stresses (Sokolovski, 1965; Karafiath, 1971). In this approach, it is assumed that certain properties for the solution are outright and that the problems, in which field equations and boundary conditions are obtainable, can be satisfied by assumed forms of solution.

This type of analysis has been adopted in wheel-soil interaction studies (Karafiath, 1975; Elsamny & Ghobarah, 1972)with the following restrictive assumptions:

(a) the soil beneath the wheel is in a state of limit equilibrium,

(b) the soil has straight surfaces in front of and to the rear of the wheel,

(c) the soil outside the failure zones is rigid,

(d) the angle of separation between front and backward failure zones is a function of slip.

As noted, these conditions are too restrictive and do not represent the physical situation of the problem. In this type of solution the discontinuity in the stress and velocity fields between the failure zone and the rigid zone is neglected. The predicted results indicate a discontinuity at the peak of the stress distribution at the wheel-soil interface (Karafiath, 1971, 75). Since no constitutive relations are used with this type of analysis no subsoil behaviour can be predicted. Figure 2-1 shows the block diagram for the solution using a limit equilibrium approach.

2.1.2 Finite Difference Technique

Since the equilibrium and compatibility equations are independent of the material-constitutive relations, it is possible to solve many non-linear material problems whose elastic solution can be obtained, by numerical method using an iterative technique based on successive elastic approach (Mendelson, 1969). In the case of plane strain or stress elasto plastic problems, it is necessary to solve an inhomogeneous biharmonic equation subjected to a special type of boundary conditions and to the appropriate plasticity relations. There is a variety of methods that can be used for solving the biharmonic equation, including the energy collocation, eigenfunction and finite difference methods. In all cases the solution is actually only approximate, although in theory the exact

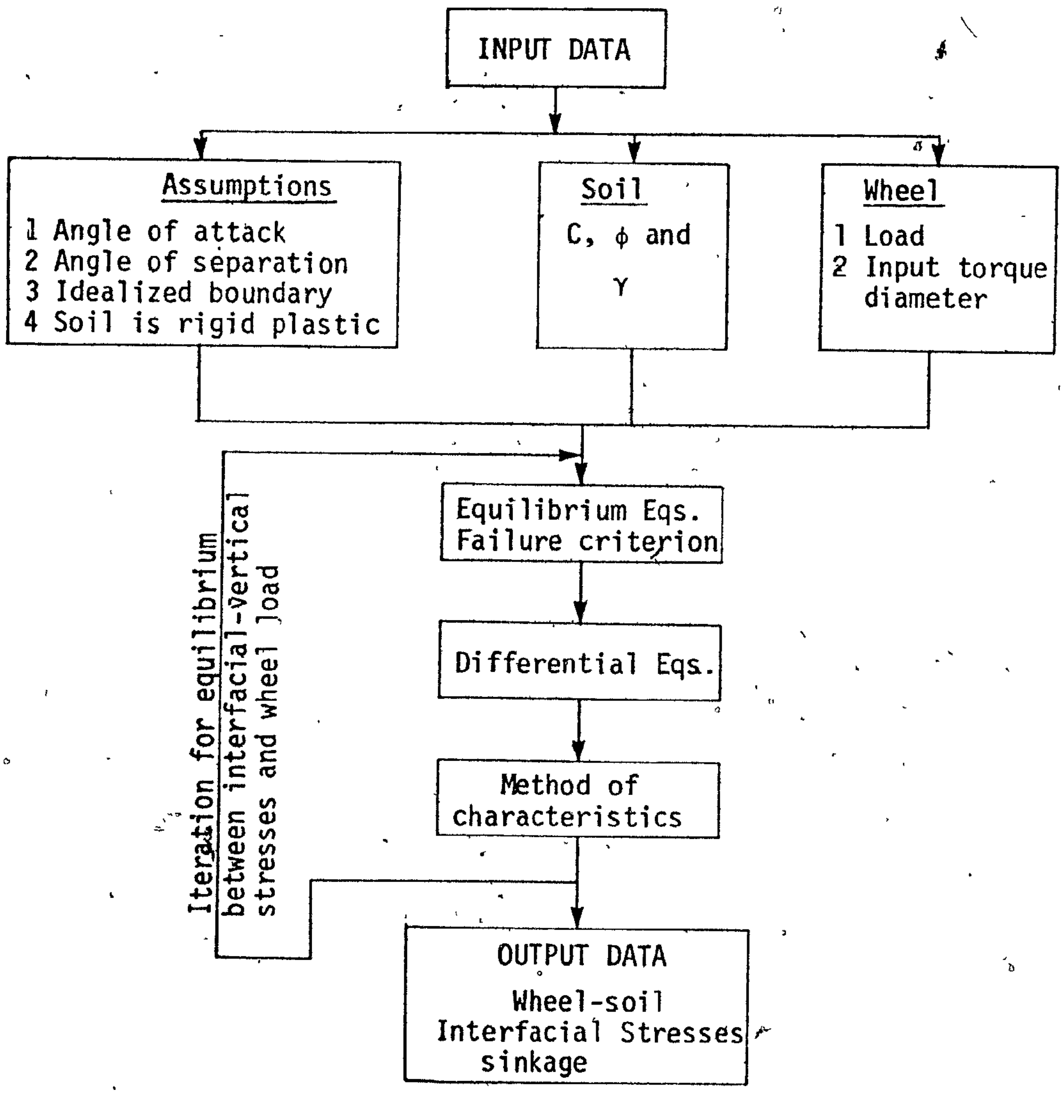

Fig. 2-1 Block diagram for semi-inverse approach (Limit Analysis)

solution can be approached as closely as desired. The simplest and most straightforward approach is to use finite differences. Details of the method are explained in many references (Mendelson, 1969).

The application of the finite-difference technique to wheel-soil interaction studies to predict subsoil behaviour requires:

(a) a knowledge of the stress distribution at wheel-soil interface,
(b) uniform geometrical boundary conditions,
(c) idealizing the stress-strain relations of the soil to elastic, elastic-plastic or strain hardening behaviour,
(d) the soil is incompressible in the elastic and plastic zones and obeys Prandtl-Reuss relations and Von Mises yield criteria.

Using uniform grid for the formulation of the finite difference equations limits its application to problems of simple geometric boundary conditions. Using the same size grid in zones of high and low stress concentrations will result in large approximations if a coarse grid is used. A block diagram of the application of the finite difference technique to wheel-soil interaction problem is shown in Figure 2-2.

2.1.3 Finite Element Method

The use of the finite element method as an approximate numerical solution procedure for solving many kinds of linear and non-linear continuum mechanics problems may be found in several references (Zienkiewicz, 1971; Oden, 1972; Desai & Abel, 1972). Its physically motivated base and its compatability with various kinds of boundary conditions and constitutive

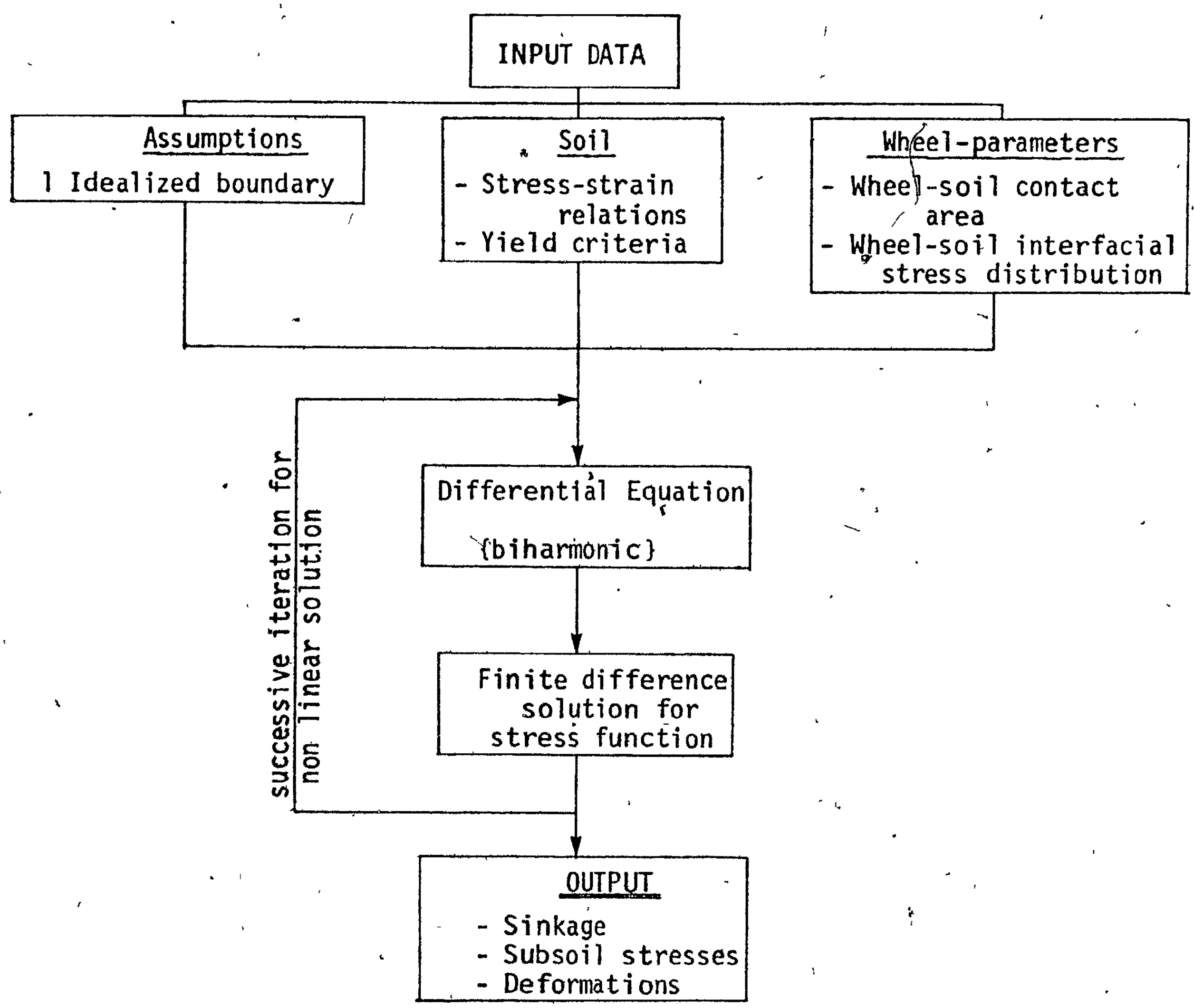

Fig. 2-2 Block diagram for predicting subsoil behaviour using Finite Difference Technique

relationships, render it a useful technique for the solution of initial boundary value problems. The technique basically adopts the Rayleigh-Ritz method by means of a variational approach, whereby formulation of the equivalent of the governing relationship in integral form, over the region of interest, allows for application of approximate methods of solution. It is noted that the true solution of the problem under consideration will always render the integral a minimum.

The basic concept of the finite element method is the idealization of an actual continuum as an assemblage of discrete elements interconnected at their nodal points. Often in soil mechanics, load deformation problems are of the plane strain variety such that triangular or higher order plate finite elements are useful in analyzing the two-dimensional strain field. Since the FEM is used in this study for evaluating wheel performance and soil behaviour beneath it, a brief development of the governing relationships is presented. Since this study is concerned with a transient phenomenon of a moving rigid wheel on soft soil, the FEM solution deals with a non-linear problem involving large deformations and associated non-linear material properties. Due to the resultant large deformations of the soil beneath the moving wheel, the FEM governing relationships can be formulated with respect to either the original or the updated soil coordinates; both formulations are presented herein in general form.

2.2 General Formulation of FEM Equilibrium Equations

In the body occupying a space S in Figure 2-3 (referred to as a rectangular frame of reference) every particle has a set of coordinates. The location of a point P in the body, before deformation is defined by:*

$$\{X\} = \{X_1, X_2, X_3\}^T \tag{2.1}$$

where

X_1, X_2 and X_3 refer to the Euclidian coordinates X, Y and Z.

After the deformation one obtains

$$\{\bar{X}\} = \{\bar{X}_1, \bar{X}_2, \bar{X}_3\}^T \tag{2.2}$$

where

$$\{\bar{X}\} = \{X\}^T + \{U\}^T \tag{2.3}$$

and

$\{U\}$ is the displacement.

$$\{U\} = \{U_1, U_2, U_3\}^T \tag{2.4}$$

Using the finite element approximation

$$\{U\} = [N]\{\delta\} \tag{2.5}$$

---

* Superscript T denotes a transposed matrix.
{ } denotes a column vector.
[ ] denotes a matrix form.

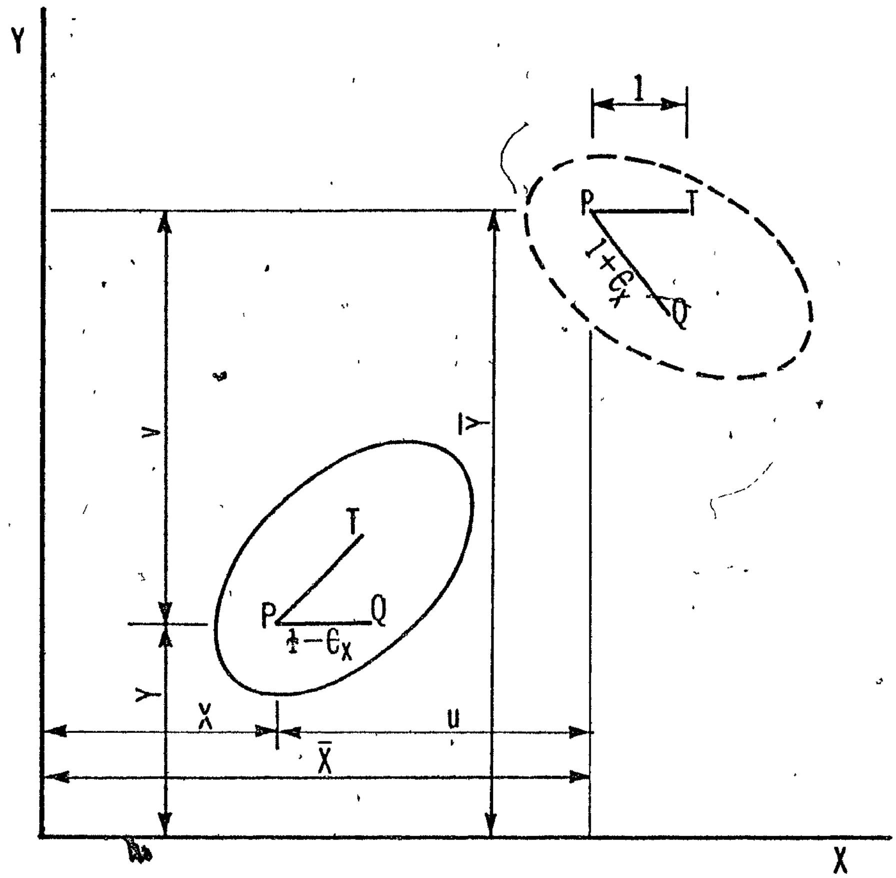

Fig. 2.3 Definition of Lagrangian and Eulerian Coordinates and Strains (Zienkiewicz, 1971).

where

{U} relates specifically to the displacement at any point within a finite element.

{δ} is the displacement at the nodal points.

[N] is the shape function which defines the displacement at any point within the element with respect to the displacements at the nodal points.

For constant strain triangular element formulation, Eq.(2.5) takes the following form in matrix notation (Fig. 2-4).

$$\begin{Bmatrix} U \\ V \end{Bmatrix} = \begin{bmatrix} N'_i & 0 & N'_j & 0 & N'_m & 0 \\ 0 & N'_i & 0 & N'_j & 0 & N'_m \end{bmatrix} \begin{Bmatrix} U_i \\ V_i \\ U_j \\ V_j \\ U_m \\ V_m \end{Bmatrix} \tag{2.5'}$$

where

$N'_i = (a_i + b_i X + C_i y)/2\Delta$

Δ = area of triangle ijm

$a_i = X_j Y_m - X_m Y_j$

$b_i = Y_j - Y_m$

$c_i = X_m - X_j$

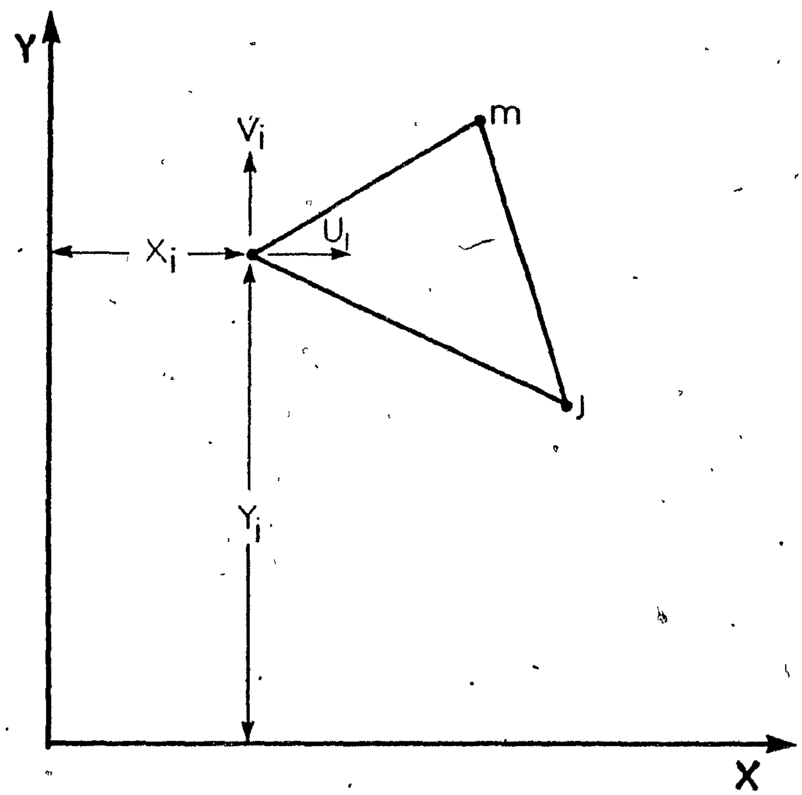

Figure 2.4 An element of a continuum in plane strain

Using the principle of virtual work and equating the external and internal work, we may obtain the [approximate] equilibrium equations in Lagrangian (original) or Eulerian (updated) coordinate form, (Zienkiewicz, 1971).

The external work done in terms of Eulerian and Lagrangian coordinates can be written as:

$$\int_{\bar{V}} \bar{P}\{q\}^T\{du\}d\bar{V} + \int_{\bar{A}} \{\bar{P}\}\{du\}d\bar{A} \qquad \text{(Eulerian)} \qquad (2.6)$$

$$\int_{V} p\{q\}^T\{du\}dV + \int_{A} [\frac{d\bar{A}}{dA}\{P\}^T]\{dv\}dA \qquad \text{(Lagrangian)} \qquad (2.7)$$

and the internal work done may be written as

$$\int_{\bar{V}} \{\bar{\sigma}\}^T d\{\bar{e}\}dV \qquad \text{(Eulerian)} \qquad (2.8)$$

$$\int_{V} \{\sigma\}^T d\{\varepsilon\}dV \qquad \text{(Lagrangian)} \qquad (2.9)$$

The relation between strain and displacement can be written in terms of Eulerian and Lagrangian coordinates respectively, as

$$d\{\bar{e}\} = [\bar{B}]\ d\{\delta\} \qquad \text{(Eulerian)} \qquad (2.10)$$

The matrix [B] defines the strain displacement relation.

$$d\{\varepsilon\} = [B]\, d\,\{\delta\} \qquad \text{(Lagrangian)} \quad (2.11)$$

Using the previous relations and equating (2.6) and (2.8), the equilibrium equations in terms of the Eulerian system are obtained as:

$$\{\bar{\psi}\} = \{\bar{R}\} - \int_{\bar{V}} [\bar{B}]^T \{\sigma\}\, d\bar{V} = 0 \qquad (2.12)$$

Similarly, in terms of the Lagrangian system, by equating (2.7) and (2.9)

$$\{\psi\} = \{R\} - \int_V [B]\{\sigma\} dV = 0 \qquad (2.13)$$

where

$$\{\bar{R}\} = \{R\} = \int_{\bar{V}} \bar{\rho}[N]^T\{q\}d\bar{V} + \int_{\bar{A}} [N]^T\{\bar{p}\}d\bar{A}$$

$$= \int \rho[N]^T\{q\}dV + \int_A [N]^T\{\bar{p}\}\frac{d\bar{A}}{dA}\, dA \qquad (2.14)$$

where

{R} represents the equivalent external nodal forces, while the second term in equation (2.12) or (2.13), the internal force reaction.

$\{\psi\}$ represents the nodal forces required to bring the assumed displacement pattern into nodal equilibrium.

$\{\bar{P}\}$ represents surface forces per unit area of the deformed body.

$\{q\}$ represents the body forces per unit mass.

$\bar{V}$ and $\bar{A}$ are the volumes and areas of the deformed body respectively.

$\bar{\rho}$ is the density in the deformed state.

$\{\bar{\sigma}\}$ and $d\{\bar{\varepsilon}\}$ are vector forms of the Eulerian (real) stress and strain increment in the distorted coordinates $\{\bar{X}\}$.

$\{\sigma\}$ and $d\{\varepsilon\}$ are vector forms of the Lagrangian stress and strain increment in the original coordinates $\{X\}$.

In general, both $\{R\}$ and $\{B\}$ depend on the displacement parameters $\{\delta\}$ and as the stress may be a non-linear function of strain, special solution methods will have to be used.

The explicit formulation of the strain-displacement matrix [B] can be easily obtained with respect to the original or the continuously updated soil coordinates if the shape function [N] is known.

If an incremental solution is used for solving the wheel-soil interaction problem and the size of each load or displacement increment is small, the strains within each increment can be considered infinitesimal and products of strains (the quadratic term of the strain-displacement relationship) may be neglected. Then both expressions for the strains (Lagrangian and Eulerian) reduce to the classical infinitesimal expression which can then be used.

2.3 Solution Outline of the Nonlinear Equations

In view of nonlinearity the solution of Eqs. (2.12) and (2.13) will have to be approached iteratively. If the Newton process is to be adopted the relation between $d\{\delta\}$ and $d\{\psi\}$ has to be found. Thus, taking appropriate variations of Eqs. (2.12) or (2.13) with respect to $d\{\delta\}$, one obtains:

$$d\{\psi\} = \int_V d[\bar{B}]^T\{\sigma\}dV + \int [\bar{B}]^T d\{\sigma\}dV \tag{2.15}$$

and from the stress-strain relations,

$$d\{\sigma\} = [D]d\{\varepsilon\} = [D][\bar{B}]d\{\delta\} \tag{2.16}$$

$[D]$ is the stress-strain relation matrix and is a function of the mechanical properties of the soil. Its derivation with respect to different idealized soil stress-strain relations is shown in Appendix D. If displacements are large, the strains are related in a nonlinear fashion to displacement, and the matrix $[\bar{B}]$ is now dependent on $\{\delta\}$. The matrix $[\bar{B}]$ can be written as:

$$[\bar{B}] = [B_0] + [B_L] \tag{2.17}$$

where

$[B_0]$ is the same matrix as that for linear infinitesimal strain analysis,

and $[B_L]$ depends on the displacement. In general it is found to be a linear function of such displacements.

From Eq. (2.17)

$$d[\bar{B}] = d[B_L] \tag{2.18}$$

Therefore

$$d\{\psi\} = \int_V d[B_L]^T\{\sigma\}dV + [\bar{K}]d\{\delta\} \tag{2.19}$$

$$[\bar{K}] = \int_V [\bar{B}]^T[D][\bar{B}]dV = [K_o] + [K_L] \tag{2.20}$$

in which

$[K_o]$ represents the usual small displacement stiffness matrix,

and $[K_L]$ is due to large displacements.

The first term in Eq. (2.19) can be written as:

$$\int_V d[B_L]^T\{\sigma\}dV = [K_\sigma]d\{\delta\} \tag{2.21}$$

where

$[K_\sigma]$ is a symmetric matrix which depends on the stress level.

Eq. (2.16) can then be written in the form:

$$d\{\psi\} = ([K_o] + [K_\sigma] + [K_L])d\{\delta\} = [K_T]d\{\delta\} \tag{2.22}$$

where $[K_T]$ is defined as the tangential stiffness matrix.

It can be noticed that Eq. (2.22) is applicable for a general problem of nonlinearity in both material and geometry. If an incremental solution is used, the strains may be considered to be infinitesimal and in such a case the quadratic term in the strain-displacement relationship can be neglected and Eq. (2.22) reduces to:

$$d\{\psi\} = [K_o]d\{\delta\} \tag{2.23}$$

A Newton-type iteration can be applied to solve Eq. (2.22) or Eq. (2.23).

2.4 Techniques for Nonlinear Analysis

As indicated in the previous section, the analysis of nonlinear problems where the nonlinearity is due to either nonlinear material properties or large deformations, or both, is much more complicated than the linear analysis because the governing set of simultaneous linear algebraic equations becomes nonlinear. In all the studies published on nonlinear behaviour, only a handful of exact solutions to specific problems can be found. These deal, without exception, with bodies of the most simple geometric shapes and boundary conditions. More often, a "semi-inverse method" is employed, in which the shape of the deformed body is assumed to be known in advance (a situation which is not often encountered in practice), and even in these cases numerical techniques must often be introduced in the final steps of the solution in order to obtain quantitative results. In short, closed-form solutions to the governing equations of most nonlinear problems are either rare or do not exist (Oden, 1972).

Generally, the nonlinear problems in the FEM can be classified as follows (Zienkiewicz, 1971):

(i) geometrically large deformations associated with small elastic strains,

(ii) geometrically large deformations associated with finite strains,

(iii) nonlinear material properties.

The case of a moving rigid wheel on soft soil can be classified as a nonlinear problem of the second and third types.

Another classification, based on methods of formulation and of the solution of the nonlinear system, has been introduced as follows:

(a) the incremental method where a "marching" type of approach is used and the equilibrium path is only approximately followed, with equilibrium checks occasionally introduced,

(b) the iterative procedures in which equilibrium is approached at all stages of the computation,

(c) the step-iterative or mixed method which is a combination of the previous two methods.

The three techniques are shown schematically in Figure 2-5.

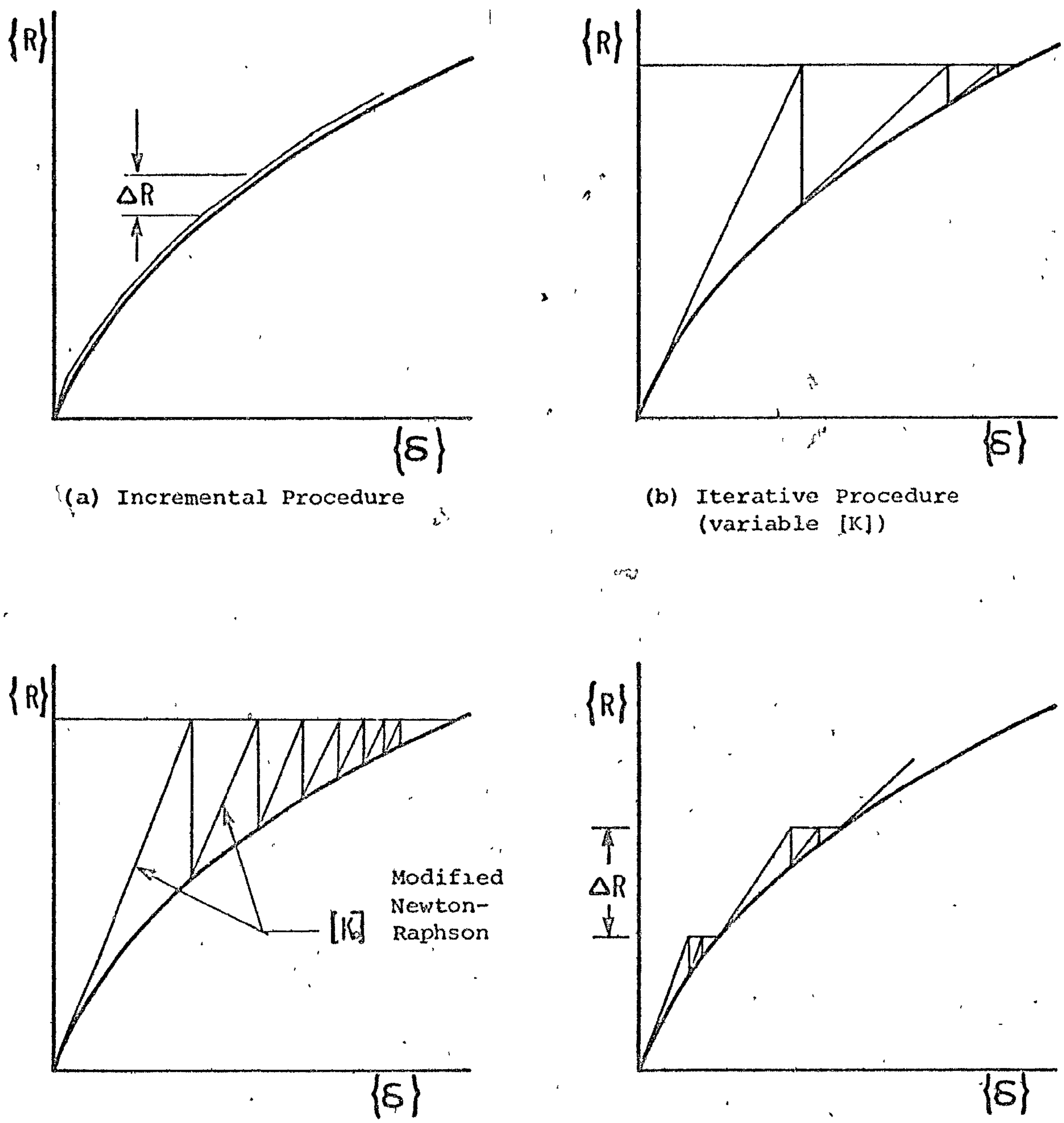

(a) Incremental Procedure

(b) Iterative Procedure (variable [K])

(c) Iterative Procedure (Constant $[K]=[K_o]$)

(d) Step-Iterative or Mixed

Fig. 2.5 Techniques for Nonlinear Analysis Comparison of Three Methods (Desai, 1972).

2.5 Summary of the Nonlinear Solution

The solution of any nonlinear finite element problem by iterative procedures or by the mixed method can be summarized in the following steps:

(a) The elastic linear solution is obtained as a first approximation $\{\delta\}$.

(b) $\{\psi\}_1$ is found, using Eqs. (2.12) or (2.13) with the appropriate definition of $[\bar{B}]$ and of the stresses as given by any linear or nonlinear stress-strain law [D].

(c) Matrix $[K_T]$ is established, and

(d) Correction is established using Eq. (2.22) as

$$\Delta\{\delta\}_1 = -[K_T]^{-1}\{\psi\}_1$$

and if the n^{th} iteration gives a non zero residual force $\{\psi\}_n$, the next iteration becomes

$$\{\delta\}_{n+1} = \{\delta\}_n + \Delta\{\delta\}_n$$

and the process is repeated until $\Delta\{\delta\}_n$ becomes sufficiently small. This process is shown schematically in Figure 2-6. A constant matrix could be used, thus increasing the number of iterating steps. Using a semi-inverted technique resolves the process at smaller computer time, provided that, at each step, $\{\psi\}_n$ is calculated by the correct expressions; however, convergence is sometimes slow using this procedure. To expedite the convergence with less computing time, the tangent stiffness matrix may be updated once only, following which it is kept constant during the iteration process.

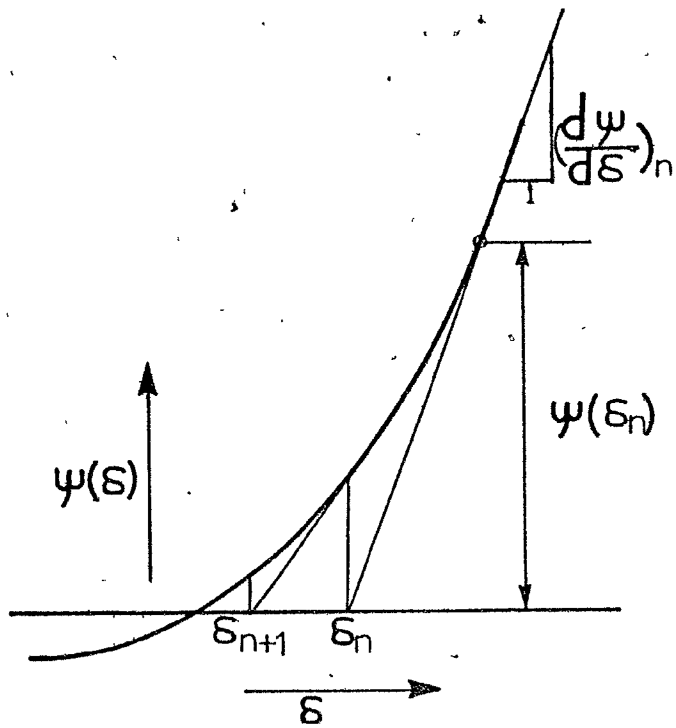

Fig. 2.6 Schematic Representation for Iteration Process

Figure 2-7 shows a block diagram of the FEM adopted to the solution of the wheel-soil interaction problem.

2.6 Summary

In conclusion, some of the different techniques of continuum mechanics applied to solve the wheel-soil interaction problem are discussed in this chapter. To lay the ground for the application of the FEM to the problem, a general formulation of the FEM governing equations together with the different techniques for solving them have been presented.

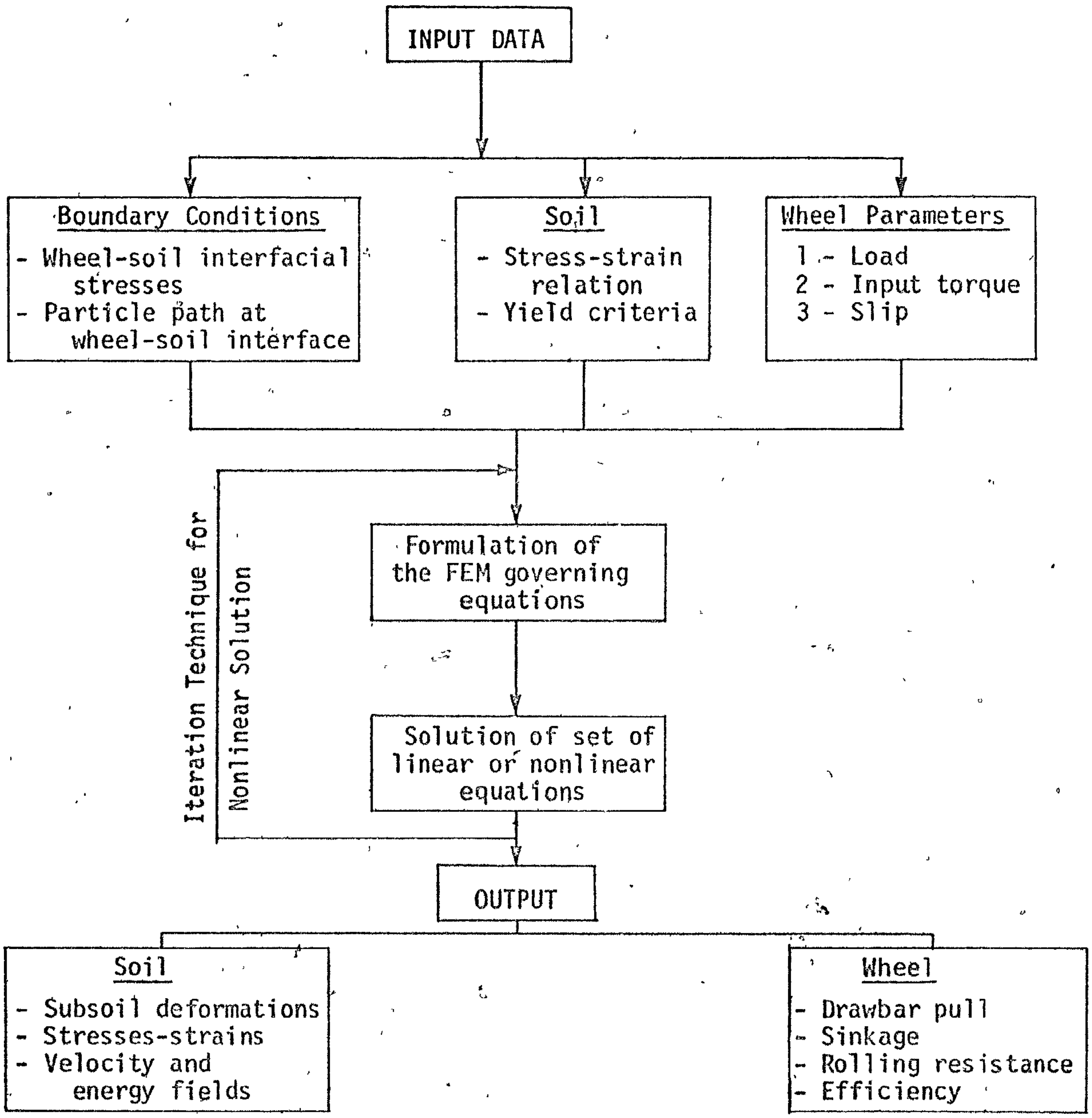

Fig. 2-7 Block diagram for predicting wheel performance and soil behaviour beneath the wheel using FEM

CHAPTER 3

APPLICATION OF THE FINITE ELEMENT METHOD TO WHEEL-SOIL INTERACTION STUDIES

This chapter is concerned with a description of the different requirements for application of the FEM to the problem of predicting both the performance of a moving rigid wheel on soft soil and the soil behaviour beneath it. The different types of stress-strain idealizations are described and the adopted constitutive relation in the present solution technique is explained. The other constitutive relations which may be adopted in soil mechanics in general, and in wheel-soil interaction studies in particular, are presented in Appendix D. The incremental iterative technique which is adopted for a FE nonlinear solution is presented. The FE idealization and methods of application of the boundary conditions at the wheel-soil interface are also presented.

3.1 Introduction

As seen in Chapter 2, the complete solution of any continuum mechanics problem in general, and wheel-soil interaction in particular, requires, besides the equations of equilibrium and continuity, a knowledge of:

(a) the boundary conditions,

(b) the constitutive relations.

The degree of accuracy to which the choice of (a) and (b) represents the conditions of the real problem greatly affects the validity of the predicted results. In general, the requirements for the solution of the wheel-soil interaction problem and the predicted results which define wheel performance and soil behaviour beneath it are shown in Figure 3-1.

In this study, the FEM employed for predicting the wheel performance and subsoil (clay) behaviour beneath it will be limited to the following considerations:

(a) rigid wheel moving on homogeneous soft soil with constant low translational velocity,

(b) the wheel is moving with low degree of slip.

In order to circumvent the mathematical difficulty of establishing the mechanics and the boundary conditions for a moving nonlinear elastic wheel (e.g., pneumatic tire) on a nonlinear soil continuum, the case of a rigid wheel is considered (e.g., a highly inflated tire moving on soft soil). This idealization in essence models the translational velocity and performance of most earthmoving and off-road equipment. The effect of mass inertia forces of the soil continuum can be neglected at low translational velocities. The wheel-soil interaction problem can be treated as a steady state case, provided the soil is homogeneous and the wheel moves at a constant low speed.

As will be shown in Chapter 4, at a high degree of slip the soil-wheel interfacial zone is subjected to a high degree of distortion and the soil in this zone behaves differently from the rest of the continuum. This is due to the high strain rate effect and the nature of the interaction

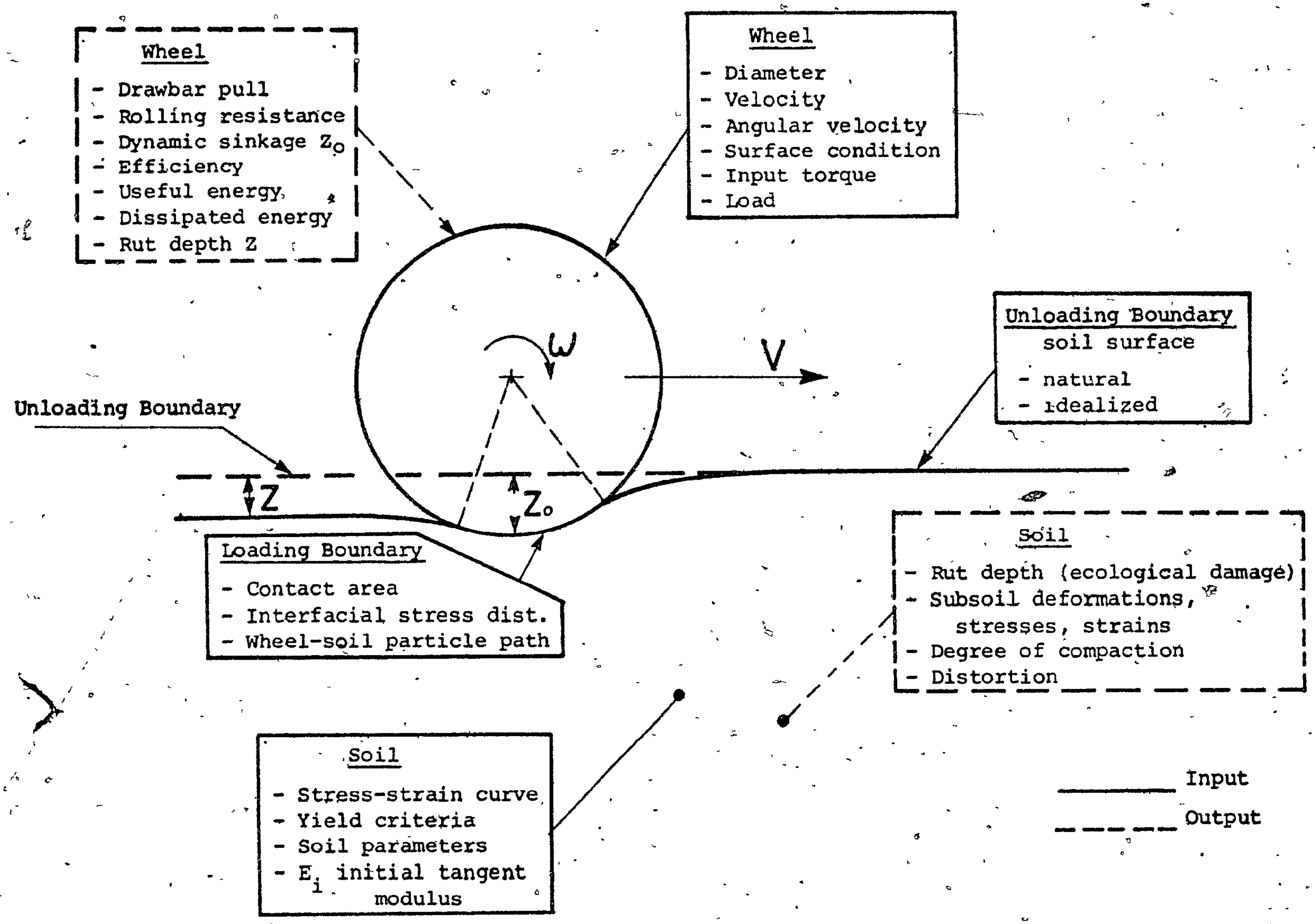

Fig. 3.1 Required Input and Output Information for Wheel-Soil Interaction Study

between the wheel material and the soil. The interfacial zone has a relatively small undefined thickness and its soil properties change rapidly with depth. Due to the difficulty in determining the mechanical properties of the soil in this zone and its rate of change with depth, a case of low degree of slip is considered.

The present analysis for performance prediction of a moving rigid wheel and of the soil behaviour beneath it, treats the soil as a nonlinear elastic material, subject to boundary conditions of an incremental nature, which will permit the growth of the stresses from their initial to their final states and also permit the soil loading path to be followed. Furthermore, most off-road vehicles have relatively wide tires so that a plane-strain type of analysis can be applied.

The solution to the soil-wheel interaction problem using FEM will be obtained with the following characteristics:

(a) the solution will be complete,

(b) it will be consistent with the equilibrium and compatibility equations,

(c) it will be in accord with the problem of nonlinear elastic or strain hardening concepts for constitutive performance,

(d) it will provide the displacements, strains, stresses, deformation energy in the soil continuum, interfacial energy, useful output energy and wheel-soil interfacial stresses (which are not possible with other methods of solution except for the visioplasticity method previously used by Yong & Webb (1969) and which to date is applicable for small scale tests in the laboratory).

It is noted that none of the approaches previously described in Chapter 1 satisfies all these requirements. In addition, none of them can predict both wheel performance and soil behaviour beneath the wheel in the field.

The FEM has the advantage of predicting the wheel-soil performance in terms of energies (input, output, deformation and interfacial energy) as a function of slip (Yong et al., 1975). This advantage will allow a complete spectrum of wheel performance to be shown for low degrees of slip. Thus the point of maximum drawbar pull, the self-propelled point, the towed point, and the point of critical slip can all be determined for any specific wheel. The details will be shown in the results presented in Chapters 5 and 6.

3.2 Constitutive Relationships

The problem is directed towards the study of the performance of a moving rigid wheel over soft soil (clay). The major aspects of the behaviour of clays are discussed in Appendix D.

"True triaxial" tests were performed under plane strain conditions in order to reproduce as closely as possible the assumed conditions during the soil-wheel tests. For the purposes of this study and for the development of the soil criterion which is to follow, the following idealized assumptions apply:

(a) The soil is essentially completely saturated, subjected to a situation which is analogous to quick, undrained test conditions. The effects of mineralogical composition, disturbance, soil structure and prior stress history can be accounted for through triaxial testing.

(b) The soil behaves as an elastic material during unloading or any similar situation.

3.3 Idealization of Nonlinear Behaviour of Soil

The theory of stress-strain relationships for nonlinear materials is perhaps one of the most complex areas of continuum mechanics. Mathematical expressions have been formed for stress-strain relationships either by using simplified assumptions (material is elastic plastic, perfectly plastic, bilinear elastic) or by empirical functional relationships(Kondner, 1963; Duncan & Chang, 1970). For soils, the empirical relationships have been obtained from curve fitting of the experimental results (Duncan & Chang, 1970).

It is known that the amount and type of structural or material idealization will affect the formulation of the problem under consideration. In general, the more complex the model chosen to simulate soil behaviour, the larger the number of variables to be taken into account and the more involved the nonlinear analysis. Moreover, for a realistic analysis it must be possible to obtain values for the constants involved in the constitutive law from laboratory experiments.

The choice of a particular idealization of nonlinear behaviour depends on the accuracy desired, the number of elastic or pseudoelastic constants which must be determined, the computational effort required for the idealization, and the generality of the method.

In general, there are four types of material idealization and two types of constitutive relations which can be used in soils. The material idealization can be classified as: (Fig. 3-2)

(1) Elastic-linear strain hardening

(2) Elastic-perfectly plastic

(3) Nonlinear

(4) Bilinear behaviour.

In the nonlinear method, the stress-strain relations may be obtained either as a direct output of triaxial test results (Chapter 6) or as a hyperbolic representation of these results (Appendix D).

The two approaches for developing constitutive relations in soils are the nonlinear elastic approach and the elastic-plastic or strain hardening approach.

3.3.1 Nonlinear Elastic Approach

This approach does not idealize the stress-strain curve but uses the equations of elasticity to solve for the stress state even after yielding has occurred in the soil; any degree of nonlinearity can be accounted for in this approach. Inasmuch as the nonlinear elastic analysis represents the actual stress-strain relation obtained from tests, it is expected that good results can be attained from this type of analysis.

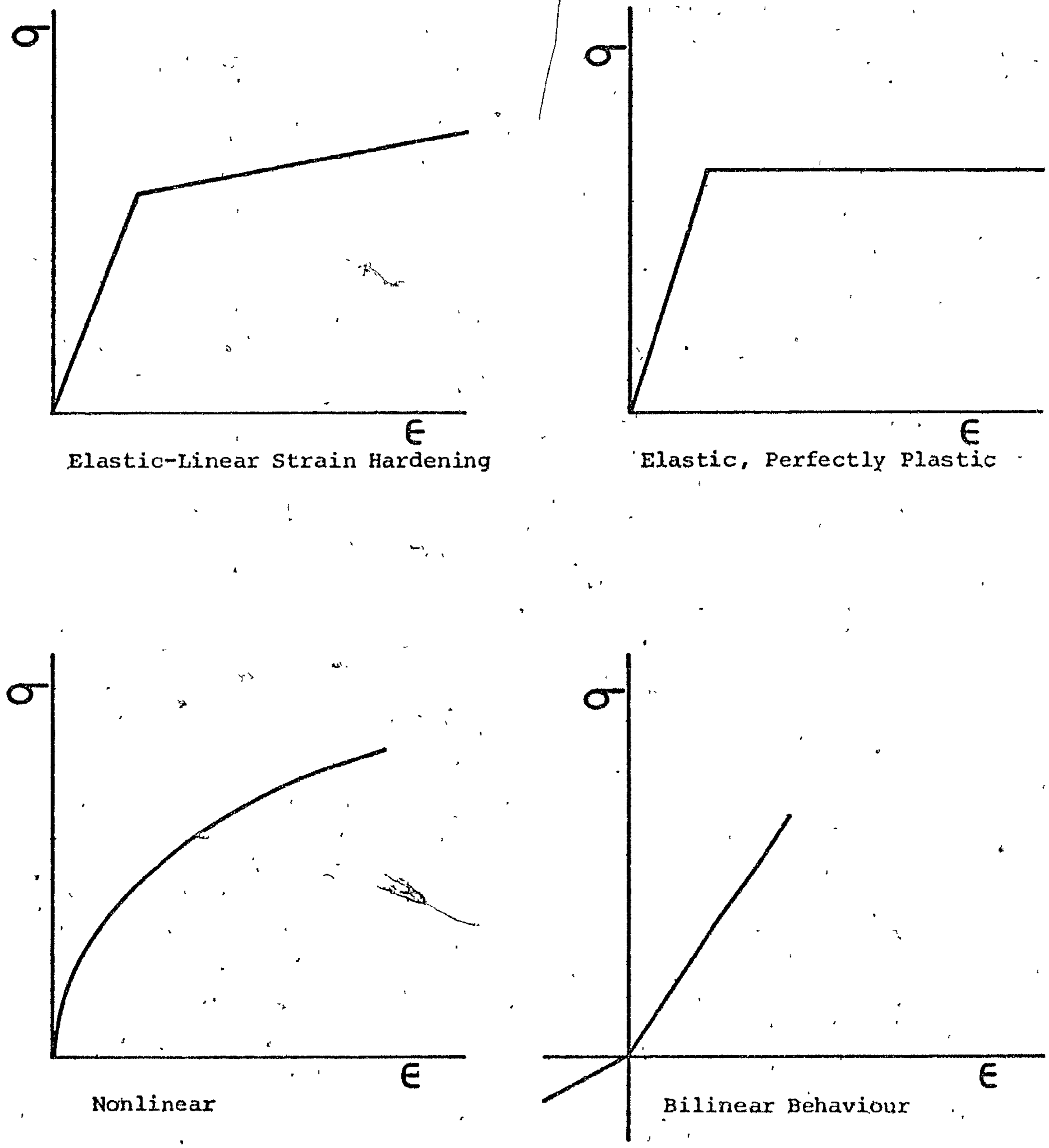

Fig. 3.2 Idealized Stress-Strain Curves

3.3.2 Elastic-Plastic or Strain Hardening Approach

Consideration is given here to the possibility of modeling the soil as an elastic-plastic or elastic-strain hardening material. Marcel & King (1967) and Zinkewicz (1971) have successfully applied this method of analysis to two dimensional stress systems.

The elasto-plastic model would be ideal in cases where the soil stress-strain curve can be approximated with fair accuracy to an elastic and a plastic (strain hardening) portion. Most soils, however, exhibit continuous nonlinearity, and in such cases the elastic-plastic idealization may not work well. Details of derivation of the elasto-plastic matrix can be found in Appendix D.

3.4 Adopted Constitutive Relations

In this thesis the nonlinear elastic approach is used for formulating the constitutive relations for the soil continuum. The stress-strain relationship for soils in the three dimensional case can be best represented using stresses and strains in the octahedral plane. Newmark (1960) states that the general constitutive law for cohesive soils can be expressed in terms of three parameters as follows:

$$
\begin{aligned}
\varepsilon_{oct} &= f_1 (\sigma_{oct}, \tau_{oct}, \phi) \\
\frac{1}{2}\gamma_0 &= f_2 (\sigma_{oct}, \tau_{oct}, \phi) \qquad (3.1) \\
\theta &= f_3 (\sigma_{oct}, \tau_{oct}, \phi)
\end{aligned}
$$

where

f_1, f_2, f_3		are arbitrary functions
ε_1		is the octahedral normal strain
γ_{oct}		is the octahedral shearing strain
σ_{oct}		is the octahedral normal stress
τ_{oct}		is the octahedral shearing stress
ϕ	=	J_3''/τ_{oct}^2
θ	=	$\varepsilon_1''\ \varepsilon_2''\ \varepsilon_3''/(\frac{1}{2}\gamma_{oct})^2$
J_3''		is the third invariant of the deviatoric stress, and
ε_1'', ε_2'', ε_3''		are the first, second, and third deviatoric strain components.

Equations 3.1 could account for volume change, distortion and the intermediate principal stress in contrast with the two parameters Mohr-Coulomb relations (Yong et al., 1975). Determination of the third parameter is possible by using true triaxial test (Yong & McKyes, 1971).

Assuming that the extended Von Mises yield criterion can be adopted for saturated clays, the third parameter has no significant effect, and the formulation of Eq. 3.1 is reduced to:

$$\begin{aligned} \varepsilon_{oct} &= f_1\,(\sigma_{oct}, \tau_{oct}) \\ \tfrac{1}{2}\gamma_{oct} &= f_2\,(\sigma_{oct}, \tau_{oct}) \end{aligned} \qquad (3.2)$$

Saturated clay does not change its volume during shear, and hence it can be considered that the change in volume due to immediate application of hydrostatic component of stress is elastic and of small magnitude. Thus, Eq. 3.2 may be reduced to

$$\tfrac{1}{2}\gamma_{oct} = f_2\ (\sigma_{oct}, \tau_{oct}) \tag{3.3}$$

This function can be determined from the results of the triaxial test at different confining pressures. The octahedral shear stress and strain τ_{oct} and γ_{oct} are defined respectively as:

$$\tau_{oct} = \tfrac{1}{3}\ [(\sigma_1-\sigma_2)^2 + (\sigma_2-\sigma_3)^2 + (\sigma_3-\sigma_1)^2]^{\frac{1}{2}} \tag{3.4}$$

$$\tfrac{1}{2}\gamma_{oct} = \tfrac{1}{3}\ [(\varepsilon_1-\varepsilon_2)^2 + (\varepsilon_2-\varepsilon_3)^2 + (\varepsilon_3-\varepsilon_1)^2]^{\frac{1}{2}} \tag{3.5}$$

The octahedral stress-strain relations plotted from the results of conventional and plane strain triaxial tests are shown in Chapter 6.

3.5 Problem Idealization

The soil continuum beneath the wheel is idealized with respect to the undeformed, unloaded soil surface using plane strain triangular elements, Figure 3-3. In order to reduce both the time needed for idealization of the soil continuum and the amount of input data required for performance prediction of a wheel with different parameters, all the geometrical dimensions are made a function of wheel diameter.

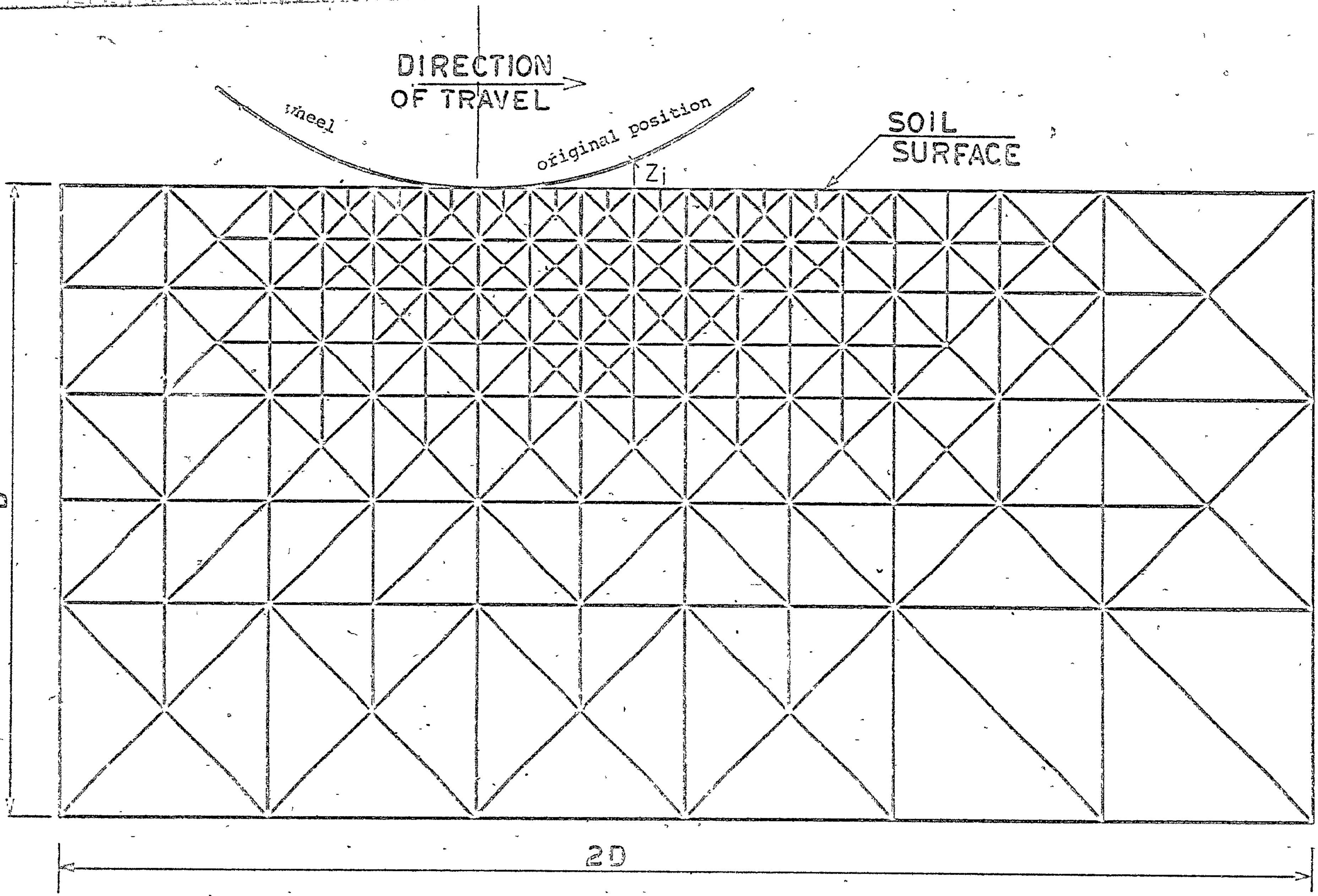

Fig. 3.3 Finite Element Ide-ization

3.6 Boundary Conditions

The analytical solution required for predicting the performance of a moving wheel and subsoil behaviour beneath it is generally faced with the difficulty of specification of the initial boundary conditions at the wheel-soil interface. Perumbral et al. (1971) and Chung et al. (1975) used the wheel-soil interfacial stresses measured by Onafeko & Reece (1967) as a loading boundary in adapting the FEM to the problem. They also implicitly assumed that the soil is in a state of zero energy, i.e., not subjected to any kind of stress history, and that the interfacial stresses are applied statically - which contradicts the physical situation.

Any soil element beneath the wheel is subjected to a transient type of loading due to the nature of the wheel motion. The state of stress at any soil element is a function of the wheel and loading parameters, the soil stress-strain relations and the wheel position with respect to the element. In order to obtain a complete and unique solution, a total spectrum from the initial (static wheel position) state to the state of constant speed wheel travel must be studied.

In general, it is assumed that at a soil depth and at a distance equal to wheel diameter from each side of the wheel instantaneous centerline, the soil movements are negligible.

At the soil-wheel interface the loading boundary conditions can be in the form of loads or displacements.

3.6.1 Load Approach

In this approach, the soil-wheel interfacial stress distribution is assumed to be known, and thus the wheel performance and the subsoil behaviour beneath the wheel are predicted. In fact, this approach is good for predicting the subsoil behaviour and possibly the dynamic sinkage and rut depth.

Figure 3-4 (Schuring, 1969) shows the different approaches for assessing the stress-distribution at the soil-wheel interface.

The measured interfacial stresses are not expected to be fairly accurate for the following reasons:

(1) the difficulty in mounting the force transducers on the wheel rim,

(2) the relative stiffness between wheel material and soil,

(3) the relative size between soil grains and transducer diameter,

(4) in the case of soft soils, the failure or the slip surface may occur between soil and soil and not between wheel surface and soil. Thus the tangential stresses cannot be measured accurately.

The wheel-soil interfacial stress-distribution can also be determined from empirical equations based on plate tests, which make no claim of interpreting the real process. Most of these equations can be reduced from the following basic idea (Schuring, 1969); the wheel contact area is divided into a series of segments small enough to represent even plates. Each of these small plates has a double function. By

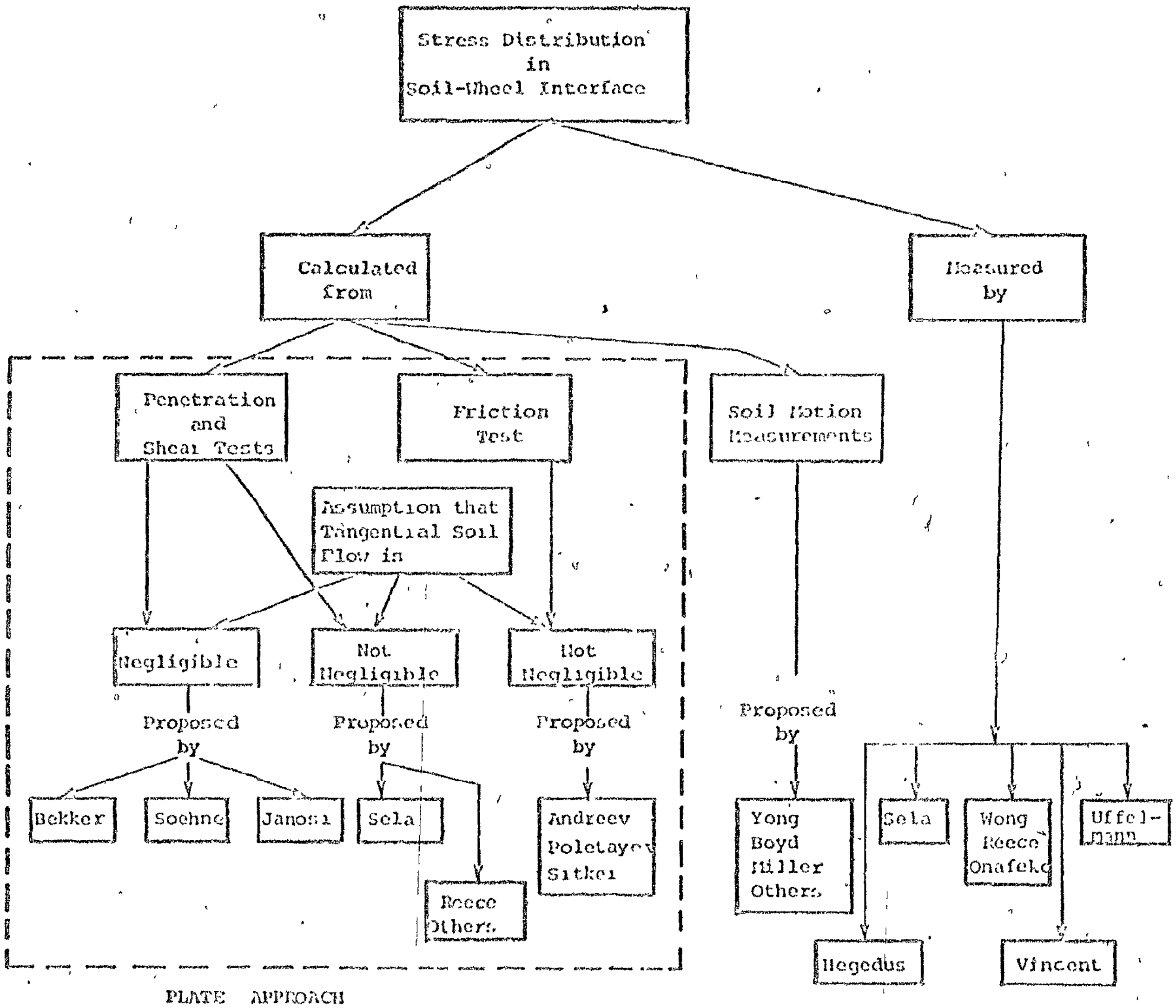

Fig. 3.4 An Attempt to Organize the Different Approaches of Assessing the Stress Distribution in Soil-Wheel Interface (Schuring, 1969)

displacing the soil radially, it is exposed to a radial stress and by sliding tangentially over the soil it is subject to a tangential stress.

All plate approaches are distinguished by the deliberate unwillingness to explain what is really happening in the soil. The mathematical models developed by Bekker (1969), Janozi (1963), Andreev (1956), Sela (1964) and Reece (1965) do not claim to reflect an understanding of the dynamic soil-deforming process; they are heuristic attempts to predict wheel performance with the help of the well-established plate tests. How successfully these attempts match real stress distributions can be checked by comparing computed stress with measured values.

In the loading boundary approach, the nonlinear solution for the wheel-soil interaction problem is obtained in one load increment by an iterative approach and thus the stress path cannot be followed (Mendelson, 1969). The equilibrium in large will be satisfied but not in small and any subsoil rate behaviour (velocities, strain rates, rate of deformation energy...etc.) cannot be predicted, if the problem is treated as a static case. It is also worthy to note that the soil continuum is considered in a state of loading and no effect for soil recovery is considered beyond the wheel rear. This does not correspond to the actual physical behaviour (Figure 3-5).

3.6.2 Displacement Boundary Conditions

An approach using the displacement boundary condition can be adopted in the finite element analysis for evaluating wheel performance and subsoil behaviour. This provides for a complete and unique solution which can satisfy the following requirements:

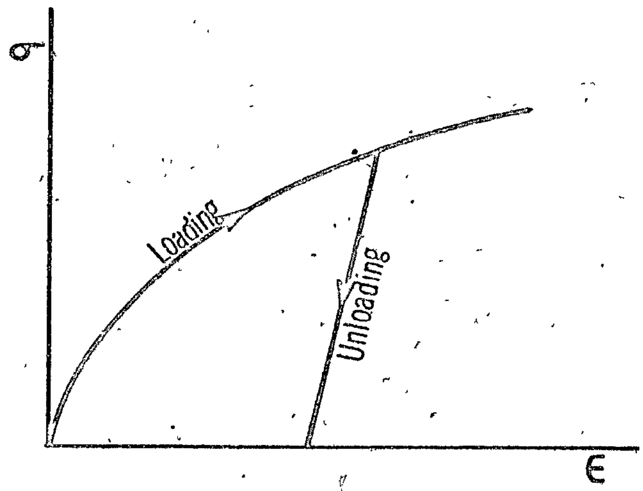

Fig. 3.5a Schematic Diagram for Stress-Strain Behaviour of Clay during Loading and Unloading

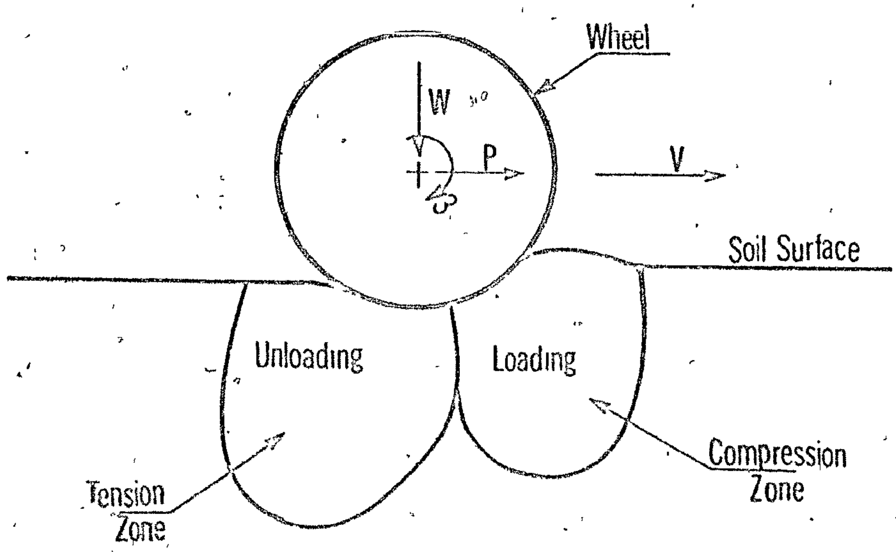

Fig. 3.5b Soil Deformation Beneath a Rigid Wheel

(1) stability in the small and in the large

(2) kinematically admissible boundary conditions

(3) actual stress path

(4) effect of soil-confining pressure

(5) soil recovery

(6) rate of energy dissipated in deforming the soil and at wheel-soil interface

(7) velocity fields.

The displacement boundary approach is mainly dependent on the soil particle path at the wheel interface. A description of the method is given in the following section.

3.6.3 Particle Path

The path of a point on the soil and subsoil surface due to a moving wheel is reproduced by plotting the measured subsoil-displacement pattern as a function of time, using an x-ray photographic technique (Yong et al., 1968), Appendix A.

Generally, a tire shape is defined as the path of a point on a deforming pneumatic tire relative to a moving reference frame, i.e., the axle centerline. If the tire does not deform, its shape is merely a circle. If the tire does deform but the surface over which the tire moves does not deform, the tire shape within the zone of contact must conform to the contour of the surface. If both the tire and the surface over which it moves are deformable, as in the case of a pneumatic tire moving over a yielding soil, the tire shape represents the balance between the resistance to the deformation of the tire and that of the surface. In such a case, therefore, the shape is indicative of the resultant force of the soil on the moving tire, insofar as the resistance to deformation is uniform along the major circumference of the tire (Freitag & Smith, 1966).

In order to establish the mathematical formulae for the particle path, a case of moving undeformed tire over yielding soil is considered. In this case, knowing the dynamic sinkage, degree of slip and wheel diameter, the particle path can be geometrically determined, using the following two formulae (Figure 3-6c)[Onafeko & Reece, 1967].

$$X = r_i\ (\theta_i - \theta) - r\ (\sin\theta_1 - \sin\theta) \quad (3.6)$$

$$Y = r\ (\cos\theta - \cos\theta_1) \quad (3.7)$$

where

X, Y are the particle path coordinates,

r is the rolling radius of the wheel,

r_i is the distance from the wheel centre to the instantaneous centre of rotation,

θ_i is the coordinate of the point where rim and soil surface meet,

θ is the angular coordinate of position on the wheel rim measured from B.D.C.

The cycloid in Figure 3-6a and b may be considered a case of undeformed rolling without slip, which contacts the soil at A in one case and at B in another, but in both cases loses contact with the soil at C. The most interesting portion of the path lies between A and C or B and C, which illustrates the relative motion between the point on the tire and the soil. This relative motion is not a slip path, as slip is normally defined. Figure 3-6a shows the path for the case of zero slip. Furthermore, these portions of the path are of different lengths. It will be noted in Figure 3-6 that the Z component of the path is simply the sinkage of the wheel. The path is considered positive when the point of soil-wheel separation, C, is forward of the point of initial contact, A or B. The curve in Figure 3-6b represents a path of undeformed tire moving with slip, contacting the soil at either A or B, and loses contact with the soil at C. From Figure 3-6b it can be seen that the path can be either positive (X_a) or negative (X_b), even though the slip may be the same in both instances. In a yielding soil, the path of a point on the centerline of the tire will always be positive when the wheel slip is zero or negative. It may be either positive or negative when the wheel slip is positive (Freitag & Smith, 1966).

Since the theoretical particle path is only a function of wheel parameters, and in view of the complex behaviour of the soil at the wheel interface, the wheel-soil slip surface and the soil recovery beyond wheel bottom dead center, the theoretical particle path cannot accurately represent the actual path. A detailed description of the actual particle path at wheel-soil interface is given in Chapter 5.

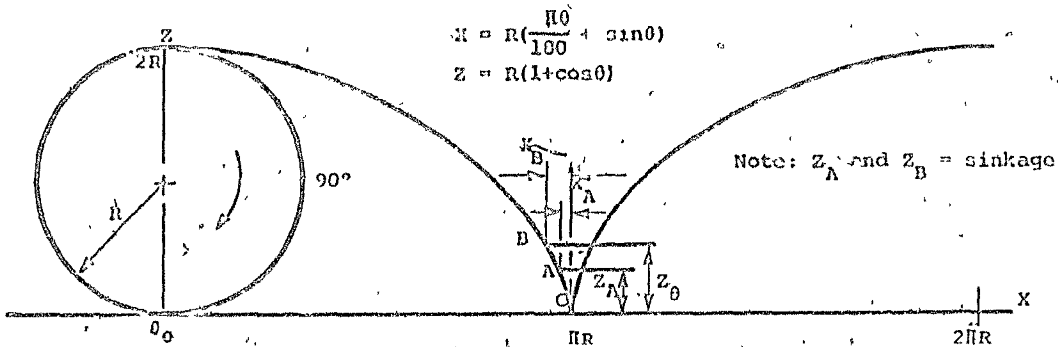

Fig. 3.6a Cycloid

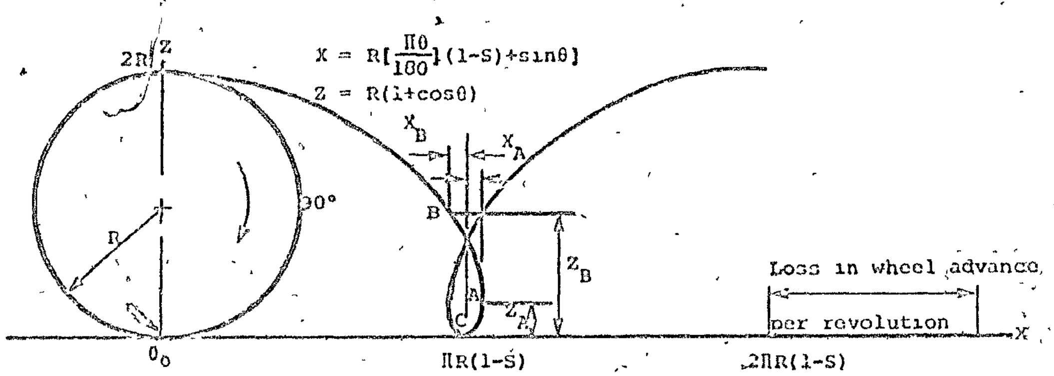

Fig. 3.6b Prolate cycloid 25 percent slip (S)

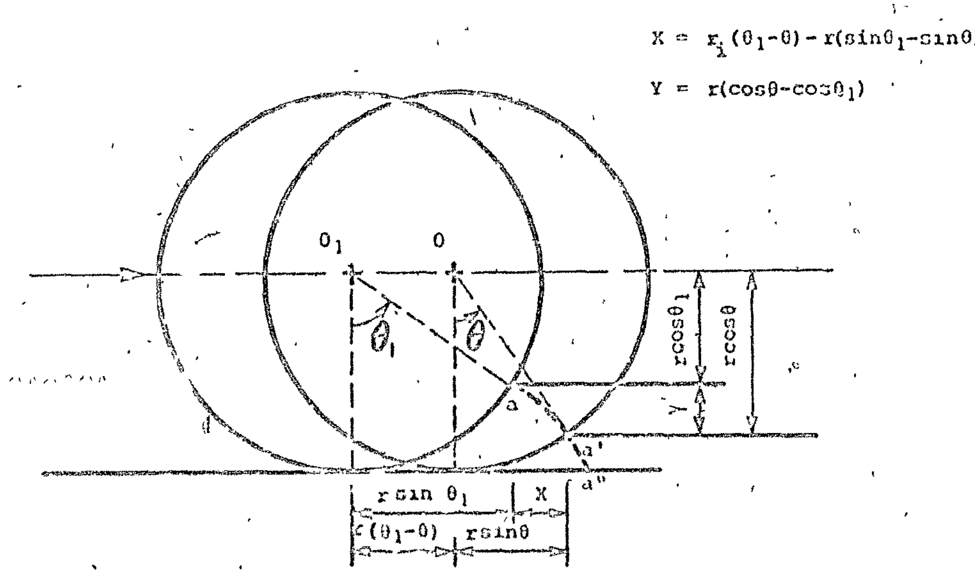

Fig. 3.6c Geometrical Determination of Theoretical Particle Path

3.6.4 Application of Displacement Boundary Approach

The boundary conditions are applied in a way to study the whole spectrum of wheel travel over soft soil, from the stationary wheel position to the state of constant speed travel. The complete solution is attained using the incremental displacement approach in two major steps.

In the first step, the case of a stationary wheel position is considered. The subsoil stresses, strains, displacements and the wheel-soil interfacial reactions are calculated for the stationary position. Displacement boundary conditions are adopted by knowing the dynamic sinkage value. The dynamic sinkage is applied in the form of vertical displacement increments, the stresses are calculated at the end of each increment using the nonlinear stress-strain relations then augmented to their previous values, and the process is continued till the augmented vertical displacements reach the value of dynamic sinkage.

At the end of each vertical displacement increment the possibility of contact occurrence of a new node with the wheel is checked as follows (Fig. 3-7):

$$W_o - W_i \geq Z_i$$

where

W_i is the vertical displacement of the soil surface at node i,

Z_i is the initial gap between the wheel and soil surface at node i,

W_o is the vertical displacement increment of the wheel.

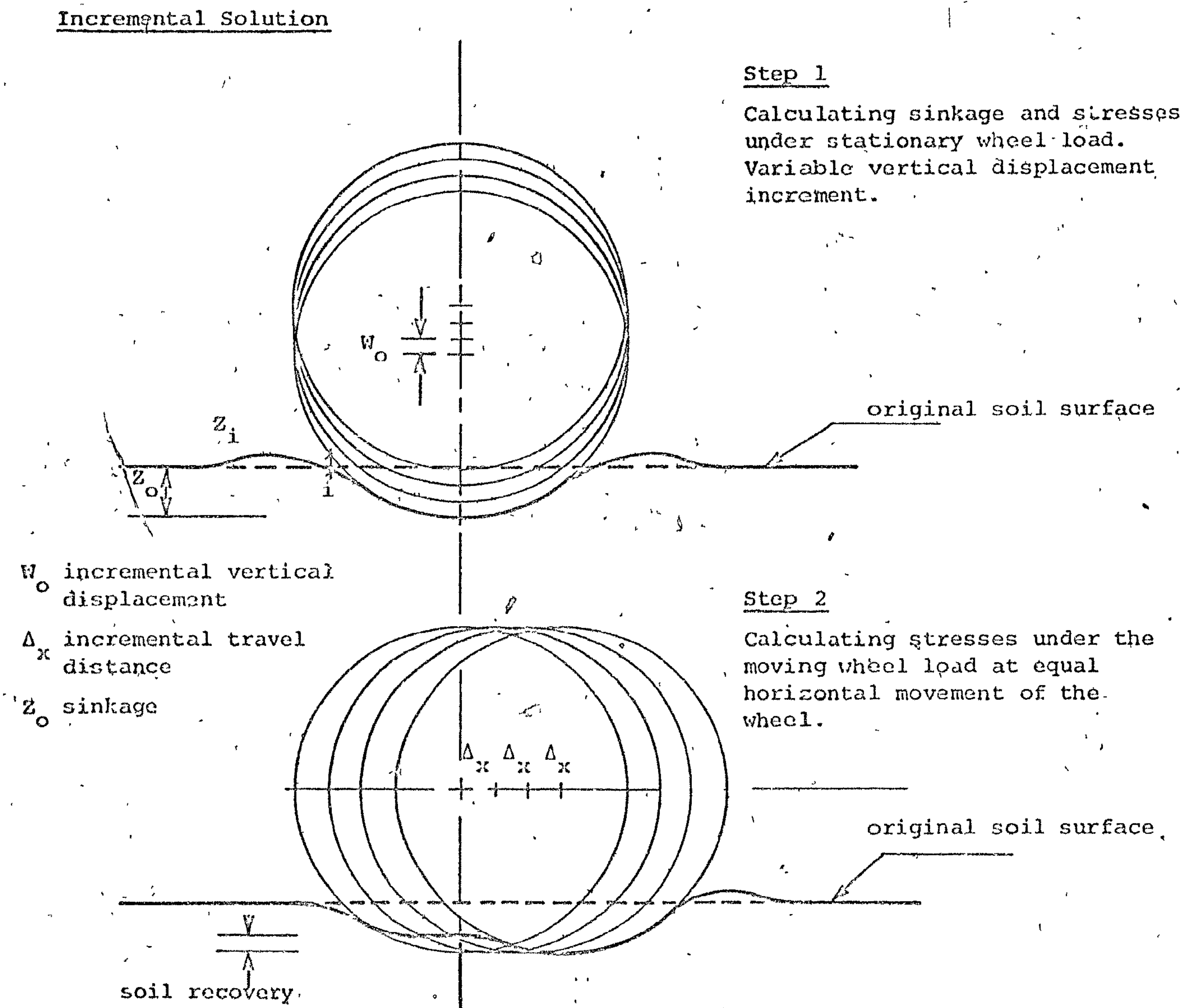

Fig. 3.7 Determination of Loading Boundary Condition using Displacement Approach

The second step in the solution is to assume that the wheel is moving with constant speed. Because of the steady nature of the wheel loading and the homogeneity of the soil medium, any tracer object will describe the same particle path as any other placed at the same initial depth. Hence the displacements of any nodal point on the soil surface can be determined by knowing the equation of the particle path and the original position of the nodal point with respect to the intersection of the wheel centerline with the original soil surface.

Using equal increments of time or wheel travel distances as shown in Figure 3-7, the nodal displacements at the wheel-soil interface can be determined, provided the shape of the particle path is known. These boundary displacements are used as the loading boundary required for calculating wheel-soil interfacial stresses, subsoil stresses, strains, velocities, deformation energy and interfacial energy. This process is continued and the results are augmented to previous values until the summation of the vertical reactions at wheel-soil interface remain constant with any incremental wheel travel distance.

A summary of the requirements for wheel-soil performance prediction using the two previously discussed loading boundary conditions, is shown in Figure 3-8.

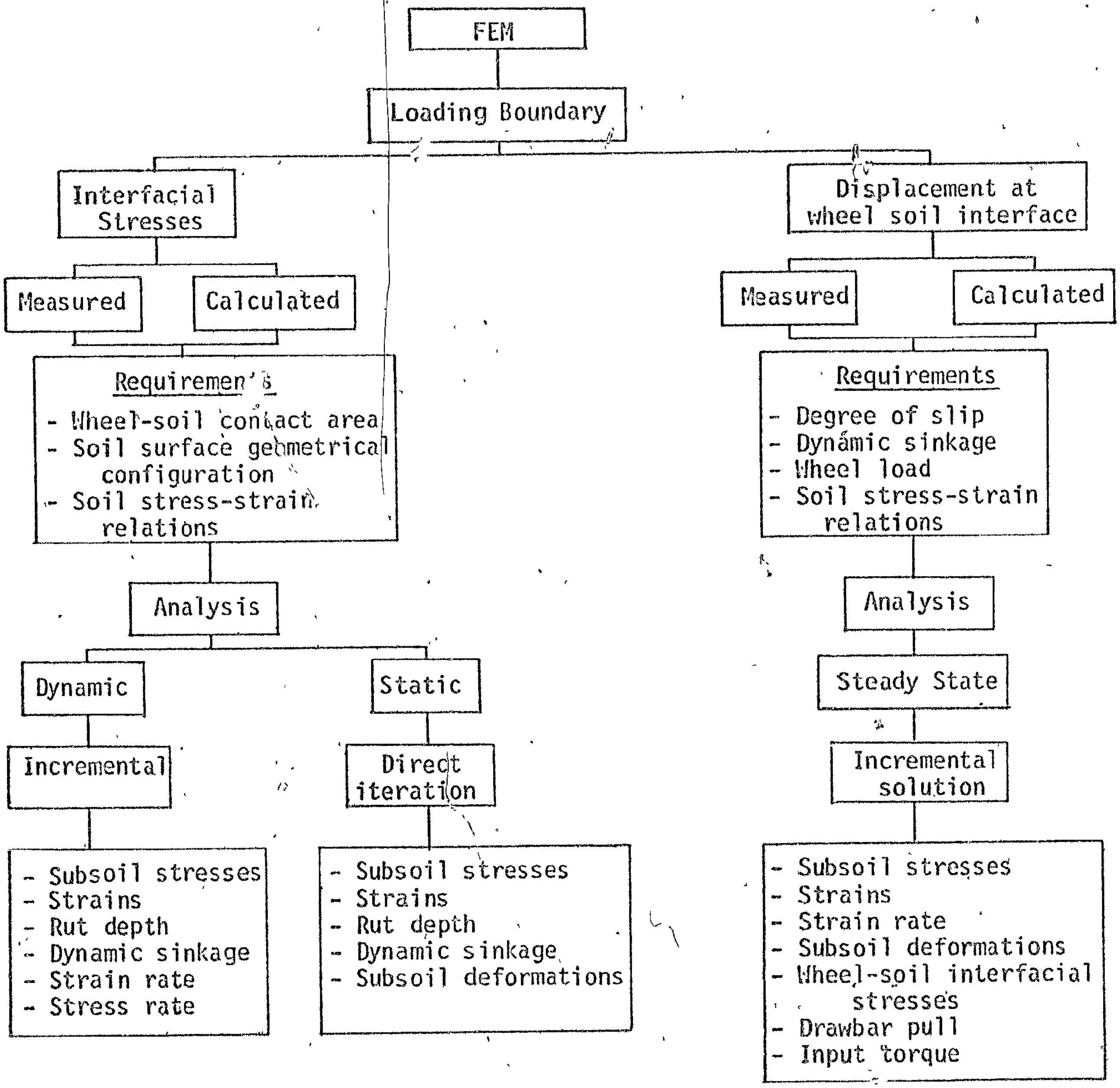

Fig. 3-8 Block Diagram for the Different Methods of Application of the Loading Boundary at Wheel-Soil Interface

3.7 Nonlinear Solution (Incremental Method)

As stated in the previous chapter, there are various techniques for incorporating the effect of either material nonlinearity or geometrical nonlinearity or both in solving continuum mechanics problems by the finite element method.

In this study, the incremental solution is adopted, in which the load or displacement is considered to be applied in incremental form. If the state of stress and strain at the start of a load (displacement) interval is known, the state at the end of the increment can be found by an addition of incremental changes. The constitutive relations to be used for each element may be determined at the beginning of each interval.

In this study plane stress-strain curves at different confining pressures are directly used to compute the value of E during each increment. The value of Poisson's ratio is kept constant in the analysis. The starting value of the modulus, E_0 , is taken as the initial slope of the plane stress-strain curve at zero confining pressure. The stresses or strains in each element due to the first increment of load or displacement, are computed using the elastic analysis. A new value for the modulus to be used in the second increment of load is computed by using the nonlinear curves to obtain the E values. The modified constitutive relations are used in the next increment of load.

Since for every increment of load the elastic constants used are those obtained from the previous increment, it is necessary that increments be quite small. Further, if there are abrupt slope changes in the stress-strain diagram, the method is likely to give unsatisfactory results. A few iterations after each displacement increment are sufficient to bring the assumed E values close to the actual values.

The number of iterations at each load increment may be reduced by predicting the value of E for a load increment based on the stresses or strains attained in the previous increment, and by using this value of E as a first trial in the computations. Linear prediction was programmed in this study and gave satisfactory performance. Figure 3-9 diagrammatically illustrates the working of the linear method.

3.7.1 Advantages of the Incremental Solution

The incremental solution for nonlinear finite element method gives a picture of the behaviour of the continuum over a whole range of loads during a single pass at less computer time. Furthermore, in many practical problems in soil mechanics such as the construction of earth dams, the excavation of slopes or moving wheel on soil, the load is applied in an incremental fashion.

In the case of a wheel moving with constant low speed over soft soil, the soil is subjected to a transient type of loading phenomenon. Due to this type of loading, the state of stress in any soil element is a function of its coordinates with respect to wheel position and so it continually changes as the wheel travels. In this type of loading the incremental solution is very important and represents the physical nature of the problem. The incremental method is also more general and can apply to both the loading and the unloading portions of the stress-strain curves.

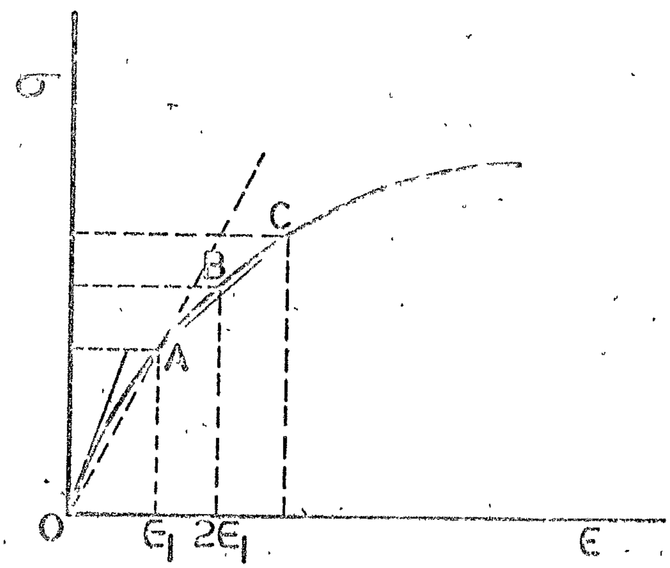

Slope of OA - First trial value for E without prediction for second increment

Slope of AB - First trial value for E with linear prediction for second increment

Slope of AC - Actual E value for second increment after iterations

Fig. 3.9 Incremental-Iterative Method with Prediction (after Radhakrishnan, 1969)

3.8 Inclusion of "Large" Strains

In addition to material non-linearity, geometric non-linearity may occur, and it is possible to assess the influence of this effect through proper modification of the stiffness method (Zinkewicz et al., 1970). Because the incremental solution is used and the load increments remain "small", it is assumed that the strain increments may be regarded as infinitesimal in the usual sense. It is recognized, however, that the same may not be true of the accumulated values (Fung, 1965). Following each load increment, therefore, the increments of displacement at each node are added to the coordinates of the node. In this manner subsequent computation is made for the deformed body.

In the limit of infinitesimal increments of load, this procedure gives the so-called logarithmic strains, rather than simple displacement gradients. While this is admittedly an approximation to the more formal definition of "large" strains (Fung, 1965; Green, 1970), the degree of approximation appears to be consistent with that of the overall method.

3.9 Loading/Unloading Logic

Due to the nature of the wheel motion, the soil beneath the wheel is subjected to loading at the front and unloading at its rear (Figures 3-5). Thus in the finite element solution it is quite possible for some elements to load while the others are unloading. It is also conceivable for the stresses in an element within an increment to change in such a way that increases (or decreases) in mean pressure are accompanied by corresponding decreases (or increases) in octahedral shear stresses. Thus, for the loading/unloading element, the code must be able to choose the appropriate modulus for the stiffness computations. The possibility of unloading a new element at every incremental distance was checked as follows:

$$\Delta W = \sigma_{ij} d\epsilon_{ij} < 0 \qquad (3.8)$$

where

σ_{ij} is the state of total stress in the element,

$d\epsilon_{ij}$ is the state of incremental strain element.

It is advantageous to use Eq. 3.8 in the finite element method; as soon as the strain increments $d\epsilon_{ij}$ are computed at any element, using the stress components σ_{ij} at the beginning of the increment, ΔW can be computed and used to decide whether it is loading or unloading.

In a forward integration procedure, the modulus value used at the beginning of any increment is the value computed at the end of the previous increment. Thus, if the previous step had been a virgin loading, loading parameters would be used, and so on. At a load/unload interface this procedure results in an error since the succeeding step is different from the previous step, requiring use of a different modulus. In the computer programme (Appendix F) the first iteration in any increment is used to check whether the correct modulus is used and if not, the incremental step is recomputed with the appropriate modulus. This check is to be done for each element and the processes should be repeated until all the moduli used are correct for the respective elements.

CHAPTER 4

EXPERIMENTAL ANALYSIS

4.1 General

One of the main objectives of this thesis is to develop an analytical model, based on the finite element method, that can be used for evaluating both the performance of a moving wheel and the behaviour of the subsoil beneath it. The experimental program has three main objectives:

(a) To provide the analytical model with the soil stress-strain relations and the loading boundary at wheel-soil interface;

(b) To check the validity of the proposed analytical model;

(c) To evaluate the effect of wheel surface conditions on wheel performance.

In this chapter the experimental program, the test results, and the techniques used for analysis of the experimental results are presented and discussed. The sequence adopted in the presentation of the test results and related discussions in this and the following chapter is shown in Figure 4.1.

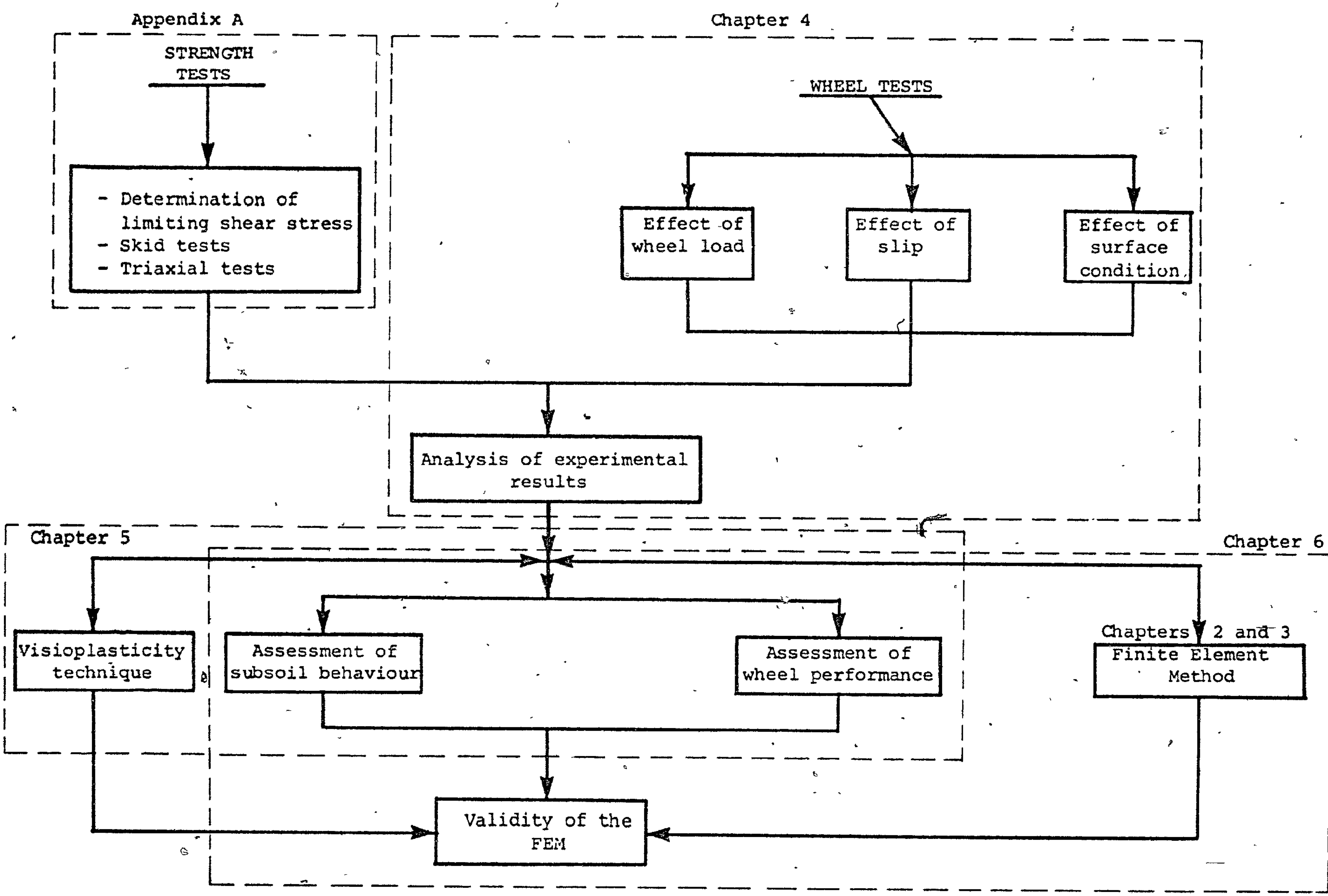

Figure 4.1 Schematic Representation of the Method of Presentation of Experimental Results, Related Discussions, and Applications

4.2 Experimental Program

The experimental program is designed to be a continuation of the McGill Soil Laboratory research program. This part of the program is concerned with studying the effect of wheel surface conditions on its performance and subsoil behaviour beneath it. The system of parameters which can be varied in the wheel-soil interaction experiments are:

(a) Parameters concerning the wheel: load, radius, width, surface condition, translational velocity, and angular velocity;

(b) Parameters concerning the soil: shear strength, moisture content, unit weight, load deformation behaviour ... etc.

To allow for a rational approach in the analysis of the test results, the experiment was limited to the following:

a - Three different wheel loads,

b - Rigid wheel with three different surface conditions:

1. smooth surface,
2. $\frac{1}{8}$" rubber strap mounted on wheel periphery;
3. lugs of $\frac{1}{4}$" thickness and $\frac{3}{4}$" width mounted on the periphery of the wheel. The lugs make 45° with the center line of the wheel periphery as shown in Figure 4.2.

c - Constant translational velocity, while varying angular velocity,

d - Torque to cover a slip range from 0 to 80 percent,

e - One type of soil with constant moisture content.

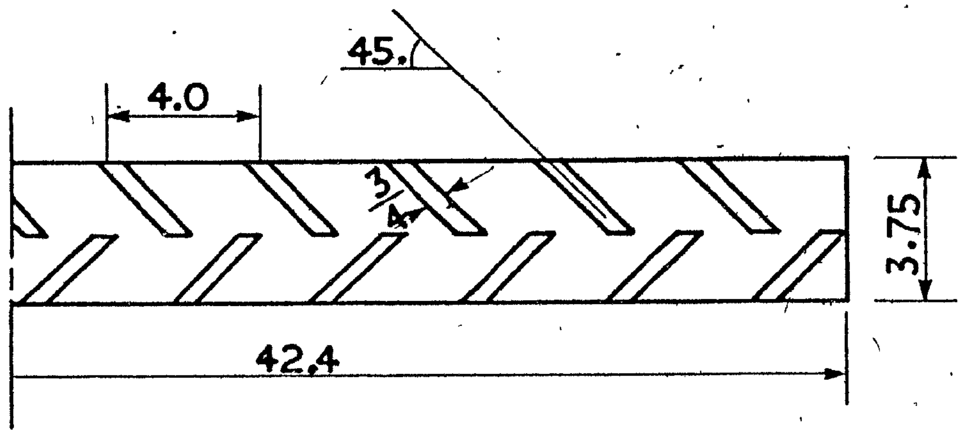

Figure 4.2 Tread Configuration

4.3 Experimental Analysis

The method of analysis of data on the soil deformation patterns beneath the moving wheel has been presented previously. The technique for recording the soil deformation beneath the wheel has been explained by Yong et al. (1967), Yong & Webb (1968), and Yong & Windisch (1970), and thus will not be fully repeated here. The McGill Soil Laboratory test facility and the test procedures are given in Appendix A. The following is a summary of the techniques used for preparing and analyzing the test results.

4.3.1 Data Reduction

A flash x-ray technique was used for recording the positions of embedded lead markers at various times corresponding to various instantaneous positions of the moving wheel; it provided the information necessary to trace the "distortion" motion of each marker, Figure 4.3. A single continuous grid can be obtained by aligning the images side by side, Figure 4.4, as the horizontal distances between their optical centers for consecutive exposures and the distance between the x-ray source and the x-ray slides are both determined (Yong et al., 1969, 1970, 1971). The velocity and displacement computations can then be made, following adjustment of the undeformed and deformed grid coordinates (Windisch, 1970). Details of the calculations are shown in Appendix B, and a schematic of the procedure used in the calculations is shown as Figure 4.5.

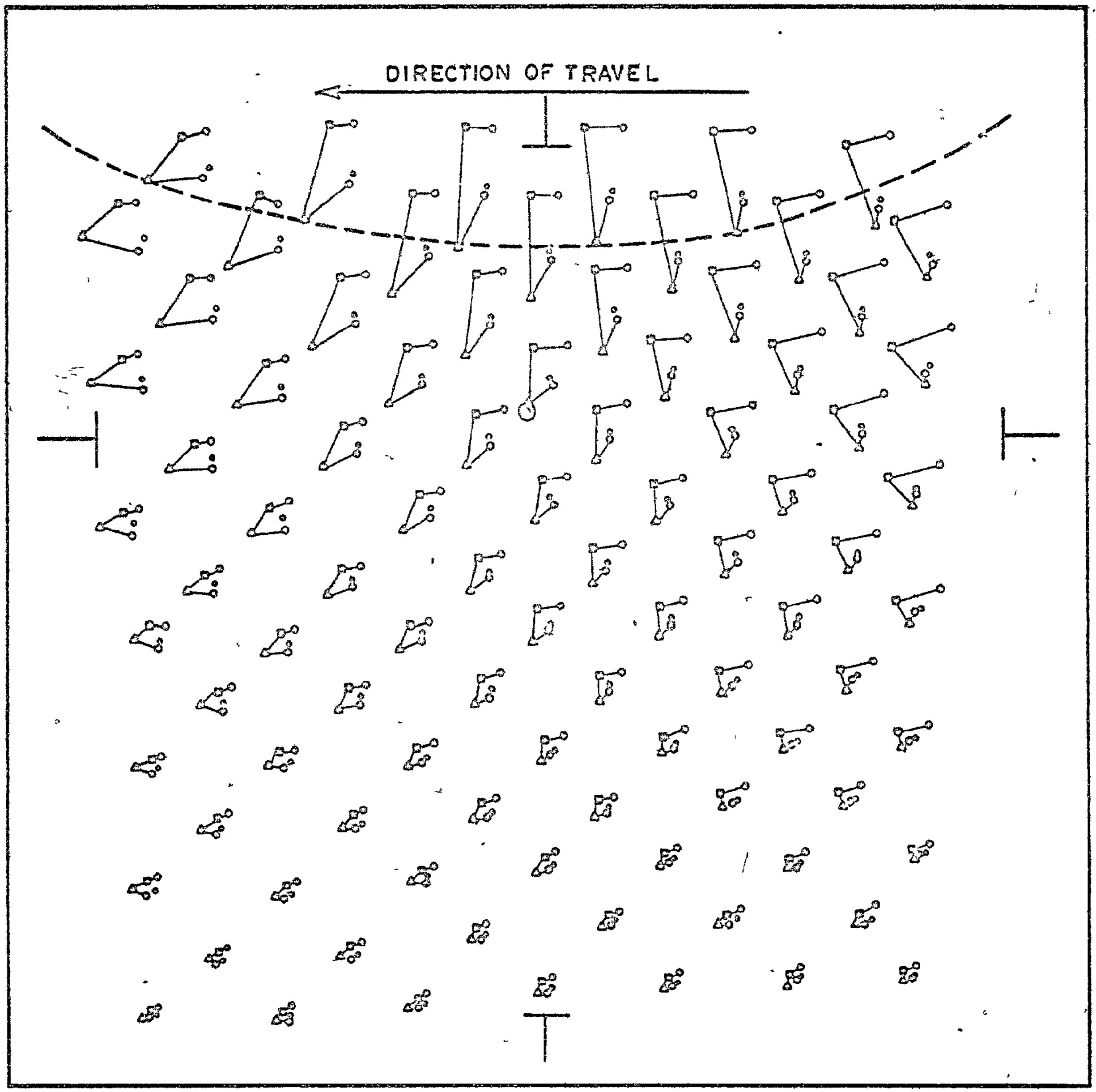

Figure 4.3 Trace Motion of Each Marker - Wheel Load 34.0 Lb
Slip 20 percent

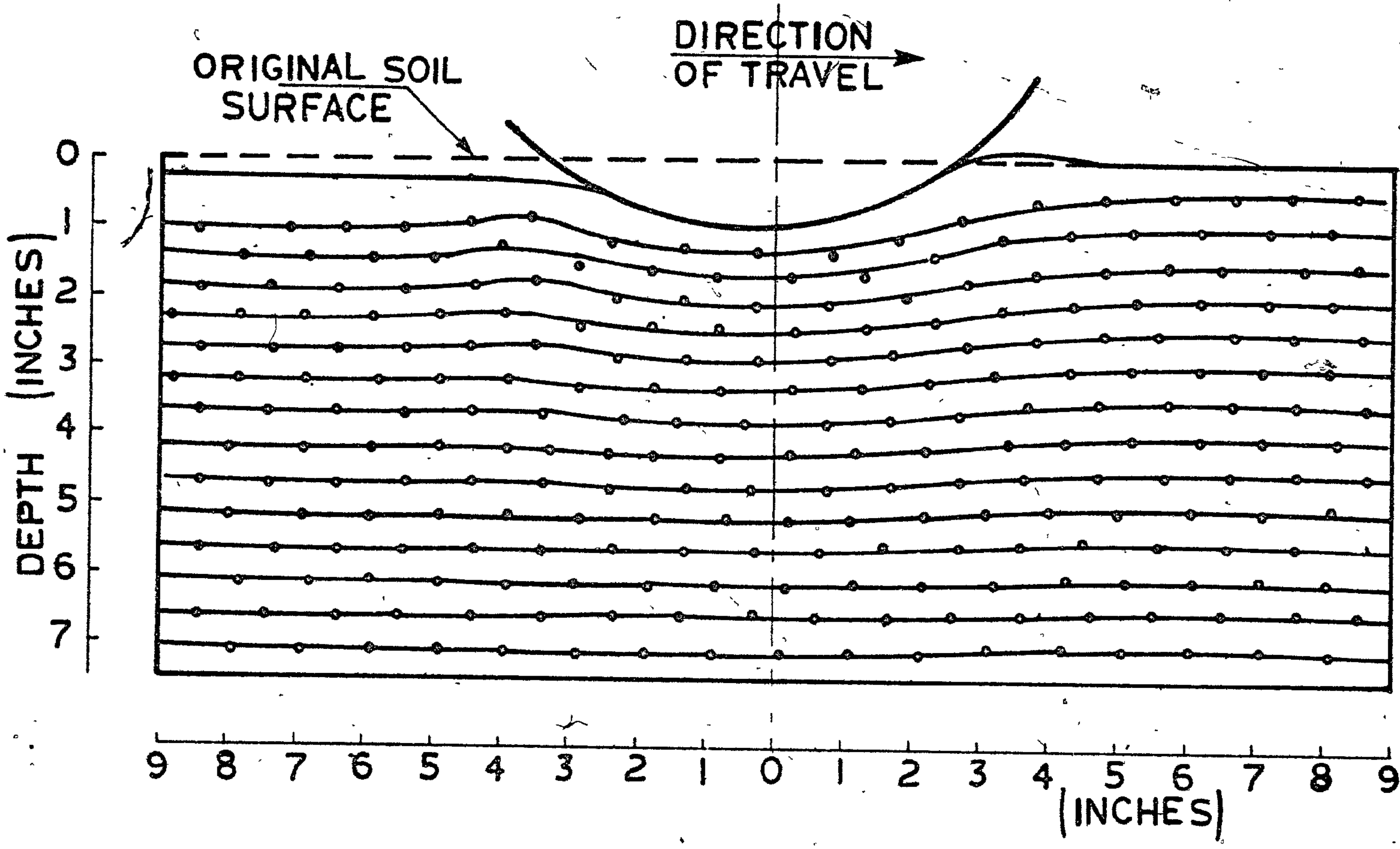

Figure 4.4 Flow of soil due to moving wheel load.

Wheel load 34.0 lb
Slip 20 percent

Measured lead markers positions on x-ray slides

Plotting of successive node locations to provide distorted grids of original and displaced node positions

Specification of coordinate locations of node points using x-y recorder and process control computer [PROGRAMME "25"]

Transfer of coordinate pairs to pinched cards PROGRAMME "TAPE 25"

1. Grid adjustments for distortions caused by placement errors
2. Calculation of incremental displacements and velocities from particle paths
3. Calculation of instantaneous strain rates
4. Estimation of volume changes
5. Calculation of effective strain by integration of strain rates
6. Calculation of power of deformation energy

Figure 4.5 Method of Data Reduction

4.4 Volume Change

Analysis of the experimental results for the subsoil measurements using plasticity theories implies zero volume change during plastic deformation in order to satisfy Saint Venant's postulate and normality condition (Hill, 1950; Mendelson, 1969). Since the actual test of moving wheel over soft soil takes only a few seconds, the rate of load application is relatively rapid, involving little time for drainage and hence insignificant pore pressure dissipation (Yong & Fitzpatrick-Nash, 1968). Under such condition, the soil can be assumed to be incompressible and amenable to a total stress ($\phi = 0$) analysis. However, as it was impossible to obtain the desired full saturation, it was expected that no volume change condition could be violated.

The volume changes computed directly from the displaced marker positions indicated local volume changes of up to 5% (Figure 4.6). The violation of the zero volume change condition also appeared in the deviation of the principal strain rates, ε'_1, ε'_2, from the plane strain analysis condition for an ideal plastic material (namely, $\varepsilon'_1 = -\varepsilon'_2$) as shown in Figure 4.7. However, the positive and negative values of volume changes may tend to compensate each other along any subsoil level beneath the wheel (Figure 4.6). The average values of volume changes are of the order of two percent, imply the validity of the compressibility assumption, hence it is possible to use the ideal plasticity theories for analysis of the subsoil measured deformation.

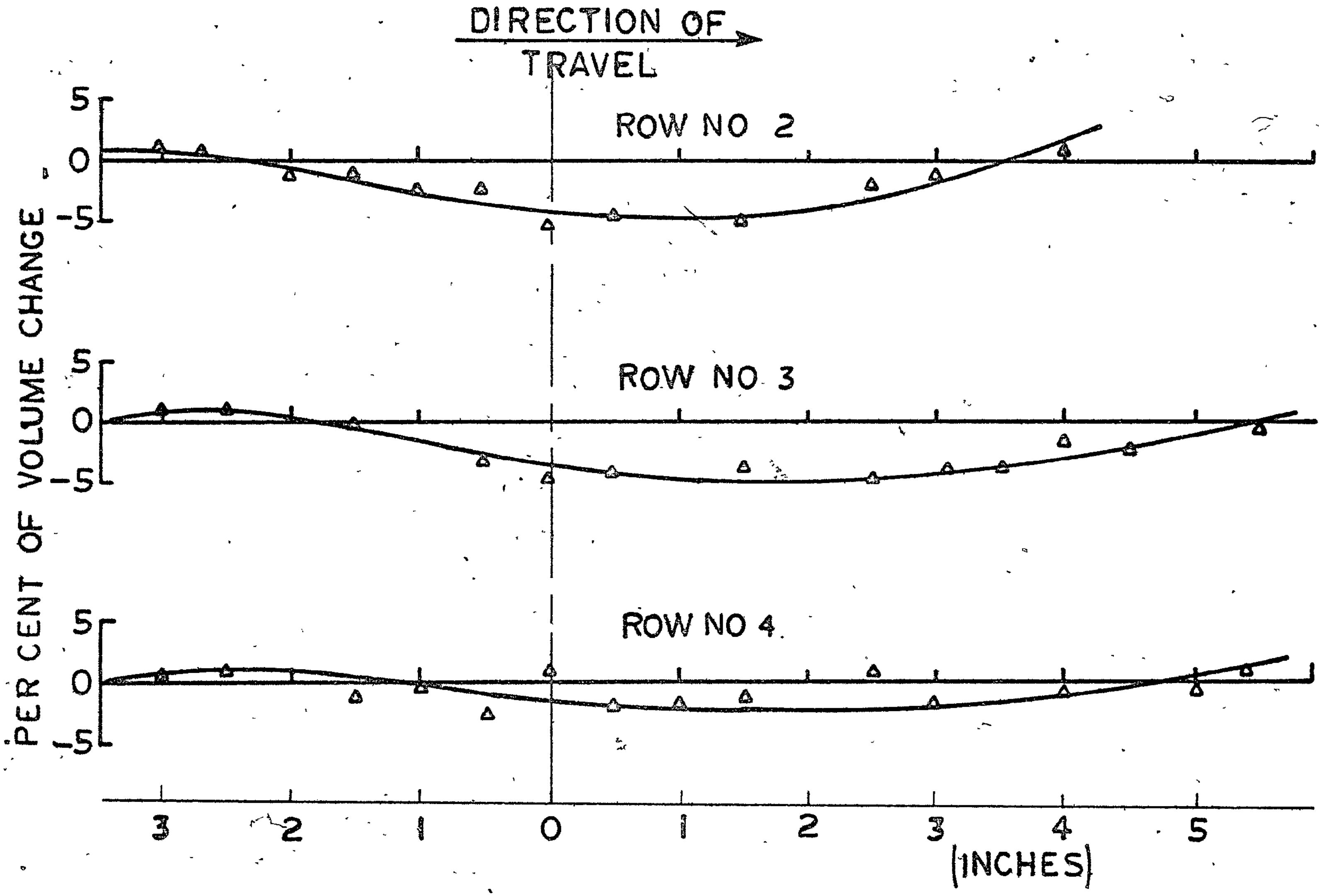

Figure 4.6 Violation of Constant Volume Condition

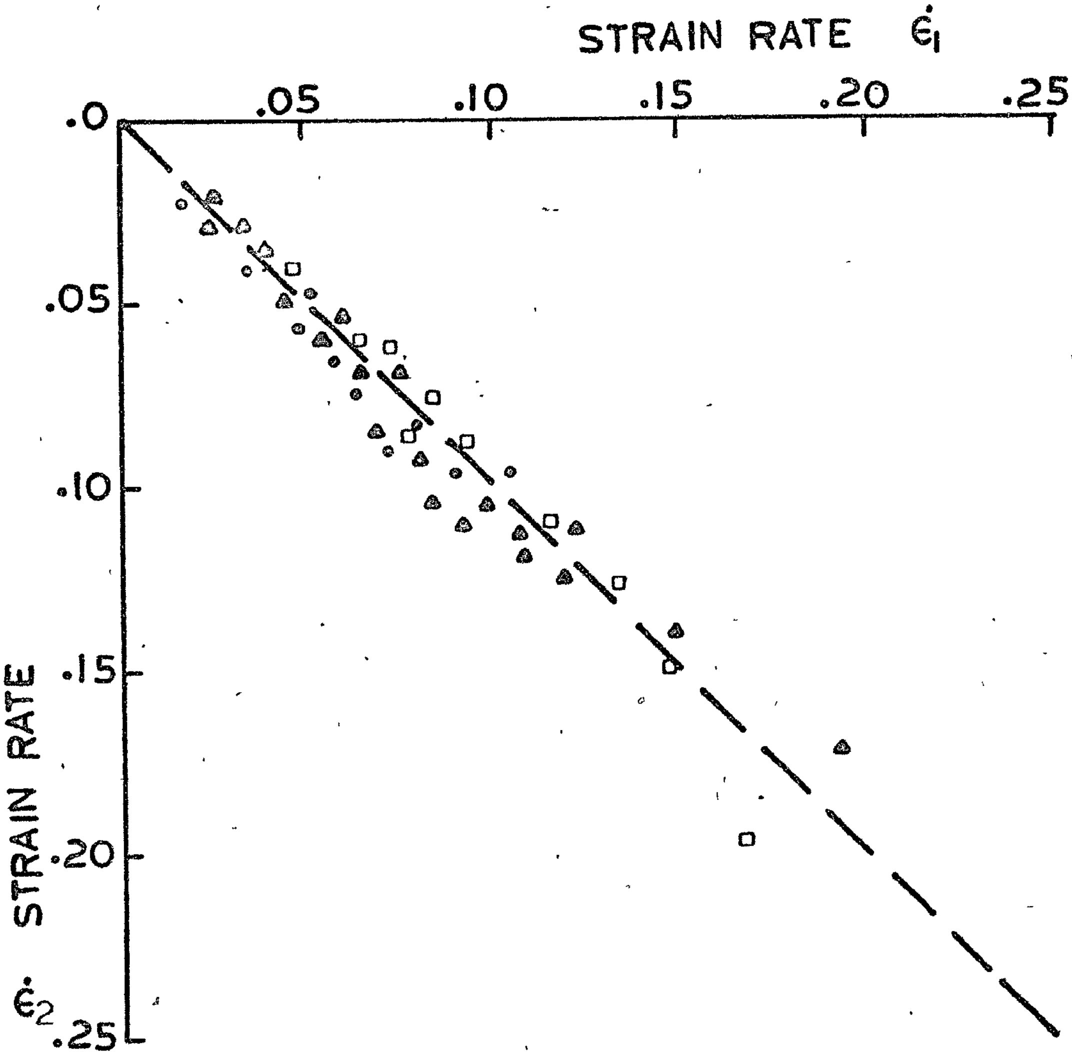

Figure 4.7 Violation of the compressibility condition

Details of volume change calculations are shown in Appendix B, and machine computations performed by the program (VISIOPLS) are given in Appendix C.

4.5 Subsoil and Soil-Wheel Interfacial Stresses

4.5.1 General

In order to check the validity of the finite element model as a tool for predicting the performance of a moving wheel and the behaviour of the soft soil beneath it, comparisons are made between the FEM predictions and the results of the experimental analysis.

Comparisons are made for direct measurements such as drawbar-pull, input torque, dynamic sinkage, and subsoil displacement fields, and for indirect measurements using the visioplasticity technique for velocity fields, stress fields, deformation energy fields and wheel-soil interfacial stresses.

4.5.2 Theoretical Assumptions

In this work only plane strain conditions are considered. The material is assumed to be an ideal homogeneous and isotropic clay, in an undrained state, with a constant shear strength, zero volume change, and no internal friction. All stresses are considered as total stresses, and the material is assumed to obey Saint Venant's postulate or the principal stress and strain directions coincide. The subsoil stresses and wheel-soil interfacial stresses are determined from the experimentally measured subsoil deformations and the application of the method of characteristics. A flow chart of the procedure used in the calculation is shown in Figure 4.8. A discussion of the analytical techniques used in some steps of the calculations is given below.

4.5.3 Principal Strain Rate Directions and Characteristics

Using the experimentally obtained strain rate components (details of the calculations are shown in Appendix B) the Mohr circle of strain rates can be constructed, and with the concept of the pole, the directions of the principal strain rates (Figure 4.9) can be defined (Abbott, 1966). Mohr circles are constructed at regular intervals along the lines of the subsoil embedded lead markers and the direction of the principal strain rate components is obtained. This allows for a network of mutually orthogonal curves, tangential to these directions, to be graphically constructed (Figure 4.9). This network is also the network of directions of the principal directions of stress, in view of Saint Venant's postulate.

It follows from the Riemann invariant solution that a new network of mutually orthogonal curves can be obtained graphically from the network of the principal strain rate directions by joining the diagonally opposite corners. These new curves are seen to be two families of characteristics. This method has been used successfully by Windisch (1970) and reported by Windisch & Yong (1970), and by Yong & Windisch (1970).

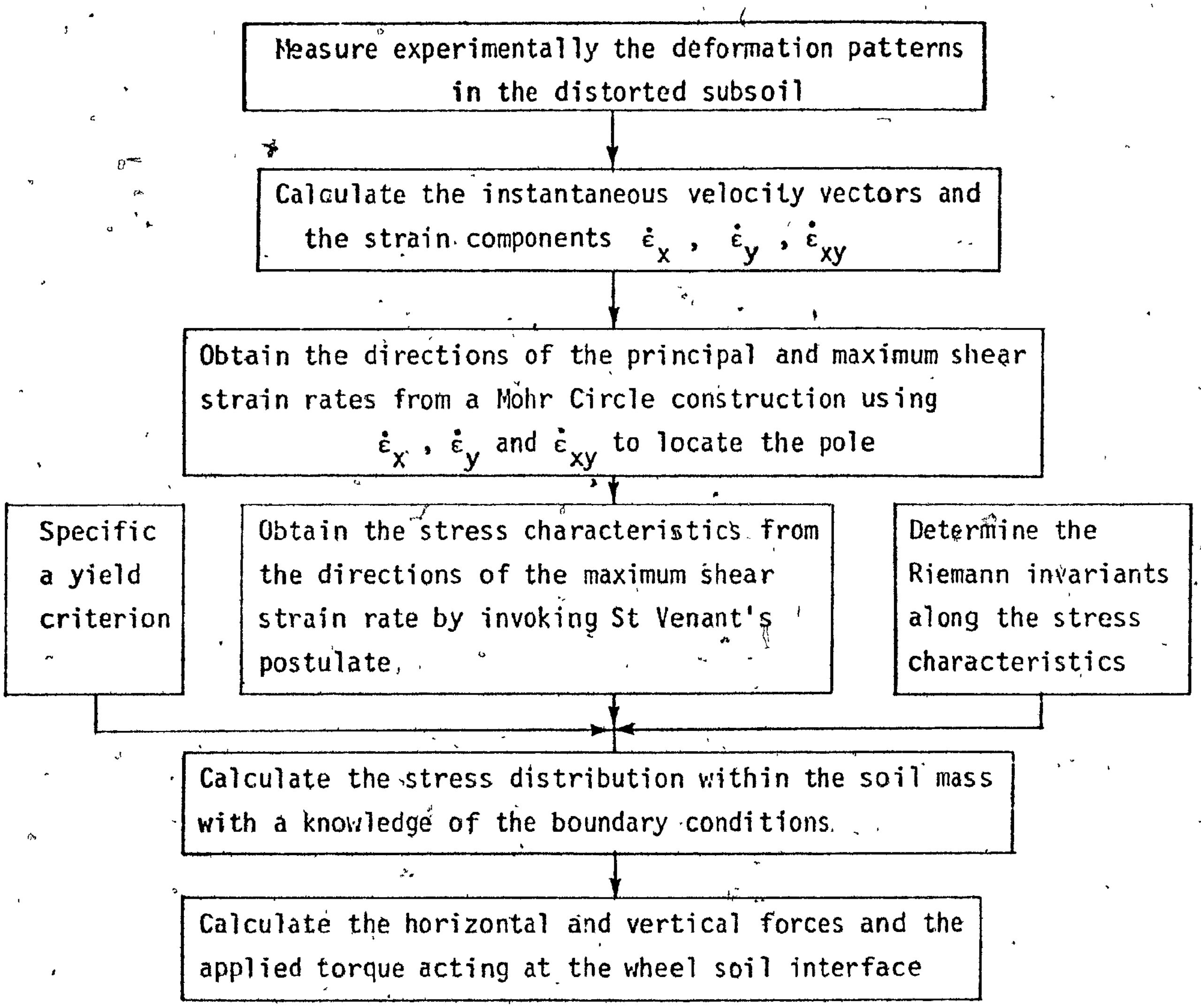

Fig.4.8 Calculation of the stress distribution by the method of characteristics (Williams 1973)

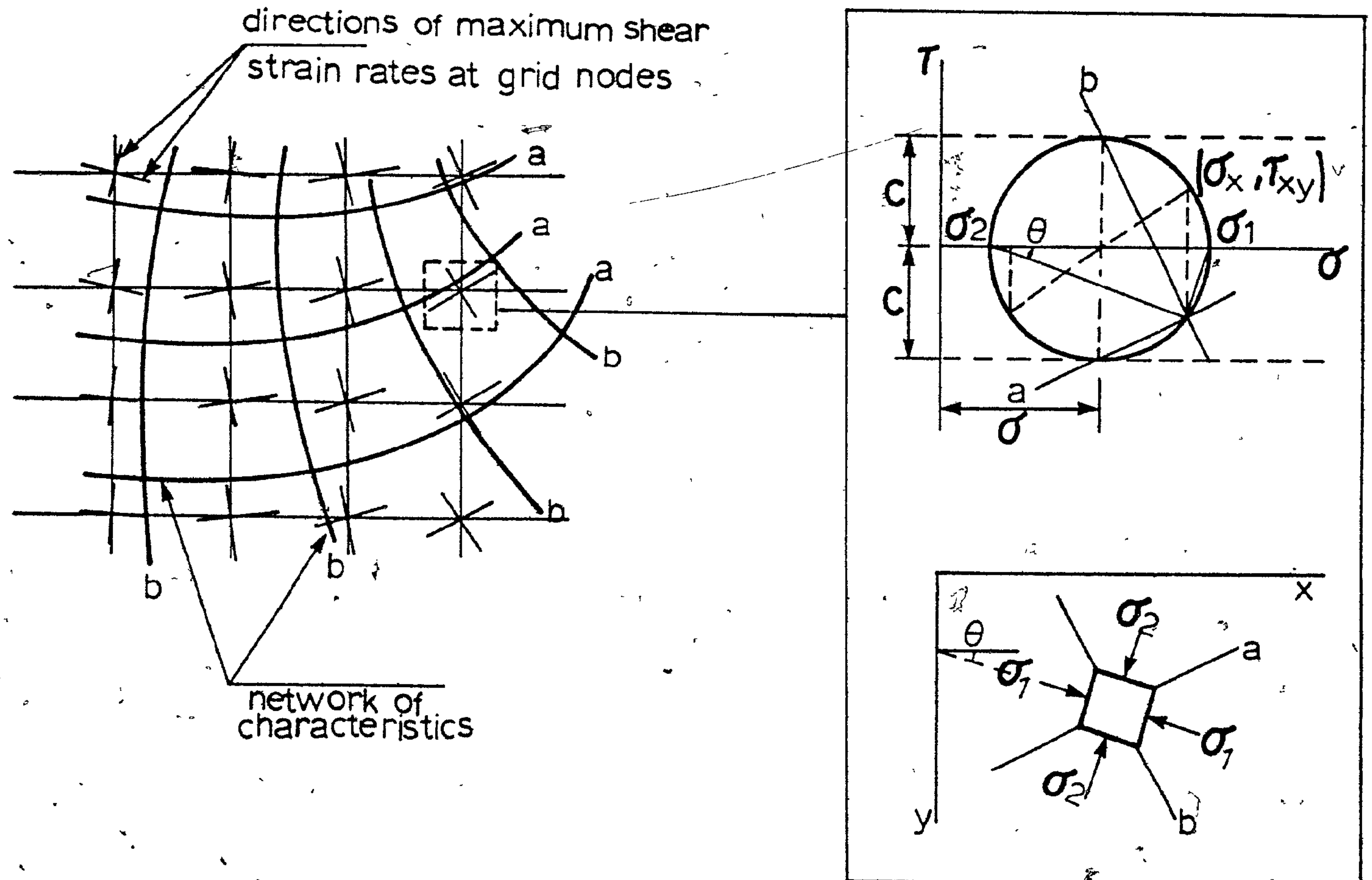

Figure 4.9 Stress characteristics and state of stress

4.5.4 Subsoil Stress Components

The material is assumed to obey the Mohr-Coulomb yield condition:

$$\tau_f = C + \sigma \tan \phi \qquad (4.1)$$

and for $\phi = 0$ $\qquad \tau_f = C$

If it is also assumed that the clay behaves as a rigid plastic material, and the shear strength is constant for a given clay soil, (i.e., the strength is independent of loading rate and confining pressure), then Equation 4.1 is equivalent to Tresca's yield criterion, provided that C is taken as the shear strength at yield.

From the network of the characteristics and the previous two assumptions, the stress components are calculated along the stress characteristics using the following two formulae, Appendix E:

$$\frac{\sigma}{2C} + m \quad = \quad \text{constant along a characteristics}$$

$$\frac{\sigma}{2C} - m \quad = \quad \text{constant along b characteristics}$$

where

σ is the mean stress $\frac{\sigma_x + \sigma_y}{2}$,

C the limiting shear stress,

m the slope of the characteristics w.r.t. horizontal.

To determine the stresses along the lines of characteristics, calculation must start at a point where either a normal stress component or the mean normal stress is known. The stress conputations can be initiated at an intersection of the characteristics with the line of compression tension divide. This is the line along which the mean normal stress is zero. Ahead of this dividing line, the state of stress is compression, and behind it, it is tension (Yong & Windisch, 1970).

4.5.5 Wheel-Soil Interfacial Stresses

Using the experimentally determined subsoil deformation beneath the moving wheel, the wheel-soil interfacial stresses can be predicted by using one of the following two approaches:

a - From the stress contours throughout the deformed region, it is possible to determine the contacting stresses at the wheel-soil interface.

b - Adopting a limit equilibrium approach and utilising the method of characteristics for problem solution, with the following information requirement:

1. wheel load and geometrical dimensions,
2. wheel dynamic sinkage, measured by a displacement transducer or using an x-ray photographic technique,
3. wheel-soil contact area, using an x-ray photographic technique,

4. angle of separation (the angle which separates the forward and backward failure zones) (Karafiath, 1971). This can be determined by using the trace motion of the subsoil-embedded lead markers, Figure 4.10.

As the second approach requires idealized flat soil surfaces at the forward and backward failure zones, the first approach is adopted for predicting the wheel-soil interfacial stresses, utilizing the experimentally determined subsoil deformation patterns.

4.6 Evaluation of Wheel Performance Using Energy Approach

The principle of conservation of energy can be used for evaluating wheel performance, provided the different wheel energy components can be measured or calculated. Energy applied to the wheel to keep it in constant uniform motion consists mainly of two components, the useful output energy and the energy losses dissipated in the wheel-soil system. Using the definition of specific energy, which is the energy per unit wheel width and unit wheel travel distance, and the energy balance equation, the performance of a moving wheel and its efficiency can be evaluated.

The energy approach was first introduced by Yong & Webb (1969) to evaluate the performance of a moving wheel on soft soil in the laboratory. In this approach the performance is expressed in terms

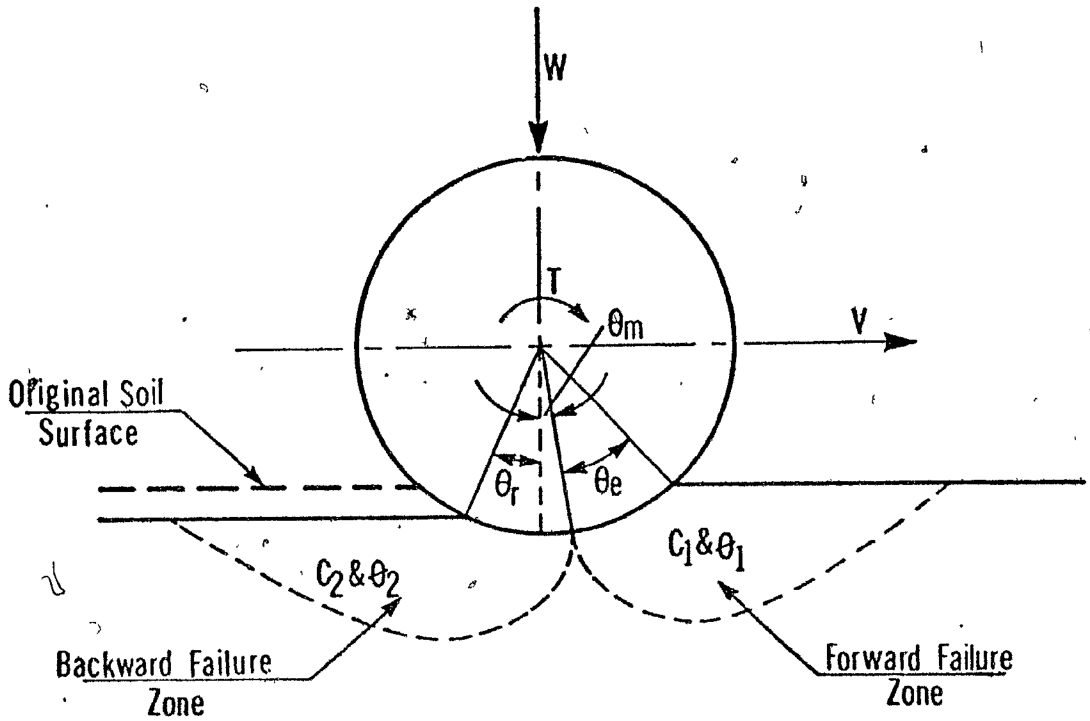

Legend:

C_1 and ϕ_1 Soil strength parameters at Forward Failure Zone
C_2 and ϕ_2 Soil strength parameters at Backward Failure Zone
θ_m Angle of separation
θ_r Rear angle
θ_e Entry angle
D Wheel diameter

Fig. 4-10 Idealization of the Physical Model for Limit Equilibrium Solution (Method of Characteristics) of wheel energy components as a function of slip. These components are input energy, parasitic energy and useful output energy. The input energy is applied at the wheel axle to keep it in constant motion. The parasitic energy consists of the deformation energy (lost in deforming the wheel and the soil beneath it in horizontal and vertical directions) and the interfacial energy (lost at wheel-soil interface due to slip). The useful output energy is the energy required to produce the drawbar pull. The graphical representation of the wheel energy components, as a function of normal slip, gives a clear picture of the whole spectrum of wheel performance from the towed point to 100 percent slip.

4.6.1 Deformation Energy

There are two methods for computing the deformation energy from the experimental test results. Both methods use the visioplasticity technique. The previous assumptions used for idealizing the soil properties to obtain subsoil and wheel-soil contact stresses are implied herein for calculating the deformation energy.

a. First Method

For a material which follows Von Mises yield criterion, the rate of doing work under plane strain conditions can be expressed as (Yong & Fattah, 1975):

$$\dot{W} = 2\,k\,\sqrt{I_2} \tag{4.2}$$

where k = yield stress in shear

I_2 = strain rate invariant

By computing ($\sqrt{I_2}$), the strain rate invariant at every node of the soil grid beneath the wheel (Appendix B), using:

$$I_2 = [(\varepsilon_x'^2 + \varepsilon_y'^2)/2 + \dot{\gamma}_{xy}^2/4] \tag{4.3}$$

where ε_x', ε_y' = normal strain rate components

$\dot{\gamma}_{xy}$ = shear strain rate components

then the deformation energy for unit width per element for the subsoil grid can be expressed as:

$$d = 2\ k*I_2^{\frac{1}{2}}*dxdy \tag{4.4}$$

and the total deformation energy can be expressed as:

$$D = 2\ k \sum_{1}^{N} \sum_{1}^{M} I_2^{\frac{1}{2}}\ dxdy \tag{4.5}$$

where M = Number of nodes in X-direction

N = Number of nodes in Y-direction

dxdy = dimension of the element.

b. Second Method

The deformation energy during a time interval can be evaluated by the following formula:

$$E = \iiint \dot{\bar{\varepsilon}} \, \bar{\sigma} \, dt \, dx \, dy \tag{4.6}$$

The effective stress can be determined by analyzing the experimental results of triaxial tests for the same clay. If the clay is assumed to be acting as a rigid plastic material the value of the effective stress will be constant.

The rate of deformation energy in the soil, on a unit time basis for each element of the grid, is:

$$\dot{d} = \dot{\bar{\varepsilon}} \, \bar{\sigma} \, dx \, dy \tag{4.7}$$

The total deformation energy per unit width can be evaluated by using Simpson's rule:

$$D = \frac{t}{3} [\dot{d}_1 + 2\dot{d}_2 + 2\dot{d}_3 + \ldots\ldots] \tag{4.8}$$

where

$$\dot{d}_j = \frac{1}{3} (\bar{\sigma}_{1j} \; \dot{\bar{\varepsilon}}_{1j} + 4 \, \bar{\sigma}_{2j} \; \dot{\bar{\varepsilon}}_{2j} + 2 \, \bar{\sigma}_{3j} \; \bar{\varepsilon}_{3j} + \ldots\ldots) \tag{4.9}$$

Comparison of the two methods

In the first method of analysis, k, the yield stress in shear, is determined from the results of plane strain triaxial tests (Appendix A). The second strain rate invariant, I_2, is determined at each of the subsoil grid nodes, provided the subsoil deformation fields as a function of time are known. Details of the calculation are shown in Appendix B.

The staggered orthogonal subsoil grid nodes are one inch apart in the vertical and horizontal directions, i.e. dx = dy = one inch. It should also be noticed that all the calculations are made with respect to original grid coordinates.

In the first method of analysis it is implicitly assumed that the second strain rate invariant is constant in the square element surrounding each node. Thus, summation has to be done for all subsoil elements in order to obtain the total deformation energy loss.

In the second method of analysis the deformation energy at each node is calculated by knowing the power of deformation energy, then integrating with respect to the time using Simpson's rule, formula (4.9). The power of deformation energy is calculated by knowing the effective stress and the corresponding effective strain at each node, then integrating using Simpson's rule with respect to distances. In this analysis the clay is assumed to behave as a rigid plastic material, so that the value of the effective stresses remains constant.

Both methods were used for calculating the total deformation energy, resulting in good agreement. The deformation energy contours are plotted for each wheel test using the first method. Figures 4.11 and 4.12 show the energy contours for two different degrees of slip.

c. Finite Element Method

In the finite element solution, stress-strain relations plotted from the results of plane strain triaxial tests are used for developing the constitutive relationships. The power of deformation energy is calculated at each incremental wheel travel distance in each finite element using the following formula:

$$\dot{W} = \tfrac{1}{2} \int \frac{T}{\Delta x} [(\sigma_{x1}+\sigma_{x2})d\varepsilon_x + (\sigma_{y1}+\sigma_{y2})d\varepsilon_y + (\tau_{xy1}+\tau_{xy2})d\varepsilon_{xy}]\, dA \qquad (4.10)$$

Since a constant strain triangular element is used in the analysis, the power of deformation energy per element is:

$$\dot{W} = \frac{T}{2\Delta x} [(\sigma_{x1}+\sigma_{x2})d\varepsilon_x + (\sigma_{y1}+\sigma_{y2})d\varepsilon_y + (\tau_{xy1}+\tau_{xy2})d\varepsilon_{xy}]\, A \qquad (4.11)$$

The total power of deformation energy can be calculated by:

$$\dot{D} = \sum_{1}^{N} \dot{W} \qquad (4.12)$$

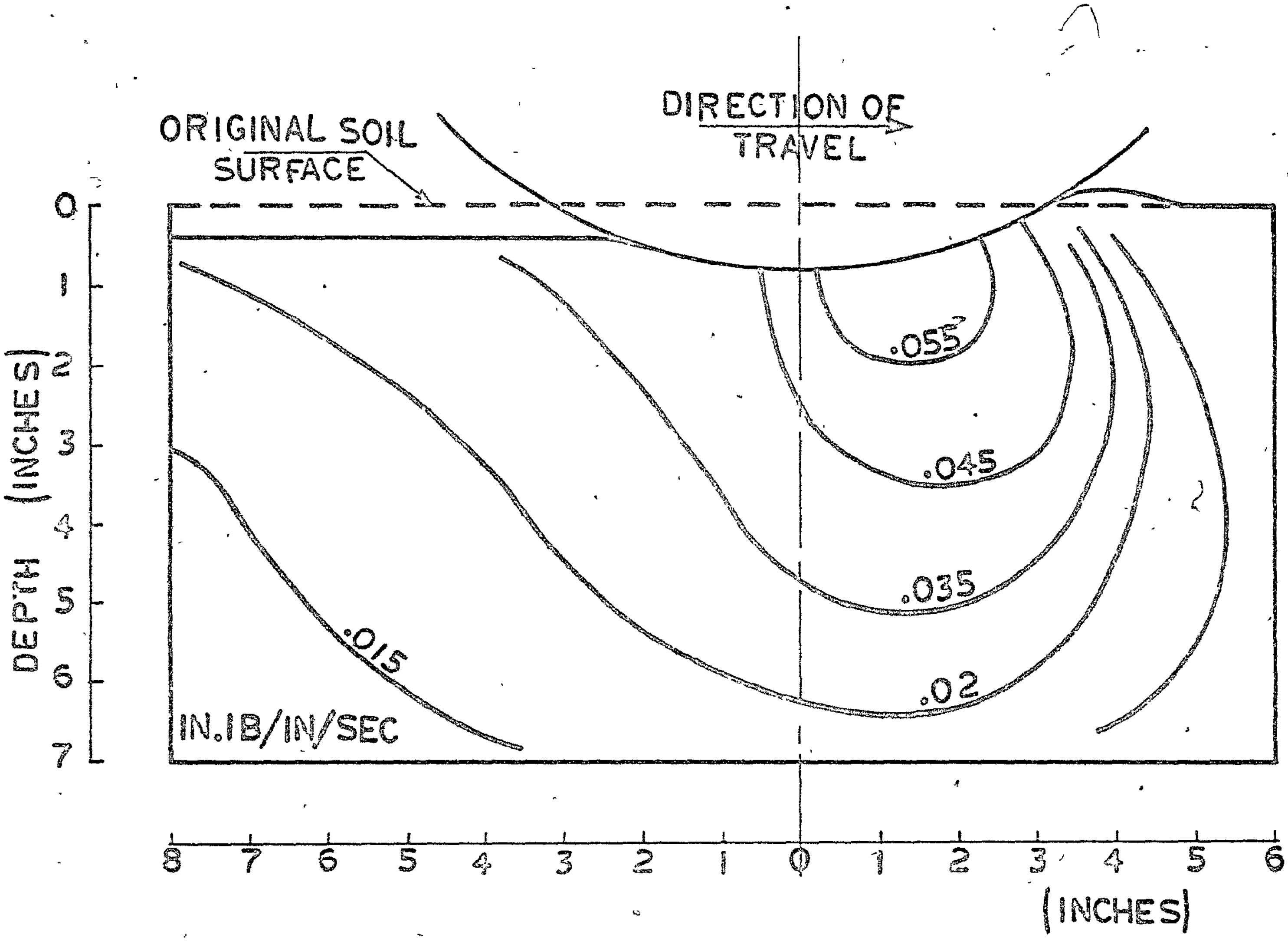

Figure 4.11 Deformation energy contours

Wheel load 34.0 lb
Slip 15 percent
Rubber coated wheel

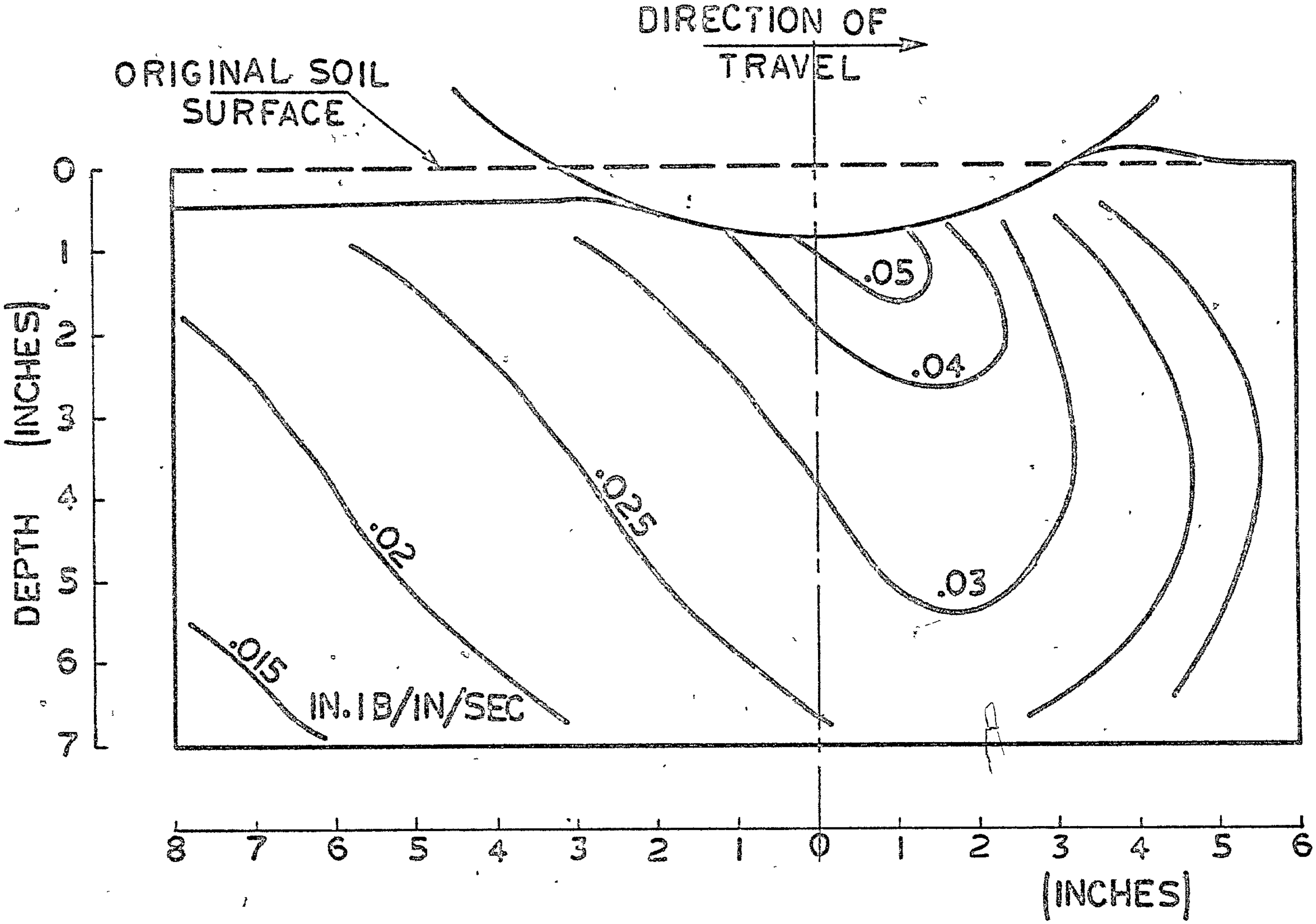

Figure 4.12 Deformation energy contours

Wheel Load 34.0 lb

Slip 50 percent

Rubber coated wheel

where

σ_{x1}, σ_{y1}, τ_{xy1}	are the states of stress at the start of the increment,
σ_{x2}, σ_{y2}, τ_{xy2}	are the states of stress at the end of the increment,
$d\varepsilon_x$, $d\varepsilon_y$, $d\varepsilon_{xy}$	are the incremental states of strains,
Δx	is the incremental wheel travel distance,
T	is the time of the incremental travel distance,
N	is the number of elements.

4.6.2 Interfacial Energy

The interfacial energy is the energy dissipated in the thin clay layer at the wheel-soil interface due to the differential velocity between the clay and wheel surfaces. The x-ray photographs of the wheel-soil interface during wheel travel indicate that the thickness of the interfacial layer varies from $\frac{1"}{8}$ to $\frac{1"}{4}$ depending on the degree of slip and wheel surface roughness. The visual inspection of the x-ray photographs indicates that the interfacial clay layer is subjected to a high degree of distortion and strain rate effect. The physical model, Figure 4.13, simulates the behaviour of the interfacial zone, which is a thin layer between two interfacial plates, one of which simulates the wheel surface and the other simulates the surface of the clay at the end of the interfacial zone.

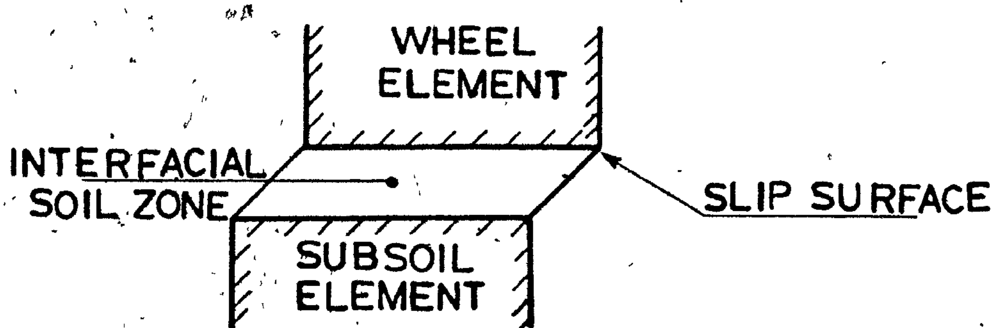

Figure 4.13 Physical Model of interfacial soil zone

Yong (1968) indicated that the mechanism for the interfacial energy loss is primarily a viscous type of phenomenon in which the energy is dissipated by the frictional shear stresses at the interface. These high shear stresses arise out of the stress transfer mechanism acting at or near the interface.

In the case of a saturated cohesive soil deforming under undrained conditions, it is possible to assume the existence of a maximum shearing stress which must be exceeded in order for slippage to occur. The onset of slippage is accompanied by the development of a slip zone in the interfacial region which is characterized by large shear distortion and consequent high shear stresses. The result of this is that energy is dissipated in this region by means of a viscous mechanism, analogous to a non-coulombic frictional dissipation process.

Work by Leitch (1964, 1967) and Japp (1967) suggests that at high strain rates, e.g., 100% per second, the increase in deviatoric stress is proportional to the logarithm of the strain rate.

The following law is therefore proposed

$$(J_2) = \eta \, Lg \, [1 + (\dot{I}_2)^{\frac{1}{2}}] \qquad (4.13)$$

where η is a viscosity parameter.

In this relationship, it is assumed that η is independent of both confining pressure and shear strain. Japp (1967) indicated that this is a reasonable assumption for strains above 4%. As strains of 70% are observed under the wheel, variations in η at low strain can be neglected.

The existence of a threshold value of interfacial stress at failure, as indicated from Equation (4.13), suggests that the rate of energy dissipation at the interface is a function of the velocity gradient across the slip interface, i.e., a function of the wheel-soil slip velocity, and hence, of the normal slip rate. In addition, it also suggests that the interfacial energy loss-slip rate characteristics will evidence a threshold value of slip rate below which the energy is sensibly close to zero. The value of the limiting shear stress of the soil is a constitutive property, and hence, independent of the wheel weight. The experimental test results indicate that the energy dissipation process in soils can generally be described with the aid of an exponential best fit curve, Figure 4.14 (Yong & Fitzpatrick-Nash, 1968).

It was found experimentally that the surface roughness of the wheel can influence the magnitude of the limiting shear stress, in view of the fact that a slip surface can develop either at the wheel-soil contact surface, or at some small distance below this surface. The effects of slip velocity and surface roughness on the magnitude of the limiting shear stress are shown in Figure 4.15. The data in this figure are plotted from results of skid tests on two types of surface conditions used in the test wheel. Details of the test and the apparatus are shown in Appendix A. The shear stress at failure is thus dictated either by the adhesive properties of the contact surface, or by the cohesive properties of the soil, depending upon which of the two is the lesser. Once the threshold shear stress has been exceeded, however, the energy dissipation

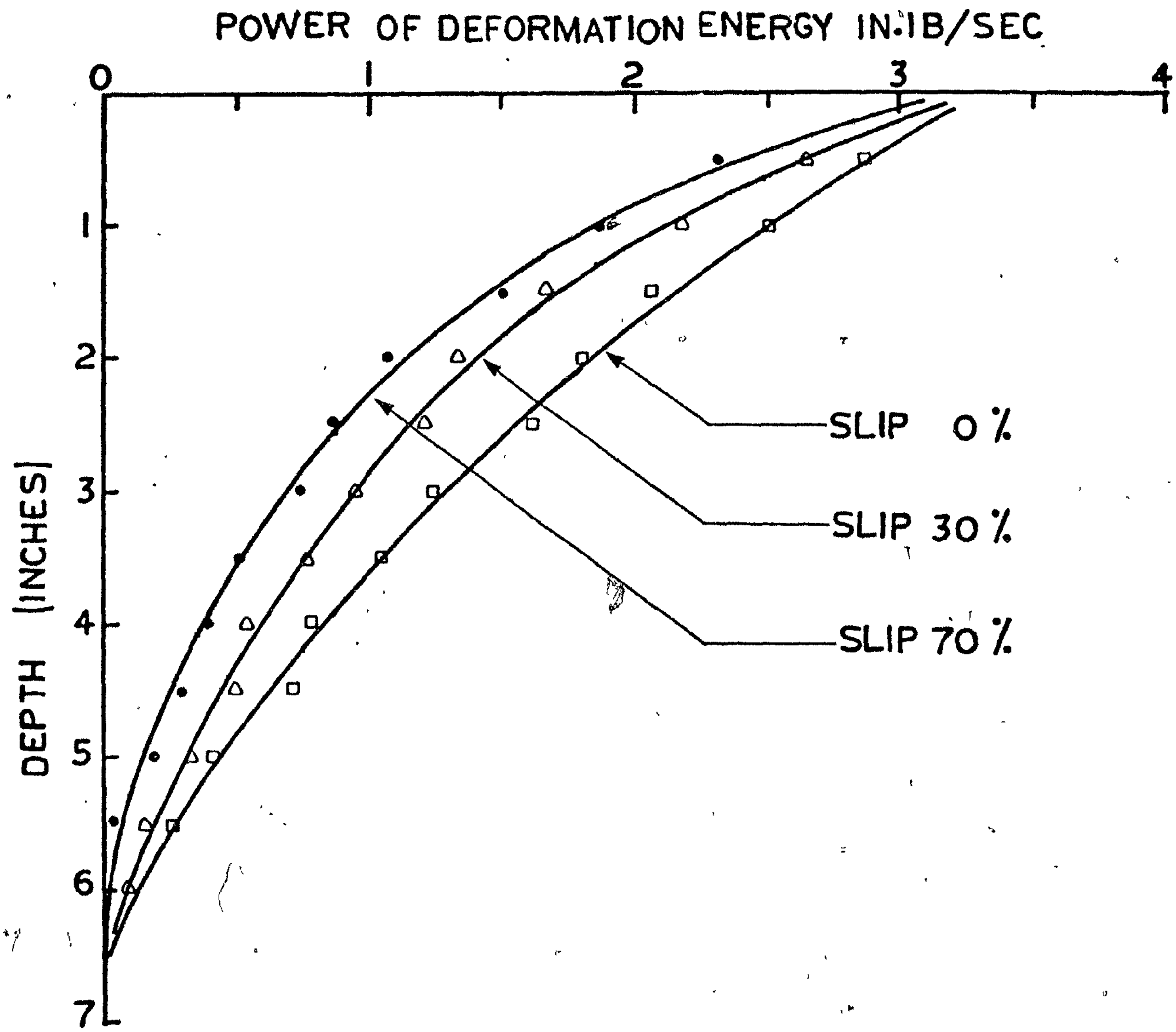

Figure 4.14 Deformation energy versus depth
Wheel Load 54.0 lbs

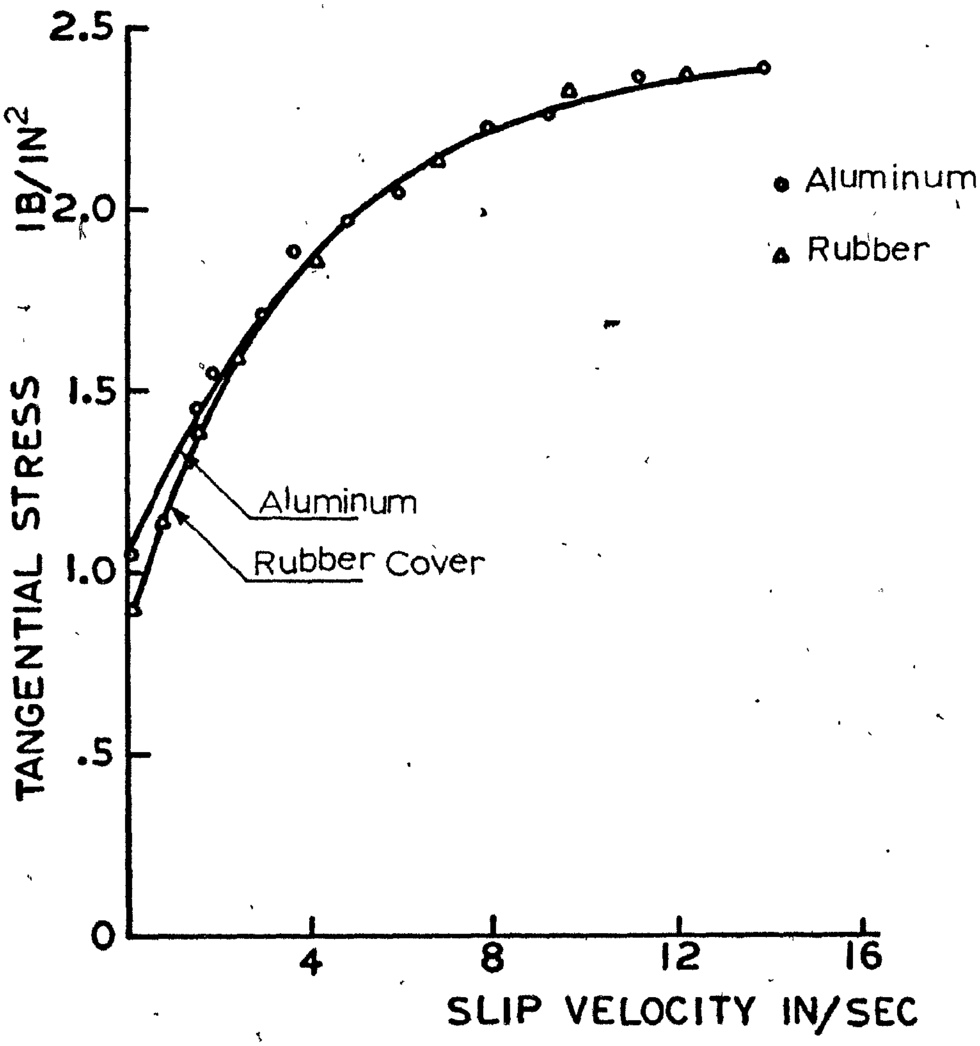

Figure 4.15 Effect of slip velocity on tangential stresses "Skid Test"

process is then solely a function of the magnitude of the actual shear stress acting at the interface of the wheel slip velocity. As a consequence, the wheel weight and geometry do not directly affect the specific interfacial energy (energy per unit contact area). The wheel radius is implicitly accounted for in terms of the slip velocity for any given wheel angular velocity.

The rate of dissipation of interfacial energy can be calculated from the experimental results using different approaches:-

(a) By determining the second strain rate invariant and consequently the corresponding second stress invariant at the interfacial zone using Equation (4.13), the interfacial energy is

$$\dot{F} = 2 \int_A \int_S (J_2 \dot{I}_2)^{\frac{1}{2}} \, dA \tag{4.14}$$

where J_2 = second invariant of the deviatoric stress tensor

$= \frac{1}{2} \sigma_{ij} \sigma_{ij}$

$\dot{I}_2$ = second invariant of the strain rate

S = thickness of the interfacial zone

A = wheel-soil area of contact.

Since the thickness of the interfacial zone is relatively small, a difficulty arises in determining its displacement pattern using the existing facility of the x-ray photographic technique.

(b) Assuming that the interfacial energy is dissipated along the surface of the soil-wheel interface, the rate of dissipation of energy can be obtained as

$$\dot{F} = \int_A \tau_f V_s \, dA \tag{4.15}$$

where τ_f = elemental shear stress

V_s = elemental slip velocity

V_s = rw - (carriage velocity + instantaneous soil velocity)

r = wheel radius

w = angular velocity

A = interfacial wheel-soil contact area.

In order to evaluate the interfacial energy, a knowledge of both the shear stress τ, and the velocity V_{soil} of the soil at the interface is needed over the entire area of contact. The interfacial tangential stress corresponding to the slip velocity is defined along each segment of the interface. The tangential stress, multiplied by the slip velocity, is then summed up over the entire area of contact to obtain the interfacial energy. From the experimentally determined subsoil displacement field, the subsoil velocity contours and the slip velocity along the wheel-soil interface can be determined.

The wheel-soil tangential stresses can be determined by applying the method of characteristics or by adopting the following approach.

It is assumed that the wheel-soil contact area consists of small plates of infinitesimal lengths of the same width as the wheel. The tangential stress at each plate can be determined from skid tests on a plate with the same surface condition and wheel width. Knowing the relationship between the tangential stress and slip velocity from the skid test, the tangential stresses at the wheel-soil interface can be determined, provided the slip velocity is known along the wheel-soil contact area.

(c) Third Approach

For high slip rates it can be assumed that the wheel-soil tangential stresses and slip velocity are fairly uniform. In this case the interfacial energy can be calculated by measuring the input torque and the translational and angular velocity, as follows: (Figure 4.16).

The input torque can be expressed as:

$$M = br \int_{\theta_1}^{\theta_2} r \, \tau \, d\theta \qquad (4.16)$$

$$\frac{M}{r} = b \int_{\theta_1}^{\theta_2} r \, \tau \, d\theta$$

$$\therefore \quad \frac{M}{r} = \tau \times A \qquad (4.17)$$

where $A = b \int_{\theta_1}^{\theta_2} r \, d\theta$ is the area of contact surface,

τA = Average shear force over the area of contact.

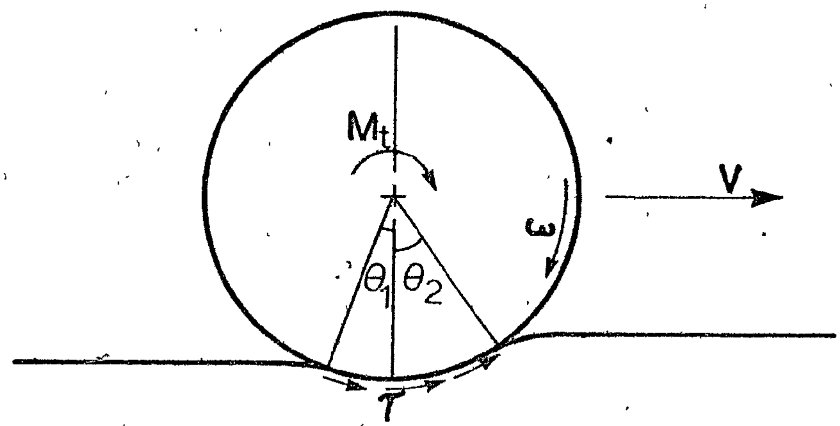

Figure 4.16 Schematic diagram of the parameters required for interfacial energy prediction at high degree of slip

The interfacial energy can then be expressed as:

$$\dot{F} = A \tau V_s = \frac{M}{r} V_s \tag{4.18}$$

where

r = wheel radius

b = wheel width

τ = average tangential stress

V_s = slip soil velocity =(rw - V)

(d) Finite Element Method

In the finite element solution the tangential reactions and velocities of the nodal points at the wheel-soil interface can be determined. The interfacial energy loss can be expressed as

$$\dot{F} = \sum_{1}^{n} R_T \, (rw - V) \tag{4.19}$$

where

n = number of nodes at wheel-soil contact surface,

R_T = nodal point tangential reaction,

rw = tangential wheel velocity,

V = nodal point tangential velocity.

It is implicitly assumed in the finite element solution that there is no strain rate effect on the mechanical properties of clay. The results, together with a corresponding comparison with the finite element solution, are presented in Chapter 6.

4.7 Test Results

The experimental program consisted of two types of tests, the first concerned a moving rigid wheel over soft soil and the second involved the determination of the physical and mechanical properties of the soil used in the tests. The test facilities and the procedure for doing a test are described in Appendix A.

A summary of the analysis of the experimental test results for the moving wheel over the soil for the surficial, above-ground parameters, and information concerning the energy balance, are shown in Tables 4.1, 4.2 and 4.3.The data concerning the physical and mechanical properties of the soil is given in Appendix A.

Test No.	Carr. veloc. vs in/sec	Ang. veloc. w.	Normal slip S%	Torque M in.lbs	Pull F lbs	Dynamic sinkage ins.	Rut Depth ins.	Energy per inch width: Torque input	Energy per inch width: Pull	Energy per inch width: Inter-facial	Energy per inch width: Defor-mation
Wheel Load = 34 lbs, D = 13.75 ins., b = 3.75 ins.											
1	6.1	.825	-7.5	30.5	-15.8	.45	.23	1.1	-4.2	.1	5.5
2	6.15	.972	8	94.9	-8.7	.52	.3	4.	-2.3	.2	6.
3	6.1	1.138	22	120.6	.8	.55	.35	6.	0.2	.8	5.5
4	6.1	1.305	32	148.7	5.6	.6	.3	8.5	1.5	1.8	5.5
5	6.15	1.72	48	181.	15.	.6	.37	13.5	4.0	4.3	5.0
6	6.15	2.236	60	206.3	16.1	.65	.37	20.	4.3	11.	5.0
7	6.15	2.755	68	231	18.8	.65	.32	28.	5.0	19.	4.12
Wheel Load = 54 lbs, D = 13.75 ins., b = 3.75 ins.											
8	6.1	.821	-8	27.7	-25.3	.8	.45	1.0	-6.5	.1	7.5
9	6.15	.972	8	123.4	-10.1	.85	.4	5.2	-2.7	.5	7.5
10.	6.15	1.118	20	165.	- 3.8	.9	.5	8.0	-1.0	.5	8.4
11	6.15	1.315	32	189.4	5.6	.97	.52	10.8	1.5	1.2	8.0
12	6.1	1.584	44	216.6	9.4	1.02	.53	15.	2.5	5.	7.5
13	6.1	2.016	56	229.2	15.	1.1	.45	20.2	4.0	10.	6.4
14	6.1	3.169	72	234.6	16.9	1.12	.5	32.5	4.5	21.5	6.75

TABLE 4.1 Summary of Test Results [Aluminum Wheel]

Test No.	Carr. veloc. vs in/sec	Ang. veloc. w	Normal slip s%	Torque M in.lbs	Pull F lbs	Dynamic sinkage ins.	Rut Depth ins.	Energy per inch width: Torque input	Energy per inch width: Pull	Energy per inch width: Inter-facial	Energy per inch width: Defor-mation
Wheel load = 74.0 lbs, D = 13.75 ins., b = 3.75 ins.											
15	6.1	.758	-17	39.2	-46.9	1.1	.45	1.3	-12.5	.1	13.
16	6.1	.792	-12	86.6	-38.3	1.02	.4	3.	-10.2	.1	13.0
17	6.05	.917	4	155.9	-18.8	1.1	.5	6.3	-5.0	.5	11.0
18	6.1	1.215	27	188.3	-4.5	1.18	.53	10.	-1.2	.8	10.25
19	6.1	1.479	40	224.3	3.8	1.25	.55	14.5	1.0	5.	8.5
20	6.	1.983	56	240.5	6.4	-.3	.5	21.2	1.7	10.8	9.0
21	6.05	2.75	68	260.	9.8	1.4	.45	31.5	2.6	20.	9.0

TABLE 4.1 Summary of Test Results (cont'd)

Test No.	Carr. veloc. vs in/sec	Ang. veloc. w rad/sec	Normal slip S%	Torque M in.lbs	Pull F lbs	Dynamic sinkage ins.	Rut Depth ins.	Energy per inch width: Torque input	Pull	Inter-facial	Defor-mation
Wheel Load = 34 lbs, D = 14.0 ins., b = 3.75 ins.											
22	6.1	.773	-15	0	-20.25	.58	.30	0	-5.4	.1	5.5
23	6.1	.847	-5	8.1	-16.88	.6	.35	.3	-4.5	.12	5.
24	6.15	.995	5	23.	-13.9	.62	.32	1.	-3.7	.15	4.75
25	6.15	1.1	18	51.2	-7.5	.63	.33	2.45	-2.0	.3	4.25
26	6.15	1.31	31	79.2	-3.75	.7	.32	4.5	-1.0	.7	5.0
27	6.15	1.68	47	126.	13.9	.68	.35	9.2	2.0	3.5	4.25
28	6.15	1.88	52	160.	7.9	.68	.35	13.	2.1	6.7	4.25
29	6.15	2.72	64	251.	7.9	.78	.38	29.7	2.0	22.5	5.0
Wheel Load = 54.0 lbs, D = 14.00 ins., b = 3.75 ins.											
30	6.15	.9	-14	2.9	-23.25	.87	.45	0.1	-6.2	.1	6.5
31	6.15	.945	5	24.4	-18.75	.92	.4	1.0	-5.0	.2	6.0
32	6.15	1.06	15	34.8	-16.9	1.0	.42	1.6	-4.5	.3	6.12
33	6.15	1.12	20	41.2	-13.5	1.02	.45	2.0	-3.6	.6	5.3
34	6.15	1.28	30	81.1	-9.4	1.02	.5	4.5	-2.5	1.	6.0
35	6.15	1.8	50	170.4	1.9	1.15	.52	13.3	0.5	6.5	6.3
36	6.15	3.	70	234.5	7.5	1.2	.5	30.5	2.0	22.5	6.

TABLE 4.2 Summary of Test Results - Rubber Strap Mounted

Test No.	Carr. veloc. vs in/sec	Ang. veloc. w rad/sec	Normal slip S%	Torque M in.lbs	Pull F lbs	Dynamic sinkage ins.	Rut Depth ins.	Energy per inch width: Torque input	Energy per inch width: Pull	Energy per inch width: Inter-facial	Energy per inch width: Defor-mation
Wheel Load = 74.0 lbs, D = 14.00 ins., b = 3.75 ins.											
37	6.15	.74	-20	0	-45.	1.06	.5	0	-12.0	.2	12.5
38	6.15	.85	-5	103.1	-26.3	1.1	.52	3.8	-7.0	.2	10.75
39	6.15	.95	5	133.5	-20.6	1.18	.55	5.5	-5.5	.5	10.5
40	6.15	1.0	10	138.4	-17.7	1.2	.5	6.	-4.7	.5	10.3
41	6.15	1.12	20	148.3	-11.3	1.25	.45	7.2	-3.	.7	10.
42	6.1	1.27	30	174.	-7.1	1.27	.5	9.6	-1.9	1.5	9.5
43	6.15	1.62	45	213.5	-1.9	1.35	.52	15.	- .5	5.3	9.25
44	6.1	1.78	50	212.	-1.9	1.32	.5	16.5	- .5	7.	9.
45	6.15	3.0	70	249.8	2.6	1.45	.55	32.5	0.7	23.	8.5

TABLE 4.2 Summary of Test Results - Rubber Strap Mounted (cont'd)

Test No.	Carr. veloc. vs in/sec	Ang. veloc. w rad/sec	Normal slip S%	Torque M in.lbs	Pull F lbs	Dynamic sinkage ins.	Rut Depth ins.	Energy per inch width			
								Torque input	Pull	Inter-facial	Defor-mation
Wheel Load = 34 lbs, D = 14.00 ins., B = 3.75 ins.											
46	6.1	.81	-13.4	8.5	-19.5	.4	.25	.3	-5.2	.1	5.75
47	6.15	.85	-7.4	54.3	-12.8	.42	.22	2.	-3.4	.12	5.5
48	6.2	.95	3.	122.4	-6.4	.44	.3	5.	-1.7	.6	6.12
49	6.15	1.035	18.	160.9	4.1	.48	.32	7.7	1.1	1.2	5.65
50	6.1	1.43	37.	216.	14.1	.52	.3	13.5	3.75	4.	5.75
51	6.15	2.02	55.	251.2	18.	.54	.35	22.	4.8	12.	5.75
52	6.15	2.28	60.	257.9	21.6	.5	.32	25.5	5.75	13.5	5.5
Wheel Load = 54 lbs, D = 14.00 ins., b = 3.75 ins.											
53	6.1	.84	-9	49.	- 0.6	.74	.45	1.8	-5.5	.1	8.0
54	6.1	.86	-5.5	79.8	-16.9	.78	.4	3.	-4.5	.4	8.70
55	6.15	1,	10.	150.	-7.5	.85	.43	6.5	-2.0	.5	8.70
56	6.15	1.085	15.6	170.	-2.6	.87	.4	8.0	-0.7	.5	8.5
57	6.15	1.17	22.	189.2	-1.9	.9	.5	9.6	0.5	1.	8.0
58	6.2	1.5	39.2	234.	10.2	.95	.45	15.1	2.7	4.5	6.8
59	6.1	1.705	47.	261.6	15.	1.02	.5	19.5	4.0	9.	6.75
60	6.15	2.07	56.4	261.8	18.	1.05	.5	23.5	4.8	12.	6.5
61	6.1	2.46	64.	293.	21.4	1.1	.52	31.	5.7	19.	6.5

TABLE 4.3 Summary of Test Results [Tread Wheel]

Test No.	Carr. veloc. vs in/sec	Ang. veloc. w rad/sec	Normal slip S%	Torque M in.lbs	Pull F lbs	Dynamic sinkage ins.	Rut Depth ins.	Energy per inch width			
								Torque input	Pull	Inter-facial	Defor-mation
Wheel Load = 74.0 lbs, D = 14.00 ins., b = 3.75 ins.											
62	6.1	.78	-15.6	58.6	-43.1	.95	.45	2.0	-11.5	.1	12.0
63	6.15	.93	2.4	151.2	-18.9	1.03	.47	6.1	-5.0	.3	11.25
64	6.15	1.02	11.	183.1	-11.3	1.08	.5	8.1	-3.0	.3	11.
65	6.1	1.14	21.6	208.7	-4.9	1.12	.52	10.4	-1.3	1.	10.75
66	6.1	1.29	30.6	223.4	1.1	1.15	.53	12.6	0.3	2.1	10.3
67	6.15	1.54	40.8	232.1	4.5	1.2	.47	15.5	1.2	3.6	10.1
68	6.15	1.94	53.	249.6	13.1	1.23	.52	21.	3.5	8.2	9.5
69	6.1	2.32	61.	261.3	13.5	1.3	.53	26.5	3.6	13.2	9.4
70	6.1	2.92	69.	274.2	13.1	1.35	.55	35.	3.5	22.	9.70

TABLE 4.3 Summary of Test Results [Tread Wheel] (cont'd)

CHAPTER 5

DISCUSSION OF RESULTS OF EXPERIMENTAL ANALYSIS

General

In this chapter the results of the experimental analysis of a moving rigid wheel on soft soil are discussed. The effect of wheel surface conditions on wheel performance and the effect of the degree of slip on the loading boundary (particle path) at the wheel-soil interface are also discussed in this chapter. The effect of slip on the different parameters which express wheel performance (sinkage, deformation energy, interfacial energy and useful output energy) is discussed. Adopting the principle of energy conservation in the form of an energy balance equation to the wheel-soil energy components in order to express wheel performance is presented.

5.1 Slip-Soil Particle Path

In order to obtain the loading boundary at wheel-soil interface (displacement) for the finite element solution, and to obtain a better appreciation of contact and interface relationships, representative soil particles or elements at some subsoil depth may be examined vis à vis soil motion under load. The soil particle paths express the motion of soil particles due to the surface motion of the wheel. These reflect the resultant soil mass deformation and distortion. If the experimental wheel moves with a constant translational velocity and constant degree of slip, and the soil is homogeneous, it is expected that all the soil particle paths should be similar for the same soil depth. The tangent, at any point on the soil particle path, indicates the displacement direction and also the velocity direction. The geometrical shape of the soil particle path, Figure 5.1, can be characterized by height of the bow wave, dynamic sinkage and rut depth.

In Figures 5.2, 5.3 and 5.4 the resultant particle paths, developed under a moving rigid wheel for rubber contact surface conditions, are given. Analysis for other conditions of loading and contact surfaces reveals that the shape of the particle path can take various forms - depending on load, degree of slip, and transfer characteristics.

Test results indicate that there is always soil recovery beneath the area of the wheel and that its value increases with increasing wheel load. This is in actual fact a phenomenon of high initial dynamic sinkage. The results also indicate that the height of the bow wave increases with increasing wheel load and decreasing degree of slip, i.e. the height of the bow wave for driven wheel (+ve slip) is less than for towed wheel (-ve slip). The dynamic sinkage value increases with increasing wheel load, and the horizontal components of the soil deformation decrease with increasing degree of slip and increase with increasing wheel load, i.e., the rolling resistance increases with increasing wheel load and dynamic sinkage. In general, the amount of soil distortion increases with increasing wheel load.

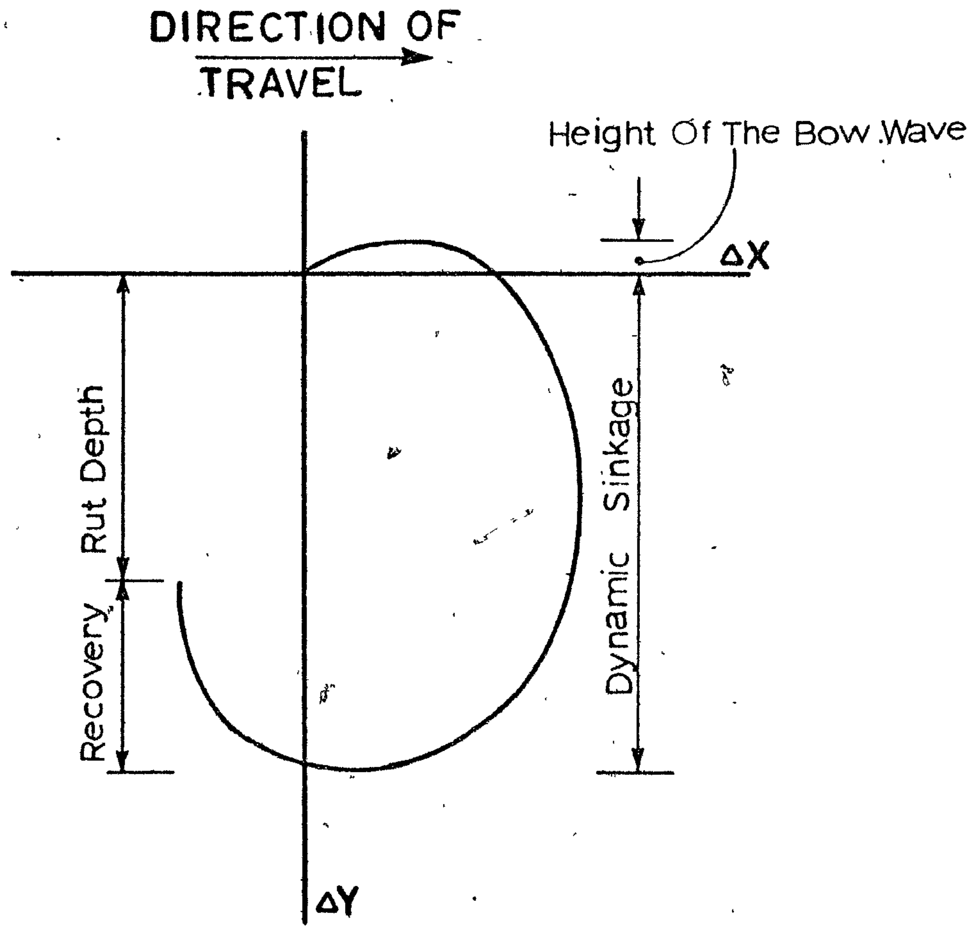

Figure 5.1 Characteristics of soil particle path due to moving wheel load

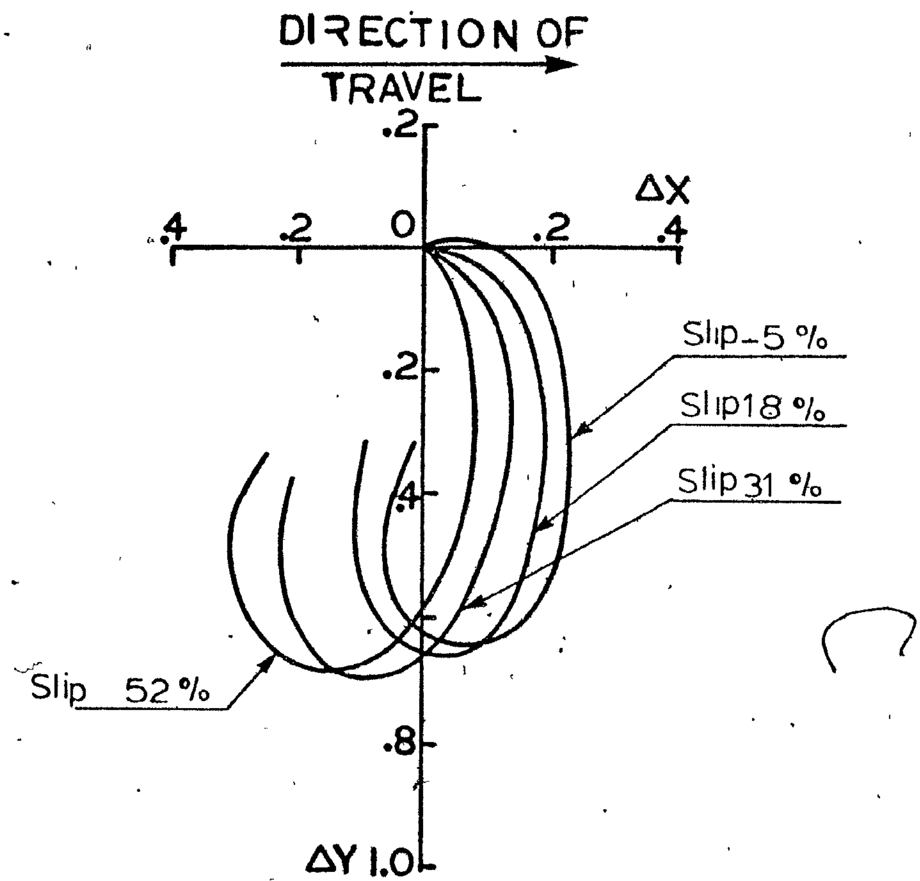

Figure 5.2 Soil particle paths at .5 inch depth beneath soil surface
Wheel Load 34.0 lbs
Rubber coated wheel

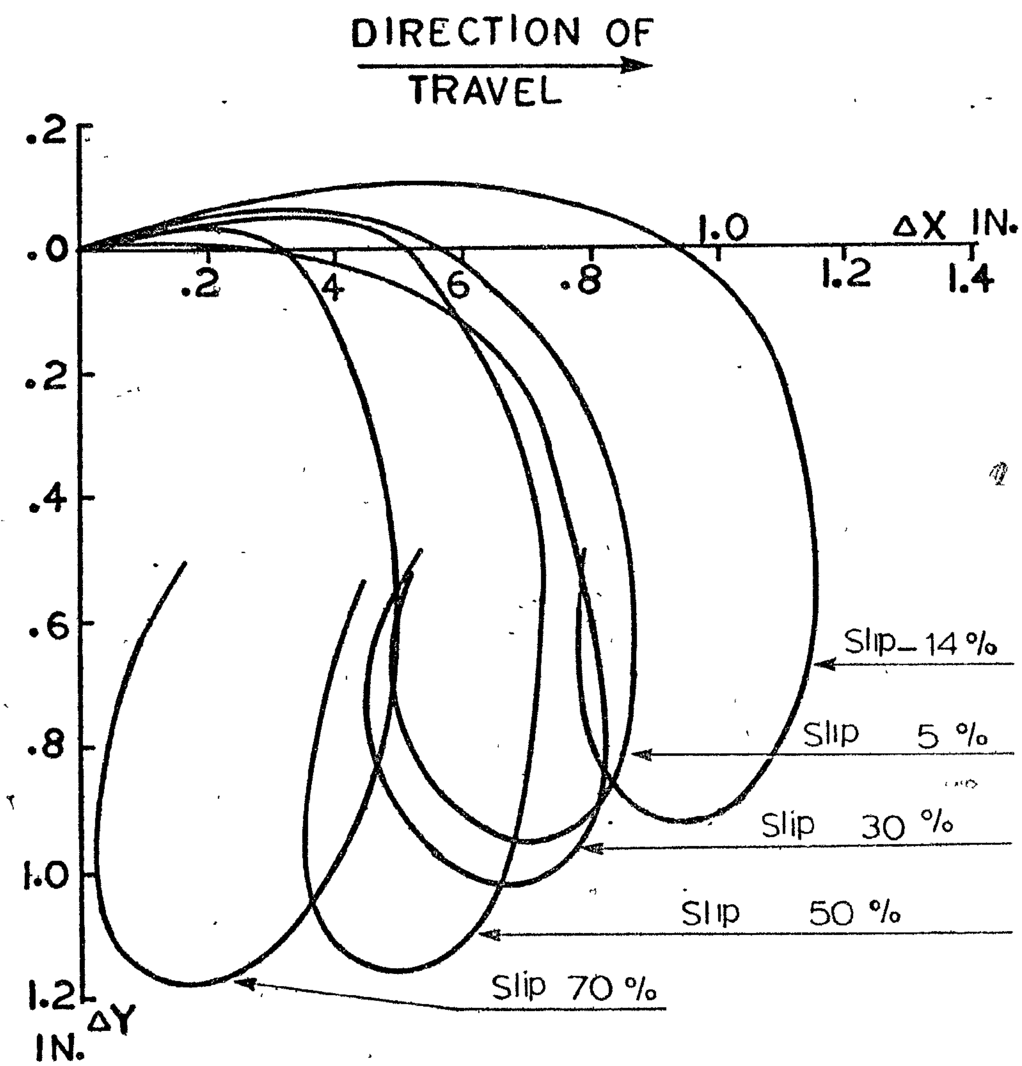

Figure 5.3 Soil particle paths at .5 inch depth beneath soil surface

Wheel Load 54.0 lbs

Rubber coated wheel

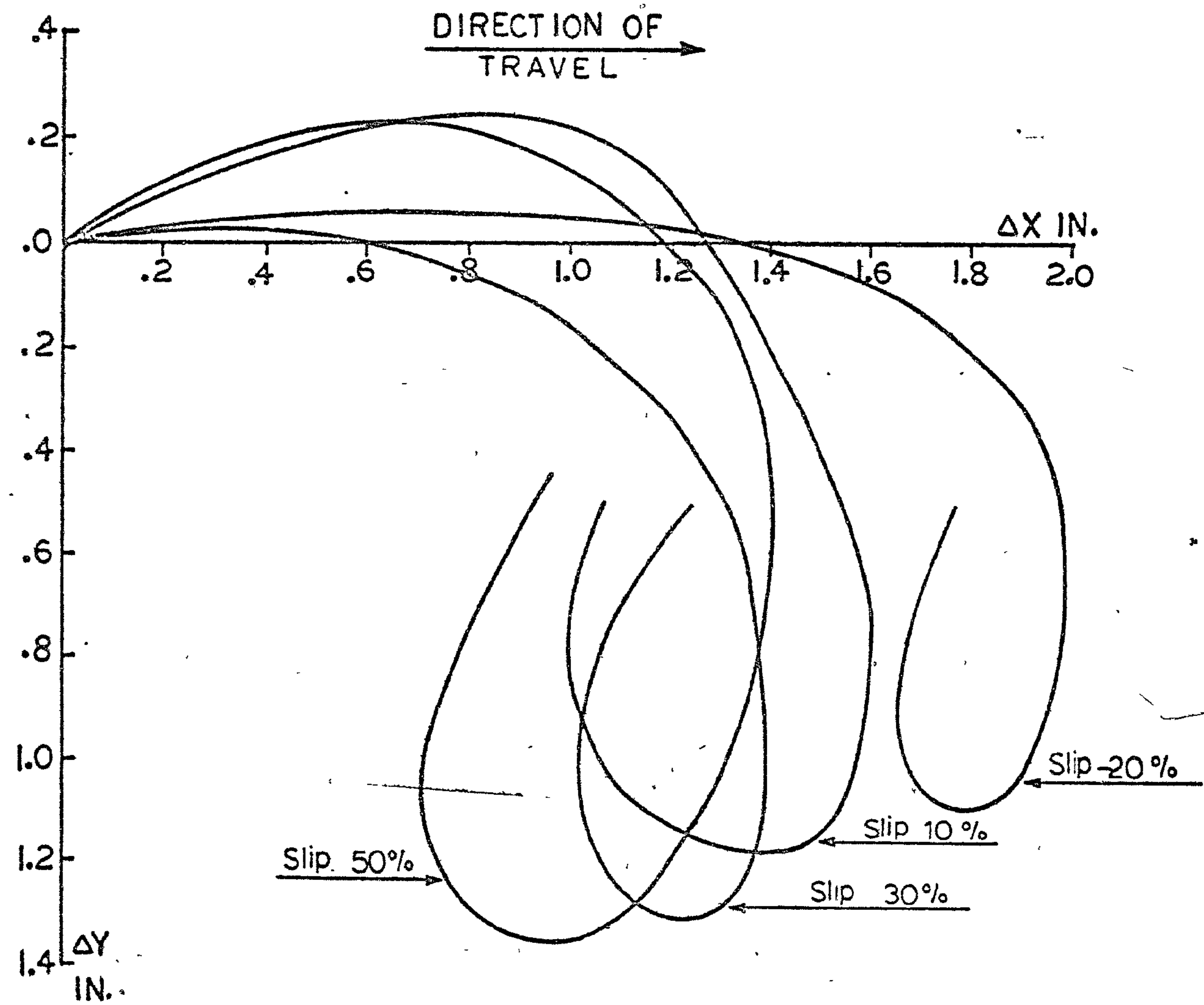

Figure 5.4 Soil particle paths at .5 inch depth beneath soil surface

Wheel Load 74.0 lbs

Rubber coated wheel

5.2 Slip Sinkage

The available semi-empirical and theoretical approaches for predicting the wheel-soil interfacial stresses require a knowledge of the dynamic sinkage and degree of slip, in addition to soil and wheel parameters. Slip is important with respect to efficiency because, for a given wheel speed, the vehicle reduces the distance over which the pull does work. Sinkage should be controlled, for it must remain smaller than the clearance of the vehicle (Goodman, 1966). Sinkage is a function of the interdependent wheel-soil parameters (P, T, D, b, V, w, surface condition, C, ϕ).

Some of the factors which affect the results of the solution of any continuum mechanics problem are the shape of the loading boundary and the mechanical properties of the continuum material. In wheel-soil interaction problem, the wheel-soil interfacial stress distribution (Onafeko, 1964) and the mechanical properties of the soil layer at the wheel-soil interface, are functions of slip, hence the dynamic sinkage which is one of the results if the continuum mechanics solution is adopted, should be a function of slip.

Bekker (1969) indicates that the sinkage (Z_0) consists of two components, one due to the static wheel load (Z_s) and the other (Z_j) due to slip:

$$Z_0 = Z_s + Z_j \tag{5.1}$$

Bekker also indicates that if the wheel load is smaller than the soil bearing capacity no soil deformation Z_j due to slip should be expected. This is not entirely correct for loose soils, though practically correct for cohesive soils. The dynamic sinkage versus degree of slip for different wheel loads and surface conditions is shown in Figure 5.5. The test results show an increase in sinkage with slip for higher wheel loads while, for small wheel loads, sinkage is nearly constant or increases slightly with increasing degree of slip.

The test results also indicate that dynamic sinkage increases with increasing wheel surface smoothness, Figure 5.5. This conclusion conforms well with expectations from continuum mechanics theories dealing with complex boundary stresses (Fung, 1965; Jaunzemis, 1967).

The slip-sinkage characteristics was studied by Yong & Webb (1968) by studying the soil behaviour under the wheel. Figure 5.6 shows the velocity distribution interpreted from resultant soil particle motion (e.g., Fig. 5.1) under the moving wheel.

Sinkage is increased slightly with the slip because the horizontal velocity contours, Figure 5.7, do not become excessively large at high slips. This is due to the soil shear discontinuity at the wheel-soil interface due to the provoking slip condition and hence to the fact that the soil work hardens in the shear boundary layer. The results also indicate that dynamic sinkage increases as a function of both increasing degree of slip and smoothness of wheel contact surface.

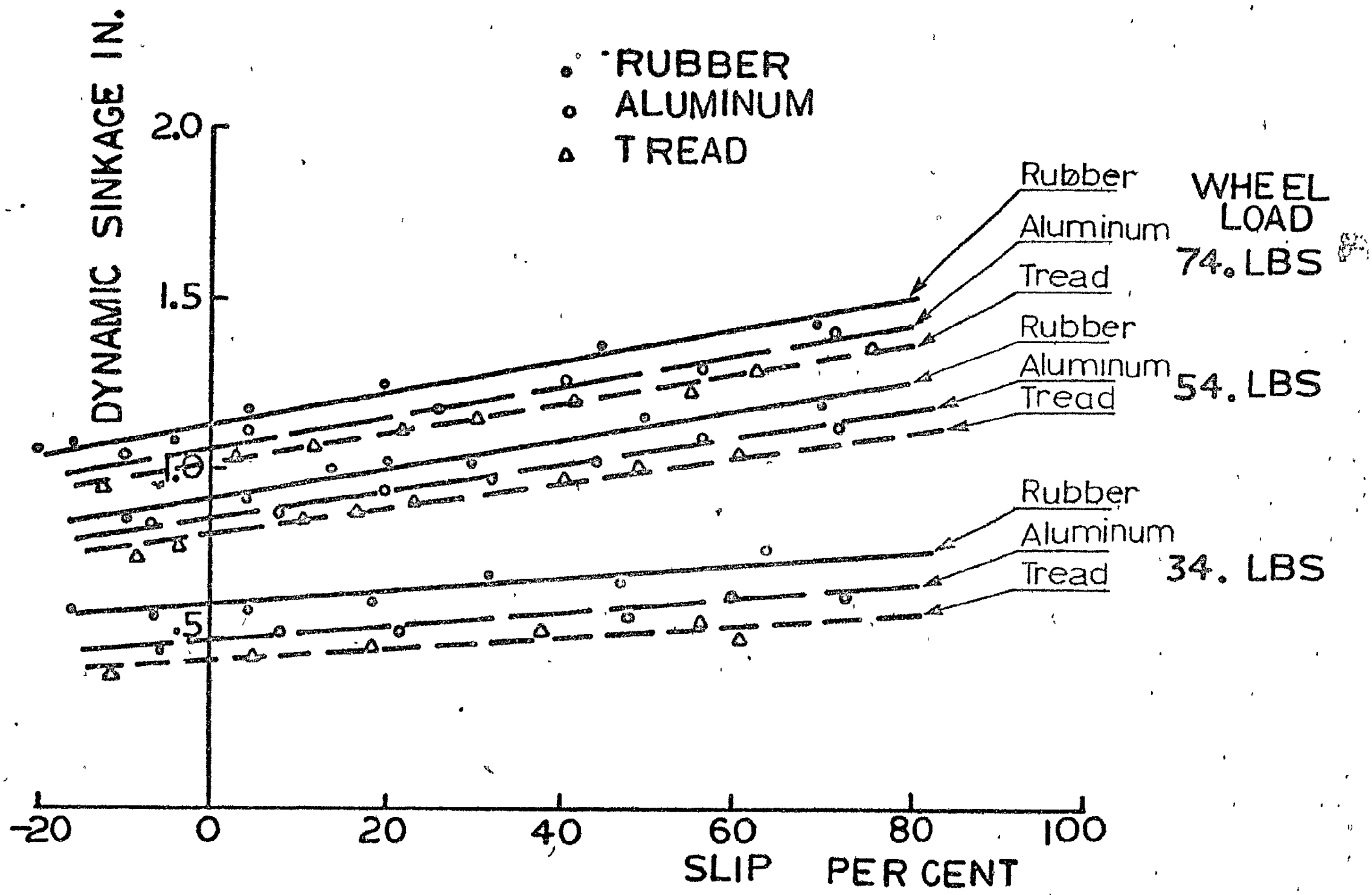

Figure 5.5 Dynamic slip relationship for different wheel loads and surface conditions

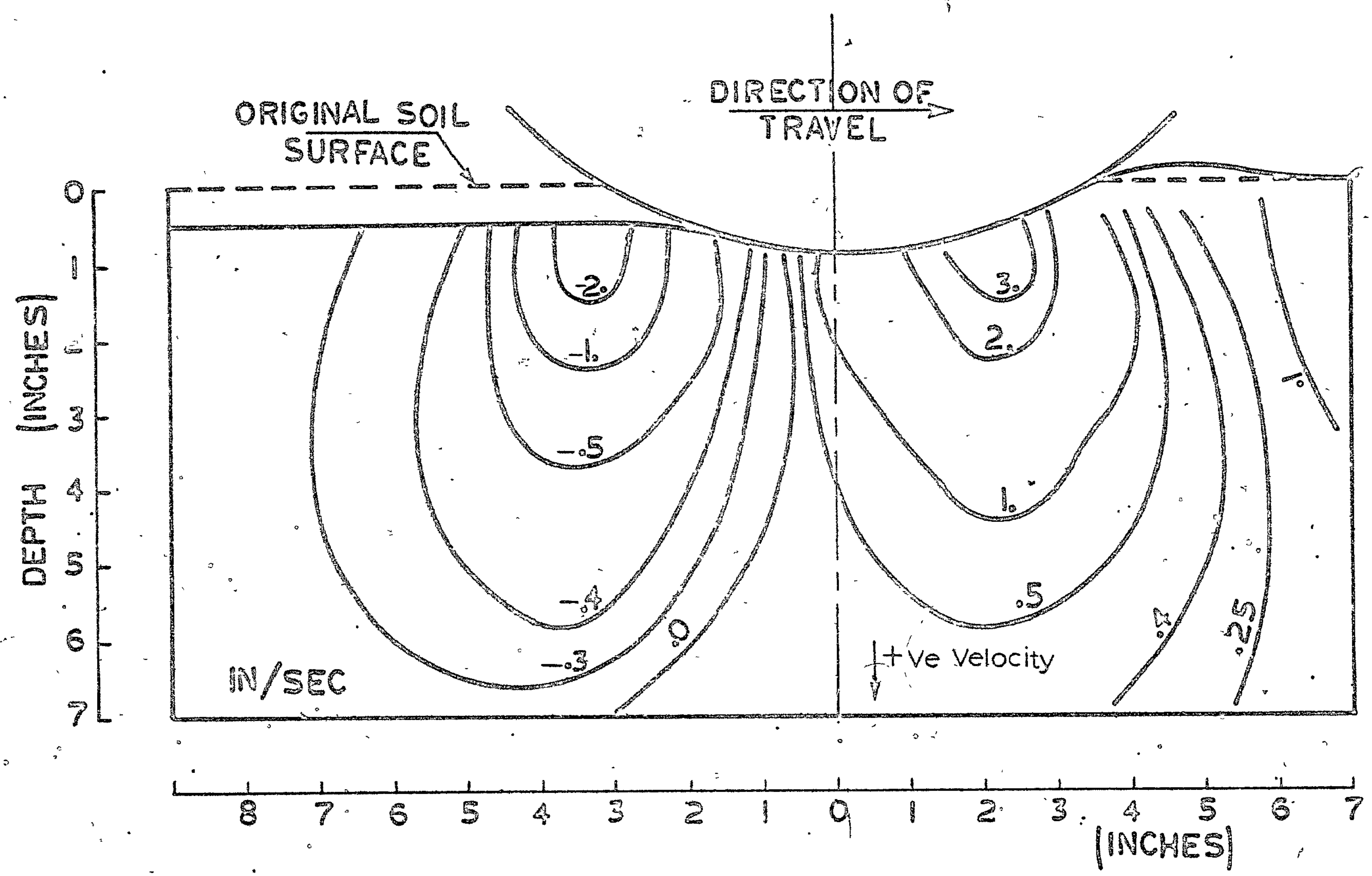

Figure 5.6 Vertical velocity contours (visioplasticity technique)

Wheel Load 54.0 lbs
Slip 20 percent
Rubber coated wheel

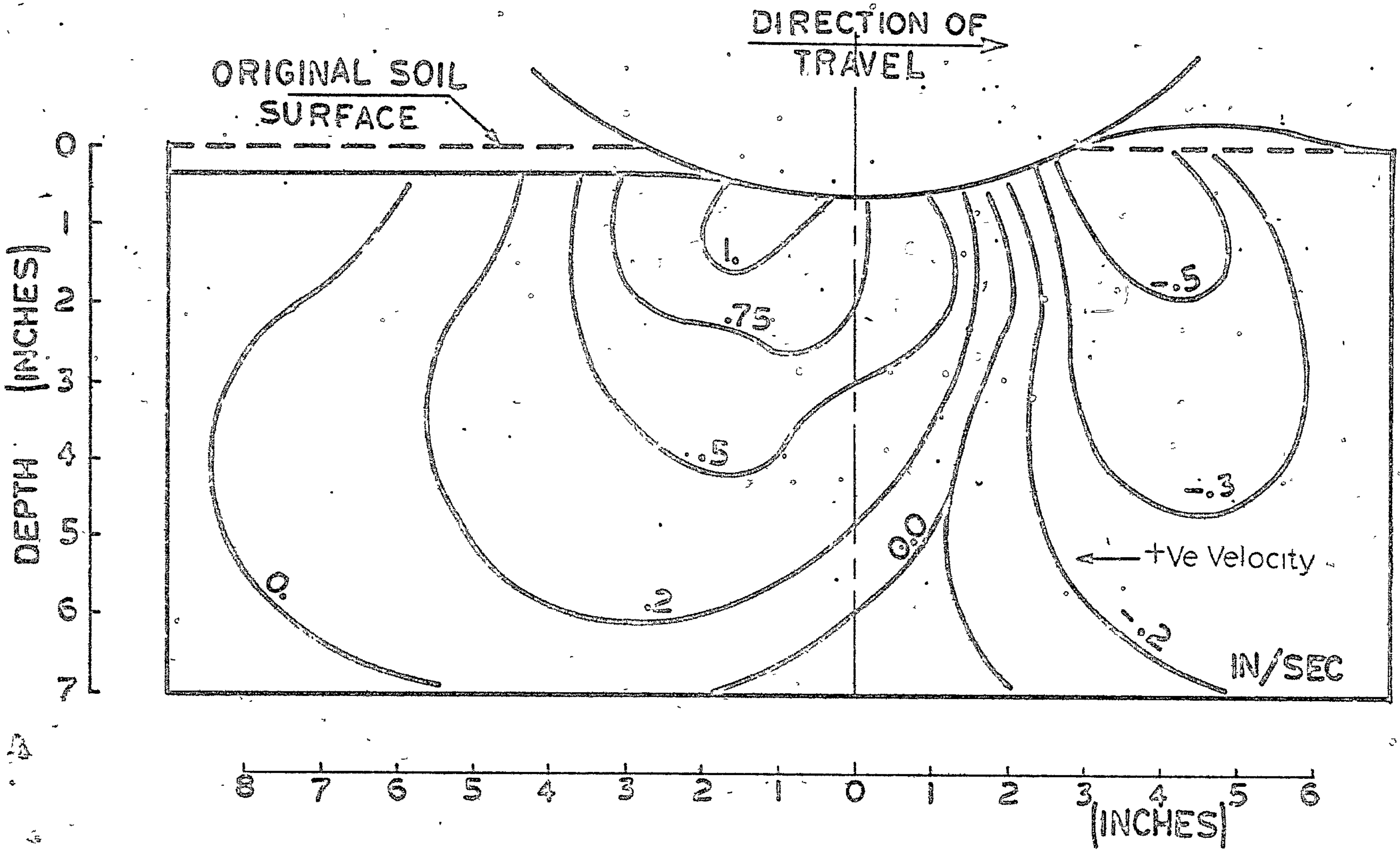

Figure 5.7 Horizontal velocity contours (visioplasticity technique)

Wheel Load 54.0 lbs
Slip 20 percent
Rubber coated wheel

5.3 Slip-Interfacial Energy

The parasitic energy due to a moving wheel over soft soil consists of two components, the interfacial energy which is dissipated in a thin layer of soil at the wheel-soil interface, and the deformation energy which is dissipated in distorting the soil beneath the wheel. The interfacial energy can be evaluated by knowing the distribution of the slip velocity and tangential stresses at the wheel soil interface (Chapter 4).

The test results demonstrate the expected dependencies between wheel load and developed interfacial energy as conditioned by wheel contact surface, soil type and degree of slip. It is interesting to note that, after a well-defined degree of slip, the interfacial energy appears to be only a function of slip and wheel load, i.e., independent of contact surface characteristics, as shown in Figure 5.8. As shown in the same figure, the rubber-surfaced wheel does indeed have an apparent smoother surface - due primarily to the properties of the clay-rubber interaction. Similar curves and relationships can be obtained for other wheel loads and contact surface characteristics, Figures 5.9 and 5.10. The characteristics singular point of slip which establishes the single valued relationship between slip rate and interfacial energy is seen to be independent of the factors and parameters associated with loading surface and subsoil.

At the singular point a thin layer of the clay coats the wheel surface; thus the slip occurs between the interfacial soil layer on the wheel and the subsoil surfaces.

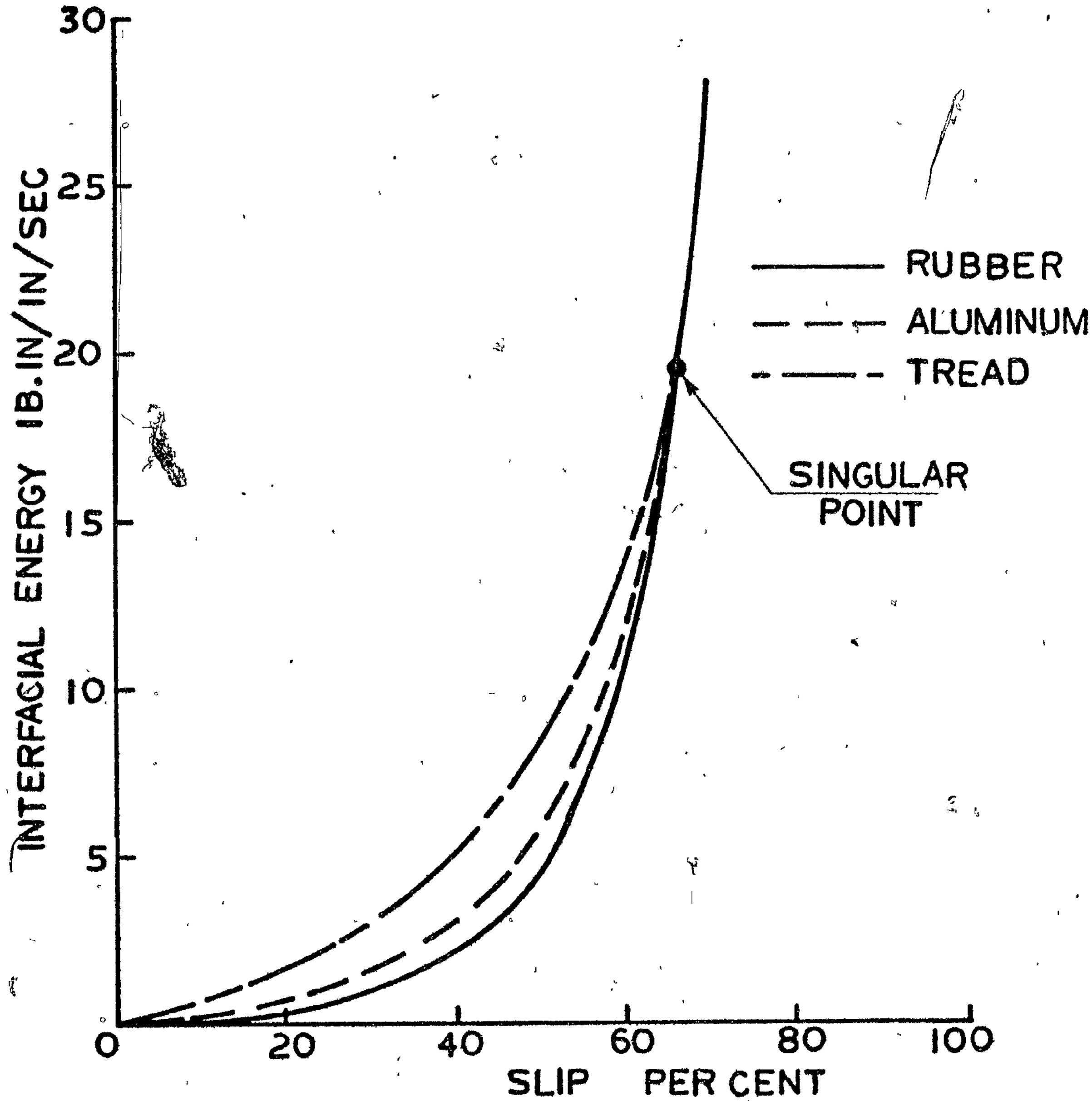

Figure 5.8 Interfacial energy slip relationship
Wheel Load 34.0 lbs

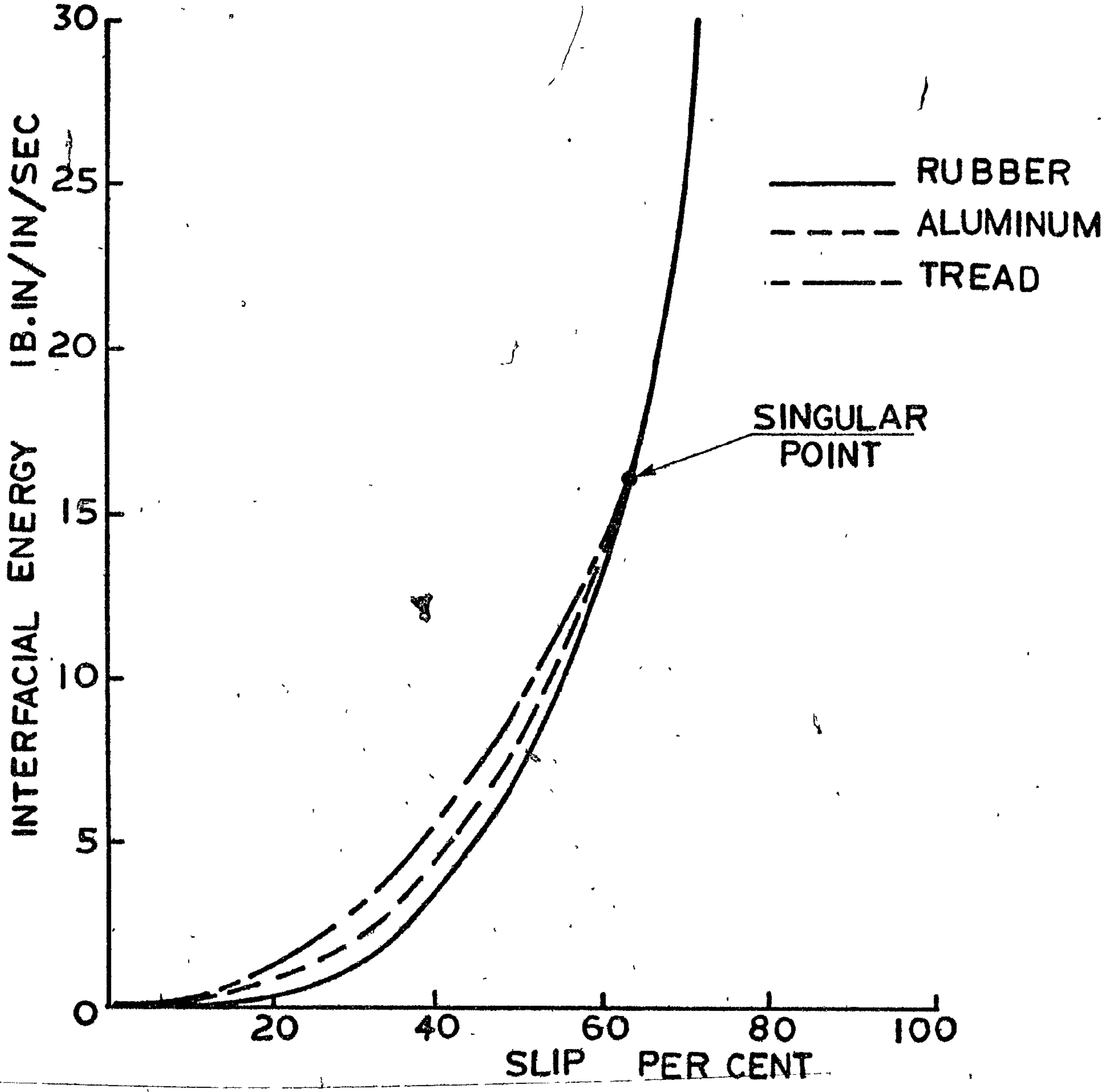

Figure 5.9 Interfacial energy-slip relationship

Wheel Load 54.0 lbs

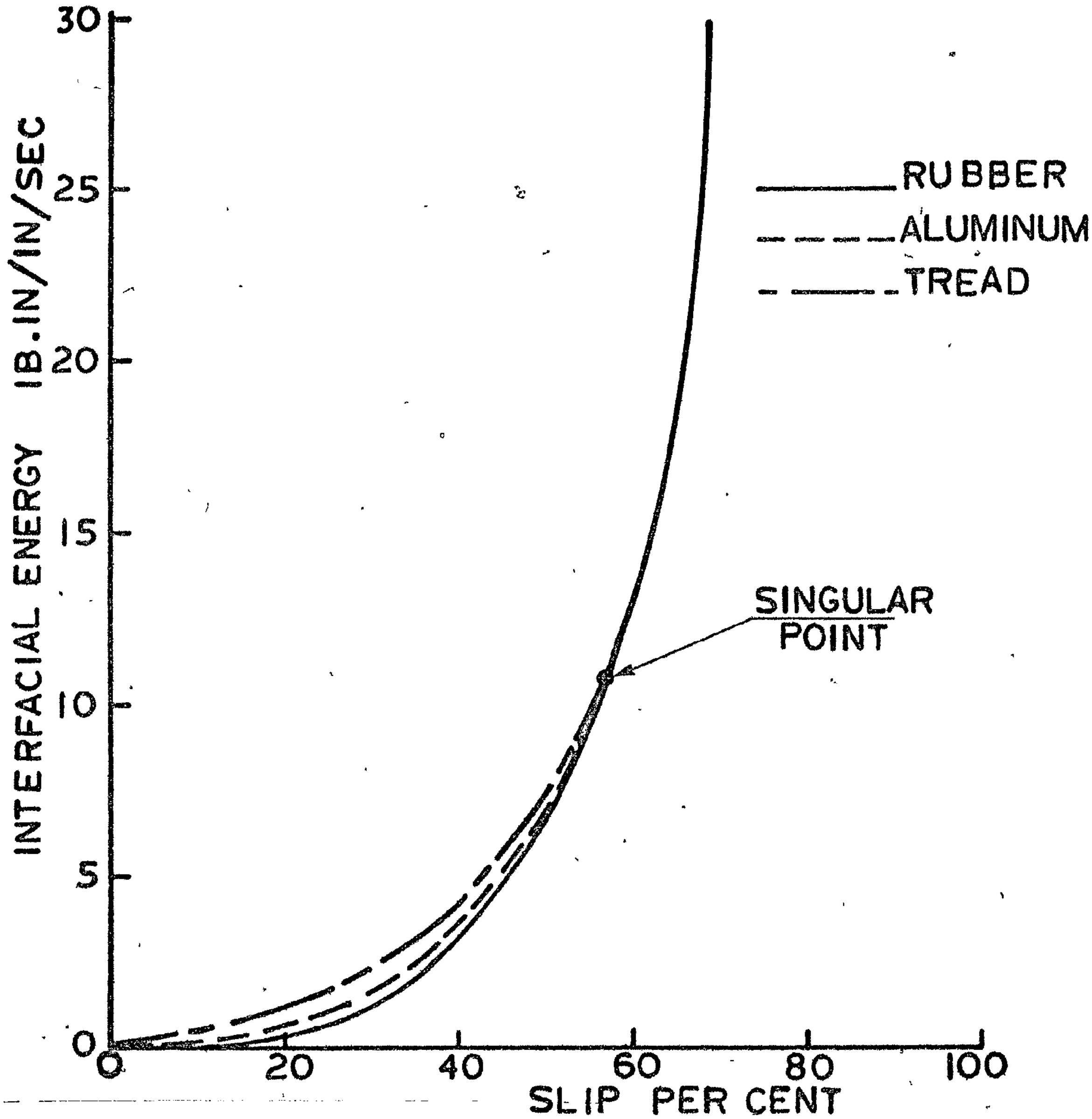

Figure 5.10 Interfacial energy-slip relationship
Wheel Load 74.0 lbs

Test results indicate, Figures 5.8 to 5.10, that the degree of slip at the singular point decreases with increasing wheel load; at higher contact stresses the interfacial soil layer coats the wheel surface at low degrees of slip.

5.4 Slip-Deformation Energy

As stated above, deformation energy is one of the two parasitic wheel-soil energy components and is a function of wheel and soil parameters. Test results indicate that at a lower degree of slip, the deformation energy increases with increasing wheel surface roughness, Figure 5.11. Also, the deformation energy dependency on slip increases with increasing wheel load due to the fact that the effect of slip on dynamic sinkage is greater for higher wheel loads than for smaller loads, as indicated by Equation 5.1 and as shown in Figure 5.5. While it may appear strange that with increasing degree of slip, sinkage increases and deformation energy decreases and asymptotes to a constant value, it should be recalled that the soil is a nonlinear material and that the work dissipated in deforming it is a function of the stress path or the displacement path length. The soil particle paths plotted from the results of x-ray photographs, Figures 5.2, 5.3 and 5.4, show that the length of the particle path increases with decreasing degree of slip. At higher degrees of slip or at a degree of slip beyond the critical slip point there is no effect of wheel surface condition on the deformation energy value, since beyond this point slip occurs between the clay-coated wheel and the clay soil.

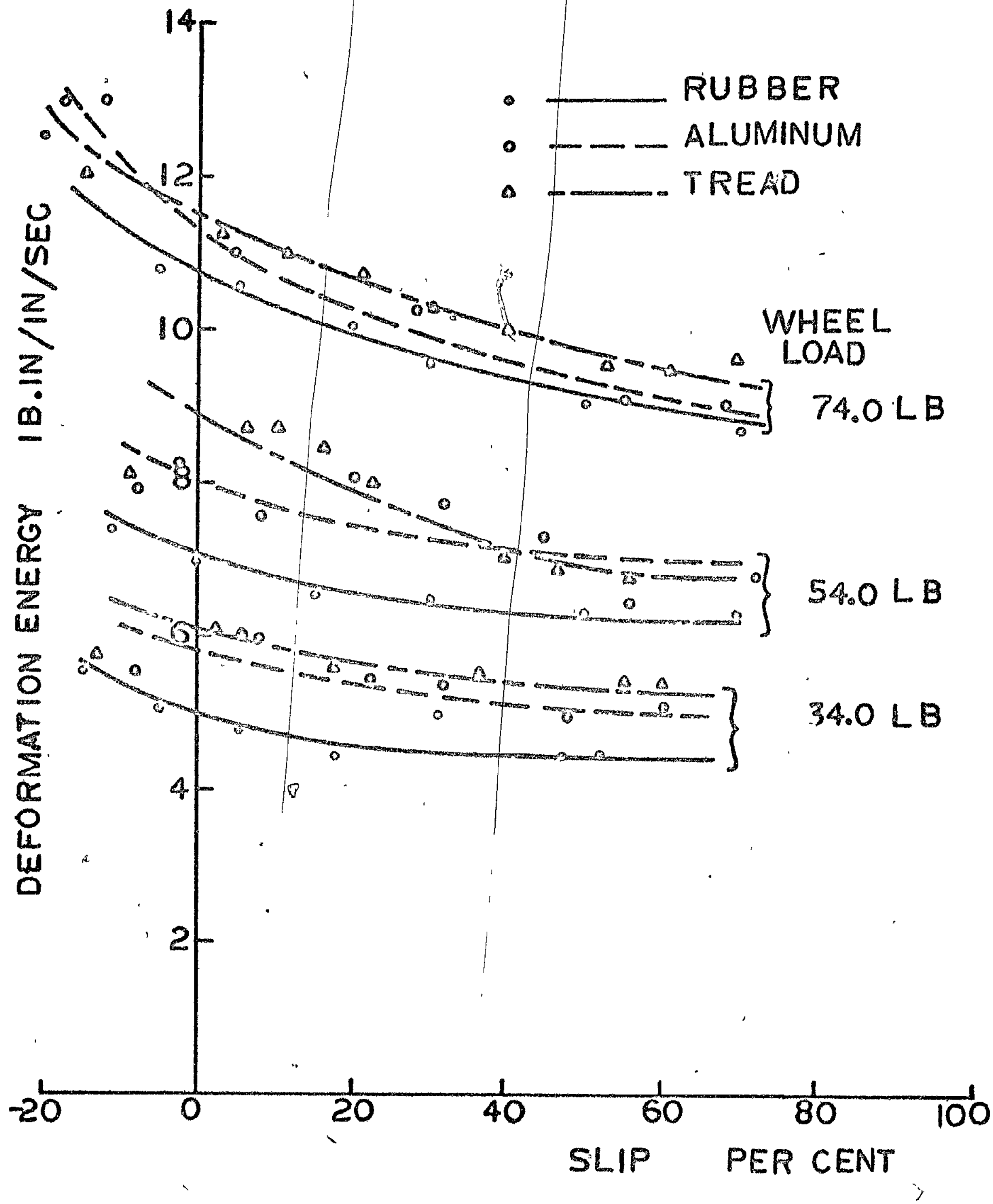

Figure 5.11 Deformation energy versus slip rate (compaction resistance)

Figures 5.12 to 5.14 show the deformation energy contours for rubber strap mounted wheels at various degrees of slip and wheel loads. It is worthy to note that the zone of high deformation energy loss is located in the direction of wheel travel.

Since the deformation energy is a direct function of subsoil stresses and strains, and the state of stress in the nonlinear material depends on the loading path, the deformation energy should be a function of the soil particle path at the wheel-soil interface.

5.5 Slip-Useful Output Energy

The useful output energy is the energy that can produce drawbar pull; it is defined as the wheel input energy minus the parasitic (interfacial and deformation) energy. This energy can be calculated from the energy balance equation as stated above, or by measuring the drawbar pull and translational velocity of the wheel, Appendix A. The slip-pull energy relationships can be characterized by three points, namely, the towed, self-propelled and maximum drawbar pull points, Figure 5.15. Characteristic details of these points will be explained later. Test results indicate that pull energy increases with increasing degree of slip, up to a certain value, then remains constant or decreases according to the stress-strain behaviour of the supporting soil. Good agreement is obtained between the predicted results using visioplasticity technique and energy balance equation, and calculated from measured drawbar pull and translational wheel velocity.

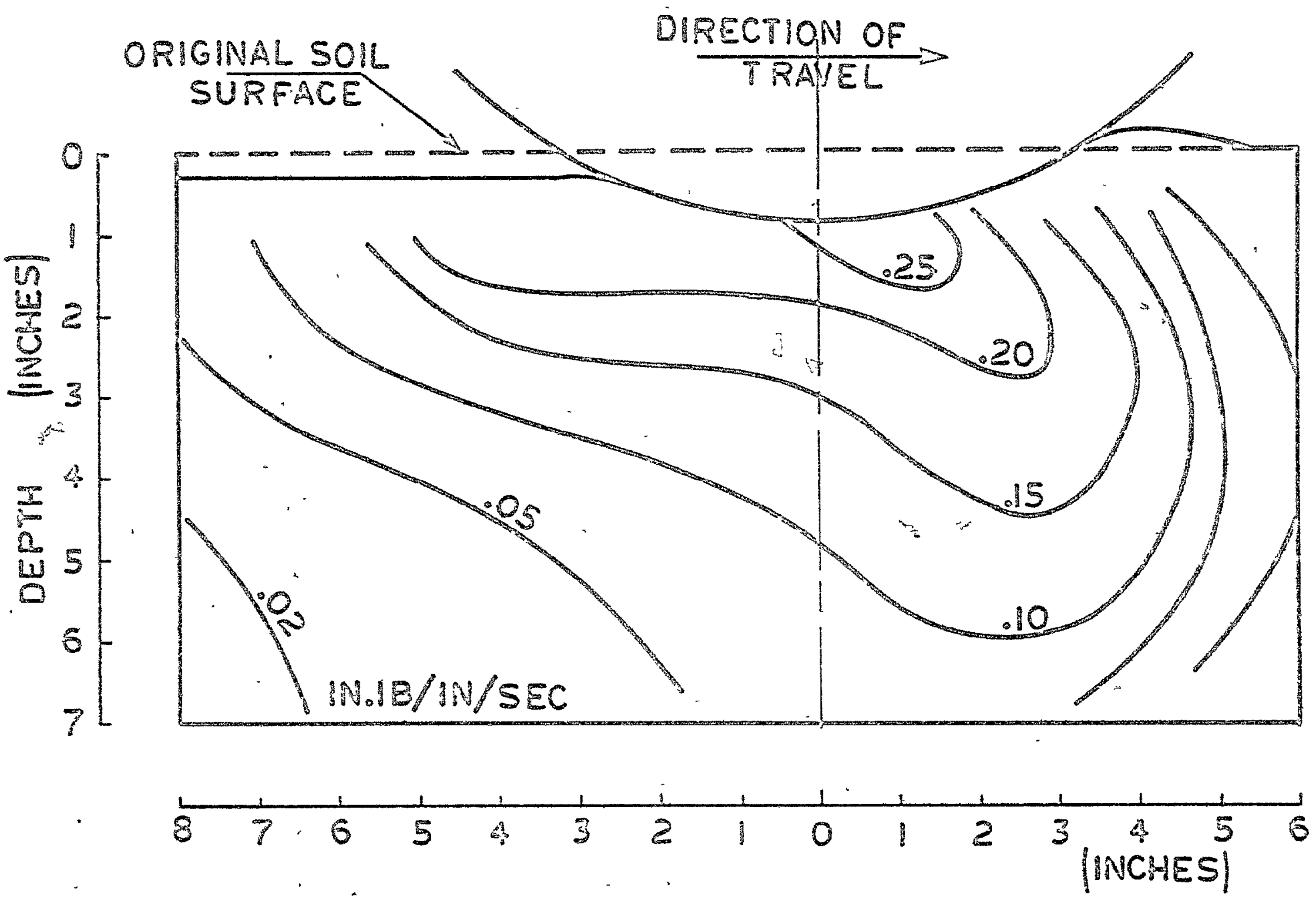

Figure 5.12 Deformation energy contours

Wheel Load 54.0 lbs
Slip 15 percent
Rubber coated wheel

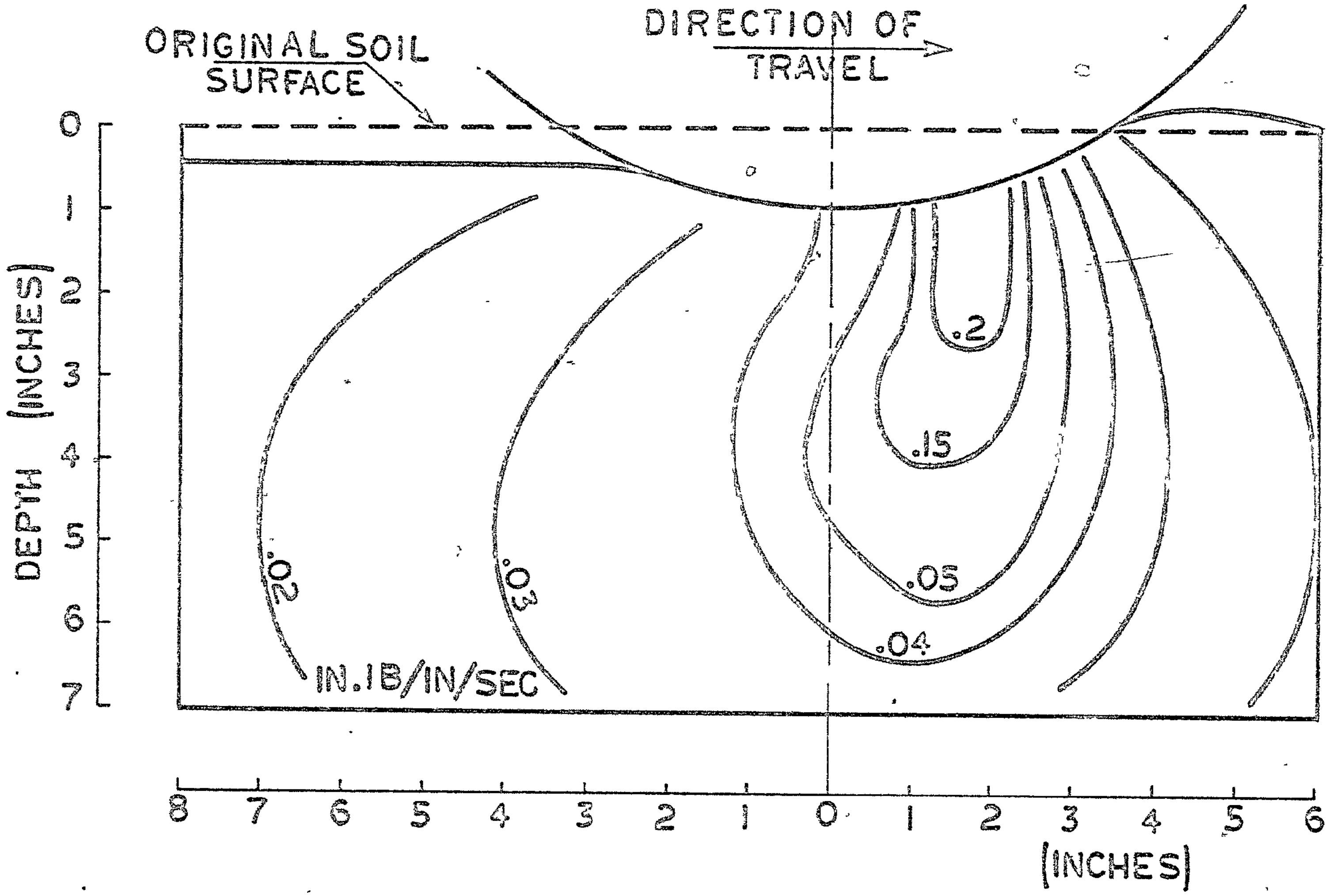

Figure 5.13 Deformation energy contours

Wheel Load 54.0 lbs

Slip 50 percent

Rubber coated wheel

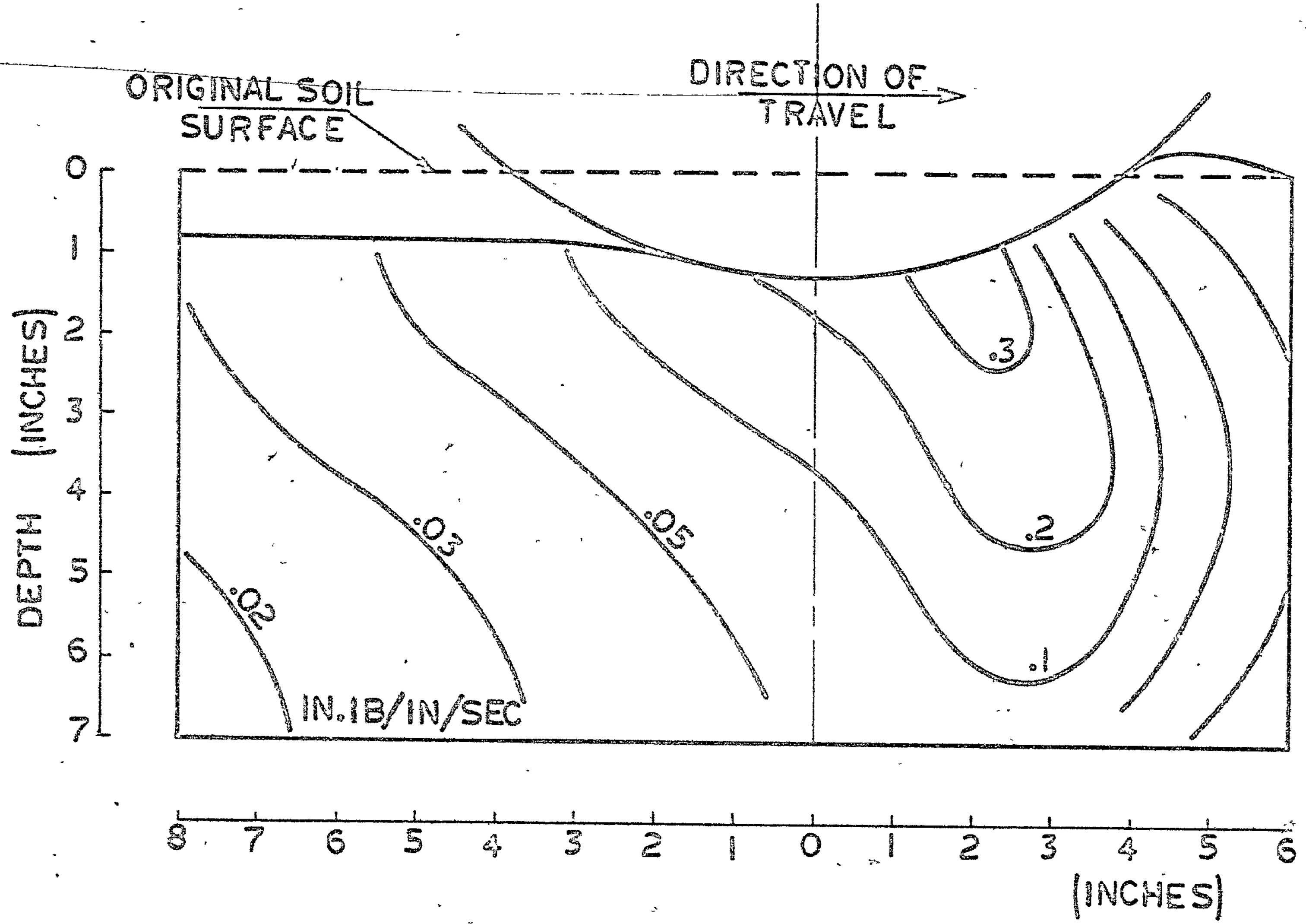

Figure 5.14 Deformation energy contours

Wheel Load 74.0 lbs
Slip 50 percent
Rubber coated wheel

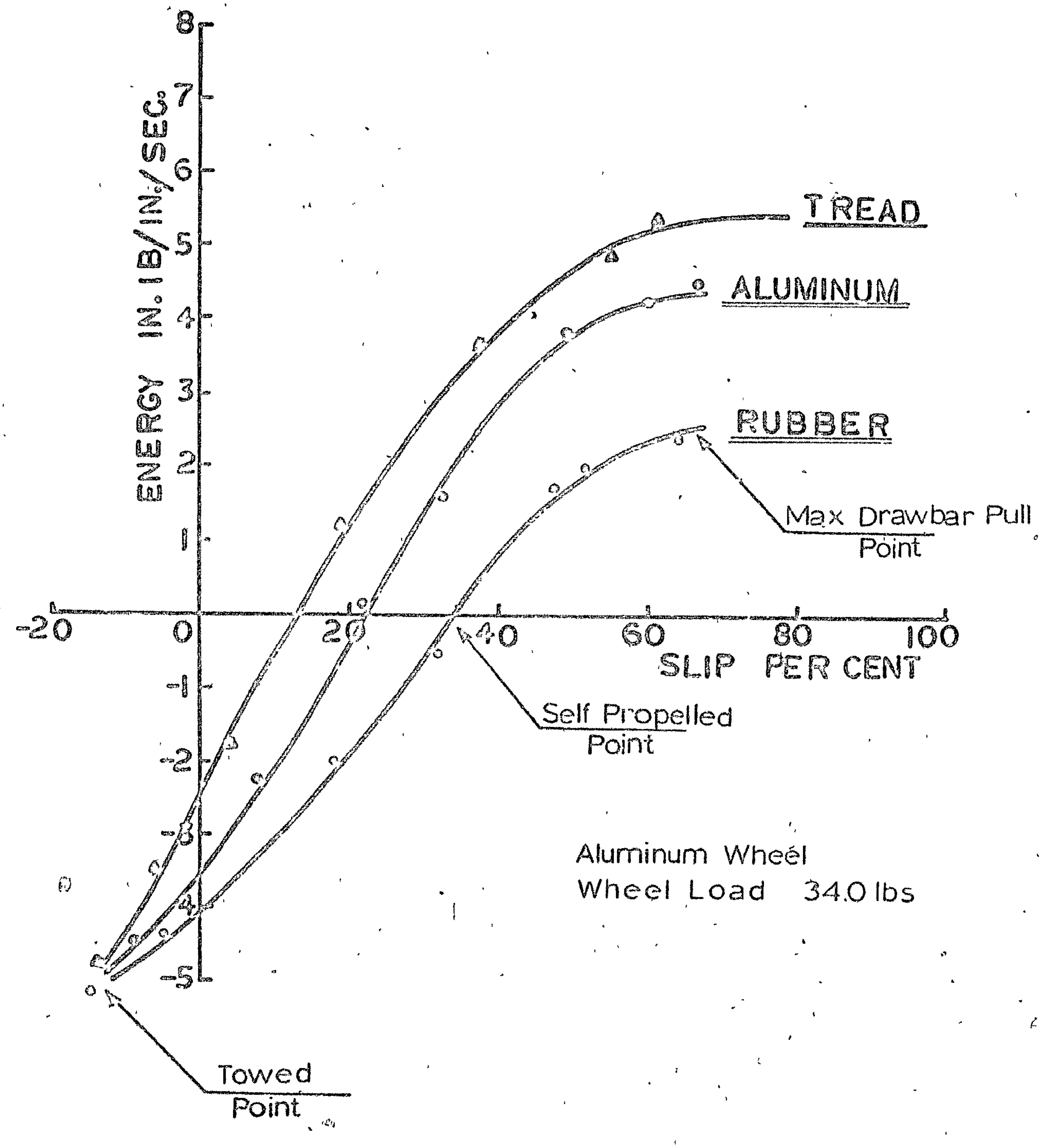

Figure 5.15 Useful output energy - slip curves (visioplasticity technique)

Since the drawbar pull is a direct function of the horizontal components of the wheel-soil interfacial stresses, i.e., a function of the wheel-soil traction forces, it should be dependent on wheel-soil surface roughness. Drawbar pull increases with increasing wheel surface roughness for the same degree of slip, as the mobilized shear forces can be higher. If the adhesion between the wheel periphery surface and the soil is stronger than that between soil and soil, a coat of clay will stick on the wheel surface. In this case, shear failure will occur between soil and soil and the effect of wheel roughness will be negligible.

5.6 Energy Balance

Yong & Webb (1969) first introduced the energy approach for evaluating the performance of a moving wheel over soft soil. They used the energy balance equation and the relations between the different components of energies and degree of slip as the basis for wheel performance evaluation.

The energy balance equation can be written as

$$M\omega = PVc + D' + F \tag{5.2}$$

where

M = input torque

ω = angular velocity

$M\omega$ = input energy per unit time

P = drawbar pull,

Vc = translational wheel velocity,

PVc = useful output energy per unit time,

D' = deformation energy per unit time,

F = interfacial energy per unit time.

In order to provide a basis for comparisons between different wheel energy components, the energy terms should be evaluated per inch width and per inch of wheel travel and the energy balance equation can be written as

$$\frac{M\omega}{Vc} = P + D'/Vc + F/Vc \tag{5.3}$$

In Figures 5.17, 5.18, and 5.19, the energy slip curves under three wheel loads for the three specific contact surfaces, are given. The differences in each figure relate to change in surface conditions. It is pertinent to observe that the characteristic performance of any wheel can be identified by three points on the energy slip curve. These are the towed, self-propelled and maximum drawbar pull points, Figure 5.16. The negative value of the drawbar pull at the towed point is a measure of the rolling resistance of the wheel. Tests show that this value increases with increasing wheel load, and can be envisaged as being directly related to the resultant increasing value of dynamic sinkage. The negative drawbar pull results at the towed point (Figs. 5.17 to 5.19) appear to demonstrate insensitivity to wheel contact surface; test results indicate that this is fortuitous.

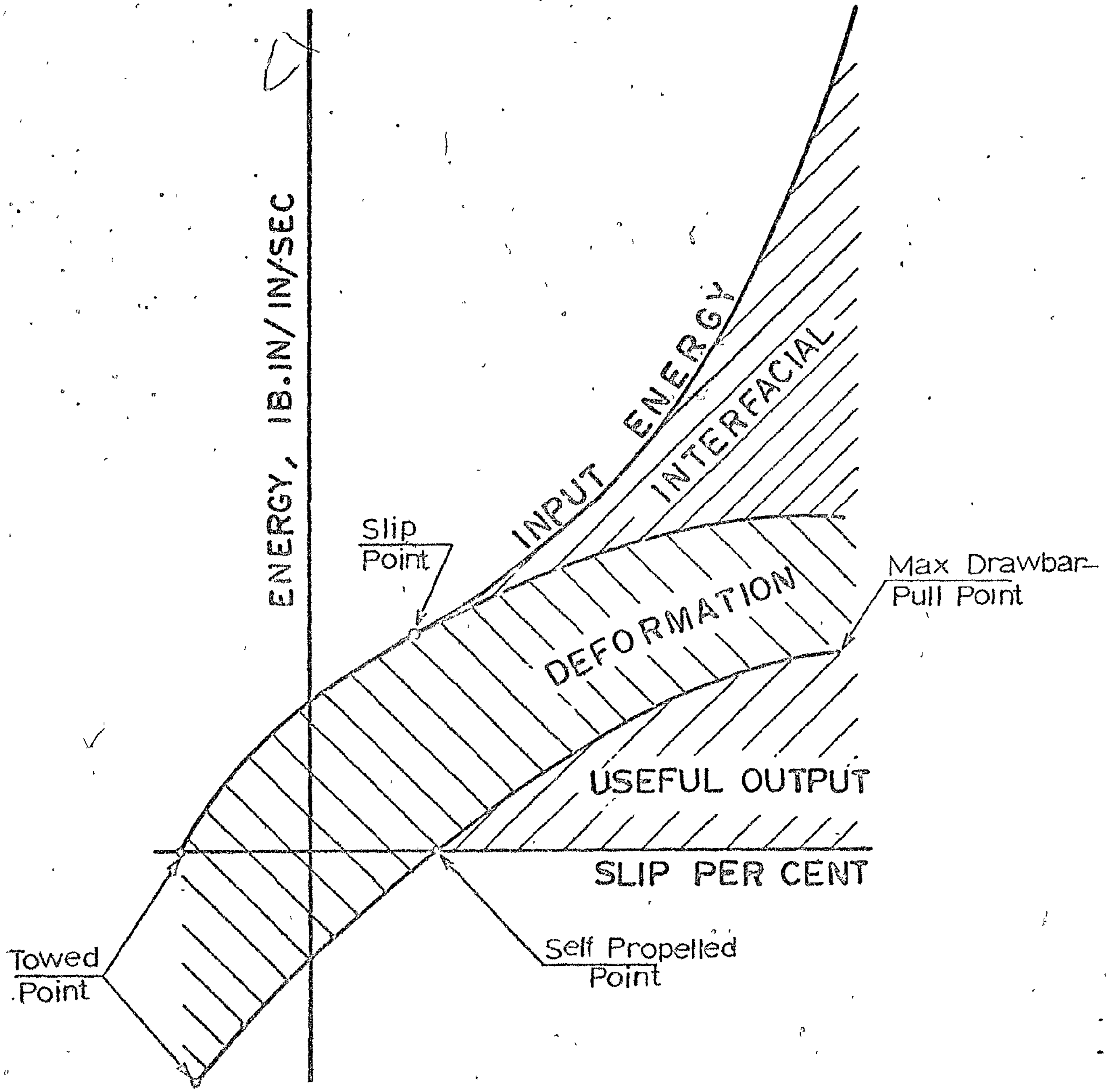

Figure 5.16 Schematic diagram for the characteristics of the energy slip curves

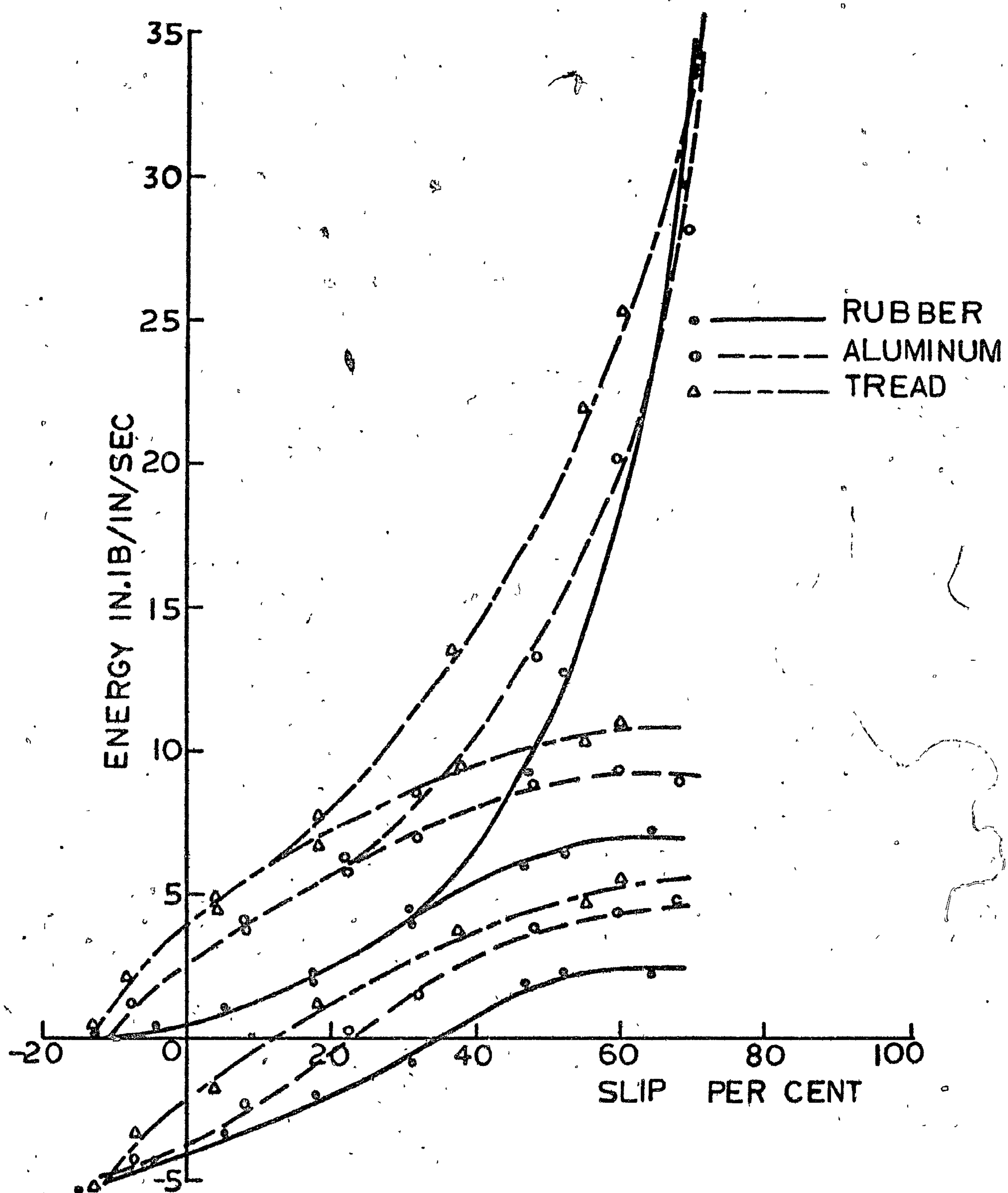

Figure 5.17 Energy balance - Wheel Load 34.0 lbs

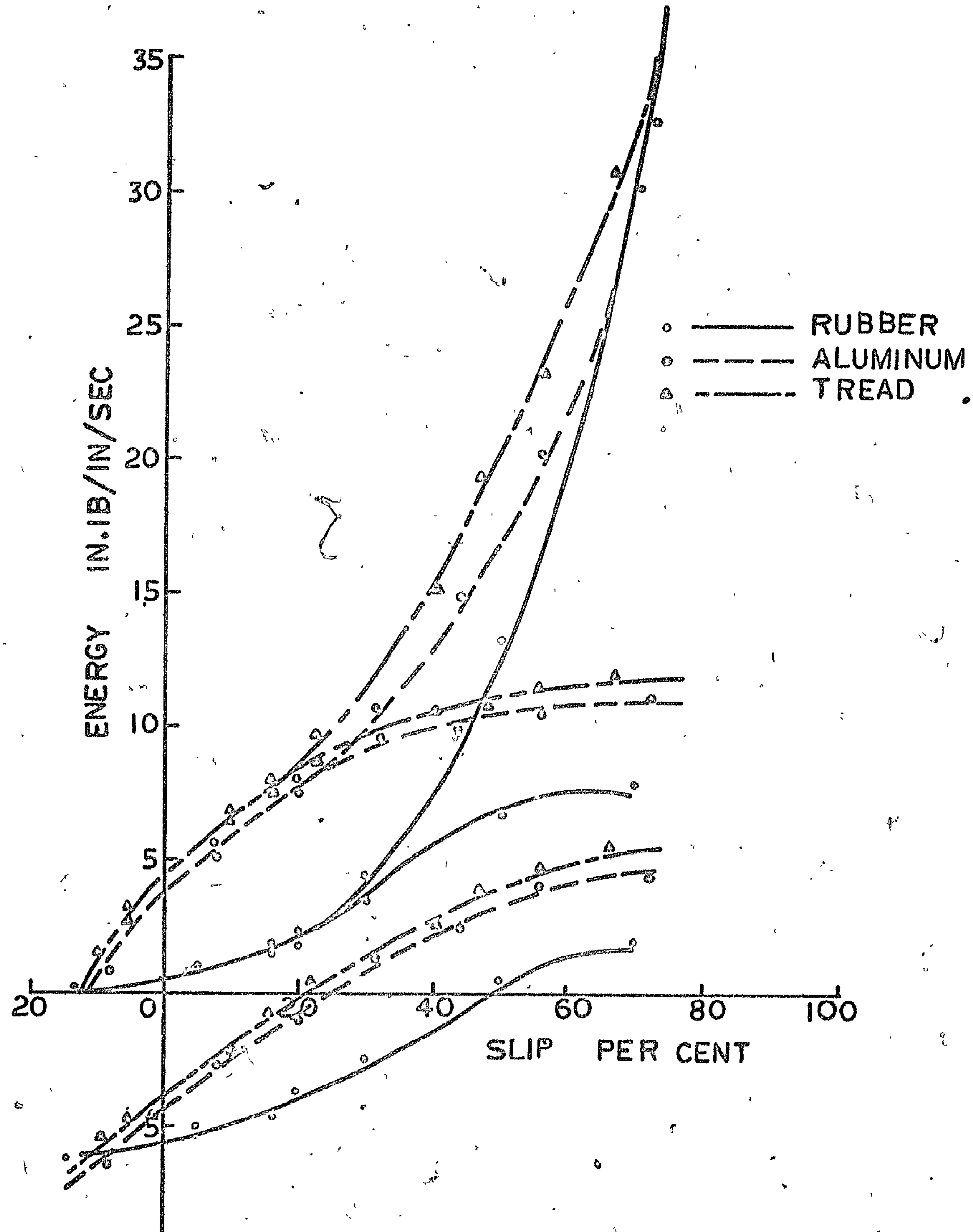

Figure 5.18 Energy balance - Wheel Load 54.0 lbs

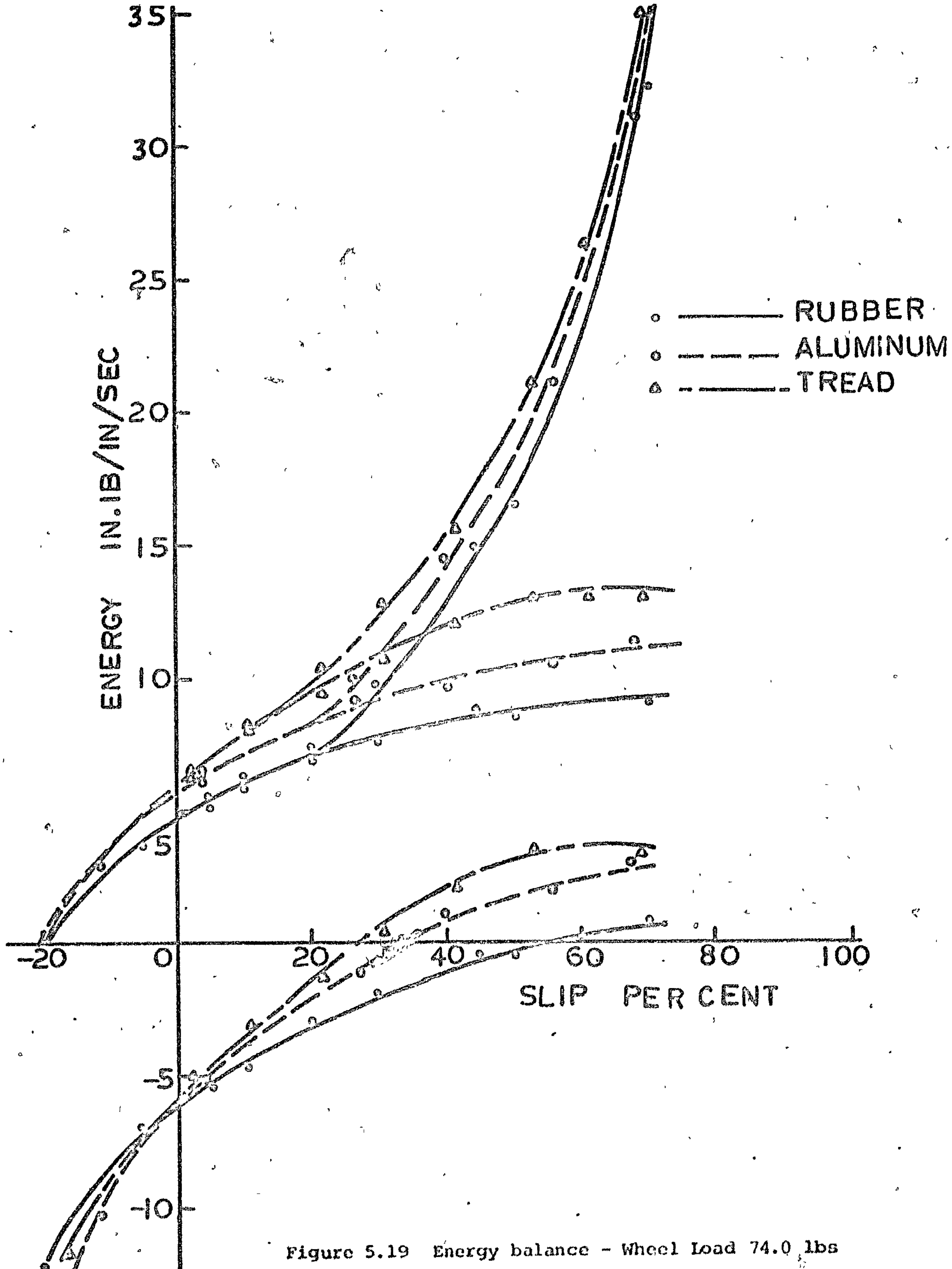

Figure 5.19 Energy balance - Wheel Load 74.0 lbs

Taking the self-propelled point as the point on the energy slip diagram where the drawbar pull is equal to zero, it is seen that this point is a characteristic of the powered wheel. It is apparent that, in order to develop sufficient traction to maintain the wheel in motion at this point, the circumferential wheel velocity should be larger than its translational velocity, i.e., the slip at this point always has a positive value. As seen from Figures 5.17, 5.18 and 5.19, this is obviously a function of wheel load and contact surface characteristic. The justification for characterizing the rubber surface as smoother than the aluminum surface may be due to:

(i) the supporting results shown in Figures 5.17, 5.18 and 5.19;

(ii) the clay-rubber interface adhesion is smaller - probably due to the less than smooth nature of the rubber and the smaller clay-rubber cohesion value.

The maximum drawbar pull for all the tests appear to occur at a high degree of slip, generally around 65 to 75 percent. The test results indicate that the drawbar pull increases by increasing the roughness of the wheel surface - with a corresponding increase in required input energy. It is interesting to note that at high slips a thin clay layer appears to coat the surface of the wheel, and thus it is expected that the tangential stresses developed would be between soil and soil. Hence at high slips the effect of wheel contact surface characteristics on the drawbar pull appears to be insignificant.

A useful point for examining the effectiveness of the surface transfer of energy is the establishment of the critical slip point. The critical slip point is defined as the point of maximum (optimum) slip, at which the interfacial energy remains sensibly zero. The slip at this point appears to be consistently positive and generally occurs before the self-propelled point. As seen from Figures 5.17, 5.18 and 5.19, the critical slip points for the three types of wheel contact surface are sufficiently different, both in terms of slip and in terms of input energy, whenever interfacial energy loss becomes significant. The usefulness of such a critical point, as a measure of contact surface effectiveness for development of drawbar pull and interface energy (surface disturbance) can be seen. However, it is obvious that in view of the limited amount of data available, much remains to be done before a proper characterization of this critical slip point can be obtained. The factors and parameters needed for characterization would include carcass stiffness, tread configuration, subsoil properties, contact area and pressure, etc. The advantages to be gained in establishing the critical slip point are (Yong & Fattah, 1975):

(a) development of drawbar-pull in view of wheel and tire constraints, and

(b) present awareness and conscious need for minimization of surface disturbance in off-road mobility; the reduction of interface energy loss is seen to be directly linked to the reduction in surface disturbance.

CHAPTER 6

DISCUSSION OF THE PREDICTED RESULTS

6.1 Introduction

This chapter is concerned with a discussion of the predicted wheel performance using FEM, as compared with experimental values analysed by the visioplasticity technique. The main concern is to check the validity of the FEM as a technique for predicting moving wheel performance and associated subsoil behaviour.

Two types of measurements are used in the laboratory to check the validity of the predicted results; these are (a) surficial measurements such as dynamic sinkage, drawbar pull and input torque, and (b) subsoil measurements such as displacement field.

The predicted wheel performance in terms of useful output, deformation and interfacial energies are presented. In addition, the subsoil contours of velocities, stresses and energies are predicted using the FEM and visioplasticity method.

Three main characteristics identify the application of the adopted finite element technique to a wheel-soil interaction problem; these are:

(a) Boundary Conditions

The soil-wheel particle path based on geometrical relations between wheel diameter, dynamic sinkage and degree of slip (theoretical particle path, Chapter 3), and the soil particle path determined from the results of x-ray photographs (experimental particle path, Chapter 4), were both used as a loading boundary at the wheel-soil interface. Figure 6.1 shows typical theoretical particle paths for a 13.5 inch diameter wheel having .7 in. dynamic sinkage; the experimental particle paths were previously shown in Chapter 5. The technique for the application of the boundary conditions to the solution is presented in Chapter 3.

(b) Stress-strain Curves

Unconsolidated, undrained triaxial tests were performed under plane strain conditions in order to reproduce as closely as possible the assumed conditions during the soil-wheel tests. The testing was conducted under three different confining pressures of 0, 2.5 and 5.0 psi, and at axial deformation rates of .1, .5 and 1. inch/minute. The test results are shown in Figure 6.2. Analogous axisymmetric triaxial tests were performed in order to verify the non-existence of a well-defined failure condition, i.e., the absence of strain-softening behaviour is not a result of the plane-strain "True Triaxial" test restraints (Figure 6.3).

The finite element analysis in this investigation is performed using an incremental procedure, and in such a case it is difficult to account for material strain-softening behaviour. The stress-strain curves do not exhibit a definite peak to failure. Instead, the stress

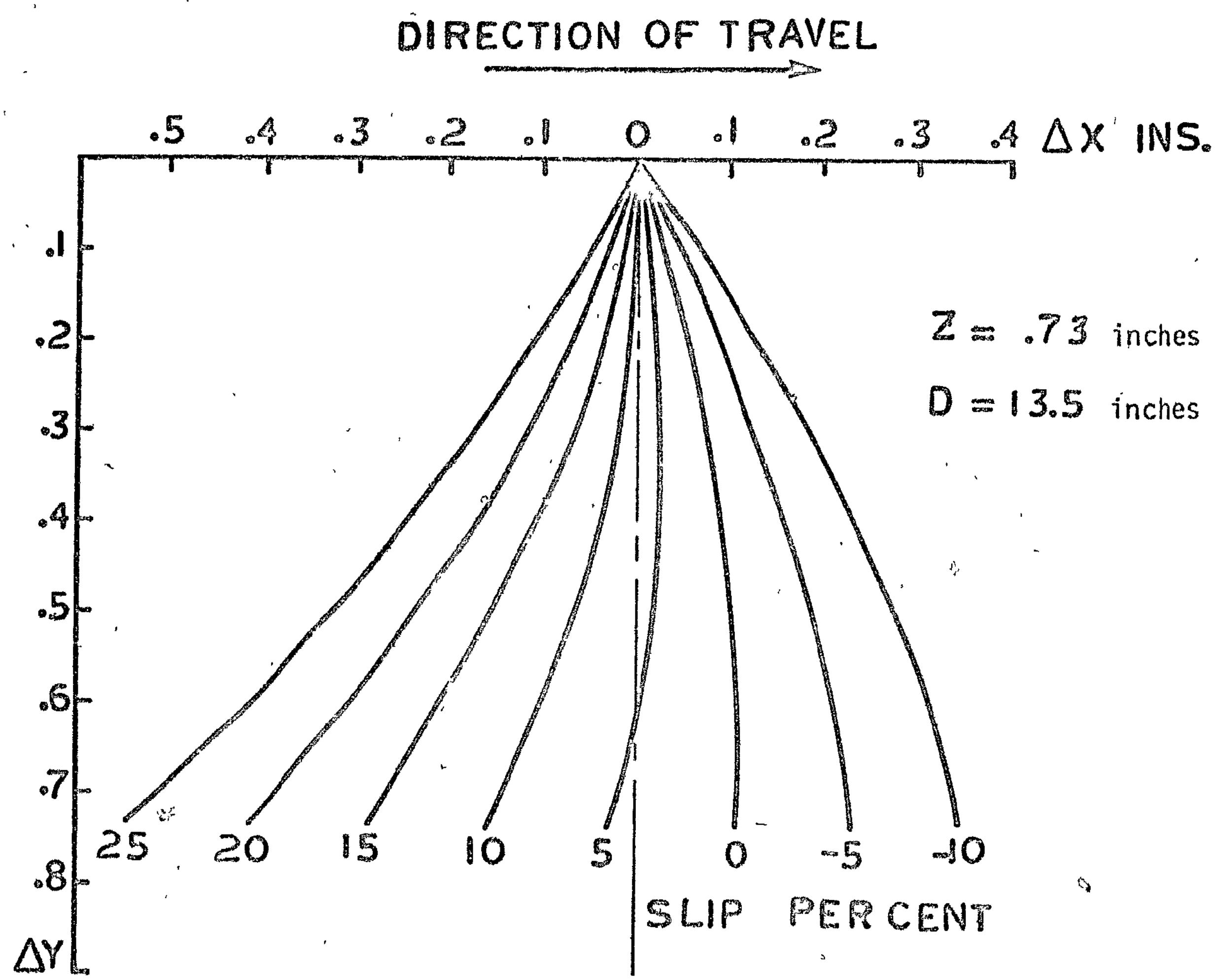

Figure 6.1 Geometrical Particle Paths for Different Degrees of Slip

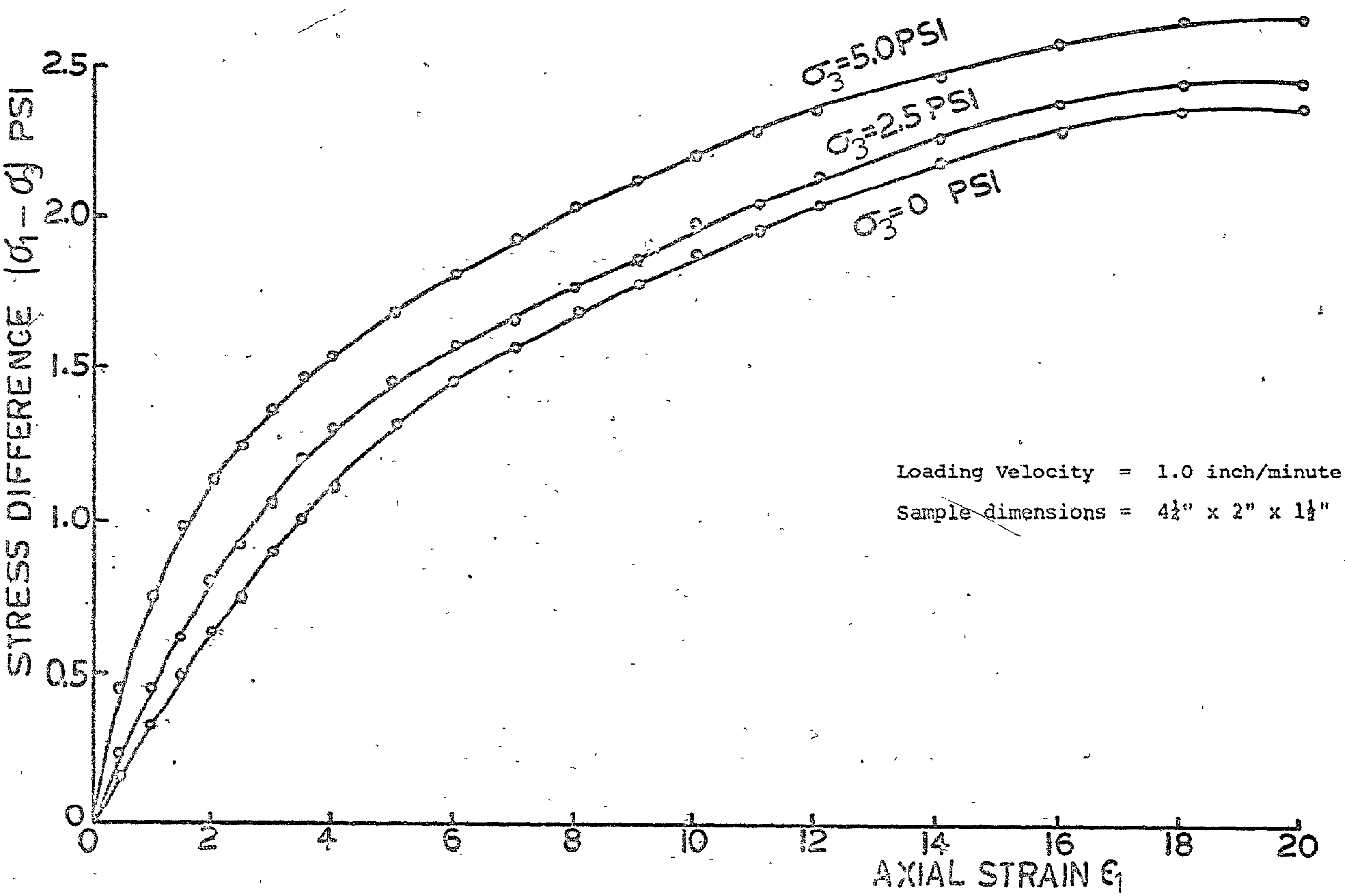

Figure 6.2 Typical Stress-Strain Curves for Plane Strain Triaxial Tests (Kaolinite Clay)

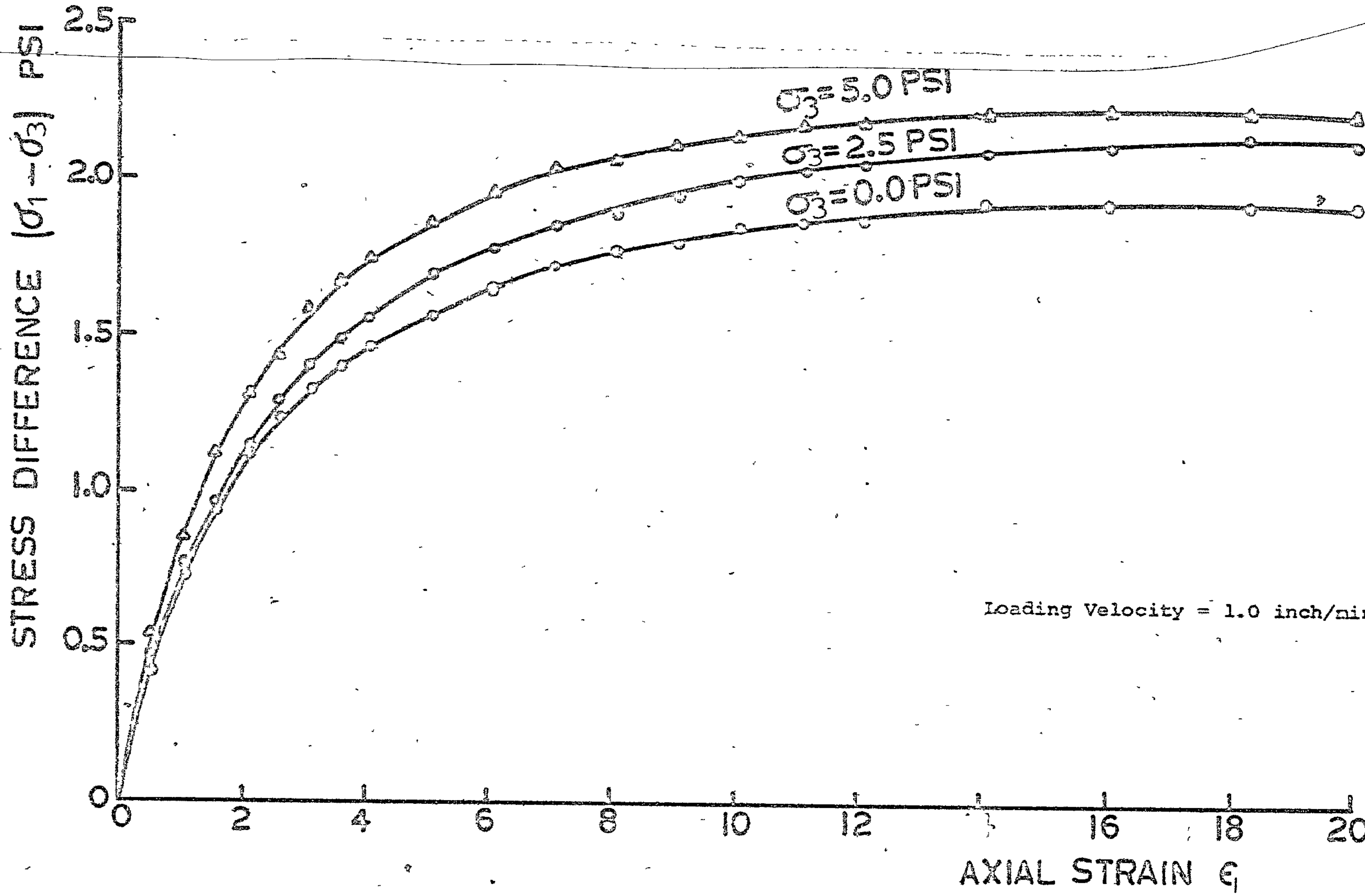

Figure 6.3 Typical Stress-Strain Curves for Standard Triaxial Tests (Kaolinite Clay)

difference ($\sigma_1 - \sigma_3$) is seen to increase with axial strain. This observed rise of the stress-strain curves eliminates the need for an approximation to the stress-strain curves and avoids the numerical difficulties arising from strain softening behaviour. Since no definite peak was in evidence, an axial strain of 20% was chosen to define failure.

There are two common procedures for incorporating a nonlinear stress-strain law into a finite element formulation for digital computations (Hanna, 1975). In the first procedure the stress-strain law derived from a laboratory test can be used directly in a tabular or digital form. Several points on that curve are then selected and constitute the input in the form of pairs of numbers each denoting stress and strain at those points. The variable material parameter such as E and ν are obtained from such curves by suitable interpolation. If the behaviour is represented by a single stress-strain curve, stresses are obtained by interpolation for a calculated state of strain. If the behaviour is represented by several curves, interpolation must also be done between two curves for different confining pressures.

In the alternative procedure, the laboratory stress-strain relationship is expressed in the form of a suitable mathematical function. The material parameters for the nonlinear analysis are again obtained on the basis of the state of stress or strain.

In this study, the tabular or digital procedure was utilized to represent the constitutive behaviour of the soil modelled by continuum (triangular) elements in the analytical solution. To start the analysis, initial values of the modulus of elasticity, E_0, and Poisson's ratio, ν, are required. The clays used can be considered to be fairly incompressible as they were nearly saturated. Therefore, it should be reasonable to choose the value of the Poisson's ratio of the soil close to 0.50. In the present study ν was assumed to be .48. Furthermore, the value of ν was assumed to remain constant throughout the entire deformation process. Similar assumptions have been made by Clough & Woodward (1967) and by Girijavallabhan & Reese (1968). The nonlinear analysis was based directly on the plane-strain triaxial curves. The starting value of the modulus, E_0, was taken as the initial slope of the stress-strain curve at zero confining pressure.

In an axisymmetric triaxial stress condition, the intermediate and minor principal stresses are the same, and the confining pressure for the sample is equal to the minor principal stress, σ_3. Since most actual problems in soil mechanics are three dimensional or plane strain, the magnitudes of the intermediate and minor principal stresses in an element will be different. In the laboratory wheel-soil interaction problem, the wheel is wide enough that it can be reasonably assumed that the soil is in plane strain condition. In this case the intermediate principal stress is given by:

$$\sigma_2 = \nu(\sigma_1 + \sigma_3) \qquad (6.1)$$

Thus it was found reasonable to express the confining pressure in an element for plane strain condition as the average of the magnitudes of the intermediate and minor principal stresses induced at the centroid of the element.

$$\sigma_c = (\sigma_2 + \sigma_3)/2 \qquad (6.2)$$

The subroutine "NONLIN" (Appendix F) developed in this study uses formula (6.1) for defining the confining pressure.

In order to compute the state of stress, $(\sigma_1 - \sigma_3)$, corresponding to a state of strain, ε, in an element from a set of non-linear curves, three interpolations are required. The program first computes the values of the stresses, strains and confining pressures in each element. Interpolations are then performed to compute intermediate values between curves at different confining pressures and within a curve between the different strains. In the subroutine NONLIN used in this study, stress values were computed from strain values obtained in the analysis.

(c) Solution Technique

In the finite element solution, the quasi-static approach is used for simulating the wheel movement on the soil surface, hence inertia effects can be neglected. A small incremental time step is used in the solution and the time increment is calculated by

$$T = \frac{\Delta X}{V} \qquad (6.3)$$

where

V is the translational wheel velocity,

and ΔX is the incremental wheel travel distance.

The incremental wheel travel distance is taken as .25 inch, the horizontal and vertical displacements at the wheel-soil nodes are calculated from the geometrical characteristics of the particle path at the wheel-soil interface. An incremental solution technique is adopted in this analysis as explained in Chapter 3.

A block diagram for the input data utilized for the FEM to predict wheel performance and associated subsoil behaviour is shown in Figure 6.4. Description of the Finite Element program is given in Appendix F.

6.2 Stream line Flow

In the experimentation of a moving wheel over soft soil, successive x-ray photographs of the subsoil lead markers, at different wheel positions, were taken. The superposition of the photographs side by side shows the flow of the soil beneath the wheel, i.e., it is implicitly assumed that the wheel is turning in its position and the soil is moving with a translational velocity equal to that of the wheel (similar to metal sheet drawings).

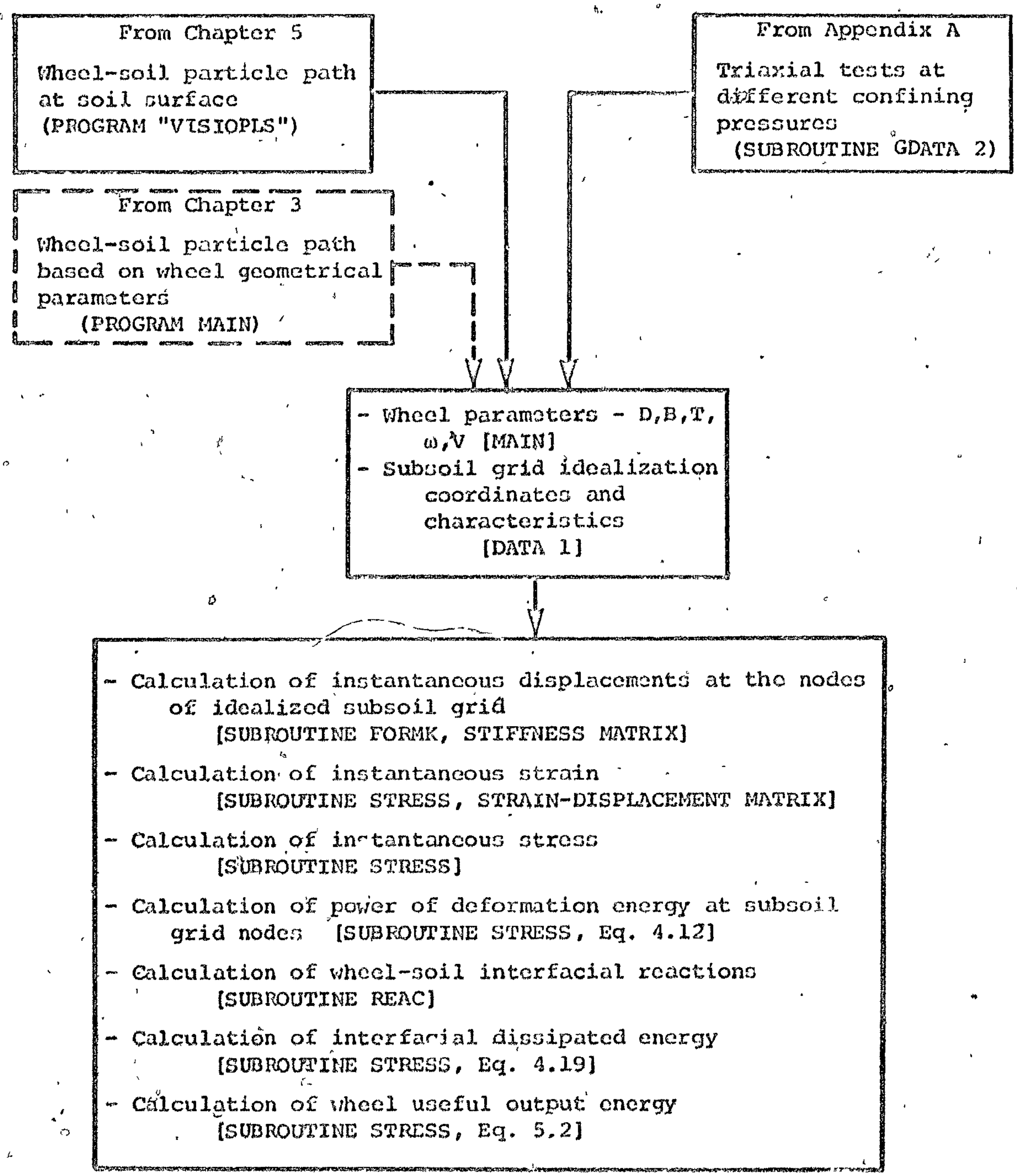

Figure 6.4 Schematic for Input and Output Information for Wheel-Soil Interaction Study Using the FEM

Figure 6.5 shows the streamline flow under the moving wheel, predicted by the FEM and measured by the x-ray photographic technique. The experimental and predicted results are both plotted at one inch depth intervals, and are staggered .5 inch apart from each other to avoid the confusion between the measured and predicted flow lines. It should be noticed that the theoretical model is capable of showing both the rut depth at the rear of the wheel and the bow wave at its front. The soil distortion decreases rapidly with the depth, and at a depth equal to the wheel diameter, the distortion is negligible. The trends of the flow lines show clearly that the soil in front of the wheel is subjected to a state of loading and to a state of unloading (recovery) at the rear of the wheel. The FE and the experimental results both indicate that the flow lines have the same trend.

6.3 Subsoil Velocities

Subsoil velocities can be calculated directly from the recorded subsoil deformations, provided that the incremental time step between the successive x-ray exposures is known (Appendix B). Since no assumptions are made in calculating the subsoil velocities, good agreement is expected between the predicted results using the FEM and the experimentally-calculated results.

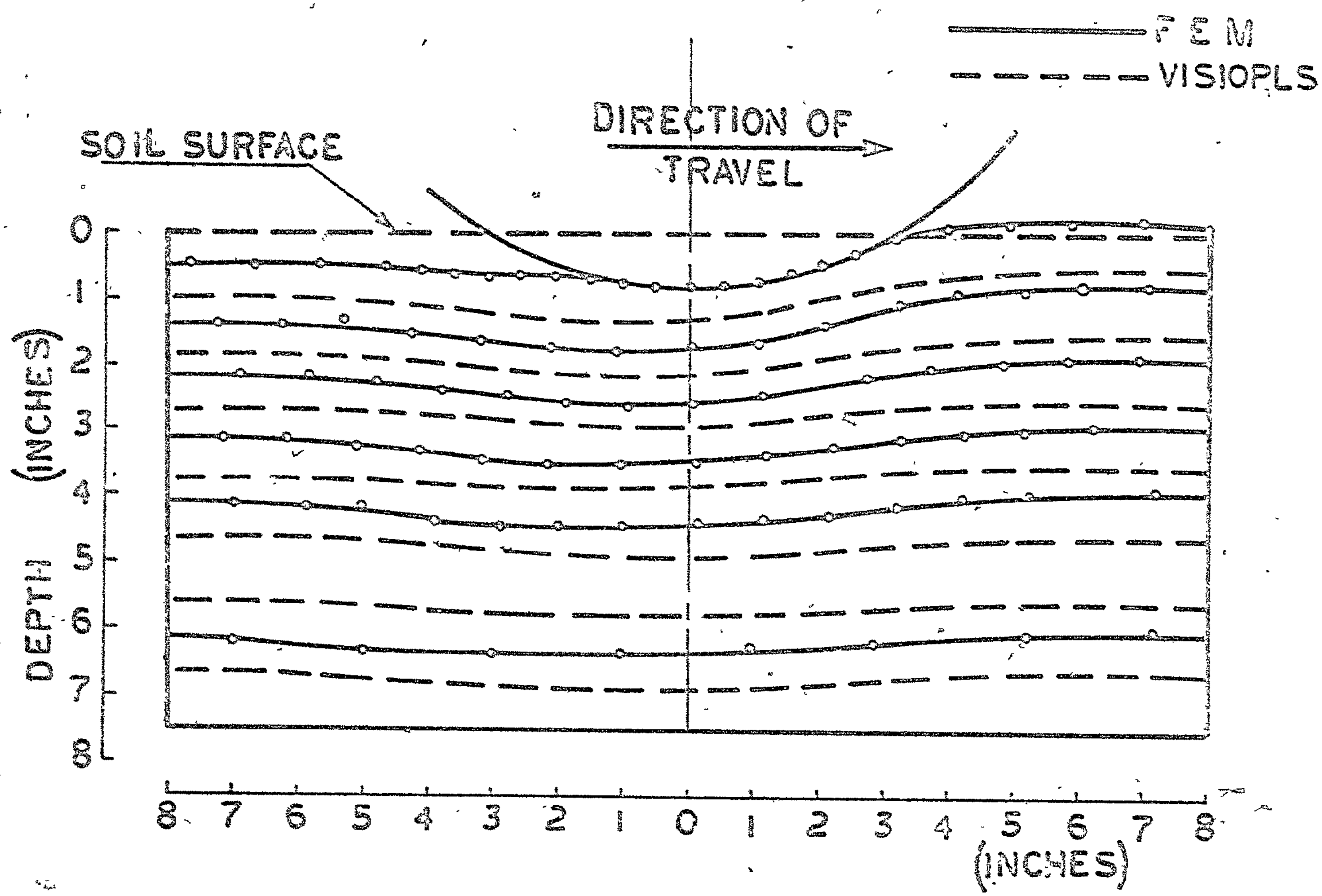

Figure 6.5 Stream line Flow Beneath a Moving Rigid Wheel

Wheel Load 34.0 lbs. 0° of slip
Dynamic Sinkage .7 in.

In the finite element solution, the velocities are calculated for the nodal points of the idealized subsoil continuum grid. Knowing the incremental time step corresponding to the incremental wheel travel distance, and the calculated displacements at every nodal point, the velocities at any incremental wheel travel distance can be calculated as:

$$V_x = \frac{D_x}{T}$$

$$V_y = \frac{D_y}{T} \qquad (6.4)$$

and

$$T = \frac{\Delta x}{V}$$

where V_x horizontal velocity component,

V_y vertical velocity component,

D_x nodal point incremental vertical displacement,

D_y nodal point incremental vertical displacement,

Δx incremental wheel travel distance,

V translational wheel velocity,

T incremental time step.

Figures 6.6 and 6.7 show the horizontal and vertical velocity contours respectively, using the experimentally determined particle path as a displacement boundary conditions at the wheel-soil interface, while the corresponding contours for higher degree of slip are shown in Figures 6.8 and 6.9. The experimentally calculated and the FE predicted

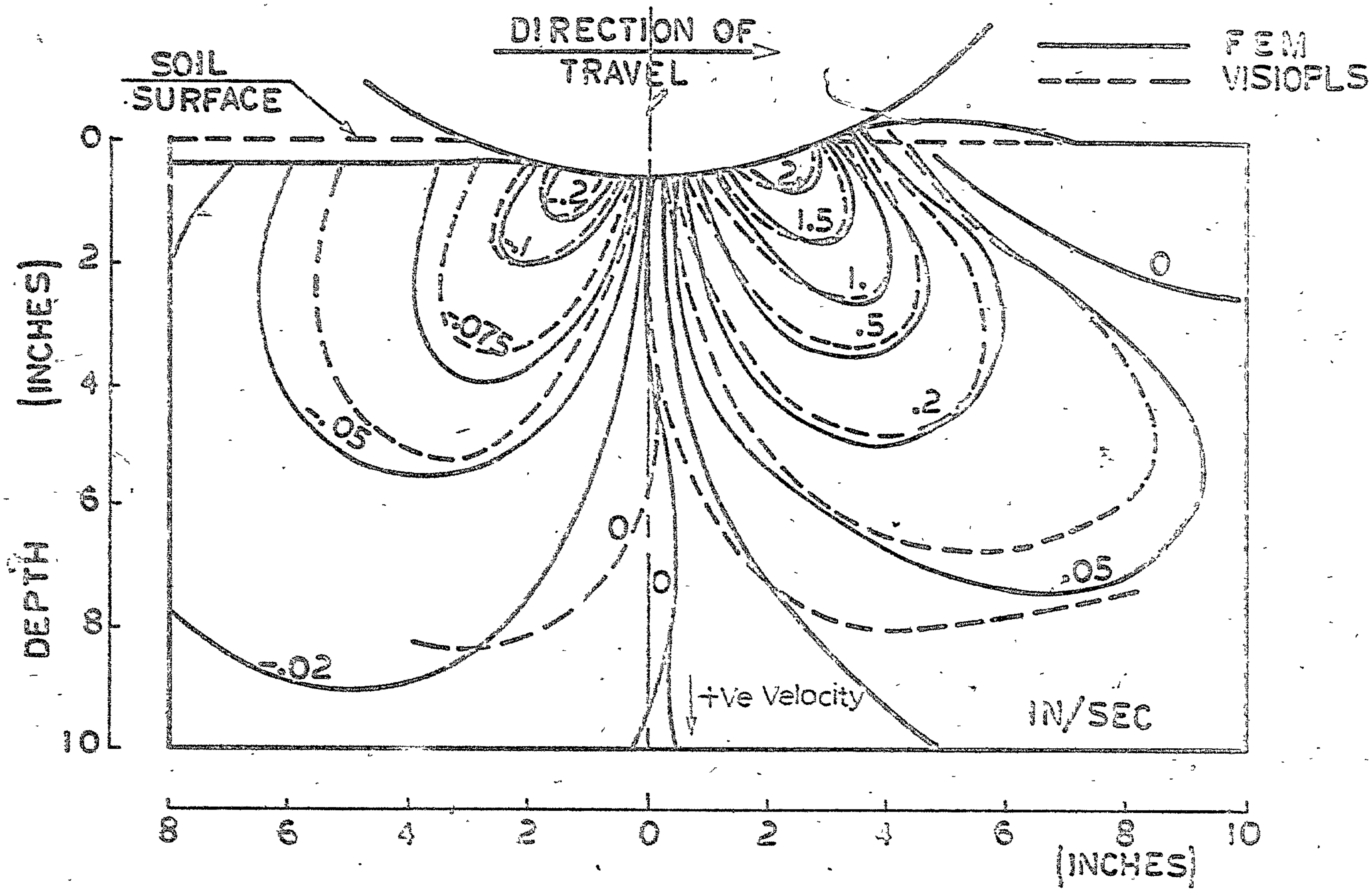

Figure 6.6 Vertical Velocity Contours Wheel Load 34.0 lbs.
Slip 08

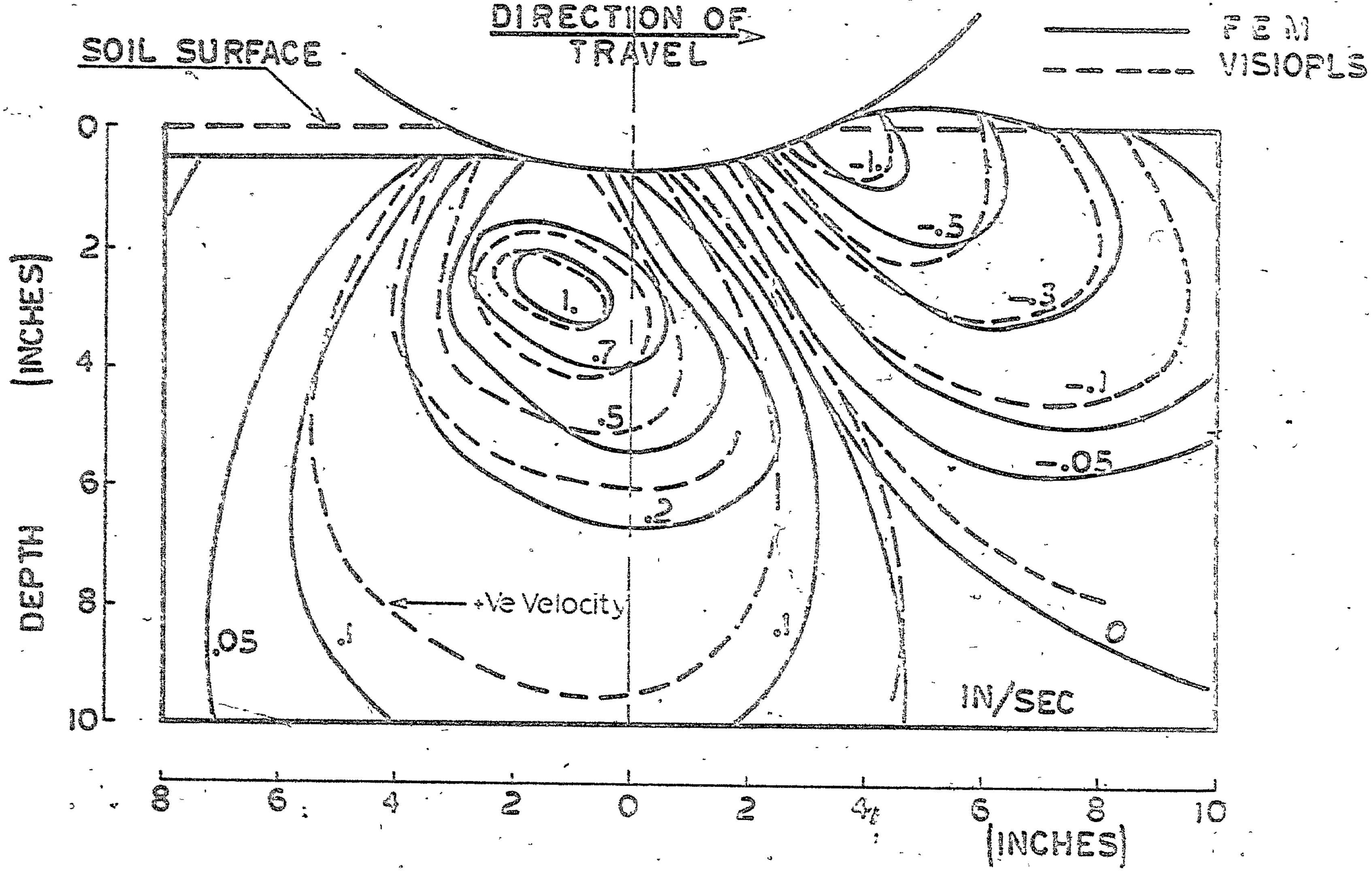

Figure 6.7 Horizontal Velocity Contours

Wheel Load 34.0 lbs
Slip 0%

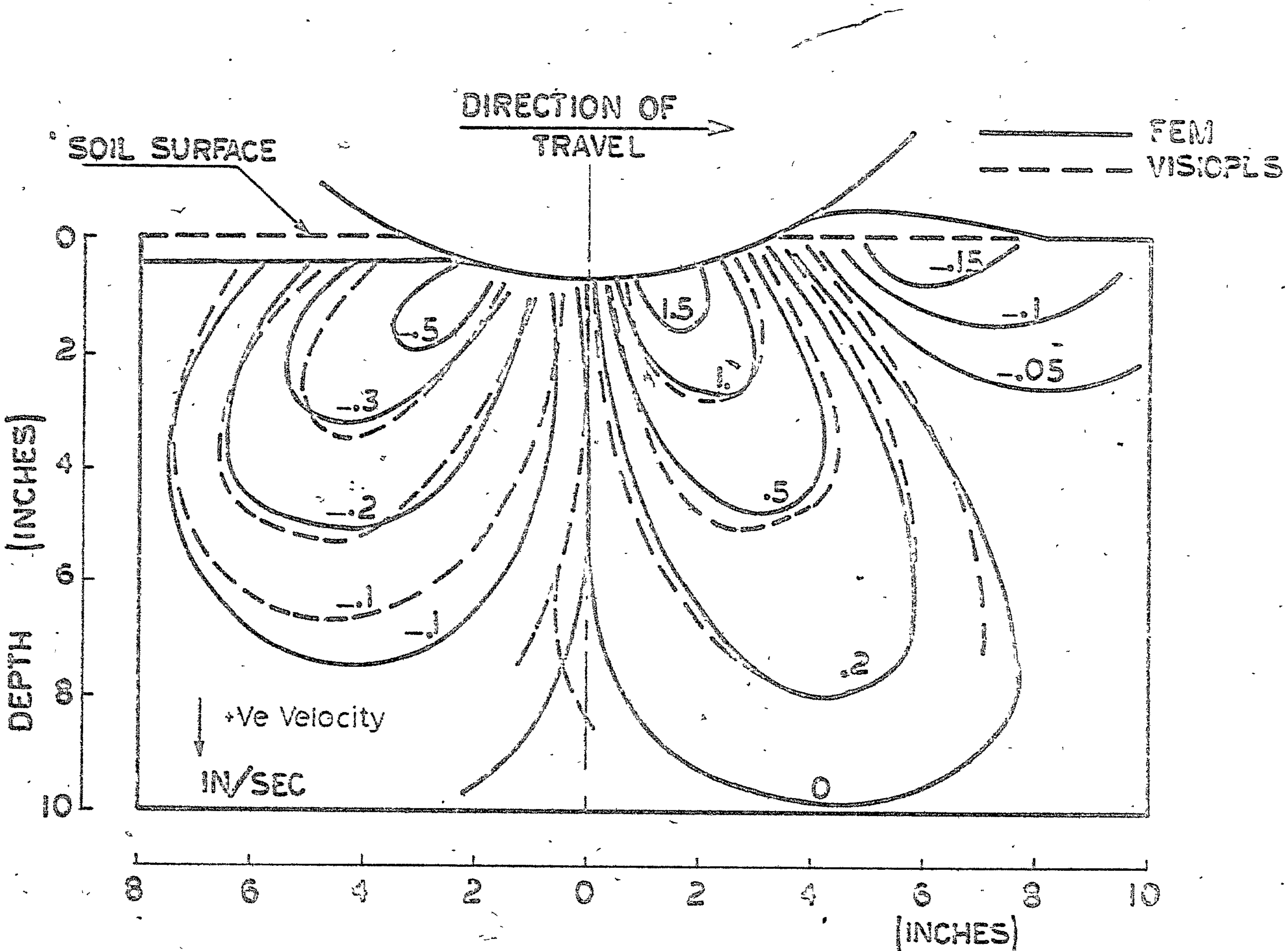

Figure 6.8 Vertical Velocity Contours Wheel Load 34 lbs
Slip 15%

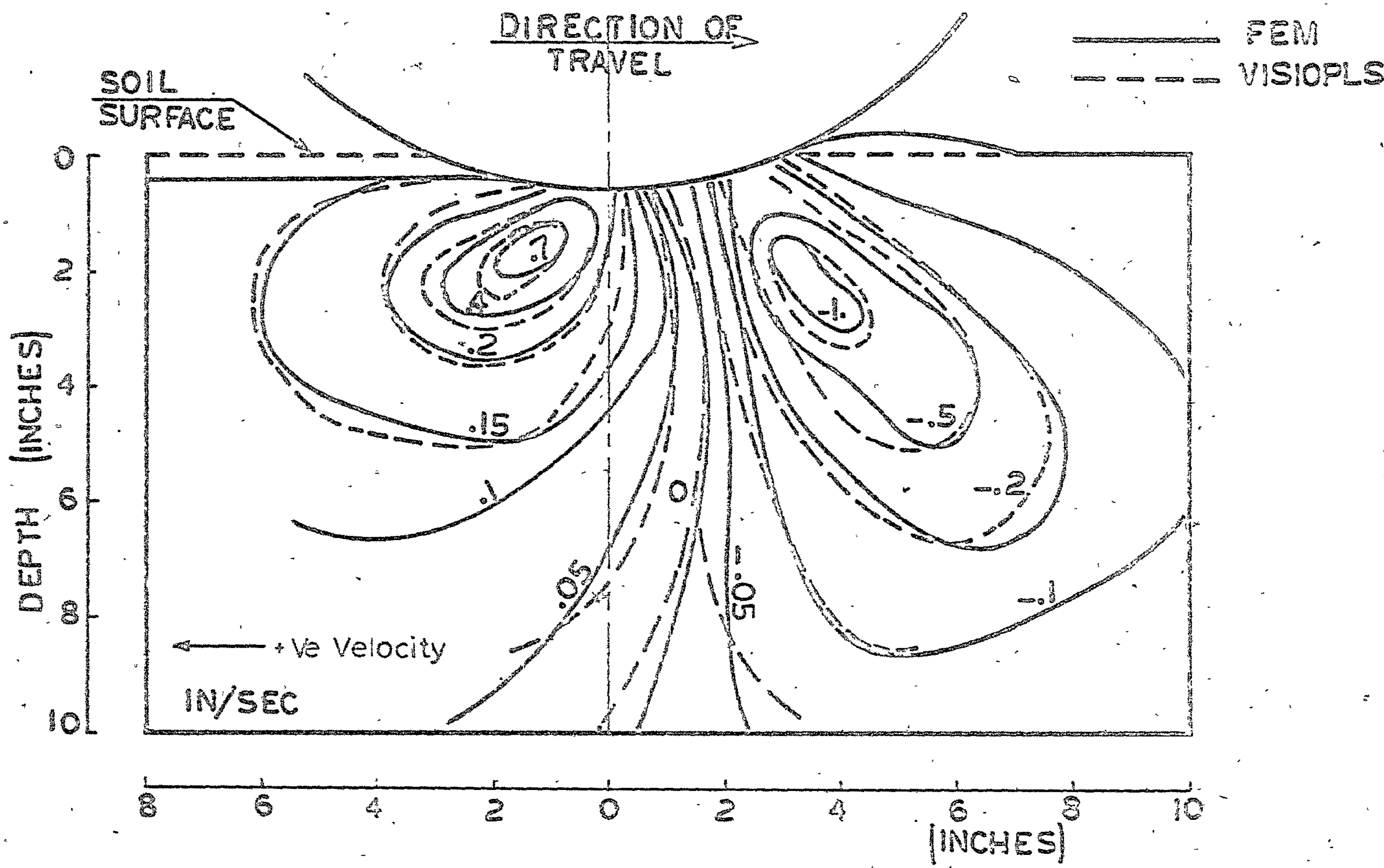

Figure 6.9 Horizontal Velocity Contours Wheel Load 34.0 lbs
Slip 15%

velocity contours are plotted on the same figures for ease of comparison of results. For vertical velocities, a positive sign means downward velocity and a negative sign means upward velocity, while for horizontal velocity contours a positive sign means that the velocity is in the direction of wheel travel. A zero magnitude velocity contour indicates that the particle displacement has reached its maximum position and is in the stage of beginning to return on the rebound cycle. Thus, in terms of velocities, no instantaneous incremental displacements are registered, and hence the computation for velocities provides for a zero value. At low degree of slip the vertical and horizontal velocities are equal to zero at wheel bottom dead center. The zero vertical velocity line starts nearly vertically from wheel bottom dead center, and its position does not change much with increasing degree of slip. The zero horizontal velocity contour starts from wheel BDC at low degree of slip but moves ahead in the direction of wheel travel. With increasing degree of slip the zero horizontal contour starts from a point ahead of BDC. The negative vertical velocity contours ahead of the wheel and to the back its BDC, correspond to the effect of the bow wave and soil recovery respectively.

It should be noticed that the predicted velocity contours, using the FEM, provided the wheel-soil particle path (loading boundary) is determined experimentally, correspond well with the experimentally calculated results, using the x-ray photographic technique.

6.4 Subsoil Stresses

Application of the method of characteristics to predict the subsoil stresses from information about the subsoil deformation pattern was explained in Chapter 4. The flow chart for the calculation steps is explained in Appendix F. Figure 6.10 shows the subsoil principal strain directions and Figure 6.11 shows the contours of the slip lines, these being the lines of characteristics. Figures 6.12, 6.13 and 6.14 show the subsoil stress contours determined by the method of characteristics, and predicted by the Finite Element Method. It should be noticed that all these contours are plotted for a 13.5-in diameter wheel moving at a constant speed of 6 in/sec. The computed variables are made for unit wheel width and the dynamic sinkage is assumed constant throughout the entire test.

An apparent significant difference is observed in the pattern of stress distribution obtained by the methods of characteristics and the Finite Element Method. This difference can be mainly ascribed to the following factors.

(a) Difference in Boundary Conditions:

In the FEM the particle path at the wheel-soil interface is used as loading boundary and the effect of soil recovery beneath wheel BDC is considered.

In the method of characteristics, the line of compression tension divide at which the mean normal stress is zero, is used as a boundary condition (Yong & Windisch, 1970). This indicates the position

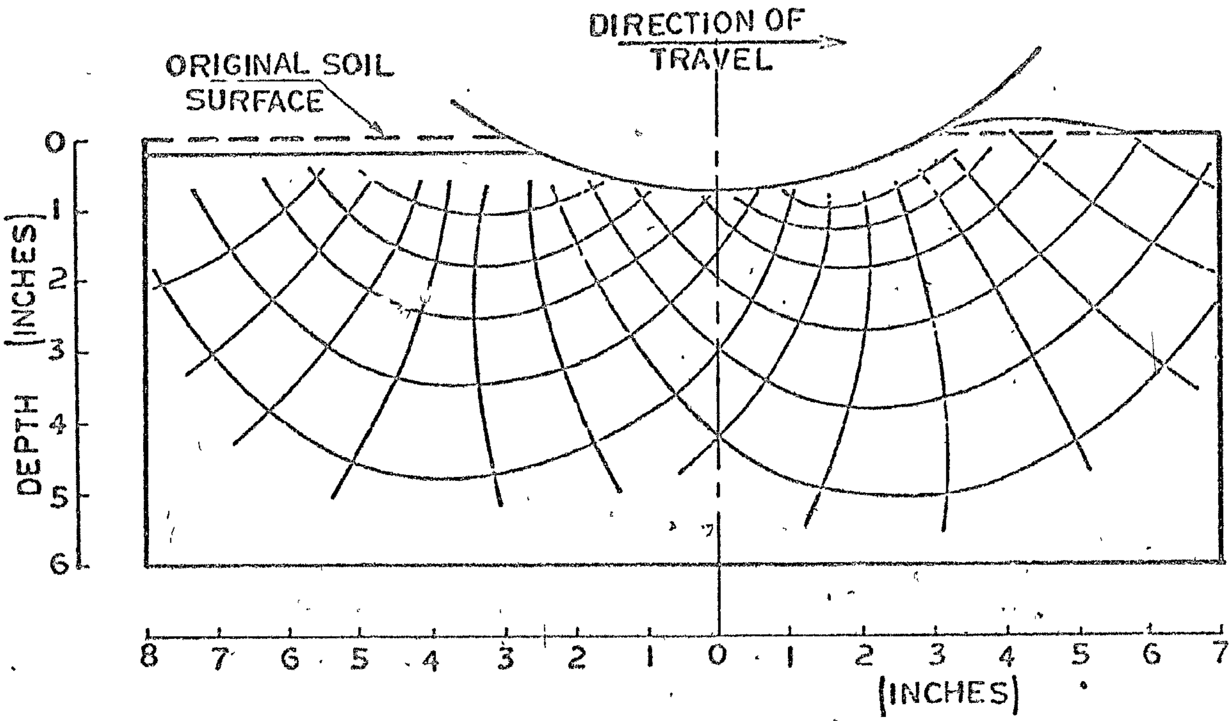

Figure 6.10 Direction of Principal Strain Rate (Visioplasticity)

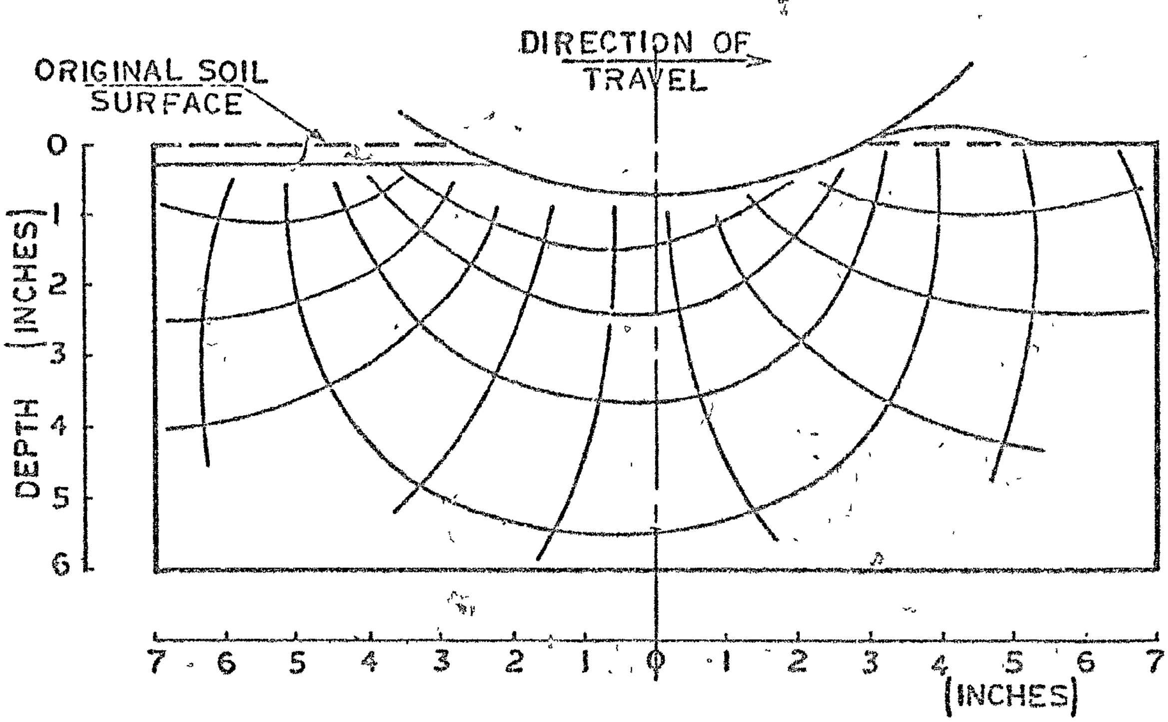

Figure 6.11 Direction of Principal Shear Strain Rate (Visioplasticity)

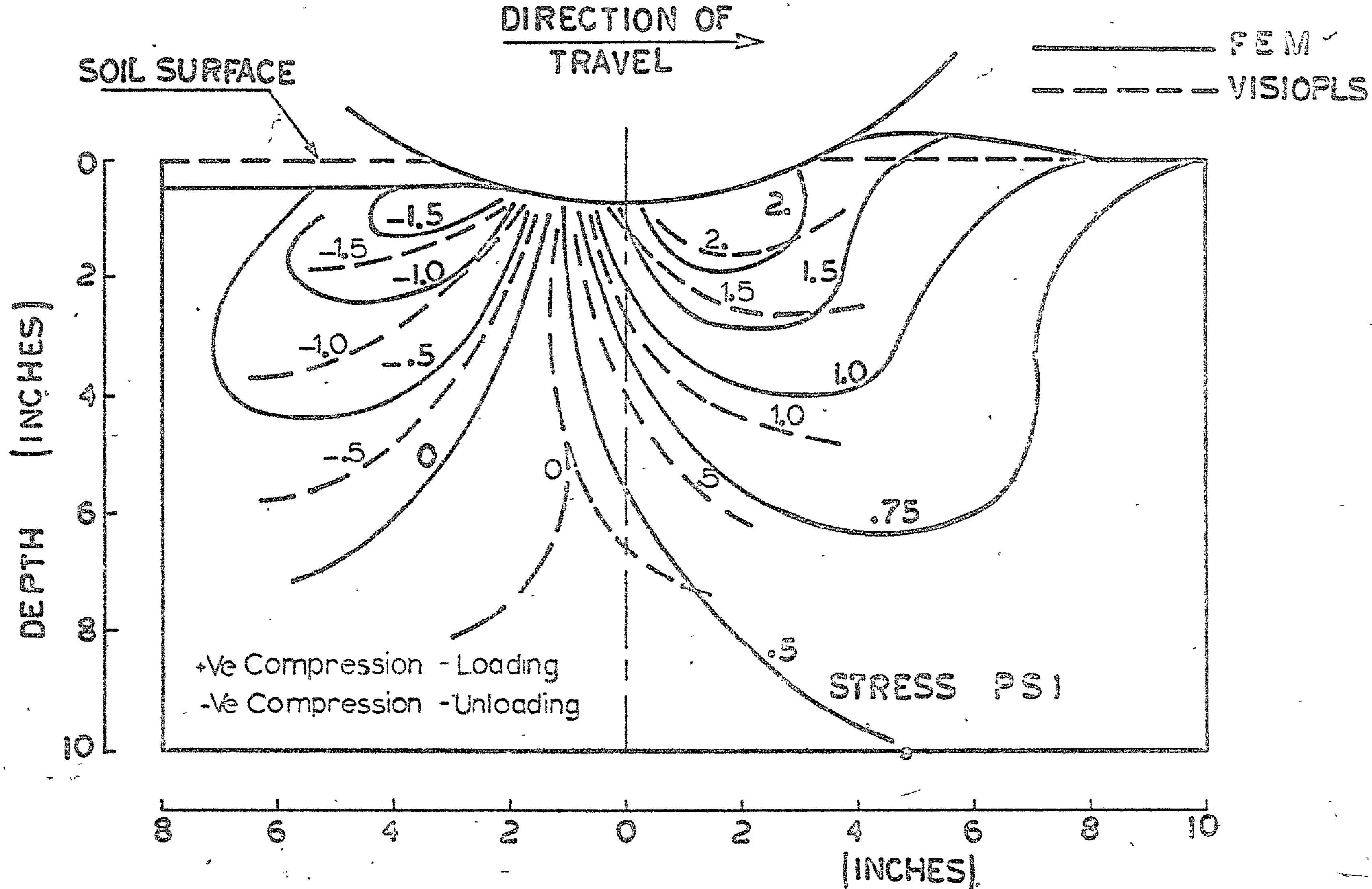

Figure 6.12 Horizontal Stress Contours Wheel Load 54 lbs

Slip 0%

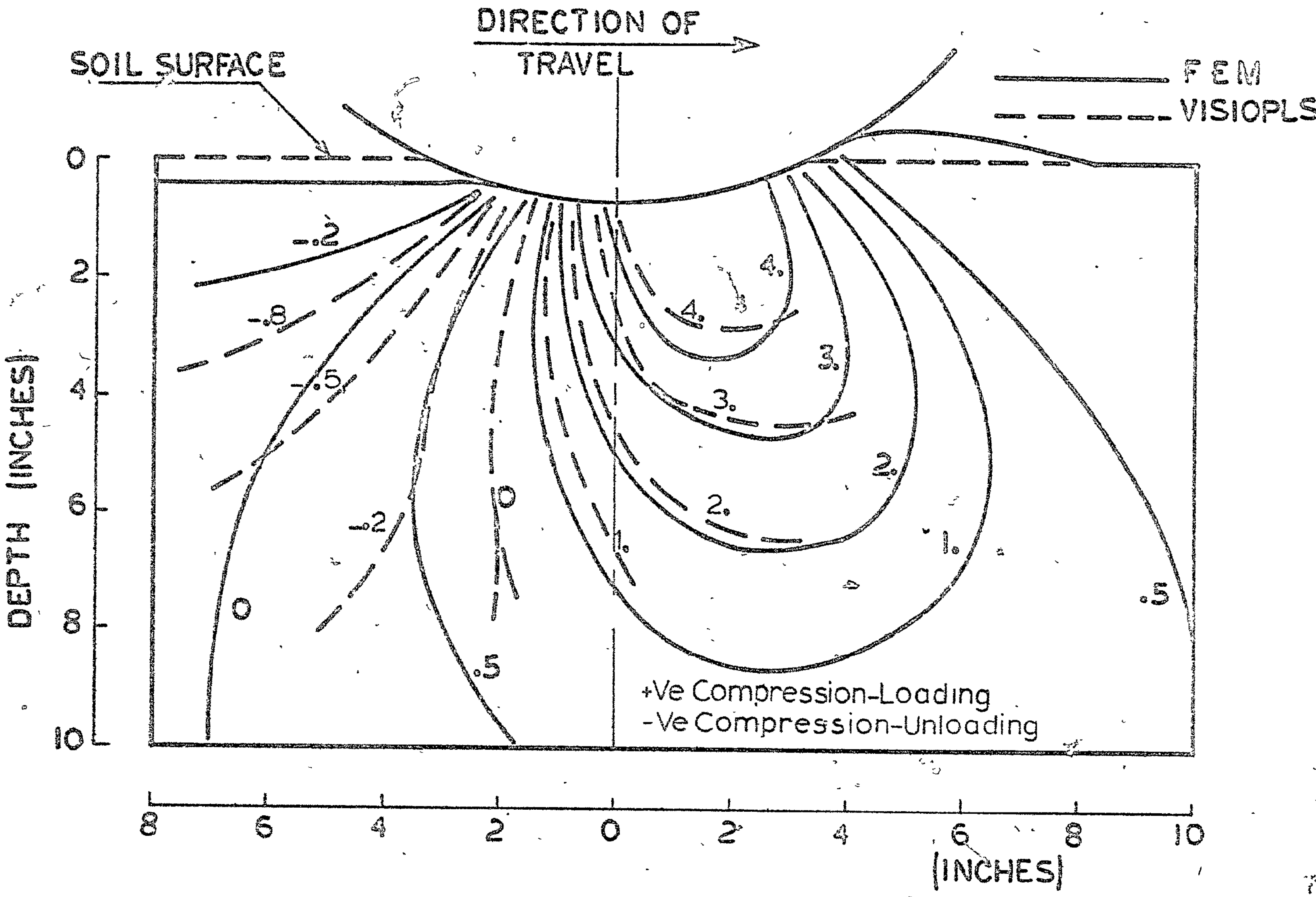

Figure 6.13 Vertical Stress Contours Wheel Load 54 lbs
Slip 0%

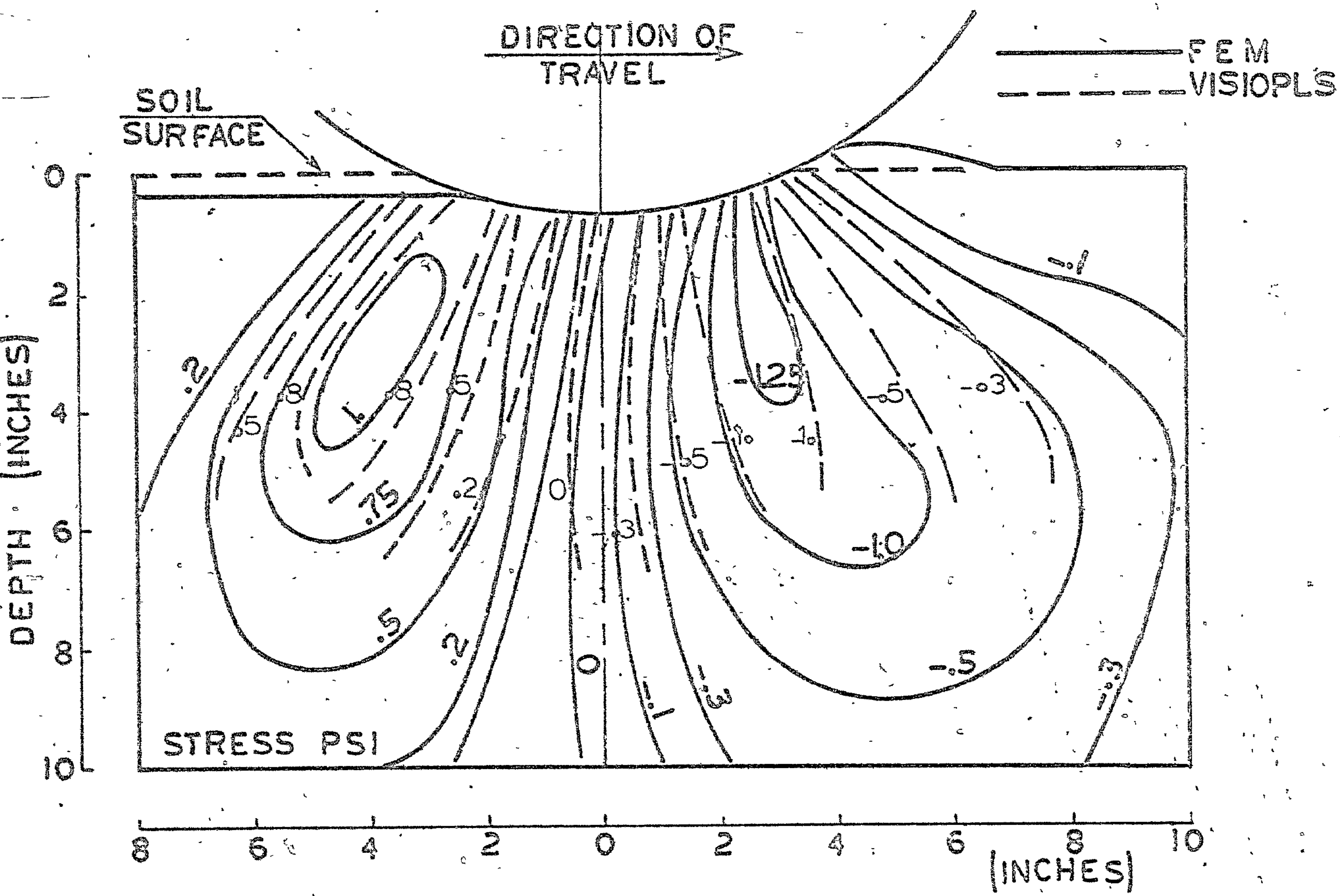

Figure 6.14 Shear Stress Contours Wheel Load 54.0 lbs
Slip = 0%

at which rebound begins to occur upon wheel unloading. The use of the compression tension divide condition which is in actual fact a load-unload condition in the soil, creates fictitious negative-positive stress regimes in view of the sign convention used, i.e. positive for loading and negative for unloading. The load-unload conditions are with respect to the soil performance. Hence the stress contours generated in regard to this kind of sign convention reflect the "positive" and "negative" stress regimes.

The FEM approach which uses load-unload in the positive sign convention sense does not produce the artificial negative stress condition in the soil. Hence it is expected that with the above and the other consideration discussed in the following pages, the stress fields generated from the FEM analysis would be a more appropriate reflection of the actual state of stress in the subsoil.

(b) Difference in Constitutive Relations

In the FEM the stress-strain relations determined from the results of triaxial tests are used in developing a constitutive relation.

In the characteristic method, the soil is assumed rigid plastic and obeys the Tresca yield criterion, and no effect of the confining pressure is considered.

(c) Difference in Solution Techniques

An incremental loading boundary approach is used in the FEM. The stress-strain relations at different confining pressures determined from the results of triaxial tests are used for determining the constitutive relations required for forming the stiffness matrix of the loading elements. For the unloading elements, a constant elastic modulus equal to the initial tangent modulus of the stress-strain curve is used.

In the method of characteristics, the solution is attained in one increment of loading (total stress approach). It is assumed also that the material is rigid plastic, the yield stress in compression being equal to that in tension and independent of the confining pressure.

The subsoil stress contours are plotted for a rigid wheel moving at 6 in./sec. translational velocity and zero degree of slip. Figures 6.12 to 6.14 show the FEM prediction for subsoil stress contours, using the experimentally determined wheel-soil particle path as loading boundary while Figures 6.15 to 6.18 show the subsoil stress contours for a case of high degree of slip. The differences between the shapes of the contour lines can be noticed.

The subsoil contours predicted using the FEM indicate that the influence of stress is much greater in the direction of motion and also that stresses diminish at a distance equal to the wheel diameter from both sides of the wheel center. The state of stress beneath the wheel is always in compression and the stress is higher at the front of the wheel than at its rear, because of soil recovery beneath the wheel BDC. This observation corresponds to the fact that at the wheel front the wheel is acting on the soil, while to the rear of the wheel the soil is acting on the wheel.

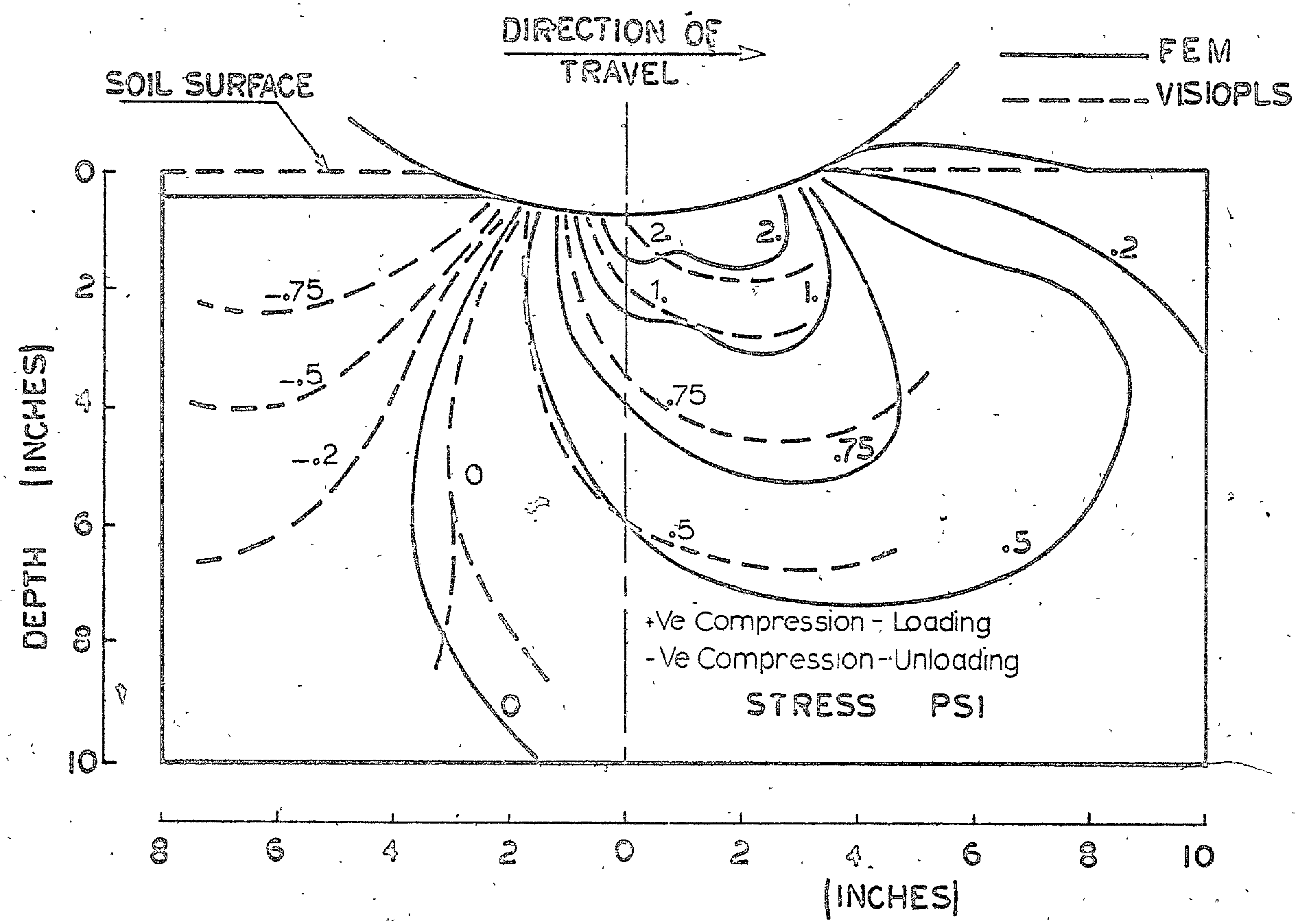

Figure 6.15 Horizontal Stress Contours Wheel Load 54 lbs

Slip [illegible]0%

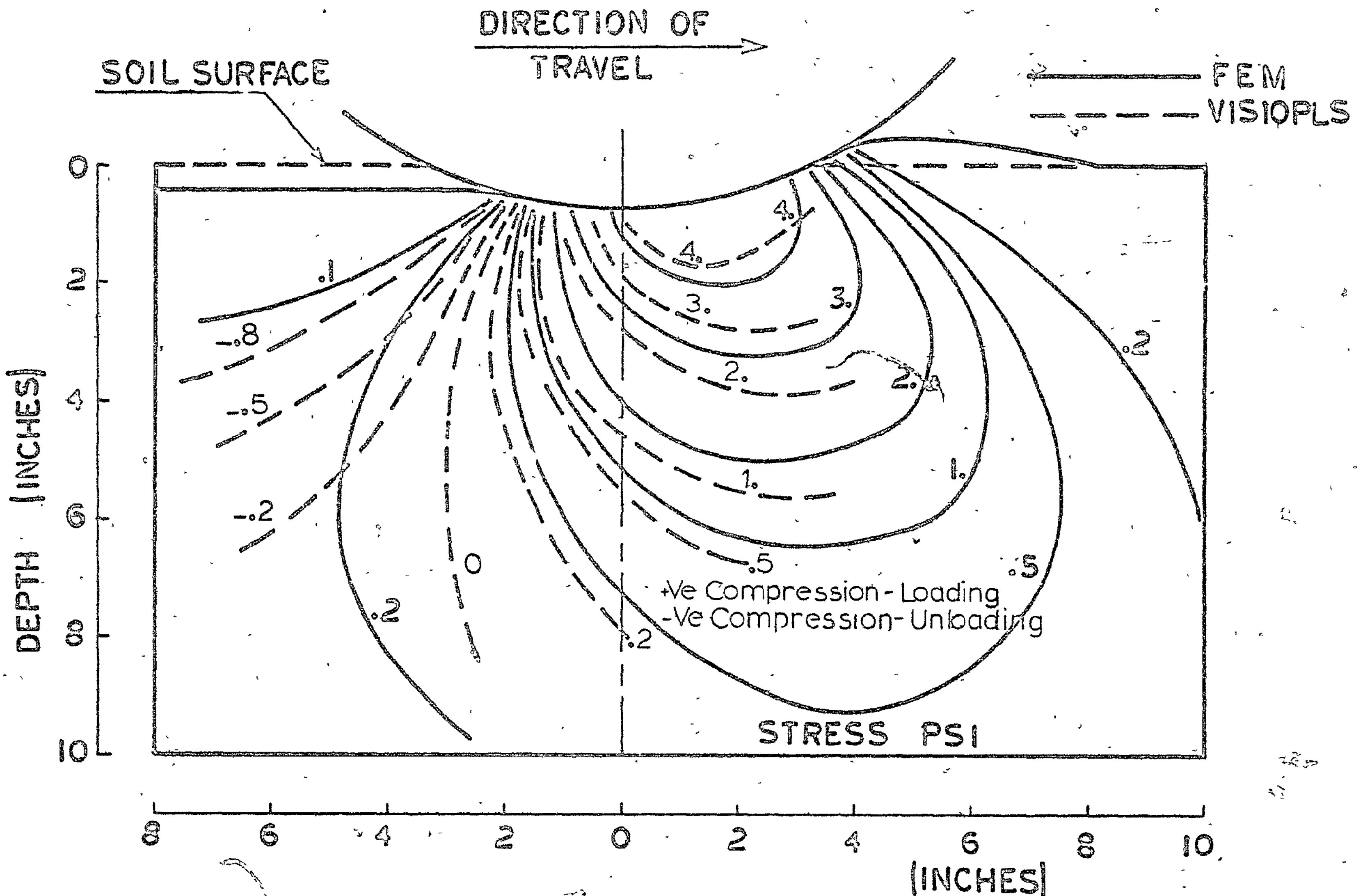

Figure 6.16 Vertical Stress Contours Wheel Load 54 lbs

Slip 30%

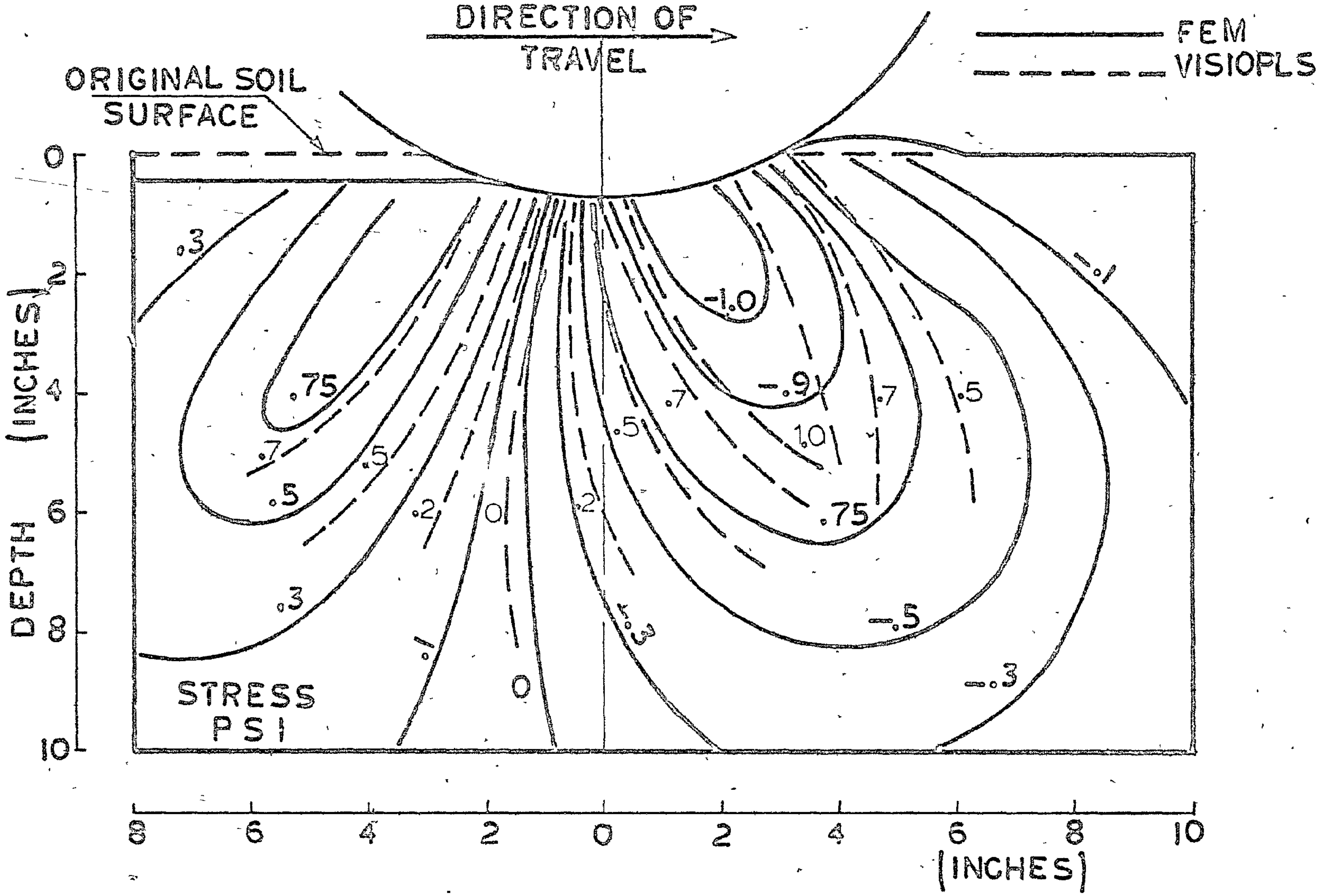

Figure 6.17 Shear Stress Contours Wheel Load 54 lbs
Slip 30%

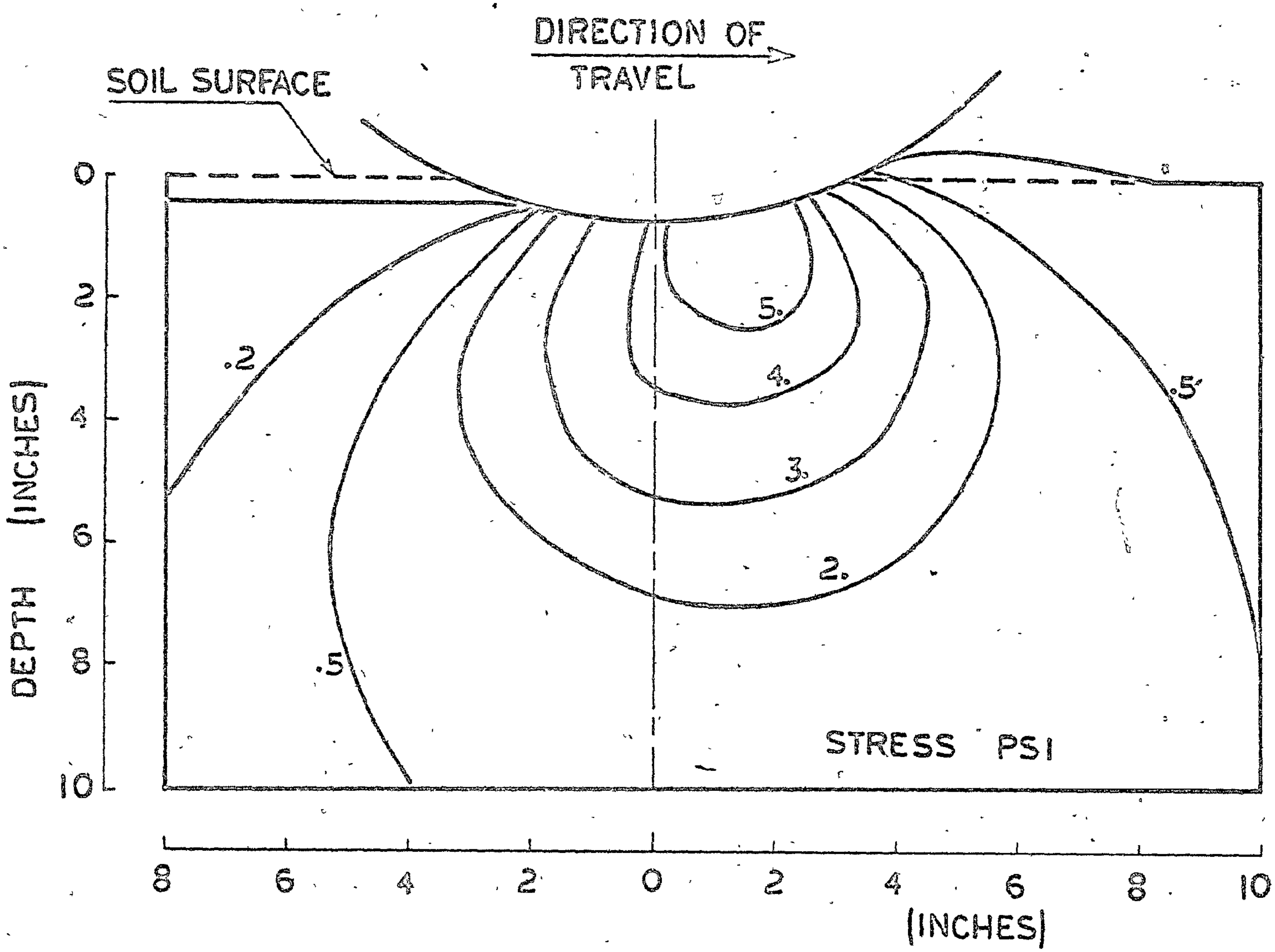

Figure 6.18 Major Principal Stress Contours, FEM Wheel Load 54 lbs
Slip 30%

In the stress contours predicted from a knowledge of subsoil deformations using the visioplasticity technique (method of characteristics), the negative sign of the horizontal component of stress indicates compression in the direction opposite to wheel travel; similarly, the negative sign of the vertical component of stress indicates compression in the upward direction.

For comparative purposes, the subsoil stresses beneath a stationary wheel penetrating in soil to a depth equal to the dynamic sinkage of a moving rigid wheel, are shown in Figures 6.19 to 6.21.

6.5 Interfacial Stresses

As stated above, in the FEM the interfacial stresses are predicted in two major steps. The first step consists of applying incremental vertical displacements to the wheel until the augmented values of displacements reach the dynamic sinkage; in the second step a quasi-static problem is considered by giving the wheel successive incremental travel distances until the calculated values of the interfacial stresses remain constant (Yong & Fattah, 1976).

The variation of contact pressure distribution as a function of depth for a stationary wheel is shown in Figure 6.22. The predicted results indicate that for a small value of sinkage the contact pressures are monotonically increasing from the initial point at the wheel-soil contact surface to the point of maximum sinkage. However, at higher

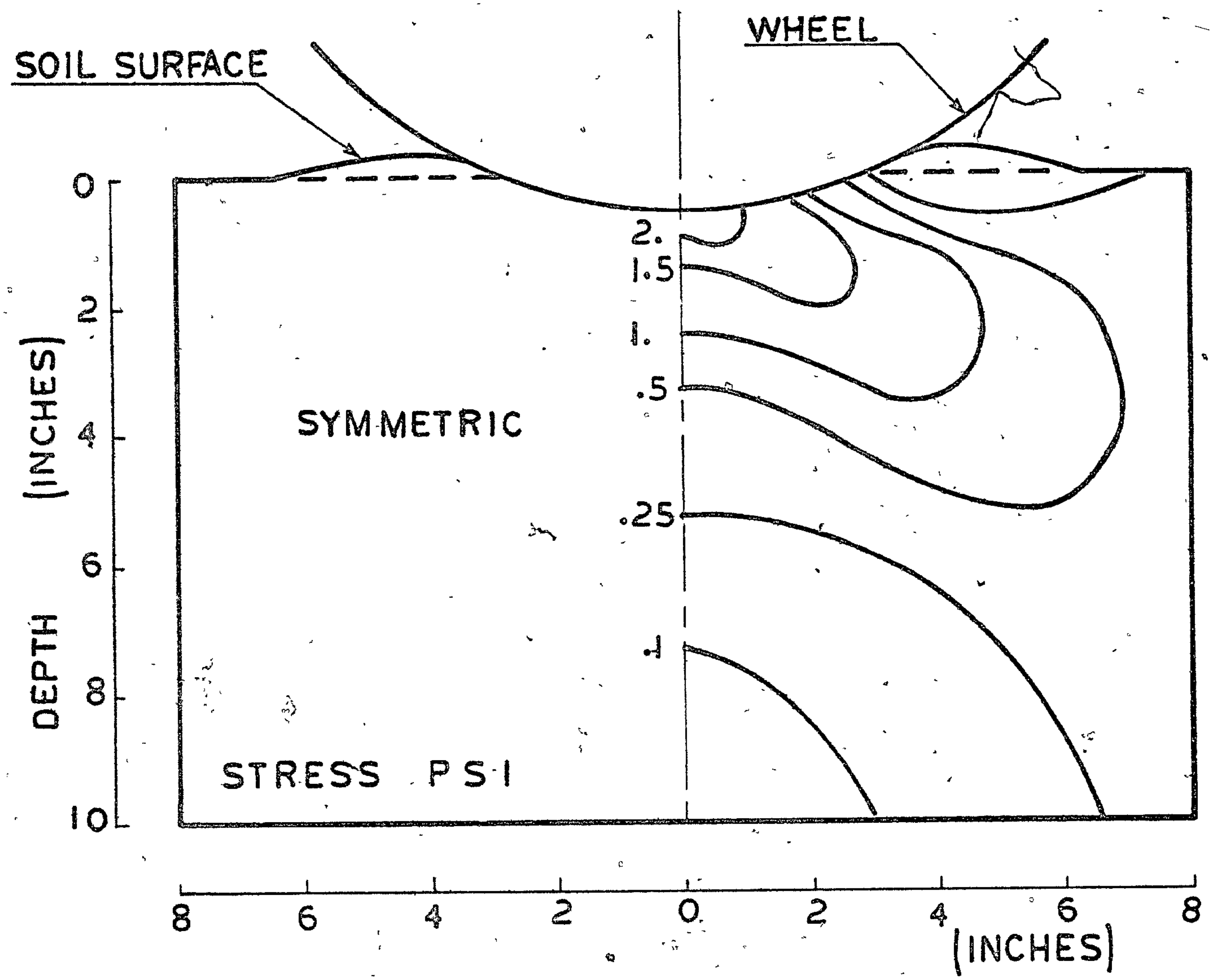

Figure 6.19 Horizontal Stress Contours Stationary Wheel
Sinkage .7in.

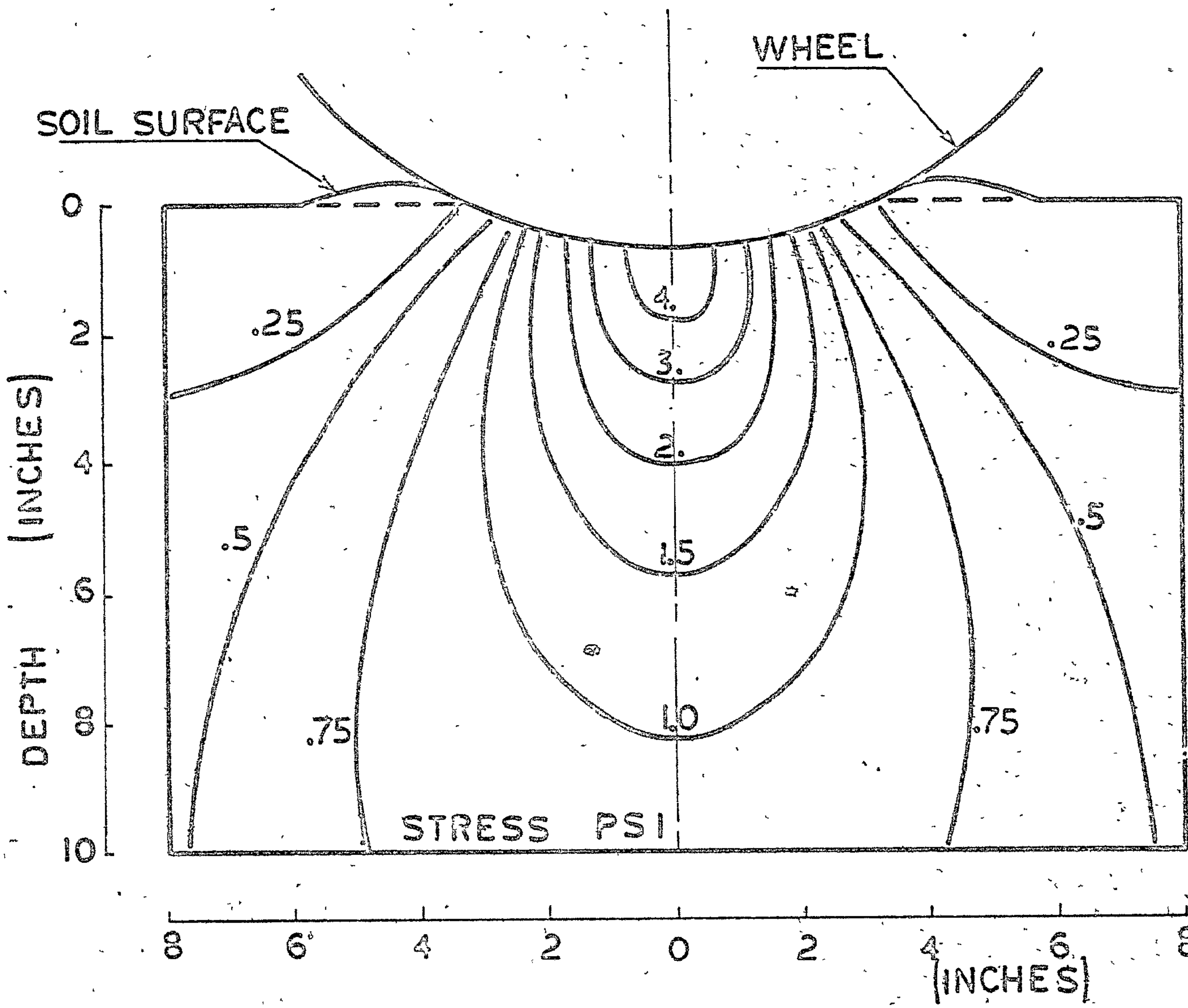

Figure 6.20 Vertical Stress Contours Stationary Wheel

Sinkage .7 in.

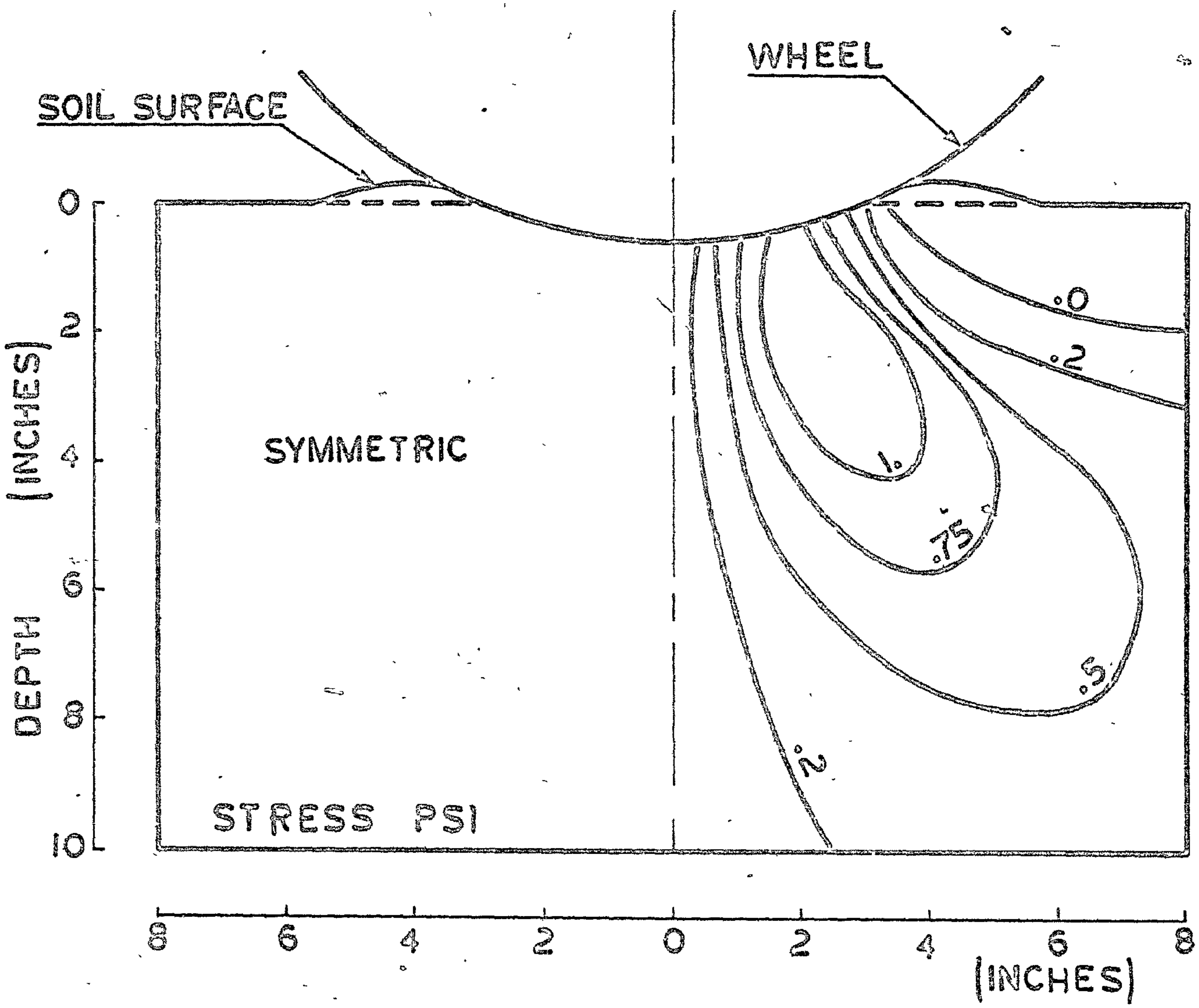

Figure 6.21 Shear Stress Contours Stationary Wheel Sinkage .7 in.

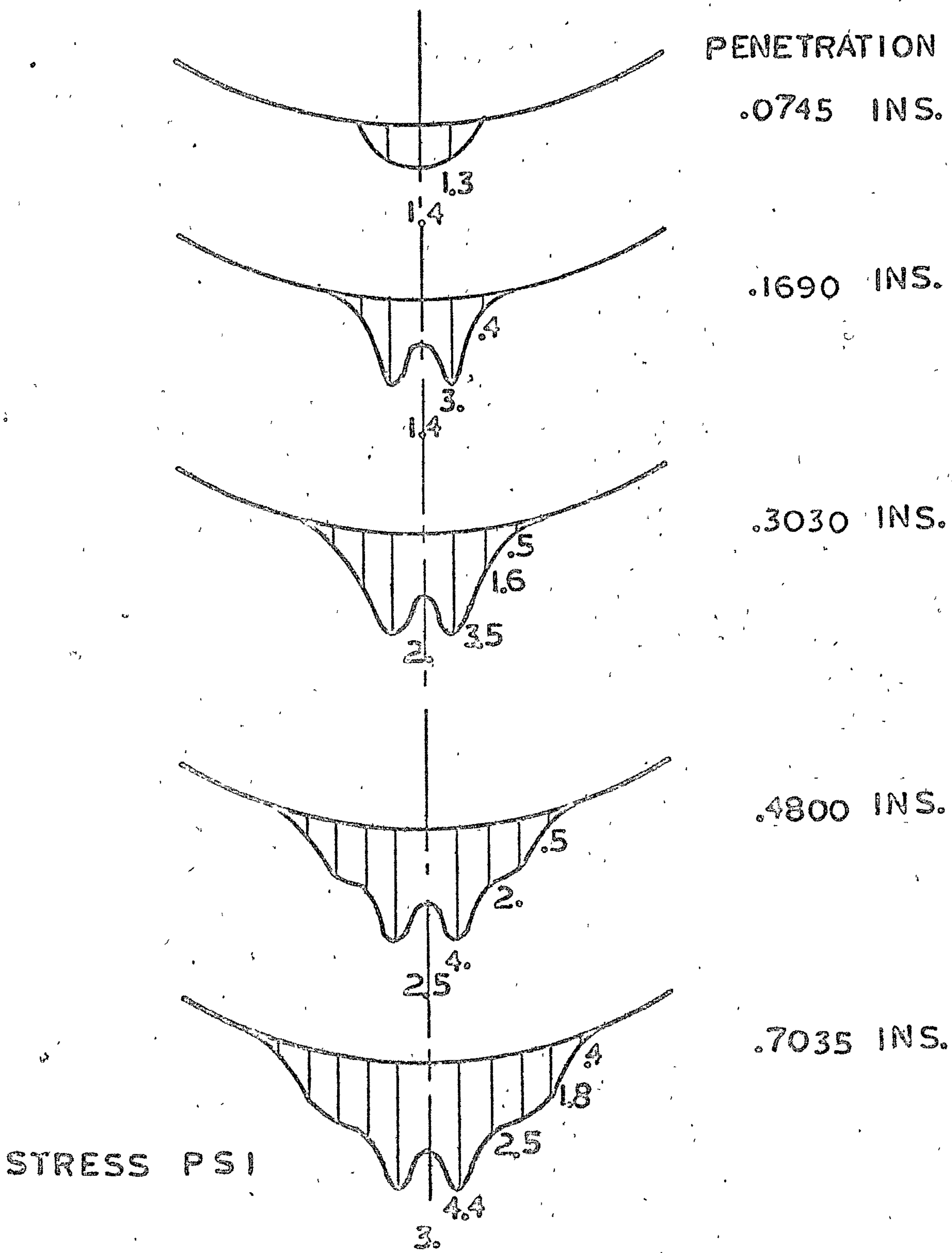

Figure 6.22 Development of Vertical Stress Distribution beneath a Stationary Wheel (FEM)

values of sinkage the point of maximum pressure does not coincide with that of maximum sinkage, i.e., the wheel is acting as a rigid foundation on soft soil.

It is noticed that the number of time intervals, or incremental wheel travel distances, at which the interfacial stresses start to become constant is determined by the time required for the first loading nodal point at the wheel-soil interface at wheel front to leave the interface at the rear. Figures 6.23 and 6.24 show typical wheel-soil interfacial stress distributions for a driven rigid wheel with different degrees of slip. As the slippage increases, the radial stresses on the wheel-soil interface decrease in the direction opposite to the wheel movement. The general distribution of the wheel-soil interfacial stresses, predicted using the finite element model, is similar to that measured by Onafeko & Reece (1967). The predicted results also indicate that the horizontal and vertical components of stresses conform with the measured drawbar pull and wheel load respectively.

For comparative purposes, Figures 6.23 and 6.24 also show the pattern of interfacial stress distributions corresponding to those determined by the FEM. These interfacial stresses are determined by the method of characteristics, provided that the subsoil slip line fields, and the line of compression-tension divide, are both known from the experimentally determined subsoil behaviour, as explained in Chapter 4.

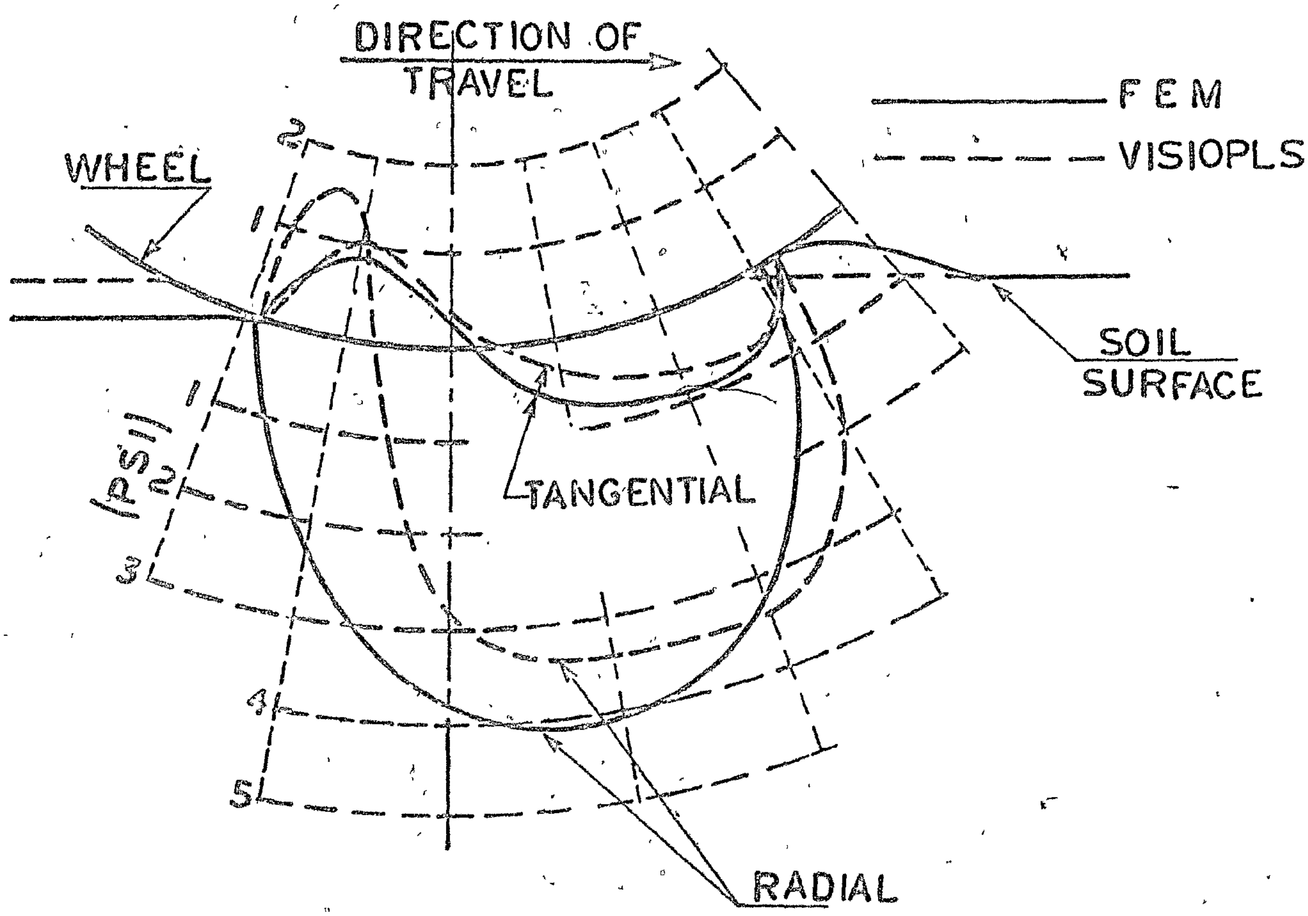

Figure 6.23 Interfacial Stress Distribution (Aluminum Wheel)

Dynamic Sinkage	.8 in.
Slip	0%
Wheel Load	54.0 lbs.

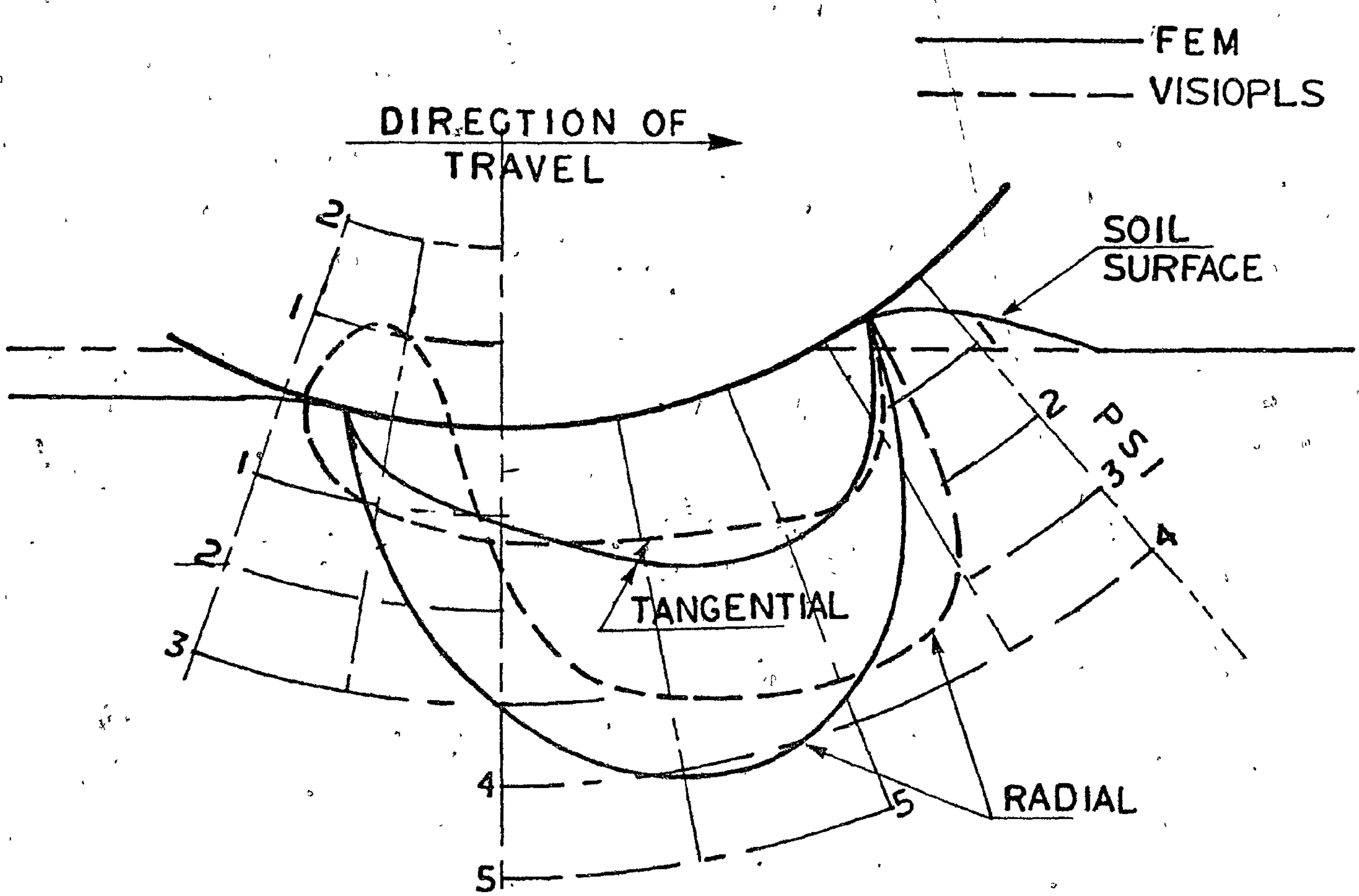

Figure 6.24 Interfacial Stress Distribution (Aluminum Wheel)

Dynamic Sinkage	.8 in.
Slip	30%
Wheel Load	54.0 lbs.

It is perhaps significant to observe that a negative (tension) radial stress is computed at the tail end of the wheel contact surface based on the response characteristics of the supporting soil. Recalling that the interfacial stress characteristics are derived from a knowledge of the soil and deformation behaviour at resultant stress distribution, it becomes important therefore to pay some attention to the relevance of the negative radial stress. In effect, this is due to the rebound behaviour of the soil which occurs during the unloading portion of the wheel-load cycle. Contact between the wheel and soil is maintained during this period. The phenomenon can be construed thus (Yong & Fattah, 1971):

(1) the subsoil is reacting passively during and at the forward portion of the contacting rim. This corresponds to the forward thrust of the wheel. The resultant pressure is largest in this time and space cycle;

(2) the subsoil reacts actively in the after portion of rim contact since maximum pressure is reduced, and effective unloading and rebound occurs. In effect, one might consider that the soil acts against the rim to provide an upward thrust because of rebound.

The significance of the above lies in the rebound ability of the soil. It becomes obvious therefore that greater rebounds would provide for a correspondingly larger thrust from the soil onto the wheel, resulting in a negative radial pressure.

The negative radial pressure cannot be adequately determined from pressure transducers located in the wheel rim since the negativity is essentially associated with the active nature of the soil. The gauge will always sense a positive pressure, so long as soil contact is maintained. In actual fact, from a knowledge of the deformation behaviour of the soil, active and passive response characteristics of the soil can both be observed as in Figure 6.25.

In spite of the fact that the interfacial stress distributions predicted by the FEM and determined by the method of characteristics are different, they both satisfy the conditions of equilibrium; the differences can be ascribed to the same reasons used in the description of the differences between predicted and experimentally determined subsoil stresses (Section 6.4).

6.6 Deformation Energy Contours

In the visioplasticity method the power of deformation energy (energy per unit width per unit travel distance) at specific points in the soil beneath the moving wheel is calculated, using information concerning the subsoil deformations determined by x-ray photographic technique (Appendix ~~A~~). The methods of calculation are explained in Chapter 4. The results are presented in the form of deformation energy contours, Figures 6.26 to 6.28, for different wheel loads and degrees of slip.

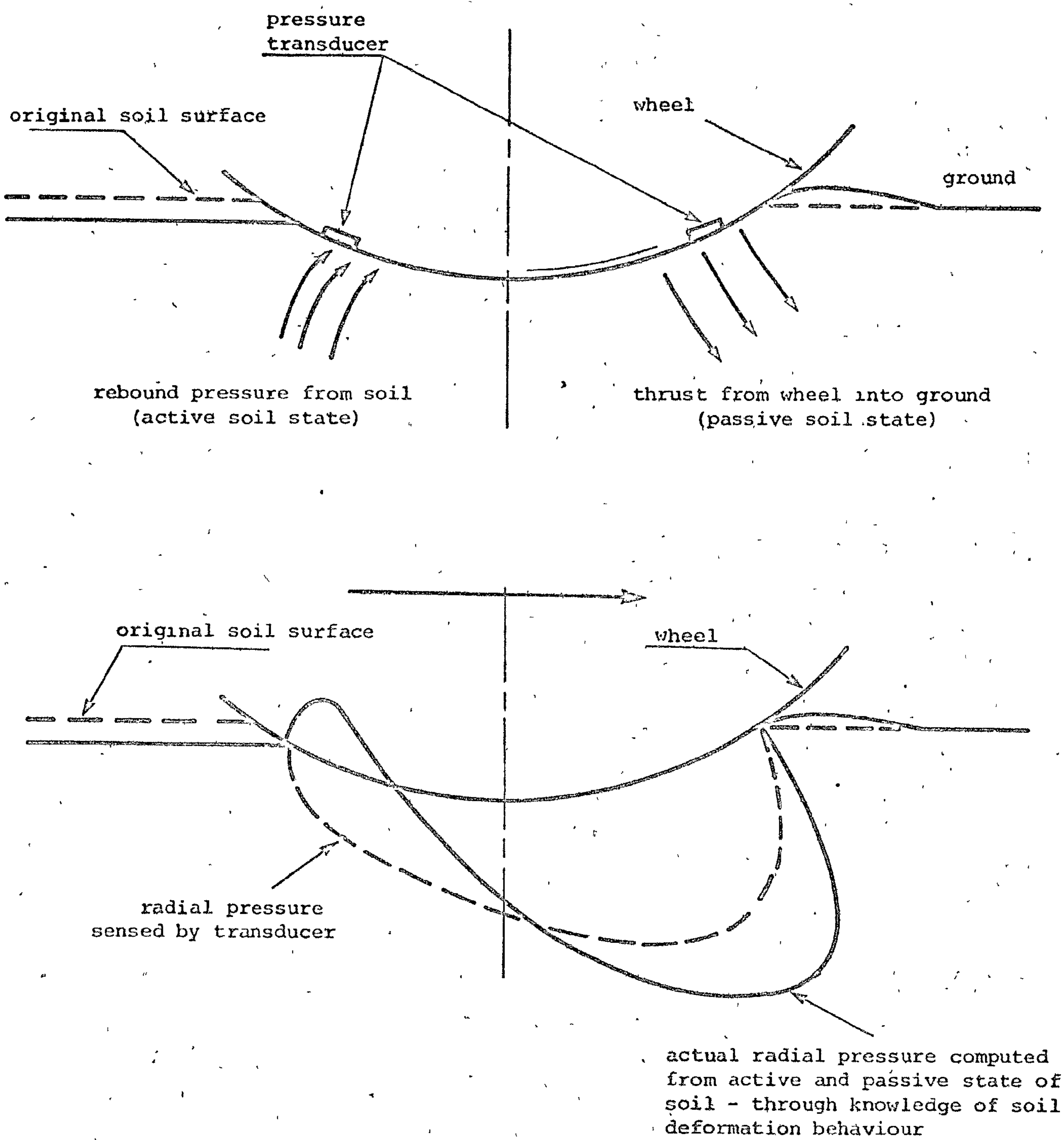

Figure 6.25 Schematic Diagram for Comparison Between Computed and Measured Interfacial Stresses (Yong & Fattah, 1971)

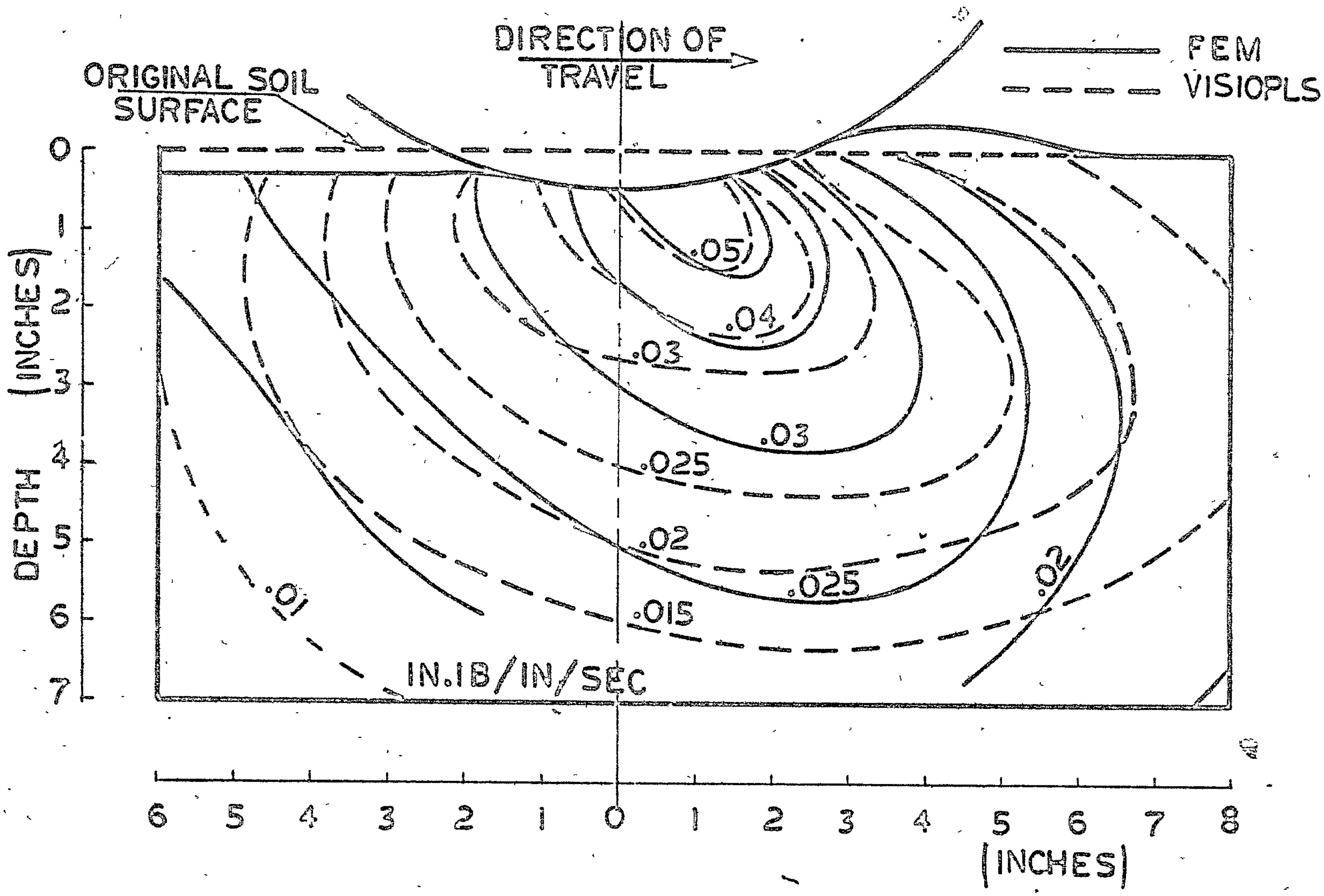

Figure 6.26 Deformation Energy Contours

Wheel Load 34 lbs
Slip 0%
Aluminum Wheel

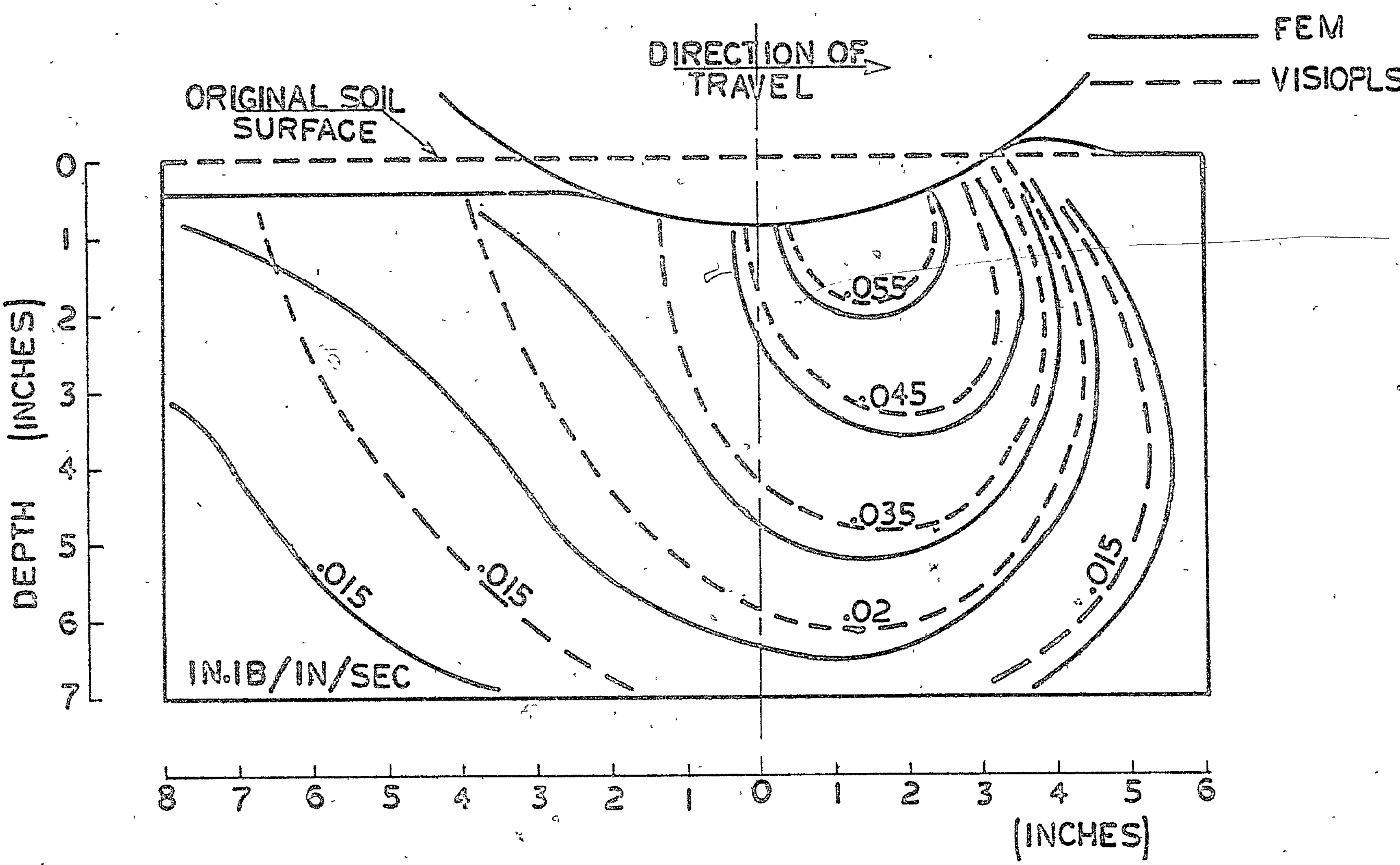

Figure 6.27 Deformation Energy Contours Wheel Load 34 lbs
Slip 15%
(Rubber STrap)

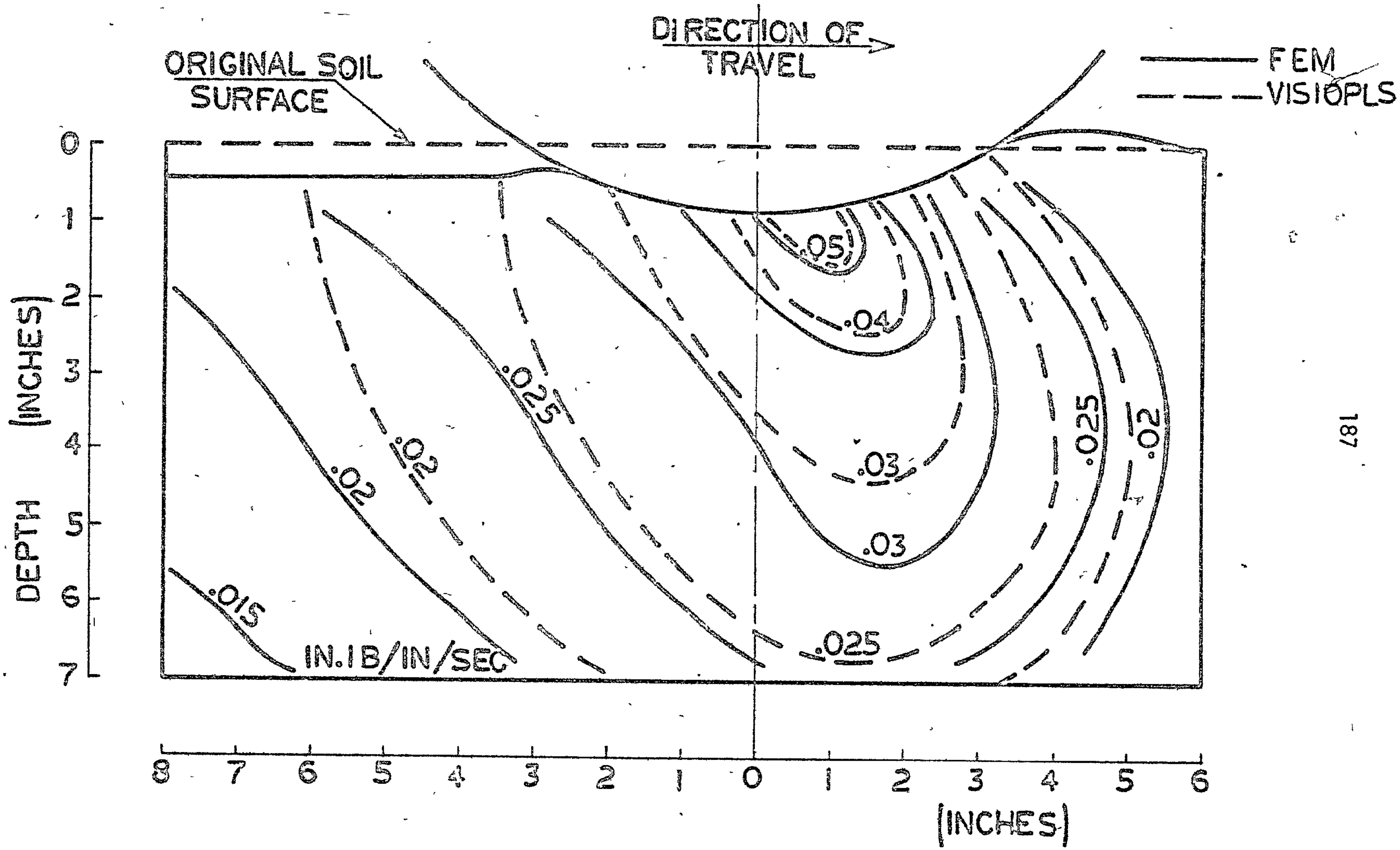

Figure 6.28 Deformation Energy Contours

Wheel Load 34.0 lbs
Slip 50%
Rubber Strap Mounted

In the FEM the power of deformation energy is determined at every nodal point of the FE idealized subsoil grid by averaging the values for all elements surrounding that nodal point. The FE energy contours and the contours obtained from the visioplasticity method are both plotted on the same figures for ease of comparison.

Generally, the contours are curvilinear in the direction of wheel travel, with the concavity towards the direction of motion; also, they are shifted in the direction of motion with decreasing degree of slip.

The deformation energy contours can express the degree of subsoil distortion, and thus the zones of maximum distortion beneath the wheel can be determined.

The results indicate that the energy contours determined using the FEM conform well with those determined by the visioplasticity method. Both methods give the same trend, but the visioplasticity method gives higher values than the FEM, especially at high degrees of slip.

The difference in the results is due to (a) differences in the soil stress-strain relations used, and (b) the choice of the soil shear strength value in the visioplasticity method.

6.7 Energy Balance

The predicted wheel performance using the visioplasticity technique together with the finite element prediction is shown, for the 34.0 lbs aluminum wheel, in Figure 6.29. The soil particle path at the

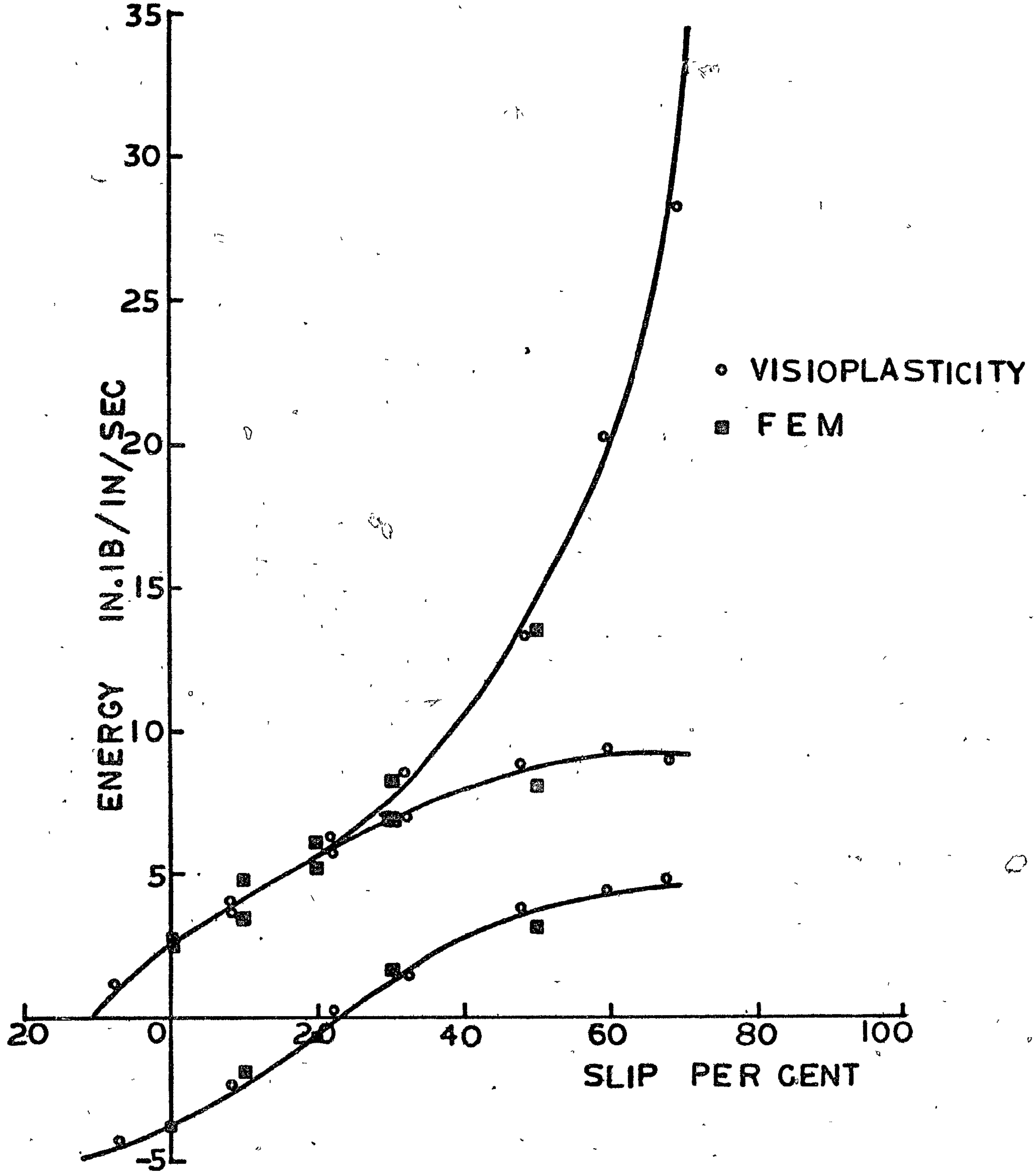

Figure 6.29 Energy Balance

Wheel Load 34.0 lbs
Aluminum Wheel

wheel-soil interface, as determined from x-ray photographic technique, was used as a loading boundary for the finite element solution. The results indicate that the degree of correlation between the finite element and visioplasticity predictions is good for low degrees of slip, and decreases with increasing slip. The discrepancy between the FEM predicted results and measured results at high slip is due to neglected effect of strain rate on the mechanical properties of soil in the FEM treatment.

It should be also noted that the predicted results using the visioplasticity technique correlate well with the measured performance, both at low and high degree of slip, as the strain rate effect is taken into account in calculating wheel-soil interfacial energy loss.

CHAPTER 7

SUMMARY AND CONCLUSIONS

7.1 Summary

A fundamental prerequisite for off-road vehicle mobility research is the exact specification of the characteristic of the vehicle tractive element and the response of the soil under vehicular loading.

The performance of a moving rigid wheel and the behaviour of the soil beneath it were predicted through application of the FEM; the predicted wheel performance was compared to the experimental surficial measurements and the subsoil response, through use of the x-ray photographic technique and application of the visioplasticity method. The FEM provides a convenient framework for field or laboratory investigations of the nature of the soil response to vehicular loading and of wheel performance over a full range of degrees of slip. The method provides a means of properly incorporating the subsoil properties and wheel dimensional parameters into a rational overall theory.

The use of the FEM to predict wheel performance and subsoil behaviour beneath it by taking into account the effect of soil recovery beyond wheel BDC, the effect of large displacements and the nonlinear behaviour of soil, represents the first application of an analytical method to the soil-vehicle problem. In this analysis use was made of the soil particle path (obtained from the x-ray photographic data) to determine boundary conditions at the wheel-soil interface. It was then possible to evaluate the wheel-soil interfacial stresses, drawbar pull, the work dissipated in deforming the soil vertically and horizontally, and the energy dissipated at wheel-soil interface.

Consideration of the energy balance of the system, making use of the computed deformations and interfacial energies, allows reasonable predictions of the useful output energies and provides a vivid picture of wheel performance and efficiency at any degree of slip.

7.2 Contribution

This study shows that theoretical aspects of the wheel-soil interaction phenomenon can be defined. A good prediction can be obtained so long as the boundary conditions and constitutive relations of the theoretical model correspond well with the physical model. Specific contributions are:

1. The development of a theoretical method (FEM) and its ability to predict wheel performance and subsoil behaviour beneath it, with specific provisions for the effect of loading and unloading, due to the nature of the wheel movement (Chapters 3 and 6).
2. The successful application of the theory (FEM) and verification of the correspondence between measured and computed performance, and between the predicted and the observed subsoil deformation patterns (Chapter 6).
3. A study of the effect of wheel surface condition on its performance and of subsoil behaviour beneath it (Chapter 5).

4. The establishment of a basis for evaluating wheel performance at any degree of slip (Chapters 5 and 6).

The above provides a useful contribution to the field of wheel-soil interaction analysis.

7.3 Conclusions

The present study may be looked upon as a step in the direction of an improved method for wheel-soil interaction analysis and performance prediction techniques.

In its immediate application, the proposed theory and technique may contribute to a systematic study of a moving wheel on soil by a rational scanning of all pertinent parameters.

Eventually, it could be attempted to rationalise the wheel performance prediction in the field, and subsoil behaviour beneath it, in terms of the significant soil and wheel parameters and hence establish a complete and unified theory for a moving off-road wheel on soft soil.

CHAPTER 8

RECOMMENDATION FOR FURTHER STUDY

The Finite Element Method represents a significant advance in the field of soil-machine interactions. It can be used in the laboratory or in field investigations to predict wheel performance and soil behaviour beneath the wheel. In addition, several other aspects of the soil-wheel problem can also be studied. These include additional modifications of the finite element computer model to account for different types of soil such as sands and soil with both cohesive and frictional properties and also to account for different characteristics such as inflation pressure and carcass stiffness for pneumatic tires.

In this study it was observed that the wheel surface configuration had some effect on its performance so that other surface configurations should be studied.

Application of the energy balance equation to wheel-soil interaction studies is reasonably successful for the case of rigid wheels; research should thus be extended to the case of pneumatic tires and the energy dissipated in tire deformation must be considered. Analysis of the experimental results show specific characteristics for the energy balance and interfacial energy curves, and investigations should be directed towards examining the effect of different wheel parameters on these characteristics (towed point, self-propelled point and singular point).

In addition to the surficial measurements of wheel performance (drawbar pull, input torque, translational and angular velocities and dynamic sinkage) and subsoil measurements (displacements), special attention should be taken to study the mechanisms of wheel-soil interaction at the interfacial soil zone.

The performance prediction of off-road vehicle tractive elements should shift from single wheel investigations to multi-wheels in tandem.

The development of a criterion for evaluating the degree of soil distortion beneath a moving wheel and the development of constitutive relations, based on results of portable apparatus in the field, are necessary in all vehicle-soil analyses.

APPENDICES

EXPERIMENTAL CONSIDERATIONS

A.1 Performance of Experiments at Soil Research Institute of McGill University

Laboratory experiments were conducted to measure the draw-bar pull, input torque, angular velocity, translational velocity, dynamic sinkage and the displacement pattern within the soil mass beneath a moving wheel. The facility for doing a test has been extensively described by Yong et al. (1967), Yong & Webb (1969), and Yong & Windisch (1970).

A.2 Vehicle Test Facility and Equipment

The machine-soil interaction test facility consists of nine main units (Figure A-1).

a. Soil Bins

The soil bin of the McGill Soil Research Institute is 32 feet long, 6 feet wide and 3 feet deep. The bin is divided longitudinally to form two separate bins whose dimensions are 32' x 4' and 32' x 6" respectively. The wide bin is used for model and three-dimensional analysis. The narrow bin is used for studying the subsoil behaviour in plane strain test condition and for developing mathematical models.

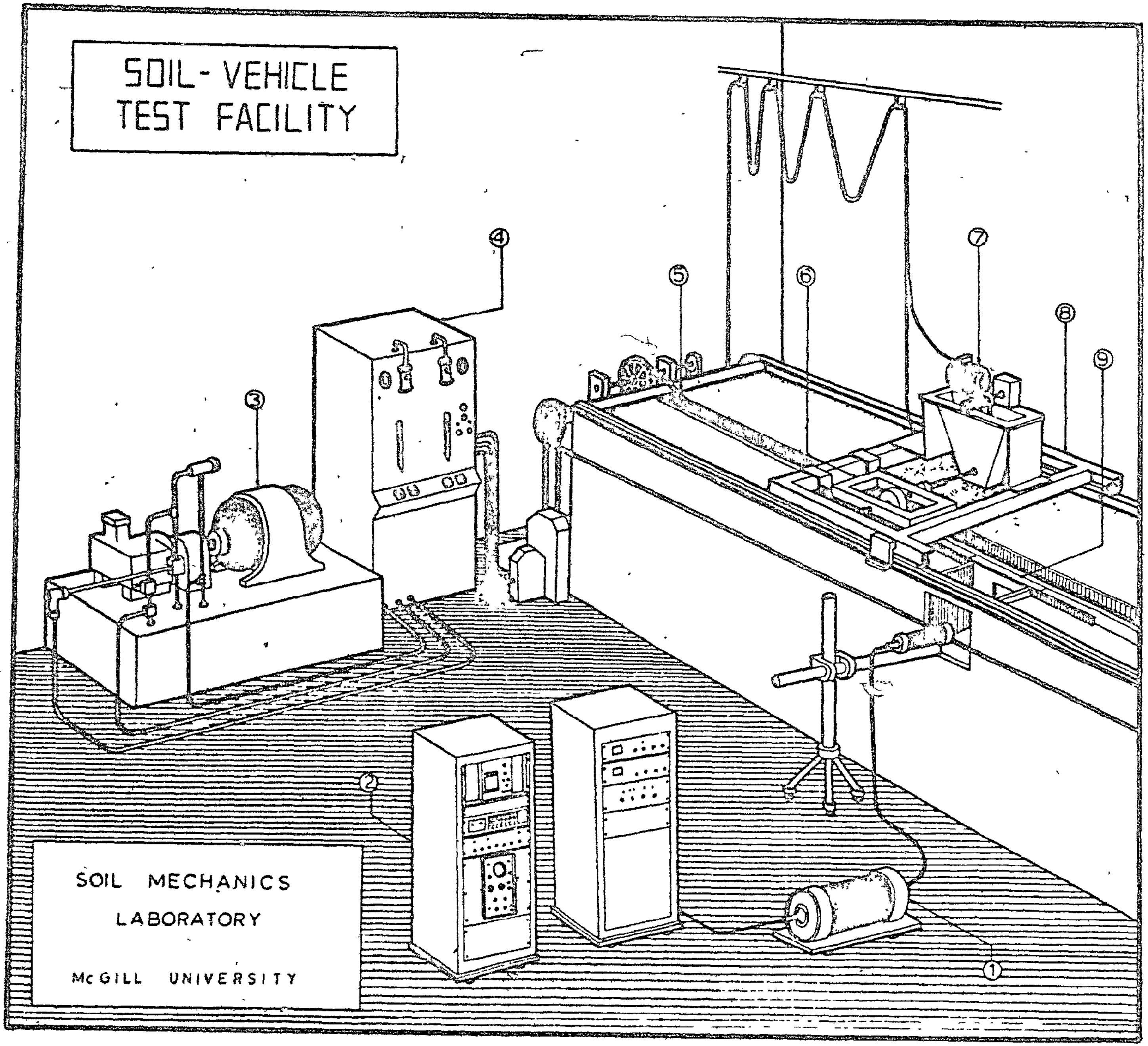

① X- RAY UNIT

② RECORDER, POWER SUPPLY, AMPLIFIERS

③ HYDRAULIC PRESSURE SUPPLY

④ HYDRAULIC CONTROL PANEL

⑤ CHAIN DRIVE FOR MOBILE X-RAY CASSETTES

⑥ FLEXURE FRAME & TEST WHEEL OR SECTION TRACK

⑦ D.C MOTOR, TRANSMISSION & TACHOMETER

⑧ DYNAMOMETER CARRIAGE

⑨ SOIL SAMPLE CONTAINING BURIED MARKERS

Figure A-1
(after Windisch, 1969)

b. Dynamometer Carriage

The dynamometer carriage contains the test wheel, the wheel drive motor, the wheel loading system and the dynamometer balance. The dynamometer carriage is guided by Z-rails mounted on the longitudinal walls of the soil bin; it is pulled by two continuous chains, one along each Z-rail.

The function of the dynamometer carriage is to provide a mobile anchor to the flexure frame of the test wheel and to support all equipment travelling along with the wheel: the electric drive unit, the tachometer measuring the angular velocity of the wheel, the L.V.D.T. measuring the vertical displacements of the wheel axis, and the required power supplies. The dynamometer carriage also has the function of triggering the X-ray unit by tripping three limit switches so located as to ensure proper synchronism.

c. Flexure Frame and Test Wheel

The Flexure Frame is a closed rectangular box on which the test wheel is mounted through bar rings. The frame is linked to the dynamometer carriage by two spring steel flexure pivots. Details of the connection is shown in Fig. A-2. The strains of these pivots measured by electric strain gauges provide draw-bar pull measurements.

The wheel used was made of aluminum, 13.5 inches in diameter and 3.75 inches wide. The surface texture was changed by mounting different types of rubber straps of 1/8" thickness on the wheel rim.

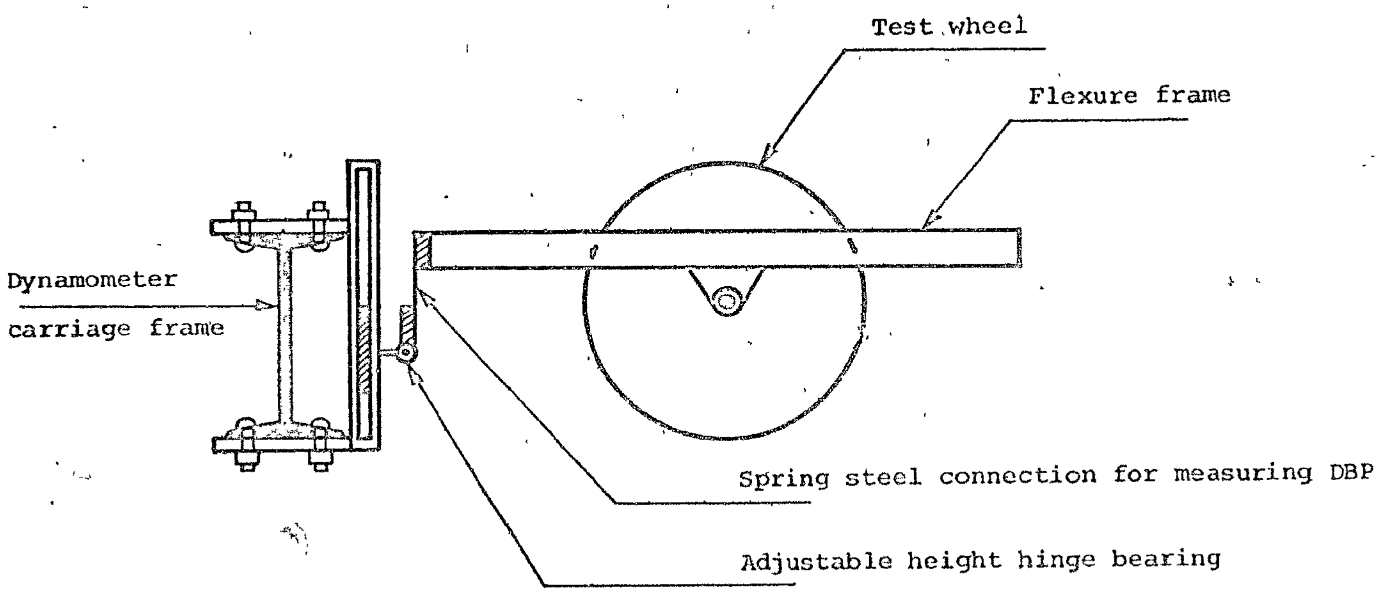

Fig. A-2 Flexure Frame and Test Wheel

d. Mobile Cassette Mechanism

The mobile cassette mechanism allows consecutive exposures to be taken on three individual radiographic plates while the wheel is passing over the sample.

The cassettes, held in the mechanised cassette holder, travel twice as fast as the wheel, the instantaneous position of the center of each cassette on the optical axis of the X-ray beam being synchronized with the triggering of the radiographic unit and the location of the test wheel (Fig. A-3).

The cassette-holder frame slides in a channel parallel to the soil bin. It advances under the pulling action of a chain activated by the same shaft as that of the dynamometer drag chains, through gearing imposing a cassette velocity twice that of the dynamometer carriage.

e. Soil Sample Holder

The soil sample holder is a trapezoidal-shaped box with dimensions 7x3x2 feet and with an interior width of 4 ins. (Figs.A-4). The holder is equipped with removable lucite sides and removable top plate; when placed in the 6" wide channel, the sample is in such a position as to allow the optical center of an embedded lead marker array to be coincident with the optical axis of the X-ray tube.

f. Hydraulic Drive Unit

The chains pulling the dynamometer carriage and the mobile cassette holder are powered by a hydraulic motor. The velocity and direction of chain motion are controlled by flow control valves and directional valves.

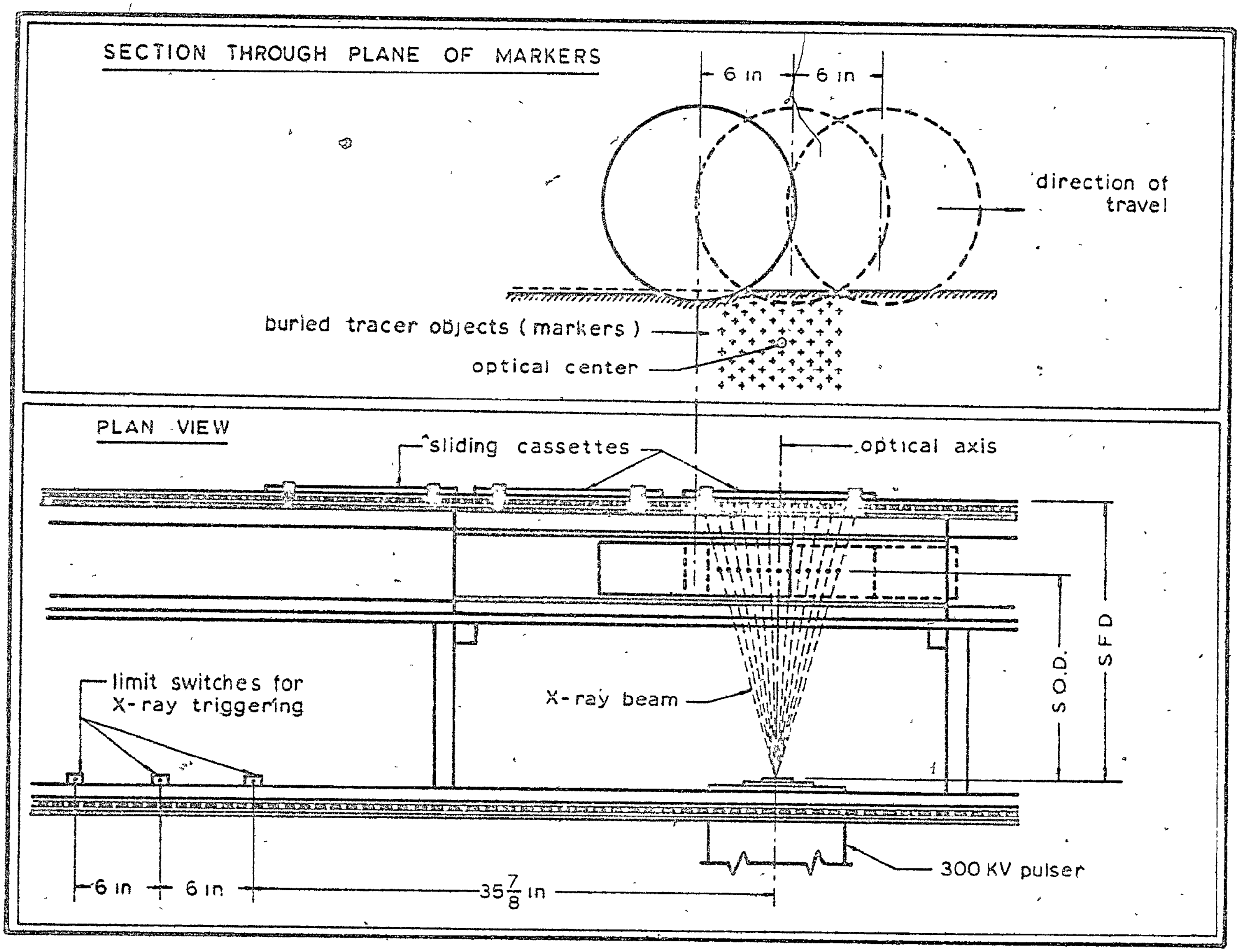

FIGURE A-3 WHEEL - PULSER - MARKER - FILM GEOMETRY

(after Windisch, 1969)

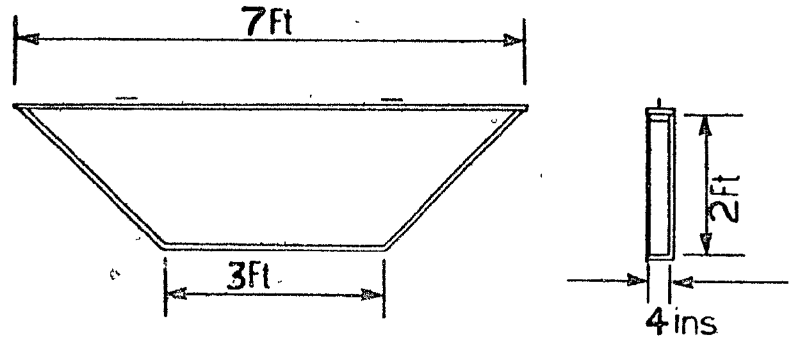

Fig. A-4a Sample Holder

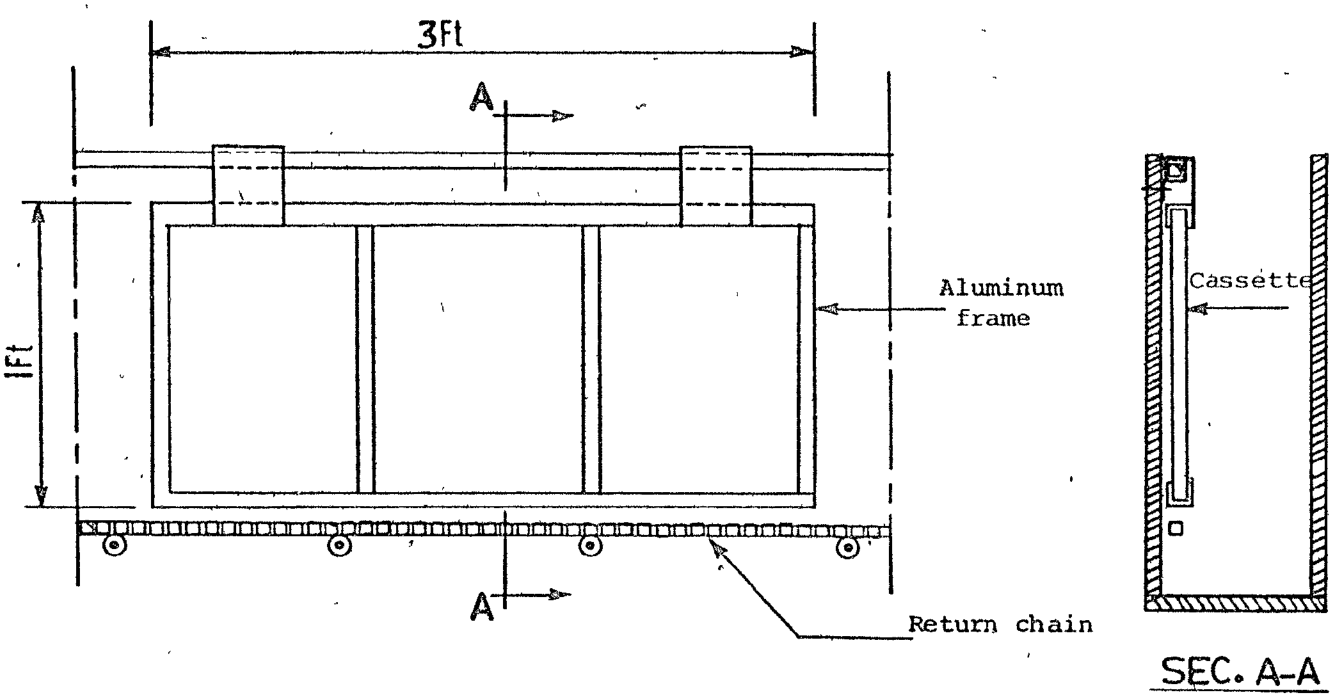

Fig. A-4b The Moving Cassette Holder

g. Electrical Wheel Drive

The angular velocity and torque input to the wheel are provided by a DC electric motor. The rotational speed of the motor, and hence the torque input and angular velocity of the wheel, is controlled by power rheostats.

The connection to the test wheel axis is completed through a chain drive, telescopic shaft and universal joint mechanism. A tachometer generator attached to the wheel-driving system is used to measure the angular velocity of the wheel, together with a torque cell to measure the torque applied to the wheel.

h. Electronic Circuitry

The electronic circuitry is designed for measuring six wheel variables. All measurements are recorded on a strip chart, ultra-violet recorder. The electric circuit corresponding to every wheel variable is shown in Figure A-5.

i. Radiographic Unit

The X-ray unit is a 300 KV flash x-ray unit which can pulse series of 10 exposures at a rate of two exposures per second. The flash x-ray tubes use a cold cathode electron source resulting in high current densities and very large information rates.

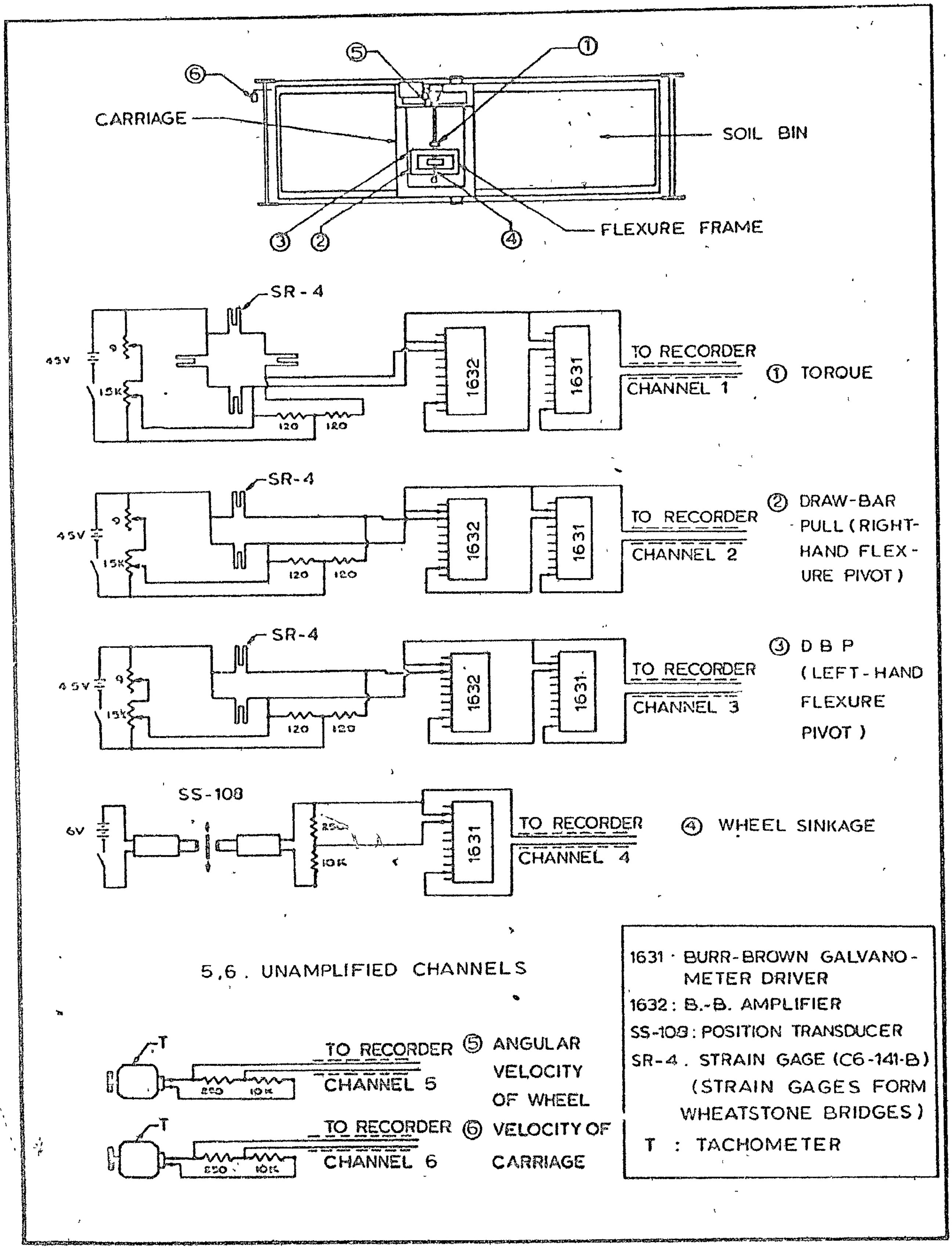

FIGURE A-5 ELECTRONIC CIRCUITRY

(after Windisch, 1969)

A.3 Skid Test Facility

The apparatus consists of a tool plate rigidly attached to a carriage which allows it to translate both horizontally and vertically but which permits no angular rotation, Figure A-6.

The carriage itself is mounted on roller bearings which travel on polished guided rails. The rails are machined to a tolerance of 0.003 inch, and as a consequence the frictional resistance of the system was reduced to a minimum, the force required to overcome this resistance being typically of the order of 2 - 4% of the total measured horizontal force.

The drive mechanism of the apparatus consists of a threaded shaft which is, in effect, a worm gear. This is driven by a 1/3 h.p. varying speed electric motor and a V-belt pulley assembly through a system of gears.

The carriage and tool assembly are mounted on a frame in such a position that it is situated directly above a soil bin whose dimensions are 22½" x 4" in plan form and which usually accommodates a depth of clay of the order of nine inches. The bin is equipped with removable lucite side walls and is mounted on castors to facilitate its removal from under the carriage. The carriage and bin are shown in Figure A-6.

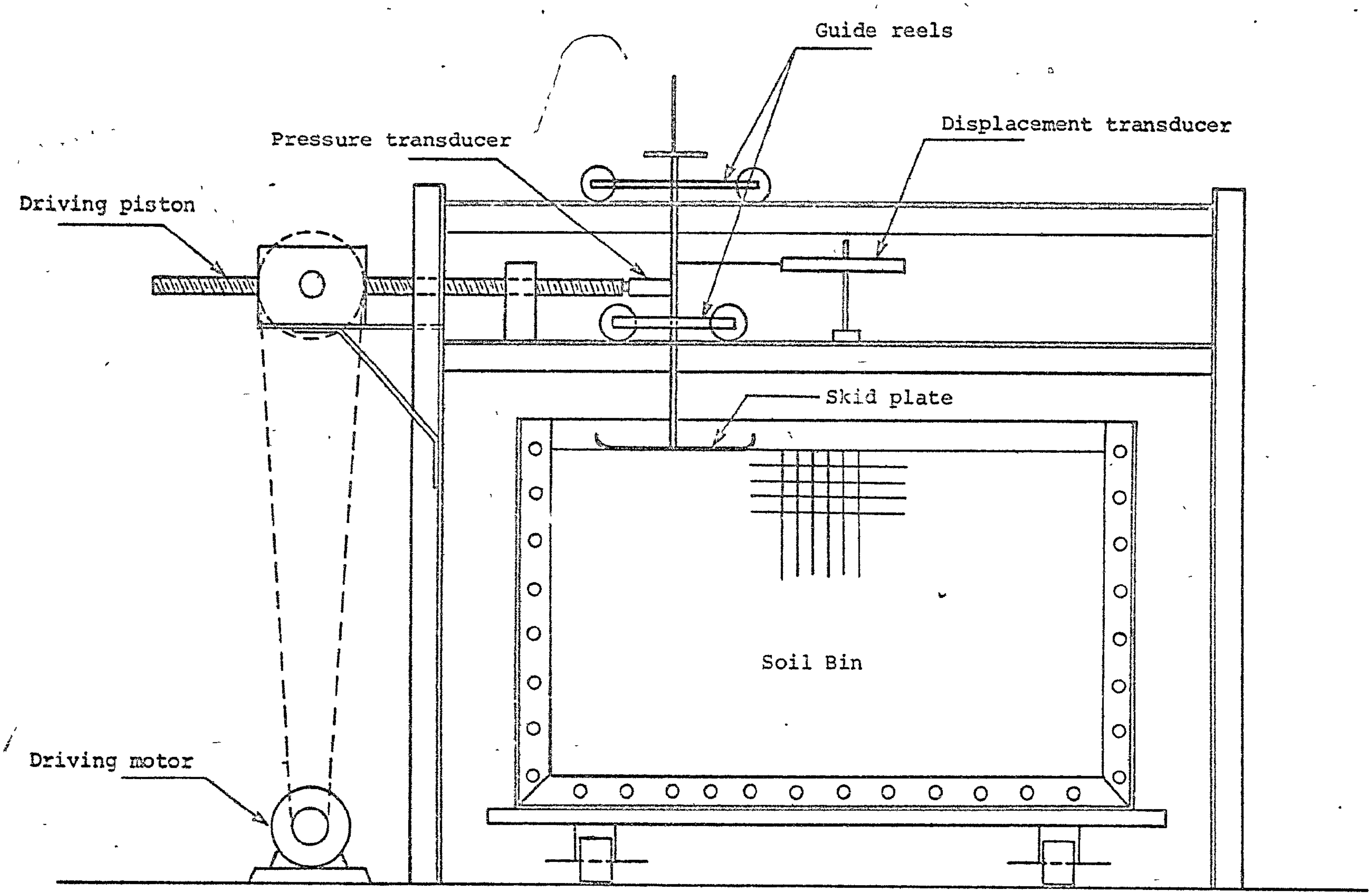

Fig. A-6 Skid Test Apparatus

A.4 Sample Preparation

The preparation of the soil test sample can be summarized in the following three steps.

a. Soil Preparation

The powdered dry kaolinite is deposited, forming approximately 2-inch deep layers in the batching reservoir. Each layer is sprinkled with sufficient water to bring the soil to the desired water-content. The water is allowed to soak in and the following lift is added. The moist soil is left to cure for one week; it is then removed and placed in polythene bags where it is allowed to equilibrate for another three or four days. The above procedure results in a mixture with very uniform moisture conditions in the range of 53.5% ± 1%.

b. Test Sample Preparation

The removable lucite side wall of the sample holder is taken off and the inside of the bin is coated with vaseline. The soil is placed in small lumps, tamped and vibrated in one-inch lifts.

After the replacement of the second soil layer, a template is pushed gently against the smoothed soil surface after being aligned and centered along the frame of the sample holder in such a way that the resulting grid pattern and its optical center are co-linear with the optical axis of the x-ray tube when the sample is set in the test bed. When the template is removed, a network of rhomboids of ½in. side dimension having 14 rows and 7 columns is left imprinted on the soil;

lead markers are then gently pushed in the imprints with tweezers. More layers are added until the sample thickness is slightly above the sample holder rim. The sample is then trimmed by a stretched wire sliding on the edges of the sample holder, the vaseline-coated removable front is clamped in place, and finally the sample holder is placed in position in the soil bin and the top surface is smoothed and levelled.

c. Testing Procedure

The following procedure has been followed in order to complete one soil-wheel test.

(i) An initial x-ray photograph is taken for the undeformed grid within the soil. If it appears that the array has been too severely distorted during sample preparation and subsequent manipulation, the sample is removed and the sample preparation procedure repeated.

(ii) The hydraulic pump is then started and the wheel brought to the starting position. At the same time initial measurements are obtained for the height of the soil surface, relative to the optical center of the grid network, together with setting the zero readings for the six measuring circuits.

(iii) The rheostat control of the electric drive mechanism and the flow control valves are then set to yield approximately the desired slip rate.

(iv) The wheel is lowered onto the soil surface and the hydraulic drive started.

(v) Three x-ray photographs are obtained automatically by triggering three successive micro-switches (Fig. A-3) and a final fifth photograph is obtained of the deformed grid at the end of the test.

A.5 Soil Properties

The soil used in the experiments is pure kaolinite clay with the following engineering properties:

Liquid limit	54.5%
Plastic limit	37.5%
Specific gravity	2.62

Particle size distribution 74% finer than 2 microns.

The grain size distribution curve for the clay is shown in Figure A-7. The complete chemical analysis, by weight, as provided by the supplier, is given as:

SiO_2	47.39%
Al_2O_3	37.94%
K_2O	1.17%
Fe_2O_3	.36%
CaO	.32%
MgO	.18%
Na_2O	.07%
TiO_2	.05%
Loss on ignition	13.02%
	100.50

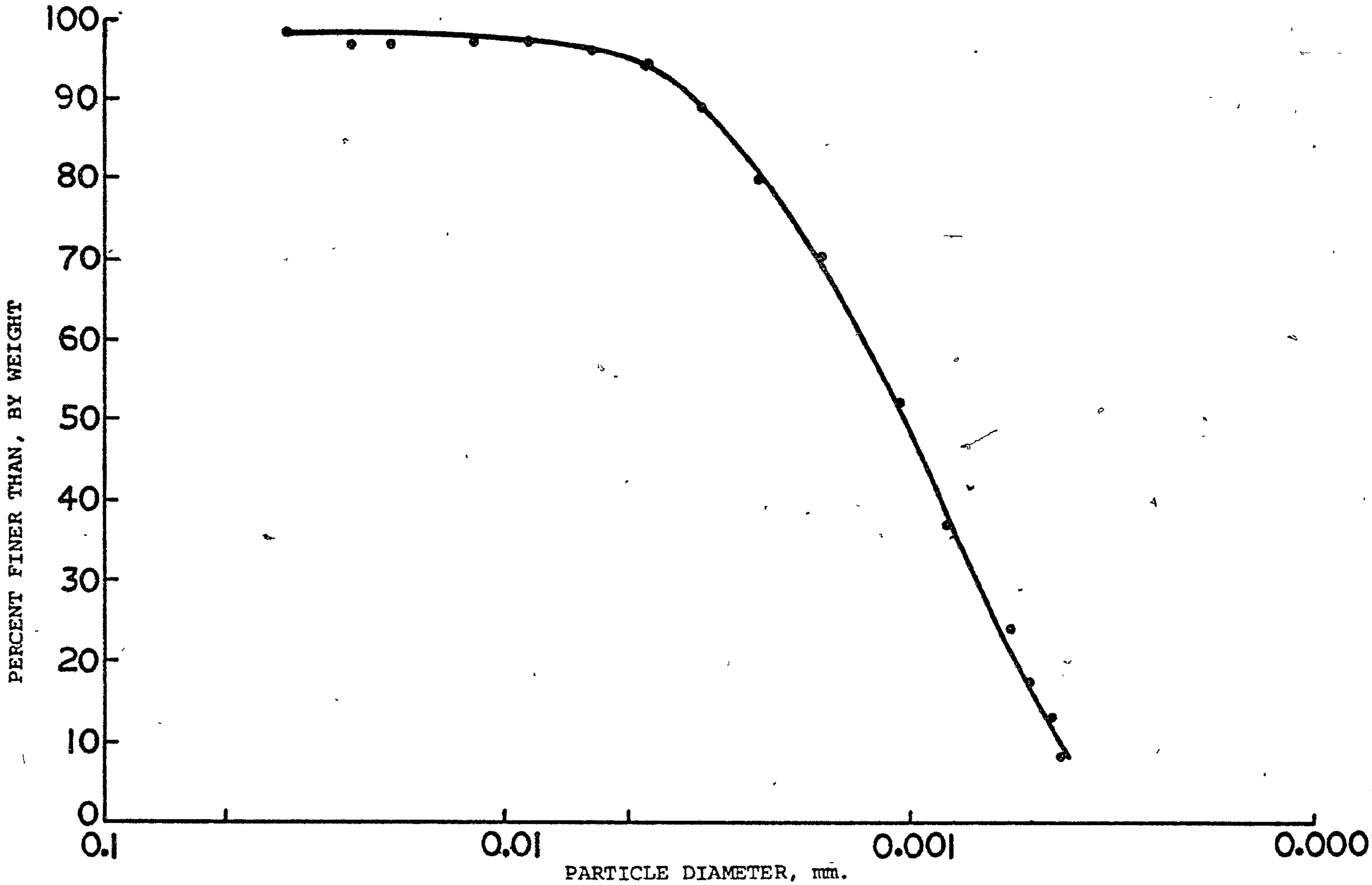

Fig. A-7 Grain Size Distribution for S-187 Clay

An x-ray diffraction, Figure A-8, revealed that the clay was primarily kaolinite (approximately 93% by weight) with some illite (about 7%).

Stress-Strain relation

"True triaxial" tests were performed under plane strain conditions in order to reproduce as closely as possible the assumed conditions during the soil-wheel tests. For this purpose, prismatic samples (2" x 1½" x 4¼") of the same clay were prepared, similar to the clay used for the soil-wheel experiments. The tests were performed at three different cell pressures (0, 2.5, 5 psi) and at axial loading velocities of .1, 1.0 and 2.0 ins/min. The results of the tests have previously been shown as Figure 6.2.

For comparison, similar tests were performed on cylindrical samples in the conventional manner of axisymmetric triaxial tests. These samples were of dimensions 1.4" (diameter) x 3 1/8" (length). The results of the tests have been included in Figure 6.3. The results verified the absence of well-defined failure conditions, i.e. no strain softening behaviour; this result is not due to the plane strain "true triaxial" test restraints. Figure A-9 shows the effect of the loading rate on the shear strength values for the kaolinite clay.

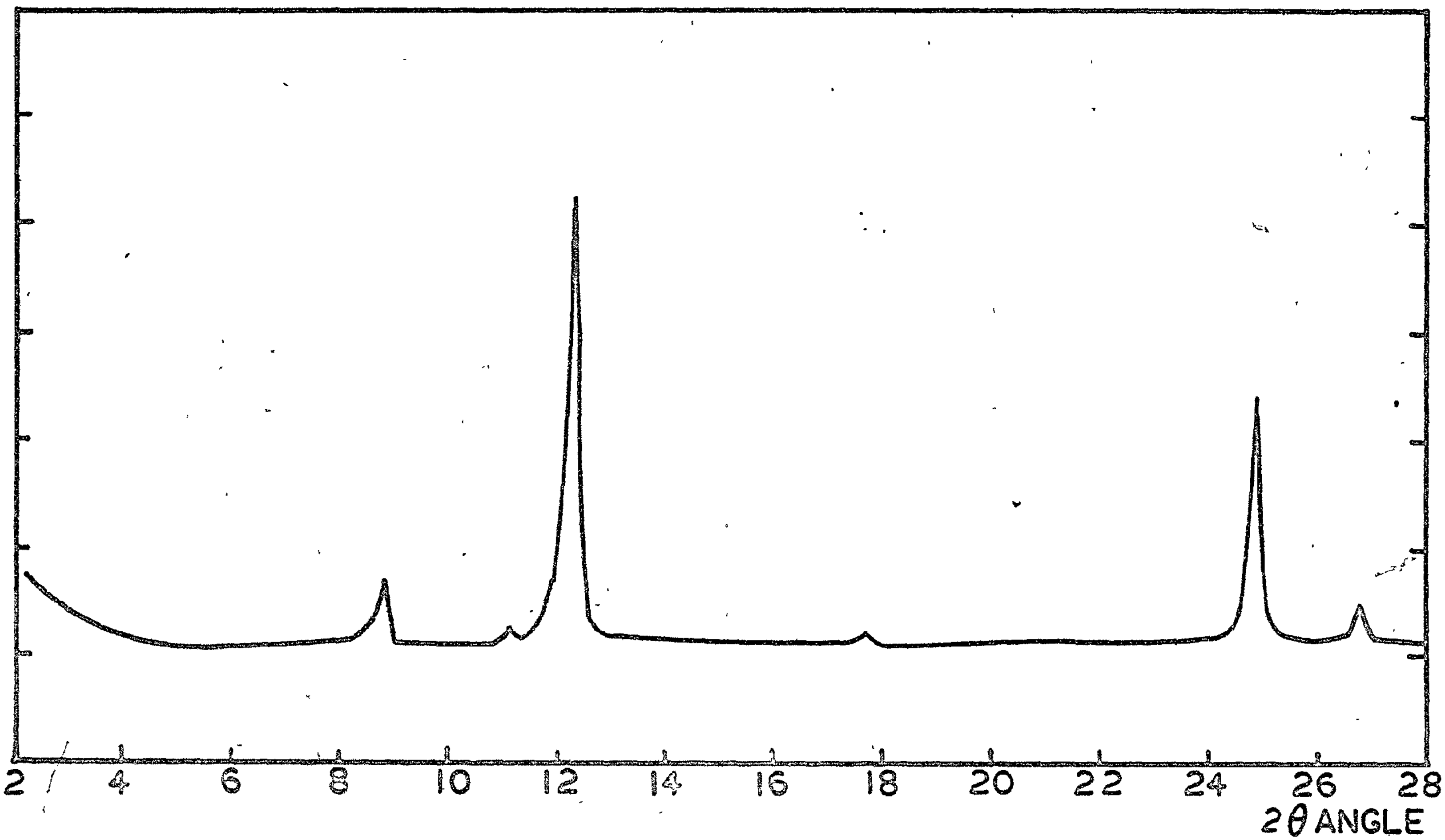

Fig. A-8 X-Ray Diffractogram of Oriented Slide of Kaolinite Clay

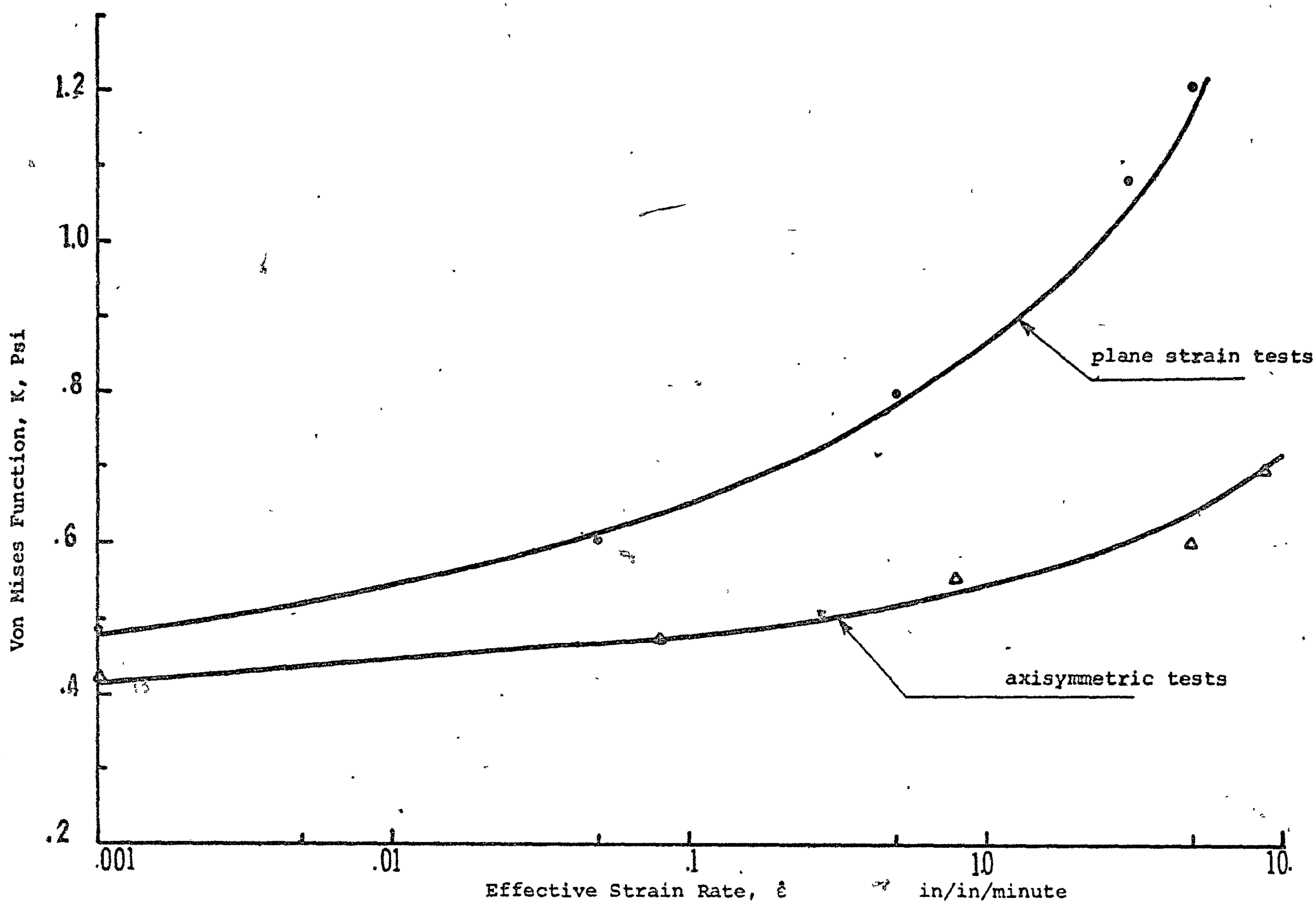

Fig. A-9 Variation of Shear Strength with Effective Strain Rate

DATA REDUCTION TECHNIQUES

There are two types of data that can be collected from soil tests. The first type concerns the surficial measurements such as draw-bar pull, input torque, translational velocity, angular velocity and sinkage. All data concerning the surficial measurements are recorded continuously during the test on an ultra-violet strip chart. The values corresponding to the recorded signals are calculated using calibration charts for every surficial measurement.

The second type of data concerns the behaviour of the soil beneath the moving wheel. The experimentally measured displacement field together with a knowledge of the constitutive relation of the soil, allows the subsoil strains, strain rate, velocities and stresses to be calculated.

For the subsoil behaviour, the methods presented here are somewhat similar to those previously reported by Yong & Fitzpatrick-Nash (1968) and by Yong & Windisch (1969) in that a grid network is used as a means of defining the deformation history of a particle in the soil mass.

B.1 Grid Plotting

As described in Appendix A, radiographic x-ray records are made of the deforming grid during the moving of the wheel on the soil. By superimposing these x-ray plates on to a sheet of paper, the locations of the grid nodes are plotted for five successive wheel positions, representing respectively the undeformed grid plus three subsequent positions at -6, 0 and 6". From the center of the grid the fifth image is then taken after removing the wheel off the soil. The plotted field for each image is a grid 6" x 6" in size. The field consists of 191 node points arranged in a staggered net to form a grid of 7 columns and 14 rows. The superimposed five images provide a complete description of the separate particle trajectories due to the moving of the wheel on the soil (Fig. B-1).

B.2 Determining the Grid Coordinates

The sheet containing the plotted grid points is mounted on an X-Y recorder which is attached to a General Electric Process Control Computer, as shown in Figure B-2. The input voltage, E_i, and the sensitivity of the recorder, in both X and Y directions, are adjusted such that full-scale deflection is obtained when the pen is allowed to cover all the grid points. The adjustment of the potentiometers R_x and R_y permits the operator to place the pen of the recorder at the desired grid point.

The output voltage of the recorder, E_0, forms the input to an Integrating Digital Voltmeter and thence to the computer logic circuits. The voltages thus produced by the X-Y recorder are converted into X and Y

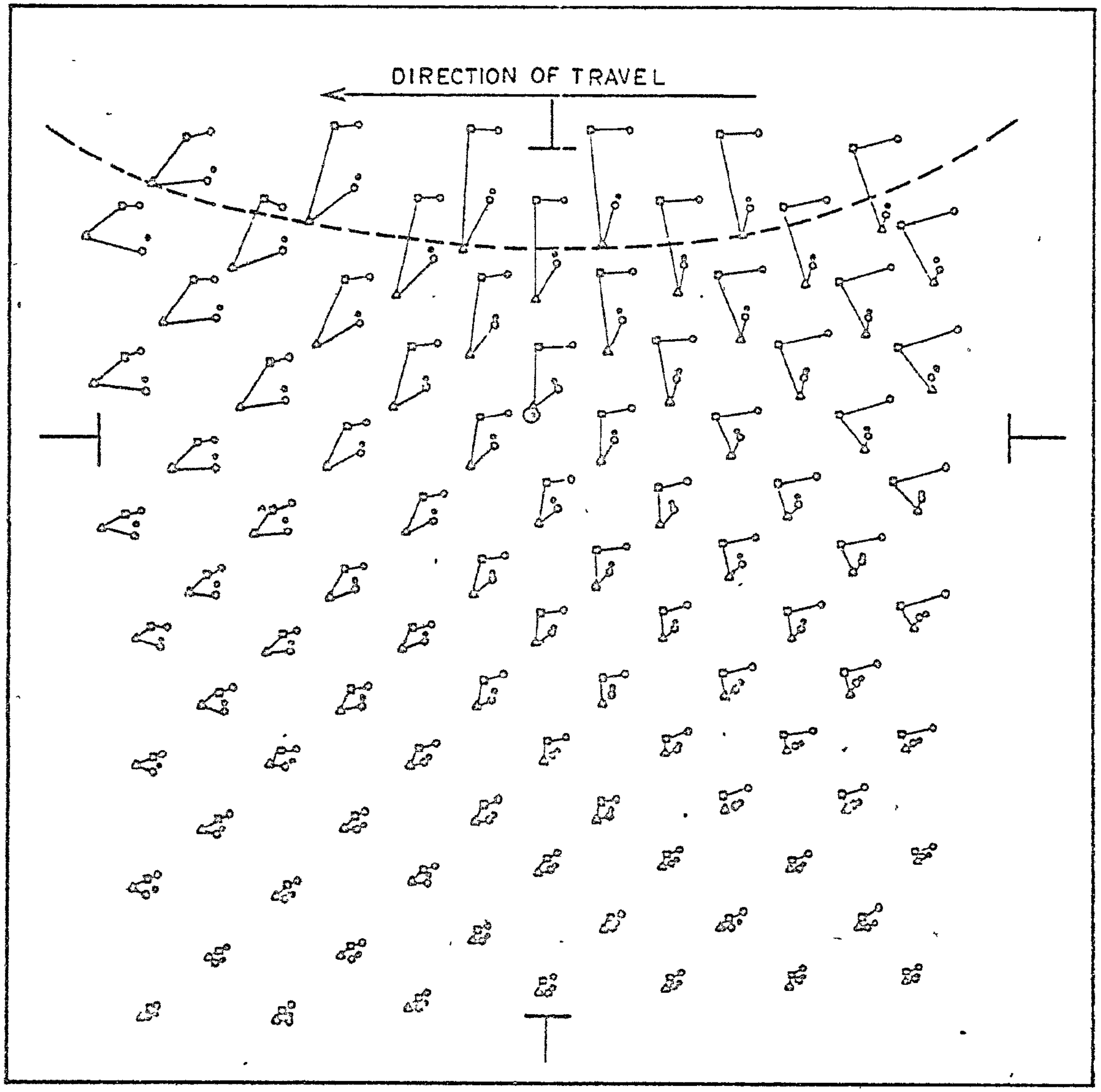

Figure B-1 Trace Motion of Each Marker - Wheel Load 34.0 lbs

Slip 20%

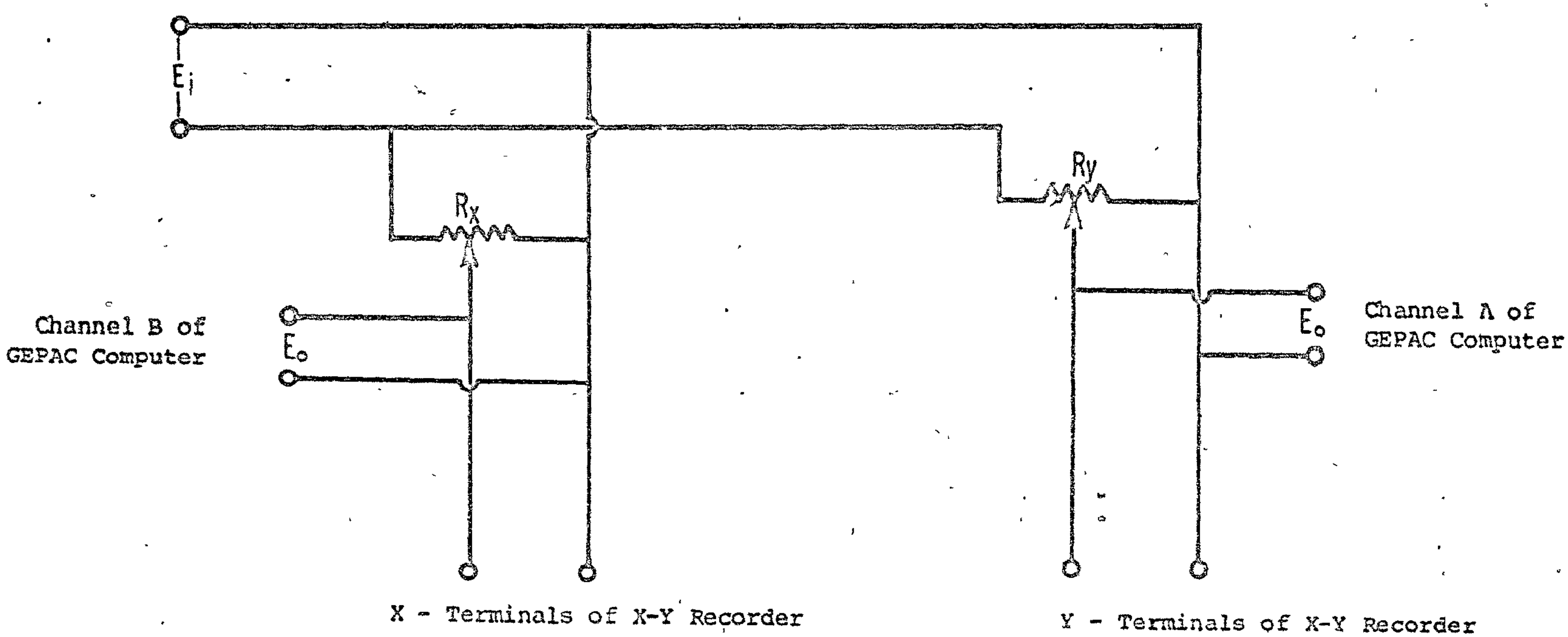

E_i - Variable Input DC Voltage

E_o - Output Voltage

Fig. B-2 Measuring Circuit for Coordinate Location coordinates, expressed in inches, relative to a chosen origin by means of program "25". The coordinates were stored on magnetic tapes then transferred to punched cards by program "TAPE 25".

The punched cards were used by program "VISIOPLAS" as an input data for determining the subsoil behaviour.

B.3 Visioplasticity Technique

This technique is concerned with the analysis of visual results using plasticity theories. It was adopted previously by Yong et al. (1969, 71). In this thesis it is used for the analysis of the x-ray photography of the displacement pattern of the soil beneath a moving wheel.

An x-ray technique is used for recording the positions of embedded lead markers at various times corresponding to various instantaneous positions of the moving wheel, and provides information which can trace the "distortion" motion of each marker. A single continuous grid can be obtained by aligning the images side by side, since the horizontal distances between their optical center for consecutive exposures and x-ray slides are determined. The velocity and displacement calculation can then be made following adjustment of the undeformed and deformed grid coordinates.

a. Grid Adjustments

The calculation of velocity and strain rate components is greatly facilitated by a regular interval between adjacent grid nodes.

Evidently, the method of manually preparing the grid together with soil heterogeneity, results in deviations of the lines from straightness and orthogonality. In order to ensure an orthogonal grid composed of straight lines, the initial undeformed and subsequently deformed grids are subjected to approximate geometrical adjustments as shown in Figure B-3.

The method of approximate geometrical adjustments, as adopted by Windisch (1969), is described in this paragraph.

New undeformed grid coordinates are arbitrarily defined to provide an "adjusted undeformed grid" of regular horizontal and vertical grid lines corresponding roughly to the original grid. The respective displaced positions on the deformed grid are adjusted geometrically.

The following symbols are used in the operations involved in these adjustments.

XI,YI = original undeformed coordinates

XIA,YIA = adjusted undeformed coordinates

XX,YY = original deformed coordinates

XXA,YYA = adjusted deformed coordinates

The adjustment in the abscissa of an undeformed grid point (I,J) is

$$DI = XIA(I,J) - XI(I,J)$$

and constitutes a first adjustment to the corresponding deformed grid point abscissa. The rate of adjusting along row J is

$$C1 = \frac{XIA(I+1,J)-XI(I+1,J)-XIA(I,J)+XI(I,J)}{XI(I+1,J)-XI(I,J)}$$

resulting in a second adjustment to the abscissa of the deformed grid point:

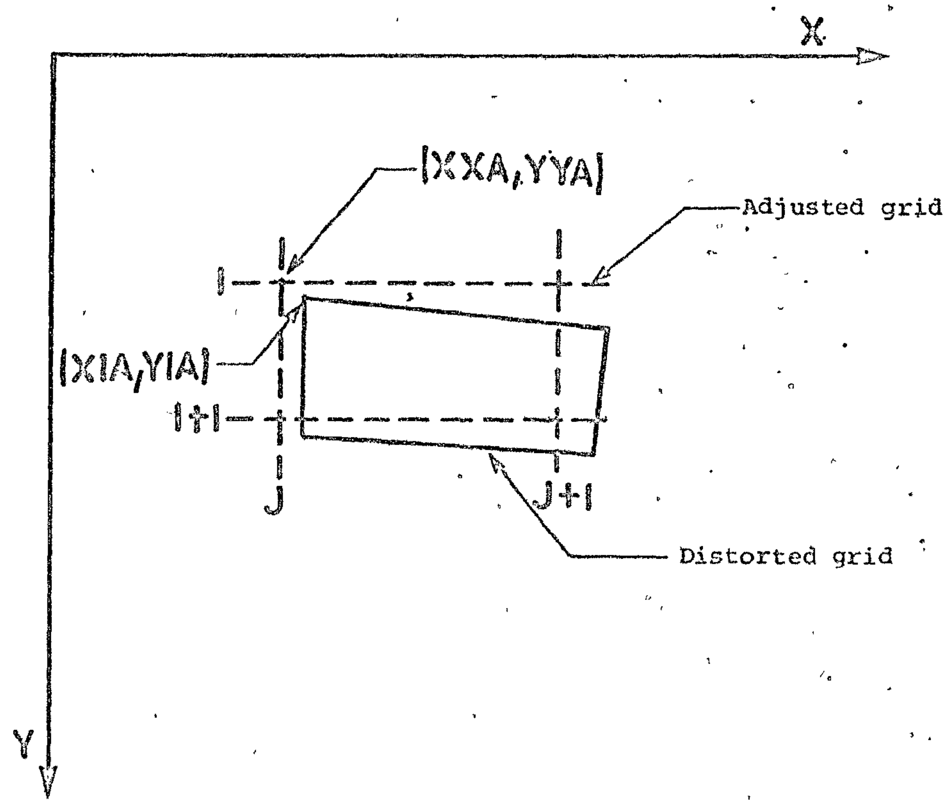

Fig. B-3 Grid Adjustment

$$D2 = [XX(I,J)-XI(I,J)]C1$$

Similarly, the rate of X-adjusting along row J+1 is:

$$C2 = \frac{XIA(I+1,J+1)-XI(I+1,J+1)-XIA(I,J+1)+XI(I,J+1)}{XI(I+1,J+1)-XI(I,J+1)}$$

resulting in the adjustment

$$D'2 = [XX(I,J+1)-XI(I,J+1)]C2$$

A third correction to the abscissa of the deformed grid point is due to vertical adjustment:

$$D3 = (D'2-D)\frac{YY(I,J)-YI(I,J)}{YI(I,J+1)-YI(I,J)}$$

The adjusted abscissa of the deformed grid point (I,J) is finally given by the sum of the above adjustments:

$$XXA(I,J) = XX(I,J)+D1+D2+D3$$

The ordinates of the deformed grid are similarly adjusted. The calculations are performed by the computer program "V1SIOPLS".

b. Displacement, Strain and Strain Rate Analysis

1. Displacement

The displacements along any rows of the grid nodes can be calculated from:

$$XD(I,J) = XXA(I,J)-XIA(I,J)$$

$$YD(I,J) = YYA(I,J)-YIA(I,J)$$

where

XD,YD	particle path coordinates
XIA,YIA	adjusted undeformed grid coordinates
XXA,YYA	adjusted deformed grid coordinates
I,J	column and row indices respectively

2. Velocity Calculations

The velocity components can be computed along any stream line using the following equations:

$$U(I,J) = (XD(I,J)-XD(I-1,J)) * VX/DX$$

$$V(I,J) = (YD(I,J)-YD(I-1,J)) * VX/DX$$

where

U,V	horizontal and vertical velocity components
VX	translational wheel velocity
DX	distance between the adjusted undeformed grid coordinates

3. Strain Rate Components

The strain rate components are defined by

$$\dot{\varepsilon}_x = \frac{\partial U}{\partial X}$$

$$\dot{\varepsilon}_y = \frac{\partial V}{\partial Y}$$

$$\dot{\gamma}_{xy} = \left(\frac{\partial U}{\partial Y} + \frac{\partial V}{\partial X}\right)$$

The actual calculation, carried out by the program "VISIOPLS" (Appendix C) is as follows:

```
EDX(I,J) = (U(I,J)-U(I-1,J))/DX
EDY(I,J) = (V(I,J+1)-V(I,J-1))/DX
GDXY(I,J) = (V(I,J)-V(I-1,J))+(U(I,J+1)-U(I,J-1)))/DX
STRR(I,J) = SQRT((EDX(I,J)**2+EDY(I,J)**2)/2.+
            GDXY(I,J)**2/4.)
```

EDX, EDY, GDXY	Strain rate components
STRR	Second strain rate invariant

The effective strain rate $\bar{\dot{\varepsilon}}$ was obtained from the calculated strain rate components

$$\bar{\dot{\varepsilon}} = \frac{2}{3}\left[(\dot{\varepsilon}_x)^2+(\varepsilon_y)^2-\dot{\varepsilon}_x\dot{\varepsilon}_y+\frac{3}{4}(\dot{\gamma}_{xy})^2\right]^{\frac{1}{2}}$$

4. Strain Components

Strain components are obtained by integrating the strain rate components with respect to time by using Simpson's rule.

$$\varepsilon = \int_{to}^{t} \dot{\varepsilon}dt$$

$$\varepsilon(I,J) = \frac{DX}{3VX}\left[\dot{\varepsilon}(I-2,J)+4\dot{\varepsilon}(I-1,J)+2\dot{\varepsilon}(I,J)+ 4\dot{\varepsilon}(I+1,J)+2\dot{\varepsilon}(I+2,J)\right]$$

The "effective strain" $\bar{\varepsilon}$ can be obtained from the strain components by using the following formula

$$\bar{\varepsilon}(I,J) = \frac{2}{3}\left[\varepsilon_x(I,J)^2+\varepsilon_y(I,J)^2-\varepsilon_x(I,J)*\varepsilon_y(I,J)+\frac{3}{4}\gamma_{xy}(I,J)^2\right]^{\frac{1}{2}}$$

5. Volume Change

The volume change is determined along the marker rows by calculating the change in each area surrounded by four marker positions as shown in Figure B-4. Applying the principle of conservation of mass,

$$\rho_1 A_1 = \rho_2 A_2$$

$$\frac{\rho_{i1}}{\rho_{i2}} = \frac{A_{i2}}{A_{i1}}\ .$$

where

ρ_{i1} = is the mass density or specific mass of the i^{th} element before deformation.

A_{i1} = is the area of the i^{th} element before deformation.

ρ_{i2} = is the mass density or specific mass of the i^{th} element after deformation.

A_{i2} = is the area of the i^{th} element after deformation.

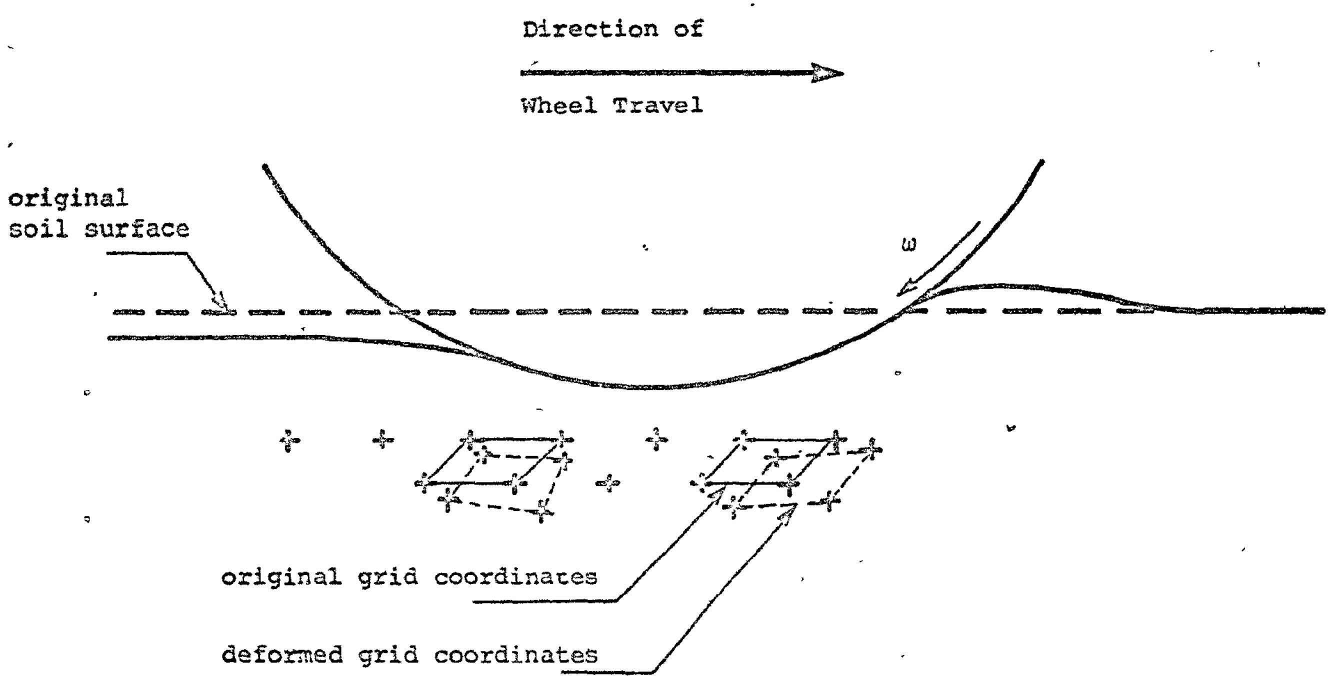

Fig. B-4 Calculation of Volume Change

B-4 LISTING OF PROGRAM "25"

```
JOB,START=10322
JOB,REMOVE,25
JOB,COMPILE,25,NOLIST
C
C
C       WHEN THE PROGRAM IS STARTED .  THE USER IS GIVEN THE OPTION
C       OF STARTING A NEW RUN OR CONTINUING AN OLD RUN
C
C       THE PROGRAM IS FAIL-SAFE.  DATA IS WRITTEN TO DISC AFTER
C       EVERY POINT ENTRY
C
C       A BUTTON PUSH WITH SW17 UP MEASURES A COORDINATE PAIR
C       IF SW16 IS NOT DOWN THAT PAIR IS PRINTED
C
C.      A BUTTON PUSH WITH SW17 DOWN GIVES THE USER 4 OPTIONS
C
C       NOP   IGNORES THE BUTTON PUSH
C       FINI    TRIGGERS THE CALCULATIONS AND REPORT
C       STOP    STOPS THE PROGRAM ALLOWING THE USER TO CONTINUE
C                 AT A LATER TIME
C       BACK    ALLOWS THE USER TO BACKSPACE   IT CALLS FOR THE
C            NEW INDICES  I,J  FOR  VW(I,J)  AND  VW(I+1,J)
C            I  MUST BE AN ODD NUMBER
C
C
C       THE PROGRAM RINGS THE I-O DEVICE BELL AFTER EACH 10 POINTS
C
C
        LOGICAL ISSW
        DIMENSION J(10),W(196,5),VW(196,5),RES(3)
        DIMENSION XC(7 ,14,5),YC(7 ,14,5)
        DATA IBELL /001603467/
        IP=IX7X
        IR=IX6X
        CALL AC1
        NU=IX5X
C
  1100  CALL MSGTYP(IP,16,16HNEW RUN=0,CONT=1 )
        K=IREPLY(IR,10,I)
       .GO TO (1110,1100,1160,9999),I
C
  1110  IF(K NE 0)  GO TO 1130
C
        DO 1120 JD=1,5
       DO 1120 ID=1,196
        W(ID,JD)=0
  1120  VW(ID,JD)=0.
C
        ID=-1
        JD=1
```

FATTAH

```
      C
            GO TO 7000
      C
            ENTER PAL
      $1130 SPB DTRC02
            LDK XFERIN
            SPB DELC30
      *
            LEAVE PAL
      C
       1200 WRITE(IP,1)   ID,JD,VW(ID,JD),VW(ID+1,JD)
          1 FORMAT(1X,10HLAST POINT,2I4,2F10 4)
            GO TO 2100
      C
       2000 IF( NOT ISSW(17))  GO TO 3000
       2100 CALL MSGTYP(IP,26,26HNOP=0,FINI=1,STOP=2,BACK=3)
            K=IREPLY(IR,10,I)
            GO TO (2110,2100,2100,9999),I
       2110 IF(K EQ 0)  GO TO 7000
            IF(K EQ 1)  GO TO 9000
            IF(K EQ 2)  GO TO 9999
            IF(K NE 3)  GO TO 2100
      C
       2200 CALL MSGTYP(IP,7,7HENTER I)
            ID=IREPLY(IR,10,I)
            GO TO (2210,2200,2200,9999),I
       2210 IF((ID LT 1) OR (ID GT 196))  GO TO 2200
      C
       2220 CALL MSGTYP(IP,7,7HENTER J)
            JD=IREPLY(IR,10,I)
            GO TO (2230,2220,2220,9999),I
       2230 IF((JD LT 1) OR (JD GT 5))  GO TO 2220
      C
            ID=ID-2
            IF(ID GT 0)  GO TO 1200
            ID=1
            JD=JD-1
            GO TO 1200
      C
       3000 ID=ID+2
            IF(ID LE 196)  GO TO 3050
            ID=1
            JD=JD+1
       3050 IF(JD LE 5)  GO TO 3100
            CALL MSGTYP(IP,11,11H 490 POINTS)
            GO TO 7000
      C
       3100 CALL SCNB(SCWD,RES)
            VW(ID,JD)=RES(1)
            VW(ID+1,JD)=RES(2)
```

FATTAH

```
          IF( NOT ISSW(16)) WRITE(IP,2)  ID,JD,RES(1),RES(2)
        2 FORMAT(1X,2I4,2F10 4)
          K = MOD(ID,14)
          IF(K EQ 13)  CALL MSGTYP(IP,1,IBELL)
C
          ENTER PAL
*
          SPB DTRC02
          LDK XFR
          SPB DELC30
*
*
$7000     LDX NU,5
          LDX IR,6
          LDX IP,7
          SPB AC4
          LDA PRIONO
          IAI
          STA XNTP00
          SPB FIXC03
          SPB OFFC01
          PRG 0,0,0,*+1,0
          LDZ
          STA XNTP00
          PAI
          SPB AC3
          BRU $2000
          LEAVE PAL
C
 9000     CONTINUE
          IP2=7
          JS = 1
          A = 8 186/(VW(43,JS) - VW(15,JS))
          B = 8 28/(VW(100,JS) - VW(72,JS))
          READ(IR,21)J4
       21 FORMAT(A3)
          DO 202 JS=1,5
          DO 202 I = 1,195,2
          W(I,JS)=VW(I,JS)*A
      202 CONTINUE
          DO 203 JS=1,5
          DO 203 I=2,196,2
          W(I,JS)=VW(I,JS)*B
      203 CONTINUE
          WRITE(IP2,47)J4
       47 FORMAT(//////////1H ,10X,19HPLOTTED COORDINATES,30X,7HTEST NO,1)
         13)
      140 JS=1
      143 JC=1
          IM=0
```

FATTAH

```
      144 IC=1
      145 I =IM + (IC*2)-1
          I1=I+1
          XC(IC,JC,JS)=W(I,JS)
          YC(IC,JC,JS)=W(I1,JS)
          IC=IC+1
          IF(IC- 7) 145,145,146
      146 IM=IM+14
          JC=JC+1
          IF(JC-14) 144,144,147
      147 JS=JS+1
          IF(JS-5)143,143,150
      150 IF(ISSW(12))GO TO 205
      160 DO 205 JS=1,5
          WRITE(IP2,175)JS
      175 FORMAT(1H0,50X,8HIMAGE NO,I2,1H0,50X,12H------------)
          DO 190 JC=1,14
          WRITE(IP2,180)JC,(XC(IC,JC,JS),IC=1,7 )
      180 FORMAT(1H0,3HROW,I3,3X,1HX,7 F7 3)
          WRITE(IP2,185)(YC(IC,JC,JS),IC=1,7)
      185 FORMAT(/1H ,9X,1HY,7 F7 3)
      190 CONTINUE
      205 CONTINUE
C
           ENTER PAL
           SPB DTRC02
           LDK XFER
           SPB DELC30
           LEAVE PAL
C
      9999 CALL AC2
           STOP
C
           ENTER PAL
BLKAD      EQL /3623000
BUF        EQL /2000
*
XFR        DEL 1,BLKAD
           FOR 0,BUF
           DEL 0,VW
XFERIN     DEL 0,BLKAD
           FOR 0,BUF
           DEL 0,VW
XFER       DEL 1,BLKAD
           FOR 0,BUF
           DEL 0,W
W          BSS 980
           CON D,-1
           CON D,1
           BSS 42
```

FATTAH

```
VW       BSS 980
ID       BSS 1
JD       BSS 1
         BSS 42
SCWD     CON 0,00336007
         CON 0,00336010
         CON D,-1
DELC30   LIB
AC3      LIB
AC4      LIB
         LEAVE PAL
         END
JOB,RELEASE,25
JOB,LJV
025,10322
JOB,END
```

B-5 LISTING OF PROGRAM "TAPE 25"

```
      DIMENSION BUF(1400)
      J = 1
  101 READ(8.3.END =999.ERR=998)
    3 FORMAT(64A3)
      READ(8.1,END=999.ERR=998)BUF
    1 FORMAT((8(64A3)))
      DO 100 I =1.980
  100 BUF(I)=AEGPAC(BUF(I))
      N=1
   27 NN=N+12
      WRITE(6.2)(BUF(I).I=N.NN.2)
      WRITE(7.2)(BUF(I).I=N.NN.2)
      M = N + 1
      MM = NN + 1
      WRITE(6.2)(BUF(I).I=M.MM.2)
      WRITE(7.2)(BUF(I).I=M.MM.2)
    2 FORMAT(7F8.3)
      WRITE(6.4)
    4 FORMAT(1H0)
      N = N + 14
       IF(N - 967)27.27.28
   28 CONTINUE
       J = J + 1
  999 IF(J.LE.4)GO TO 101
      STOP
  998 STOP 1
      END
```

```
*OPTIONS IN EFFECT*  NOTERM,ID,EBCDIC,SOURCE,NOLIST,NODECK,LOAD,NOMAP,NOTEST
*OPTIONS IN EFFECT*  NAME = MAIN     , LINECNT =          56
*STATISTICS*     SOURCE STATEMENTS =        27,PROGRAM SIZE =       6574
*STATISTICS*  NO DIAGNOSTICS GENERATED
```

```
001                     FUNCTION AEGPAC(N)
                C
                C          CONVERTS 24 BIT GEPAC FLOATING POINT TO 32 BIT IBM FLOA
                C          THE RETURNED VARIABLE IS REAL
                C
002                     DATA L17/131072/
003                     DATA L24/16777216/
004                     DATA L26/67108864/
005                     DATA L30/1073741824/
                C
006                     IF(N) 1,2,2
007                   1 NEG = 1
008                     M =(N + L30*2)/256
009                     GO TO 3
010                   2 NEG = 0
011                     M = N/256
012                   3 M17 = M/L17
013                     I = 16*2**MOD(M17+3,4)
014                     J = ((MOD(M17,64)+ 32)*L26)/L26
015                     IF(J.GT.0) J = J + 3
016                     J = (J/4)*L24 + MOD(M,L17)*I + L30
017                     CALL SWMDE(X,J)
018                     IF(NEG.EQ.1) X = -X
019                     AEGPAC = X
020                     RETURN
021                     END

*OPTIONS IN EFFECT*  NOTERM,ID,EBCDIC,SOURCE,NOLIST,NODECK,LOAD,NOMAP,NOTEST
*OPTIONS IN EFFECT*  NAME = AEGPAC  , LINECNT =        56
*STATISTICS*     SOURCE STATEMENTS =        21,PROGRAM SIZE =       768
*STATISTICS*  NO DIAGNOSTICS GENERATED
```

```
)01                 SUBROUTINE SWMDE(I,J)
            C
            C        THIS SUBROUTINE IS USED TO DEFEAT THE IMPLICIT CHANGE OF
            C        MODE IN THE STATEMENT    X = J
            C
)02                 I = J
)03                 RETURN
)04                 END

*OPTIONS IN EFFECT*  NOTERM,ID,EBCDIC,SOURCE,NOLIST,NODECK,LOAD,NOMAP,NOTEST
*OPTIONS IN EFFECT*  NAME = SWMDE    , LINECNT =       56
*STATISTICS*     SOURCE STATEMENTS =       4,PROGRAM SIZE =       302
*STATISTICS*  NO DIAGNOSTICS GENERATED

*STATISTICS*  NO DIAGNOSTICS THIS STEP
```

VISIOPLASTICITY

The behaviour of soil under a moving rigid wheel is determined by the visioplasticity technique. The governing equations for the technique were explained in Chapter 4 and Appendix B. A program based on this approach was developed to determine from the five x-ray photographs of the embedded lead markers the soil particle path, velocity, strain, strain rate, direction of the principal strain rate and deformation energy contours. The following identifiers are used in the program.

Identifier	Definition
XI(,)	Undeformed grid coordinates-X
YI(,)	Undeformed grid coordinates-Y
XX(,)	Deformed grid coordinates-X
YY(,)	Deformed grid coordinates-Y
XIA(,)	Adjusted undeformed grid coordinates-X
YIA(,)	Adjusted undeformed grid coordinates-Y
XXA(,)	Adjusted deformed grid coordinates-X
YYA(,)	Adjusted deformed grid coordinates-Y
XD( )	Particle path coordinates-X
YD( )	Particle path coordinates-Y
U( )	Horizontal velocity components
V( )	Vertical velocity components
AREA(,)	Area of the quadrilateral element surrounded by four adjacent markers

EDX(,)	Strain rate -X component
EDY(,)	Strain rate -Y component
GDXY(,)	Strain rate -XY component
STRR(,)	Second strain rate invariant
STRX(,)	Strain component -X
STRY(,)	Strain component -Y
STRXY(,)	Deformation energy
W (,)	Principal strain rate direction
NT	Test number
WL	Wheel load
WD	Wheel diameter
WW	Wheel width
VX	Translational wheel velocity
OMEGA	Angular wheel velocity
Y (,)	Coordinates of wheel-soil contact point with respect to x-ray optical center
SOSFD	Ratio of source-object distance and source-film distance
A2	Soil shear strength

C-1 LISTING OF PROGRAM "VISIOPLS"

```
C
C             UNDEFORMED AND DEFORMED AND DEFORMED COORDINATES
C
C             READ AND PRINT TEST NUMBERAND WHEEL PARAMETERS
C
C
      DIMENSION XB(7,14,5),YB(7,14,5),XE(7,14,5),YE(7,14,5)
      DIMENSION YYA(30,14),AREA(30,14),DEN(30,14),DE(30,14)
      DIMENSION XC(7,14,5),YC(7,14,5),XI(30,14),YI(30,14),XX(30,14)
     1 ,YY(30,14),XIA(30,14),YIA(30,14),XXA(30,14),XD(30,14),YD(30,14)
      DIMENSION U(30,14),V(30,14),EDX(30,14),EDY(30,14),GDXY(30,14),
     1 STRR(30,14),STRX(30,14),STRY(30,14),GXY(30,14),STRXY(30,14),
     1 W(30,14)
      DO 1111 IJKL =1,1
C             INITILIZATION
      DO 14 J = 1,14
      DO 14 I = 1,30
      XI(I,J) = 0.
      YI(I,J) =0.
      XXA(I,J) = 0.
      YYA(I,J) = 0.
      XIA(I,J) = 0.
      YIA(I,J) = 0.
      AREA(I,J) = 0.
      XD(I,J) = 0.
      YD(I,J) = 0.
      U(I,J) = 0.
      V(I,J) = 0.
      EDX(I,J) = 0.
      EDY(I,J) = 0.
      GDXY(I,J) = 0.
      STRR(I,J) = 0.
      DE(I,J) = 0.
      DEN(I,J) = 0.
      STRX(I,J) = 0.
      STRY(I,J) = 0.
      GXY(I,J) = 0.
      STRXY(I,J) = 0.
      W(I,J) = 0.
   14 CONTINUE
      WRITE(6,105)
      READ (5,103)NT,WL,WD,WW,VX,OMEGA
  103 FORMAT(I5,5F12.9)
      WRITE(6,100)NT,WL,WD,WW,VX,OMEGA
  100 FORMAT(1H0,10X,I5,5X,5F15.9)
  105 FORMAT(1H0,5X,' TEST NO       WHEEL LOAD      WHEEL DIAM    WHEEL WID
     1 TH     TRANSL VEL     ANGULAR VEL '/)
C
C             READ WHEEL SOIL CONTACT POINT COORDINATES AT IMAGE NO 3
C             AND THE RATIO BETWEEN S.C.D/S.F.D
C
      READ(5,111)Y,A,SCSFD,A2
  111 FORMAT(4F12.9)
      WRITE(6,110) Y,A,SCSFD ,A2
```

```
  110 FORMAT(1HC,5X,'WHEEL COORDINATES',2F15.9,'SCD/SFD =',F15.9,'K',
     1F15.9)
C
C
C               READ MARKERS COORDINATES
C
         DO 10 JS = 1,5
      DO 10 JC = 1,14
      READ(5,5)(XB(I,JC,JS),I=1,7)
      READ(5,5)(YB(I,JC,JS),I=1,7)
   10 CONTINUE
      DO 11 JS = 1,5
      DO 11 JC = 1,14
      JJ = 15 - JC
      DO 11 I = 1,7
      XE(I ,JJ,JS) = XB(I,JC,JS)
      YE(I ,JJ,JS) = YB(I,JC,JS)
   11 CONTINUE
    5 FORMAT(7F8.3)
C
C               TRUE COORDINATES OF THE MARKERS
      DO 20 JS = 1,5
      DO 20 JC = 1,14
      DO 20 I = 1,7
      XC(I,JC,JS) = (XE(I,JC,JS) -XE(1,5 ,1))*SCSFD
      YC(I,JC,JS) = (YE(I,JC,JS) -YE(1,5 ,1))*SCSFD
   20 CONTINUE
      DO 18 JS = 1,5
      DO 18 JC = 1,14
      WRITE(6,5)(XB(I,JC,JS),I=1,7)
      WRITE(6,5)(YB(I,JC,JS),I=1,7)
   18 CONTINUE
      DO 21 JS = 1,5
      DO 21 JC = 1,14
      WRITE(6,5)(XE(I,JC,JS),I=1,7)
      WRITE(6,5)(YE(I,JC,JS),I=1,7)
   21 CONTINUE
       DO 19 JS = 1,5
      DO 19 JC = 1,14
      WRITE(6,5)(XC(I,JC,JS),I=1,7)
      WRITE(6,5)(YC(I,JC,JS),I=1,7)
   19 CONTINUE
C
C               CONTINUOUS UNDEFORMED AND DEFORMED GRID COORDINATES
C
      JC = 1
  244 B = 12.
      I = 1
      JS = 1
  245 IC = 2
  250 XI(I,JC) = XC(IC,JC,JS) - (A + B)
      YI(I,JC) = Y-YC(IC,JC,JS)
      IC = IC + 1
      I = I + 1
```

```
      IF (IC - 7) 250,250,255
  255 B = 6.
      IF(I - 12)245,245,260
  260 B = 0.
      IF(I - 18)245,245,265
  265 B = -6.
      IF(I - 24) 245,245,270
  270 B = -12.
      IF(I - 30) 245,245,275
  275 JC = JC + 1
      IF(JC - 14) 244,244,276
  276 WRITE(6,280)
  280 FORMAT(1H1,'UNDEFORMED GRID COORDINATES'//)
      DO 287 JC = 1,14
  282 WRITE(6,283)JC
  283 FORMAT(1H0,3X,'ROW NO',I3)
      IM = 1
  284  IMM = IM + 9
      WRITE(6,285)(XI(I,JC),I=IM,IMM)
  285 FORMAT(1H0,'X',10X,10F10.3)
      WRITE(6,295)(YI(I,JC),I=IM,IMM)
  295 FORMAT(1H0,'Y',9X,10F10.3)
      IM = IM + 10
      IF(IM - 31)284,287,287
  287 CONTINUE
      DO 305 JC = 1,14
  297 B = 12.
      JS = 1
      I = 1
  299 IC = 2
  300 XX(I,JC) = XC(IC,JC,JS) -(A+B)
       YY(I,JC) = Y -YC(IC,JC,JS)
      IC = IC +1
      I = I + 1
      IF(IC - 7)300,300,301
  301 IF(I - 12) 306,306,302
  306 B = 6.
      JS = 2
      GO TO 299
  302 IF(I - 18) 307,307,303
  307 B = 0.
      JS = 3
      GO TO 299
  303 IF(I - 24)308,308,304
  308 B = -6.
      JS = 4
      GO TO 299
  304 IF(I - 30)309,309,305
  309 B = -12.
      JS = 5
       GO TO 299
  305 CONTINUE
      WRITE(6,340)
  340 FORMAT(1H1,'DEFORMED GRID COORDINATES'//)
```

```
      DO 370 JC = 1,14
  344 WRITE(6,345)JC
  345 FORMAT(1H0,3X,'ROW NO',I3)
      IM = 7
  349 IMM = IM + 11
      WRITE(6,350)(XX(I,JC),I=IM,IMM)
  350 FORMAT(1H0,'X',10X,12F8.3)
      WRITE(6,365)(YY(I,JC),I=IM,IMM)
  365 FORMAT(1H0,1X,'Y',9X,12F8.3)
      IM = IM + 12
      IF(IM - 31)349,370,370
  370 CONTINUE
C
C                ADJUSTED DEFORMED AND UNDEFORMED GRID COORDINATES
C
      DO 117 J = 1,14,2
      X = -14.5
      DO 117 I = 1,30
      XIA(I,J) = X
      X = X + 1.
  117 CONTINUE
      DO 120 J = 2,14,2
      X = -14.
      DO 120 I = 1,30
      XIA(I,J) = X
      X = X + 1.
  120 CONTINUE
      Y = 0.
      DO 130 J = 1,14
      Y = Y + .5
      DO 130 I = 1,30
      YIA(I,J) = Y
  130 CONTINUE
      J = 1
      J2 = J + 2
  131 DO 140 I = 7,29
      II = I + 1
      D1 = XIA(I,J) -  XI(I,J)
      D2 = XIA(II,J)-XI(II,J) - XIA(I,J) + XI(I,J)
      D3 = XI(II,J) - XI(I,J)
      IF(D3 - 0.)133,132,133
  132 D4 = 0.
      GO TO 134
  133 D4 = (XX(I,J) - XI(I,J))/D3
  134 D5 = XIA(II,J2) - XI(II,J2) -XIA(I,J2) +XI(I,J2)
      D6 = XI(II,J2) - XI(I,J2)
      IF(D6 - 0.)136,135,136
  135 D7 = 0.
      GO TO 137
  136 D7 = (XX(I,J) -XI(I,J))/D6
  137 D8 = YI(I,J2) - YI(I,J)
      IF(D8 - 0.)139,138,139
  138 D9 = 0.
      GO TO 140
```

```
139 D9 = (YY(I,J) - YI(I,J))/D8
140 XXA(I,J) = XX(I,J) + D1+D2*D4 + (D5*D7 -D2*D4)*D9
    J = J + 1
    J2 = J + 2
    IF(J - 12)131,131,145
145 DO 154 J = 1,12
    J2 = J + 2
    DO 154 I = 7,29
    II = I + 1
    D1 = YIA(I,J) -YI(I,J)
    D2 = YIA(I,J2) -YI(I,J2) -YIA(I,J) + YI(I,J)
    D3 = YI(I,J2)-YI(I,J)
    IF(D3 - 0.)147,146,147
146 D4 = 0.
    GO TO 148
147 D4 = (YY(I,J) - YI(I,J))/D3
148 D5 = YIA(II,J2) - YI(II,J2) - YIA(II,J) + YI(II,J)
    D6 = YI(II,J2) - YI(II,J)
    IF(D6 - 0.)150,149,150
149 D7 = 0.
    GO TO 151
150 D7 = (YY(I,J) - YI(I,J))/D6
151 D8 = XI(II,J) - XI(I,J)
    IF(D8 - 0.)153,152,153
152 D9 = 0.
    GO TO 154
153 D9 = (XX(I,J) - XI(I,J))/D8
154 YYA(I,J) = YY(I,J) + D1 + D2*D4 +(D5*D7 -D2*D4)*D9
    I = 30
    DO 155 J = 1,12
    XXA(I,J) = XX(I,J)+XIA(I,J) - XI(I,J)
155 YYA(I,J) = YY(I,J) + YIA(I,J) - YI(I,J)
    DO 157 J = 13,14
    DO 157 I =1,30
    XXA(I,J) = XX(I,J) + XIA(I,J) -XI(I,J)
    YYA(I,J) = YY(I,J) + YIA(I,J) - YI(I,J)
157 CONTINUE
    WRITE(6,200)
200 FORMAT(1H1,'ADJUSTED UNUNDEFORMAE GRID'/,'----------------------'/)
    DO 206 J = 1,14
    WRITE(6,314)J
314 FORMAT(1H0 , 'ROW NO',I3)
     IM = 1
203 IMM = IM + 9
    WRITE(6,204)(XIA(I,J),I=IM,IMM)
204 FORMAT(1H0,'X',10X,10F10.3)
    WRITE(6,205)(YIA(I,J),I=IM,IMM)
205 FORMAT(1H0,1X,'Y',9X,10F10.3)
    IM = IM + 10
    IF(IM - 31)203,206,206
206 CONTINUE
    WRITE(6,221)
221 FORMAT(1H1,'ADJUSTED DEFORMED GRID',/'----------------------'/)
     DO 227 J = 1,14
```

```
      WRITE(6,223)J
  223 FORMAT(1HC,'X','ROW NC',I3)
      IM = 7
  224 IMM = IM + 7
      WRITE(6,225)(XXA(I,J),I=IM,IMM)
  225 FCRMAT(1HC,'X',10X,8F10.3)
      WRITE(6,226)(YYA(I,J),I=IM,IMM)
  226 FORMAT(1HC,1X,'Y',9X,8F10.3)
      IM = IM + 8
      IF(IM - 31)224,227,227
  227 CONTINUE
      WRITE(6,113)NT
  113 FORMAT(1H1,10X,'AREA  REL.DENS',72X,'TEST NC',I5,//)
      DO 216 J = 1,13
       DO 216 I = 7,29
      AREA(I,J) = (ABS((XXA(I,J+1)-XXA(I,J))*(YYA(I+1,J+1) -YYA(I,J))
     1 -(XXA(I+1,J+1) -XXA(I,J))*(YYA(I,J+1)-YYA(I,J)))
     1 + ABS((XXA(I+1,J) -XXA(I,J))*(YYA(I+1,J+1)-YYA(I,J)) -
     1 (XXA(I+1,J+1) - XXA(I,J))*(YYA(I+1,J) -YYA(I,J))))/2.
  216 DEN(I,J) = 2.*AREA(I,J)
C
C              PARTICAL PATH AT .5INC DEPTH INTERVAL
C
      DO 850 JJ = 1,14
      XD(1,JJ) = C.
      YD(1,JJ) = C.
      XD(2,JJ) = XXA(7,JJ) - XIA(7,JJ)
      YD(2,JJ) = YYA(7,JJ) -YIA(7,JJ)
      DC 115 I = 3,24
      I1 = I - 1
      I2 = I + 6
      I3 = I + 5
      XD(I,JJ)=XD(I1,JJ)+XXA(I2,JJ)-XIA(I2,JJ)-XXA(I3,JJ)+XIA(I3,JJ)
  115 YD(I,JJ)=YD(I1,JJ)+YYA(I2,JJ)-YIA(I2,JJ)-YYA(I3,JJ)+YIA(I3,JJ)
      WRITE(6,913)JJ
  913 FORMAT(1H0,'ROW NC',I3/)
      WRITE(6,109)
  109 FORMAT(1HC,'PARTICLE PATH CCORDINATES'/,'----------------------'/)
      IM = 1
  750 IMM = IM + 7
      WRITE(6,121)(XD(I,JJ),I=IM,IMM)
  121 FORMAT(1HC,'X',10X,9F10.3)
      WRITE(6,123)(YD(I,JJ),I=IM,IMM)
  123 FORMAT(1HC,2X,'Y',8X,9F10.3)
      IM = IM + 8
      IF(IM - 17)750,750,850
  850 CONTINUE
C
C              CALCULATE VELCCITY , STRAIN RATE ,STRAIN RATE INVARIENT ,
C              STRAINS , AND DEFORMATION ENERGY
C
C         VELOCITIES
C
      AZ=1./VX
```

```
      DO 851 J = 1,14
       DO 851 I = 8,30
      U(I,J)=((XXA(I,J)-XIA(I,J))-(XXA(I-1,J)-XIA(I-1,J)))*VX
      V(I,J)=((YYA(I,J)-YIA(I,J))-(YYA(I-1,J)-YIA(I-1,J)))*VX
  851 CONTINUE
C
C              STRAIN RATE AND DEFORMATION ENERGY
C
      SUN = 0.
      DO 251 J = 2,13
      DO 251 I = 9,30
      ID = I -2
      JD=J -1
       EDX(I,J)=U(I,J) - U(I-1,J)
       EDY(I,J) = V(I,J+1) - V(I,J-1)
       GDXY(I,J) = (V(I,J) - V(I-1,J))+(U(I,J+1) - U(I,J-1))
       STRR(I,J) = SQRT((EDX(I,J)**2 + EDY(I,J)**2)/2. + GDXY(I,J)**2/4.)
     1)
      DE(I,J) = .25*(AREA(ID,JD)+ AREA(ID+1,JD) + AREA(ID,JD+1)+AREA(ID+
     1 1,JD+1))*STRR(I,J)
      DE(I,J) =   A2*DE(I,J)/VX
      SUN = SUN + DE(I,J)
  251 CONTINUE
      SUNN = 0.
      DO 459 J=2,13
      DO 459 I=9,23
      SUNN = SUNN + DE(I,J)
  459 CONTINUE
C
C              STRAINS
C
       DO 252 J = 2,13
       DO 252 I = 11,28
      K = I -2
       L = I - 1
       M = I + 1
      N = I + 2
  252 STRX(I,J) = .333*(EDX(K,J) + 4.*EDX(L,J) + 2.*EDX(I,J) + 4.*EDX(M,J)
     1J) + 2.*EDX(N,J))*AZ
       DO 253 I = 9,30
       DO 253 J = 4,11
      K1 = J -2
      L1 = J -1
      M1 = J + 1
      N1 = J + 2
       STRY(I,J) =.333*(EDY(I,K1) + 4.*EDY(I,L1) +  2.*EDY(I,J)
     1 +4.*EDY(I,M1) + 2.*EDY(I,N1))*AZ
  253 CONTINUE
       DO 254 J = 4,11
       DO 254 I = 11,28
      K1 = I -2
      L1 = I - 1
      M1 = I + 1
      N1 = I + 2
```

```
      K = J - 2
      L = J - 1
      M = J + 1
      N = J + 2
      GXY(I,J) =.333*((GDXY(K1,J) + GDXY(I,K)) + 4.*(GDXY(L1,J)+GDXY(I,
     1 L )) + 2.*( GDXY(I,J) + GDXY(I,J)) + 4.*( GDXY(M1,J)+GDXY(I,M))
     1  + 2.*( GDXY(N1,J) + GDXY(I,N )))*A7
      STRXY(I,J) = .333*((STRR(K1,J) + STRR(I,K)) + 4.*(STRR(L1,J) +
     1 STRR(I,L)) + 2.*( STRR(I,J) + STRR(I,J)) + 4.*( STRR(M1,J) + STRR
     1 (I,M)) + 2.*( STRR(N1,J) + STRR(I,N))) *A7
      STRXY(I,J)=    A2*STRXY(I,J)/VX
  254 CONTINUE
       SUM = 0.
      DO 855 J = 4,11
       DO 855 I = 11,28
  855 SUM = SUM + STRXY(I,J)
      SMM =0.
      DO 888 J = 4,11
       DO 888 I = 11,23
      SMM = SMM + STRXY(I,J)
  888 CONTINUE
      DO 705 J = 2,13
       DO 705 I = 9,30
      IF(ABS(EDX(I,J)-EDY(I,J)).LT..00001)GO TO 704
      W(I,J) = 28.66366*ATAN(ABS(GDXY(I,J)/(EDX(I,J)-EDY(I,J))))
      GO TO 705
  704 W(I,J) = 90.
  705 CONTINUE
      DO 903 J = 1,14
      WRITE(6,904)J
       WRITE(6,201)
      DO 903 I = 1,30
      WRITE(6,202) XIA(I,J),YIA(I,J),U(I,J),V(I,J),EDX(I,J),EDY(I,J)
     1,GDXY(I,J),STRX(I,J),STRY(I,J),GXY(I,J),STRR(I,J),STRXY(I,J),
     1 W(I,J)
  903 CONTINUE
      WRITE(6,905)SUM
      WRITE(6,905)SMM
  201 FORMAT(1H0,10X,'X        Y       U       V     STR-X     STR-Y     STR-XY
     1     STRAN-X     STRAN-Y     STRAN-XY     STR-I     DEF-ENE     ANGLE')
  202 FORMAT(1H0,5X,4F7.3,9F10.6)
  904 FORMAT(1H1,10X,'      ROW NO. = ',I5)
  905 FORMAT(1H0,10X,'DEFORMATION ENERGY =',F10.6)
       WRITE(6,907)
      DO 911 J = 1,14
      DO 911 I = 1,30
      WRITE(6,906)I,J,AREA(I,J),DEN(I,J),DE(I,J)
  911 CONTINUE
  906 FORMAT(1H0,10X,2I5,3F10.6)
  907 FORMAT(1H0,' ROW NO    COLUMN NO    AREA     R DENSITY   DEF. ENE.   ')
      WRITE(6,908)SUN
      WRITE(6,908)SUNN
  908 FORMAT(1H0,'TOTAL DEFORMATION ENERGY = ',F10.6)
 1111   CONTINUE
```

```
      STOP
      END
EFFECT*  NOTERM,ID,EBCDIC,SOURCE,NOLIST,NODECK,LOAD,NOMAP,NOTEST
EFFECT*  NAME = MAIN    , LINECNT =       56
*    SOURCE STATEMENTS =      377,PROGRAM SIZE =    65374
* NO DIAGNOSTICS GENERATED
```

APPENDIX D

CONSTITUTIVE RELATIONSHIPS

D.1 Introduction

The major aspects of the behavior of clays can be summarized as follows:

Clays are masses of microscopic, generally plate-shaped mineral particles, in a surrounding medium of water solutions of ions and air. At relatively low stress levels, the cause of dissimilarities in the mechanical behavior of metals and clays is the fact that the former derive their elastic properties from the recoverable deformations of strong bonds between molecules, whereas any straining of clay fabric gives rise to a disruption of the comparatively weak connections between mineral particles and to a subsequent alteration of material stiffness (Yong & Warkentin, 1975).

If a sample of saturated clay is placed in a triaxial cell and subjected to a confining pressure equal to that at which the clay was previously consolidated, and the sample is then subjected to an additional confining stress, such that $\sigma_1=\sigma_2=\sigma_3$, there will be a subsequent rise in the pore water pressure u, which is equal to the increase in confining stress. Under the application of an increasing deviatoric stress $\Delta\sigma_1$, Figure D-1a, the sample will eventually fail or reach a state which can be considered as failure. Typical stress-strain curves resulting from such a test are similar to the curve shown in Figure D-1b. If a second sample of the same material were to be placed in a triaxial cell, subjected to a greater confining pressure and loaded

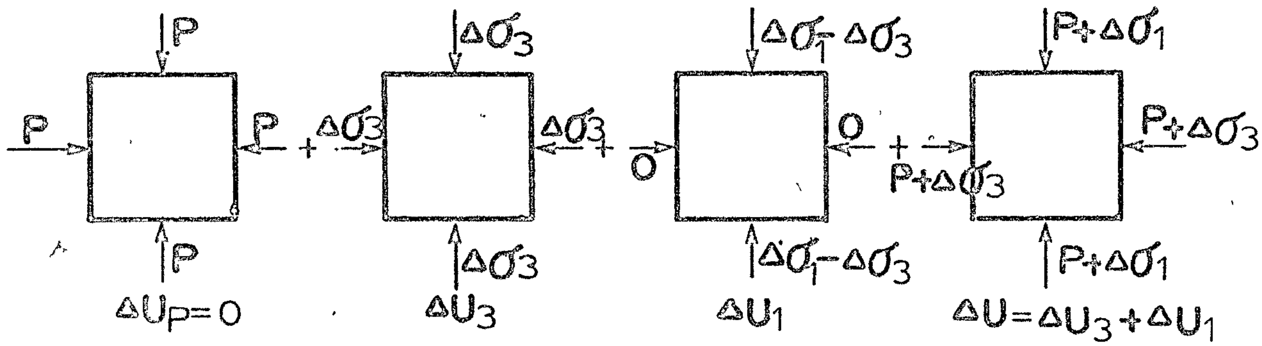

Fig. D-1a Representation of Soil Element subject to Stress Increments and Associated Pore Pressure Response

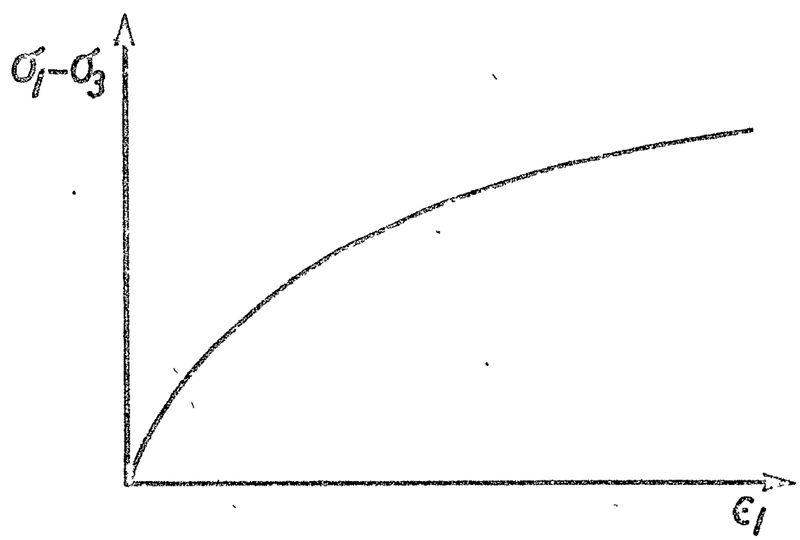

Fig. D-1b Stress-Strain Behaviour

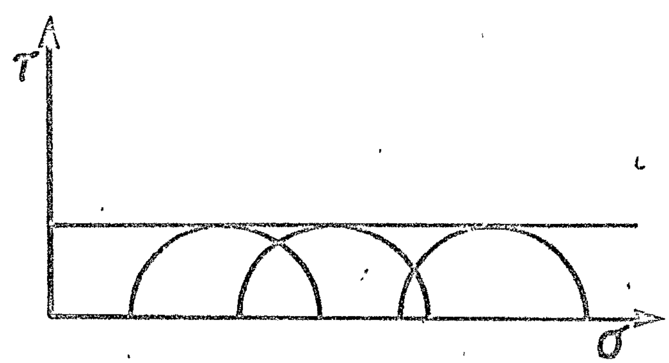

Fig. D-1c Strength Characteristics

Fig. D-1 Behaviour of Cohesive Soil under Undrained Quick Test Conditions to failure, the resulting stress-strain curve would be very similar to that obtained in the first test. Similar stress-strain curves will be obtained for still higher confining pressures. This observation points to the conclusion that the stress-strain behavior of a saturated clay is independent of the confining pressure to which the soil is subjected, provided the soil is completely saturated and is tested in quick conditions with no drainage allowed. The validity of this conclusion is limited, however, by a physical limitation imposed by the triaxial cell, in that the intermediate and minor principal stresses must always be equal.

Not all clay soil exhibit the same nonlinear characteristics as the saturated clay discussed previously. The variables which can affect the nonlinear behavior of clay soils are: partial saturation, prior stress history, time, mineralogical composition, disturbance and soil structure.

There are few techniques for representing the nonlinear behavior of soil and each technique depends on the associated constitutive relations which are used with it. These are: the nonlinear elastic approach, the hyperbolic representation and the elasto-plastic representation. These will be briefly discussed in the following sections.

D.2 Nonlinear Elastic Approach

In this approach two techniques can be adopted, one by using directly the results of triaxial test at different confining pressure for forming the stress-strain relationships of soil as explained in Chapter 6; the other by using formulas based on curve-fitting of the triaxial stress-strain results. A summary of the hyperbolic representation which is the most famous fitting technique is presented here.

D.3 Hyperbolic Representation

Kondner and his co-workers (Duncan & Chang, 1970; Kondner, 1963; Kondner & Zelasko, 1963; Kondner & Horner, 1965) have shown that the nonlinear stress-strain curves of both clay and sand may be approximated by hyperbolae. The hyperbolic equation proposed by Kondner was

$$(\sigma_1-\sigma_3) = \frac{\varepsilon_1}{a+b\varepsilon_1} \qquad \text{(D-1)}$$

in which σ_1 and σ_3 are the major and minor principal stresses

ε_1 is the axial strain

a and b are constants whose values may be determined experimentally.

The physical meaning of the constants a and b is shown in Figure D-2a. Kondner and his co-workers showed that the values of the coefficients a and b may be determined most readily if the stress-strain data are plotted on transformed axes, as shown in Figure D-2b.

It is commonly found that the asymptotic value of $(\sigma_1-\sigma_3)$ is larger than the compressive strength of the soil by a small amount. This would be expected, because the hyperbola remains below the asymptote

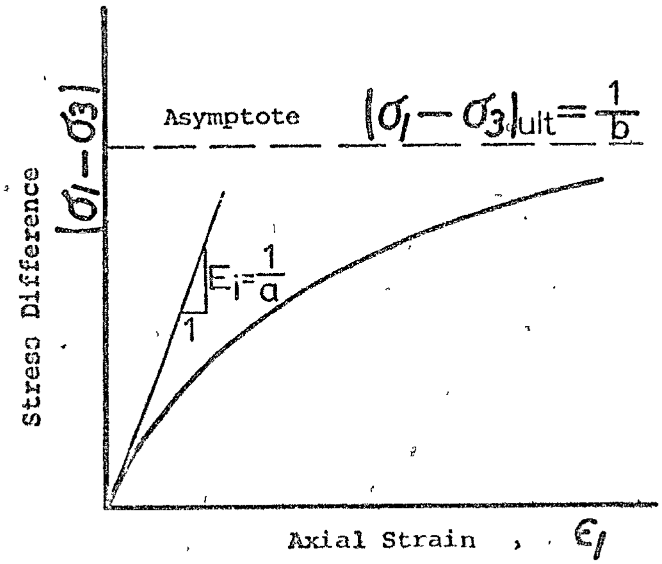

Fig. D-2a Hyperbolic Stress-Strain Curve (Duncan and Chang, 1970)

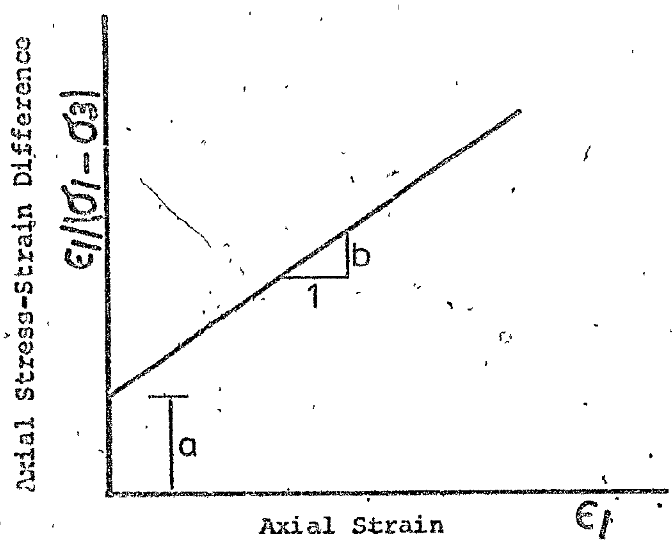

Fig. D-2b Transformed Hyperbolic Stress-Strain Curve (Duncan and Chang, 1970) at all finite values of strain. The asymptotic value may be related to the compressive strength, however, by means of a factor R_f as shown by

$$(\sigma_1-\sigma_3)_f = R_f(\sigma_1-\sigma_3)_{ult} \tag{D-2}$$

in which $(\sigma_1-\sigma_3)$ is the compressive strength, or stress difference at failure

$(\sigma_1-\sigma_3)_{ult}$ is the asymptotic value of stress difference

and R_f is the failure ratio.

Duncan & Chang (1970) expressed the parameters a and b in terms of the initial tangent modulus value ~~and the~~ compressive strength; Eq. D-1 may be written as

$$(\sigma_1-\sigma_3) = \frac{\varepsilon_1}{\left[\frac{1}{E_i} + \frac{\varepsilon_1}{(\sigma_1-\sigma_3)_f}\right]} \tag{D-3}$$

This hyperbolic representation of stress-strain curves was developed by Kondner et al. (1963).

Stress Dependency

Experimental studies by Janbu (1963) have shown that, except in the case of unconsolidated-undrained tests on saturated soils, both the tangent modulus value and the compressive strength of soils have been found to vary with the confining pressure employed in the tests. The relationship between initial tangent modulus and confining pressure may be expressed as

$$E_i = K P_a \left(\frac{\sigma_3}{P_a}\right)^n \qquad \text{(D-4)}$$

in which

E_i = the initial tangent modulus

σ_3 = the minor principal stress

P_a = atmospheric pressure expressed in the same pressure units as E_i and σ_3

K = a modulus number

n = the exponent determining the relation between E_i and σ_3.

Both K and n are pure numbers. Values of the parameters K and n may be determined readily from the results of a series of tests by plotting the values of E_i against σ_3 on log-log scales and fitting a straight line to the data, as shown in Figure D-3.

Assuming that failure will occur with no change in the value of σ_3, Duncan & Chang (1970) indicate that the relationship between compressive strength and confining pressure may be expressed conveniently in terms of the Mohr-Coulomb failure criterion as

$$(\sigma_1-\sigma_3)_f = \frac{2C\cos\phi+2\sigma_3\sin\phi}{1-\sin\phi} \qquad \text{(D-5)}$$

where C and ϕ are the Mohr-Coulomb strength parameters.

Eqs. D-4 and D-5 in combination with Eq. D-3, provide a way of relating stress to strain and confining pressure by means of the five parameters K, n, C, ϕ and R_f. Techniques for utilizing this relationship in nonlinear finite element stress analysis were developed by Duncan & Chang (1970).

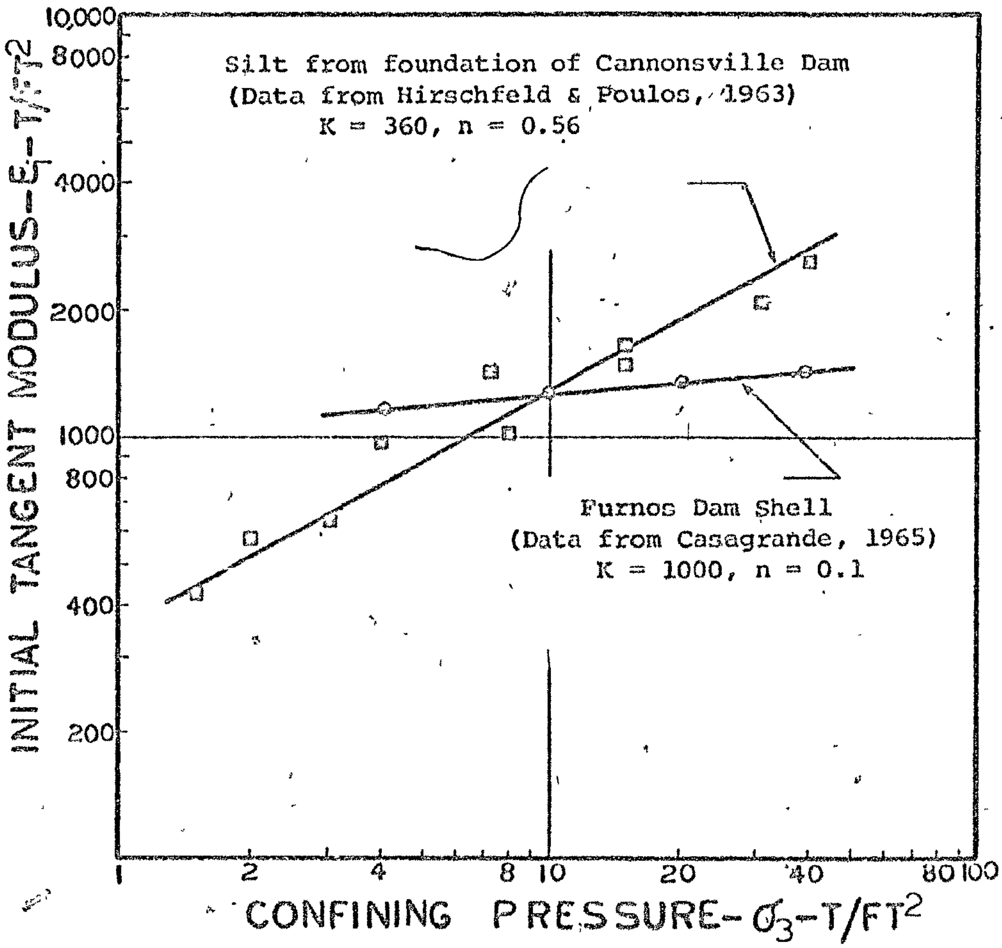

Figure D-3 Variations of initial tangent modulus with confining pressure under drained triaxial test conditions (Duncan & Chang, 1970)

The stress-strain relationship expressed by Eq. D-3 may be employed very conveniently in incremental stress analyses because it is possible to determine the value of the tangent modulus corresponding to any point on the stress-strain curve. If the value of the minor principal stress is constant, the tangent modulus, E_t, may be expressed as

$$E_t = \frac{\partial(\sigma_1 - \sigma_3)}{\partial \varepsilon 1} \qquad \text{(D-6)}$$

By differentiating Eq. D-3, the following expression for the tangent modulus may be obtained.

$$E_t = \frac{\frac{1}{E_i}}{\left[\frac{1}{E_i} + \frac{R_f \varepsilon 1}{(\sigma_1 - \sigma_3)_f}\right]^2} \qquad \text{(D-7)}$$

The strain, ε_1, may be eliminated from Eq. D-7 by rewriting Eq. D-3 as

$$\varepsilon 1 = \frac{\sigma_1 - \sigma_3}{E_i\left[1 - \frac{R_f(\sigma_1 - \sigma_3)}{(\sigma_1 - \sigma_3)_f}\right]} \qquad \text{(D-8)}$$

Substituting this expression for strain into Eq. D-7, E_t can be written as

$$E_t = (1 - R_f S)^2 E_i \qquad \text{(D-9)}$$

where S, the stress level, is given by

$$S = \frac{(\sigma_1 - \sigma_3)}{(\sigma_1 - \sigma_3)_f} \tag{D-10}$$

Thus the tangent modulus value for any stress condition can be written as

$$E_t = \left[1 - \frac{R_f(1-\sin\phi)(\sigma_1 - \sigma_3)}{2C\cos\phi + 2\sigma_3\sin\phi}\right]^2 K\,P_a\left(\frac{\sigma_3}{P_a}\right)^n \tag{D-11}$$

This expression for tangent modulus was employed in incremental stress analysis using finite element method by Duncan & Chang (1970).

As shown from the tangent modulus expression, the relationship contains six parameters whose values may be determined very readily from the results of a series of triaxial or plane strain compression tests involving primary loading, unloading, and reloading. Two of these parameters are the Mohr-Coulomb strength parameters, C and ϕ, and the other four also have easily visualized physical significance.

D.4 Elastic Plastic Representation

If one examines a clay which is initially homogeneous and isotropic, that is, it has the same macroscopic properties at all points and in all directions, it should remain so over a limited range of applied stresses and the principle of Saint Venant (1870) should apply (Yong & McKyes, 1971). Clay soils with randomly oriented particles satisfy the isotropic condition in the undisturbed state, but if extensive shear strains should produce a situation of preferred particle orientation, different conditions of non-isotropic behavior of the material would be expected (Yong et al., 1970).

It is quite generally postulated, as an experimental fact, that yielding can occur only if the stresses $\{\sigma\}$ satisfy the general yield criterion

$$f(\{\sigma\},K) = 0 \qquad \text{(D-12)}$$

where $\{\sigma\}$ represents the stress components in vector notation and K is the hardening parameter .

If it is assumed that the material has the same mechanical properties in all directions at any stress level, the relations of Levy (1871) and von Mises (1913) may apply and the increment of plastic strain can be calculated

$$\delta\{\sigma\}_p = \lambda \frac{\partial F}{\partial\{\sigma\}} \qquad \text{(D-13)}$$

where λ is a proportionality constant and F is the yield function.

The strains due to an increment of stress are assumed to be divisible into elastic and plastic parts. Thus,

$$\delta\{\varepsilon\} = \delta\{\varepsilon\}_e + \delta\{\varepsilon\}_p \qquad \text{(D-14)}$$

The relation between the elastic strain increments and stress increments is given by the elasticity matrix

$$\delta\{\varepsilon\}_e = [D]^{-1}\delta\{\sigma\} \tag{D-15}$$

Therefore

$$\delta\{\varepsilon\} = [D]^{-1}\delta\{\sigma\} + \frac{\partial F}{\partial\{\sigma\}}\lambda \tag{D-16}$$

By differentiating the equation of the yield surface, Eq. D-13, we can write

$$0 = \frac{\partial F}{\partial\sigma_1}\delta\sigma_1 + \frac{\partial F}{\partial\sigma_2}\delta\sigma_2 + \ldots\ldots + \frac{\partial F}{\partial K}dK \tag{D-17}$$

or, in matrix form,

$$0 = \left(\frac{\partial F}{\partial\{\sigma\}}\right)^T\delta\{\sigma\} + \lambda H^1 \tag{D-18}$$

where $H^1 = \frac{\partial F}{\partial K}dK \cdot \frac{1}{\lambda}$

Equations D-16 and D-18 can be written in a matrix form as (Marcel & King, 1967)

$$\begin{pmatrix} \delta\varepsilon_1 \\ \delta\varepsilon_2 \\ \vdots \\ \overline{O} \end{pmatrix} = \left[\begin{array}{cc:c} & & \frac{\partial F}{\partial\sigma_1} \\ & [D]^{-1} & \frac{\partial F}{\partial\sigma_2} \\ & & \vdots \\ \hdashline \frac{\partial F}{\partial\sigma_1} & \frac{\partial}{\partial\sigma_2} \cdots & H^1 \end{array}\right] \begin{pmatrix} \delta\sigma_1 \\ \delta\sigma_2 \\ \vdots \\ \overline{\lambda} \end{pmatrix} \tag{D-19}$$

λ can be eliminated and this results in an explicit expansion which determines the incremental stress-total strain relation

$$\delta\{\sigma\} = [D]_{ep}\,\delta\{\varepsilon\}$$

where

$$[D]^*_{ep} = [D]-[D]\{\frac{\partial F}{\partial\{\sigma\}}\}\;\{\frac{\partial F}{\partial\{\sigma\}}\}^T[D]\left[H^1+\;\{\frac{\partial F}{\partial\{\sigma\}}\}^T[D]\{\frac{\partial F}{\partial\{\sigma\}}\}\right]^{-1} \qquad \text{(D-20)}$$

$[D]_{ep}$ is the elasto-plastic matrix and

H^1 is a strain hardening parameter.

In plane strain condition, Eq. (D-20) can be written as (Zienkewicz et al., 1969)

$$\begin{pmatrix} \delta\varepsilon_x \\ \delta\varepsilon_y \\ \delta\gamma_{xy} \\ \hline 0 \end{pmatrix} = \left[\begin{array}{c|c} [D]^{-1} & \begin{matrix} \left(\frac{\partial F}{\partial\sigma_x} - \frac{a_{14}}{a_{44}}\frac{\partial F}{\partial\sigma_2}\right) \\ \left(\frac{\partial F}{\partial\sigma_y} - \frac{a_{24}}{a_{44}}\frac{\partial F}{\partial\sigma_2}\right) \\ \left(\frac{\partial F}{\partial\tau_{xy}} - \frac{a_{34}}{a_{44}}\frac{\partial F}{\partial\sigma_2}\right) \end{matrix} \\ \hline & \left(H^1 - \frac{1}{a_{44}}\left(\frac{\partial}{\partial\sigma_2}\right)^2\right) \end{array}\right] \begin{pmatrix} \delta\sigma_x \\ \delta\sigma_y \\ \delta\tau_{xy} \\ \hline \dot{\lambda} \end{pmatrix} \qquad \text{(D-21)}$$

where

$[D]^{-1}$ is the plane strain elastic matrix,

$a_{44} = \frac{1}{E}$, $a_{14} = a_{24} = \frac{-\nu}{E}$, and $a_{34} = 0$

In the case of randomly oriented particles of clays, it has been established that the shear forces induced in the interparticle connections by externally applied stresses will disrupt these connecting bonds to a certain extent and cause a change in the stiffness of the clay structure. This change will occur isotropically and will be a result of the equivalent shear stress acting in the materials, provided the density remains constant. The equivalent shear stress can be written as

$$\tau_{oct} = \frac{1}{3}\left[(\sigma_1-\sigma_2)^2 + (\sigma_2-\sigma_3)^2 + (\sigma_3-\sigma_1)^2\right]^{\frac{1}{2}} \qquad \text{(D-22)}$$

If a unique relation exists between the average shear strain and the equivalent shear stress above, the material is identified as a von Mises work-hardening plastic material, and the relation can be written as:

$$F = \frac{1}{2}\left[(\sigma_1-\sigma_2)^2 + (\sigma_2-\sigma_3)^2 + (\sigma_3-\sigma_1)^{-2}\right]^{\frac{1}{2}} - \overline{K} \qquad \text{(D-23)}$$

An explicit form for the stress-strain relations can then be developed from Eqs. D-21 and D-23.

The strain hardening parameter H' is a function of density and stress level in clays; its variation will result from the physical changes occurring in particle connections and from indirect forces as the clay fabric is altered by shearing movements. The strain hardening parameter of any specific clay type may be found from the standard soil mechanics triaxial test in which two principal stresses are equal. From the triaxial test the quantity H' can be expressed in terms of principal stress difference and major principal strains as follows

$$H' = \frac{d\tau_{oct}}{d\varepsilon_{oct}} = \frac{2d(\sigma_1 - \sigma_3)}{3d\varepsilon_1}$$

In the analysis of a plane strain continuum using the finite element method (initial stress approach) and constant elasto-plastic matrix at every load (displacement) increment, the convergence is very slow despite the fact that iteration after every displacement increment exists; the method is then no better than a more general stress-strain relationship.

The elasto-plastic model outlined here would be ideal in cases where the soil stress-strain relations can be idealized with fair accuracy, to obtain an elastic and a plastic portion. Most of the soils, however, exhibit continuous nonlinearity, and in such cases the elastic-plastic idealization may not work well.

METHOD OF CHARACTERISTICS

E.1 Introduction

The method of characteristics is adopted in this thesis to predict the subsoil stress distribution beneath a moving rigid wheel, provided the subsoil slip line fields can be determined from the experimentally measured subsoil deformations.

The following derivations, after Hansen (1965), is limited to the application of the method of characteristics to an ideal rigid-plastic material, deformed under plane strain conditions and satisfying the Tresca yield criterion.

E.2 Equilibrium Conditions

The state of stress may be represented by the stress components σ_x, σ_y and τ_{xy} at any point in relation to the coordinate system, Figure E-1. The stress components related to any other coordinate system may be found by means of Mohr's circle for stresses, Figure E-1. Alternatively, if the mean normal stress σ, the maximum shear stress τ, and the angle θ between the x-axis and the major principal stress direction are known, all other stress components can be found as follows:

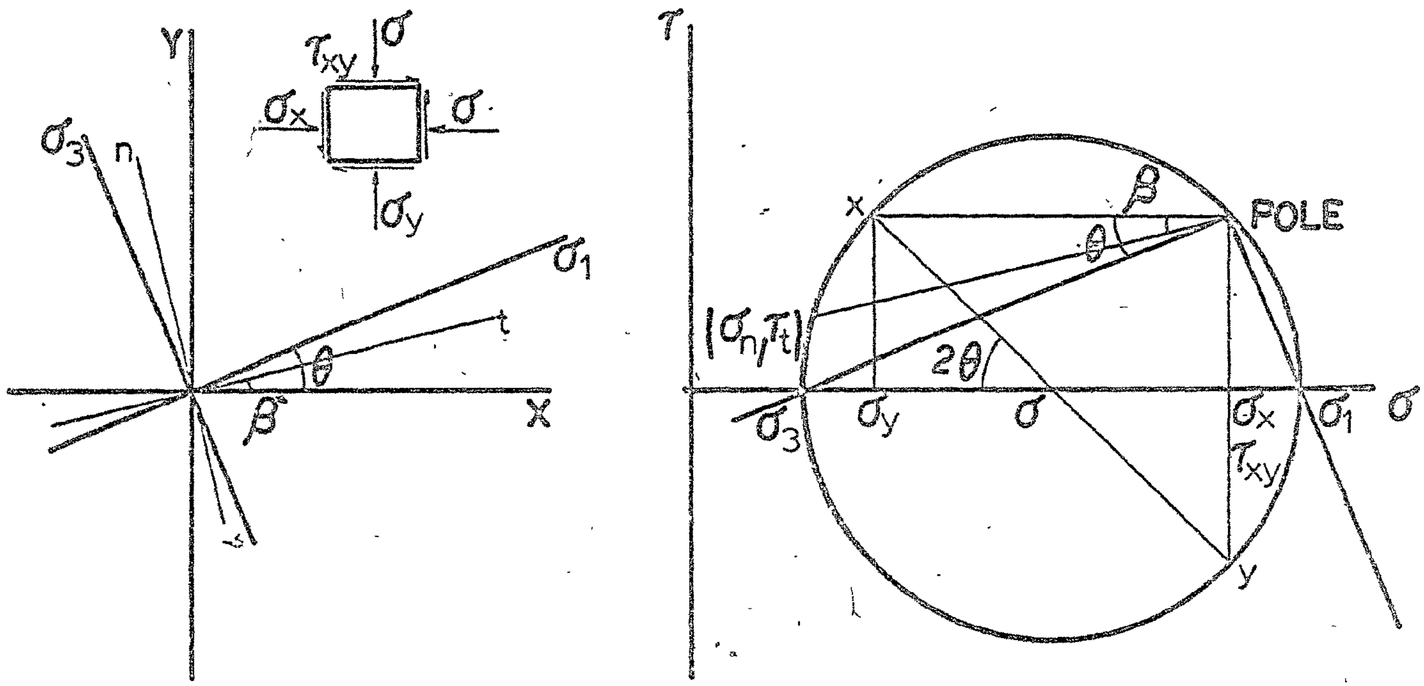

COORDINATE SYSTEMS MOHR CIRCLE FOR STRESSES

Fig. E-1 Mohr Circle for Stresses and Coordinate Systems

$$\sigma_x = \sigma + \tau \cos 2\theta$$

$$\sigma_y = \sigma - \tau \cos 2\theta \qquad \text{(E-1)}$$

$$\tau_{xy} = \tau \sin 2$$

where

$$\sigma = \frac{1}{2}(\sigma_1 + \sigma_3)$$

$$= \frac{1}{2}(\sigma_x + \sigma_y)$$

$$\tau = \frac{1}{2}(\sigma_1 - \sigma_3)$$

$$\tan 2\theta = \frac{2\tau_{xy}}{\sigma_x - \sigma_y}$$

If the body forces are neglected, the equilibrium equations for the plane strain case can be written as:

$$\frac{\partial \sigma_x}{\partial X} + \frac{\partial \tau_{xy}}{\partial Y} = 0$$

$$\frac{\partial \tau_{xy}}{\partial X} + \frac{\partial \sigma_y}{\partial Y} = 0 \qquad \text{(E-2)}$$

E.3 Failure Condition

An ideal rigid-plastic material is in a state of failure when the maximum shear stress τ is equal to the shear strength of the soil C.

$$\tau = C$$

If the material is in a state of failure, the stress distribution can be determined by σ and θ only; thus Eq. E-1 can be written as

$$\begin{aligned} \sigma_x &= \sigma + C\cos 2\theta \\ \sigma_y &= \sigma - C\cos\theta \\ \tau_{xy} &= C\sin 2\theta \end{aligned} \qquad \text{(E-3)}$$

Knowing the stress boundary conditions for the failure zone, the two unknown quantities σ and θ can be determined uniquely by the two equilibrium equations (E-2).

E.4 Stress Characteristics

Combining Eqs. E-2 and E-3, one can obtain

$$\begin{aligned} \frac{\partial\sigma}{\partial X} - 2C\sin 2\theta\,\frac{\partial\varepsilon}{\partial X} + 2C\cos 2\theta\,\frac{\partial\theta}{\partial Y} &= 0 \\ \frac{\partial\sigma}{\partial Y} + 2C\cos 2\theta\,\frac{\partial\theta}{\partial X} + 2C\sin 2\theta\,\frac{\partial\theta}{\partial Y} &= 0 \end{aligned} \qquad \text{(E-4)}$$

Assuming that a curve is given in the x,y plane (Fig. E-2), and that σ and θ, which are scalar functions of X and Y, are known along this curve, the variation of σ and θ between any two points (A and B) on the curve must, then, satisfy the identities:

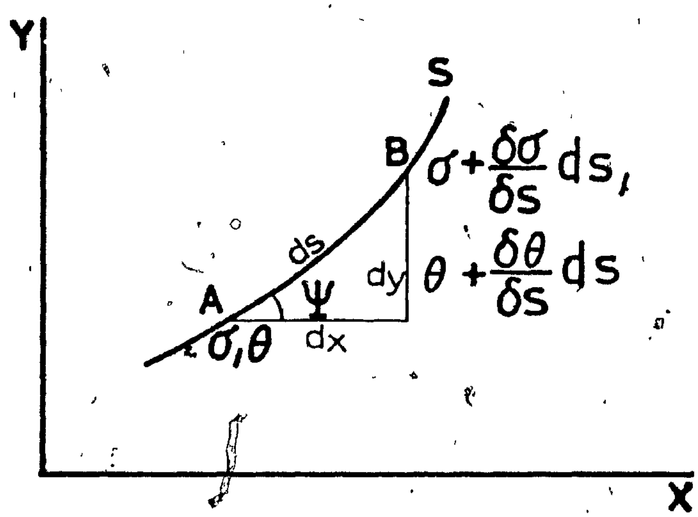

Fig. E-2 Variation of σ and θ along a slip line in a failure domain.

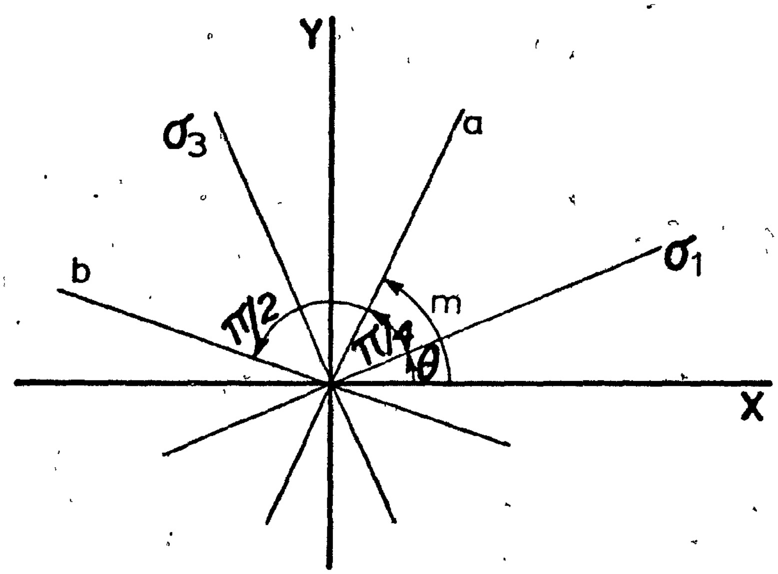

Fig. E-3 Characteristic Directions through a point in a Failure Zone.

$$\cos\psi \frac{\partial\sigma}{\partial X} + \sin\psi \frac{\partial\sigma}{\partial Y} = \frac{\delta\sigma}{\delta S}$$

$$\cos\psi \frac{\partial\theta}{\partial X} + \sin\psi \frac{\partial\theta}{\partial Y} = \frac{\delta\theta}{\delta S} \qquad \text{(E-5)}$$

where

$$\cos\psi = \frac{\delta X}{\delta S}$$

$$\sin\psi = \frac{\delta Y}{\delta S}$$

S is the arc length along the curve, and

ψ is the tangent angle.

The four equations (E-4) and (E-5) determine the four unknown quantities $\frac{\partial\sigma}{\partial X}$, $\frac{\partial\sigma}{\partial Y}$, $\frac{\partial\theta}{\partial X}$ and $\frac{\partial\theta}{\partial Y}$ so that σ and θ can be found, using numerical integration, in the vicinity of all ordinary curves of this kind. This process can be repeated for another curve drawn inside the domain where σ and θ are known.

If the determinant of Eqs. E-4 and E-5 vanishes for a certain value of ψ, the derivatives of σ and θ cannot be determined from known variations along the curves, and they may be discontinuous.

On the other hand, if the determinant of the coefficients is zero, the rank of the augmented coefficient matrix must be three, in order that the equations shall not be contradictory. Therefore, for such curves a relationship must exist between $\frac{\delta\sigma}{\delta S}$ and $\frac{\delta\theta}{\delta S}$. The condition of a vanishing determinant of coefficients in Eqs. E-4 and E-5 can easily be reduced to:

$$\sin^2\psi\cos 2\theta - 2\sin\psi\cos\psi\sin 2\theta - \cos^2\psi\cos 2\theta = 0 \qquad \text{(E-6)}$$

Eq. E-6 is a hyperbolic equation; its two real roots define the directions of the two families of characteristics.

$$\tan\psi = \tan 2\theta \pm \sec 2\theta = \begin{cases} \tan\left(\theta+\frac{\pi}{4}\right) = \tan m \\ \tan\left(\theta+\frac{3\pi}{4}\right) = \tan\left(m+\frac{\pi}{2}\right) \end{cases} \qquad \text{(E-7)}$$

Figure E-3 shows the direction of the characteristics. The relation between σ and θ along the characteristics curves can be obtained by replacing the fourth column of the coefficient matrix by the column of constant terms and equating the resulting determinant to zero, hence

$$\cos\psi \frac{\delta\sigma}{\delta S} - 2C \sin(2\theta-\psi) \frac{\delta\theta}{\delta S} = 0 \qquad \text{(E-8)}$$

Substituting the value of ψ in Eq. E-8, one obtains:

$$\begin{aligned} \frac{\delta\sigma}{\delta S_a} + 2C \frac{\delta m}{\delta S_a} &= 0 \\ \frac{\delta\sigma}{\delta S_b} + 2C \frac{\delta m}{\delta S_b} &= 0 \end{aligned} \qquad \text{(E-9)}$$

[Kotter (1903) and Hencky (1923)]

Equations E-9 can be derived by considering the equilibrium of an element cutout between consecutive slip lines, Figure E-4. It is assumed that the shear stresses are known along all four sides. Neglecting all the second order quantities, the Eqs. E-9 are obtained by considering the equilibrium of all forces along the a and b directions respectively.

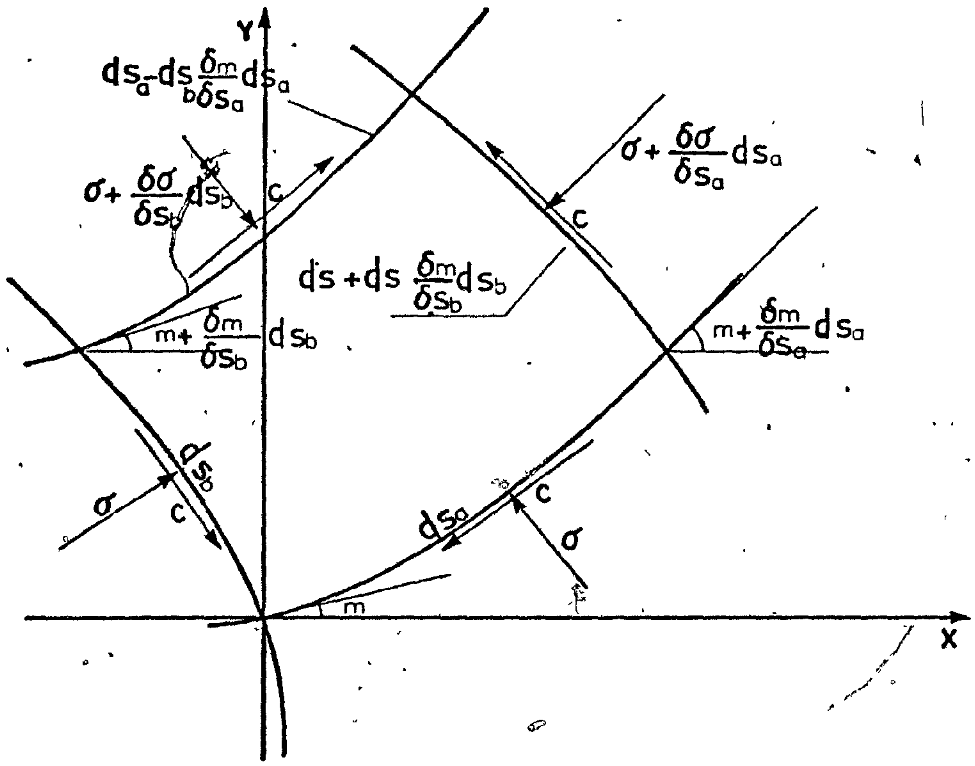

Fig. E-4 State of Stress for a Soil Element in the Failure Zone

E.5 Stress Computations

Equations E-9 are sufficient to compute the stress components along characteristics provided that these characteristics can be constructed and that the state of stress is known at some starting point.

The flow chart for calculating the subsoil stresses using the method of characteristics is shown in Figure E-5 (Williams,1973).

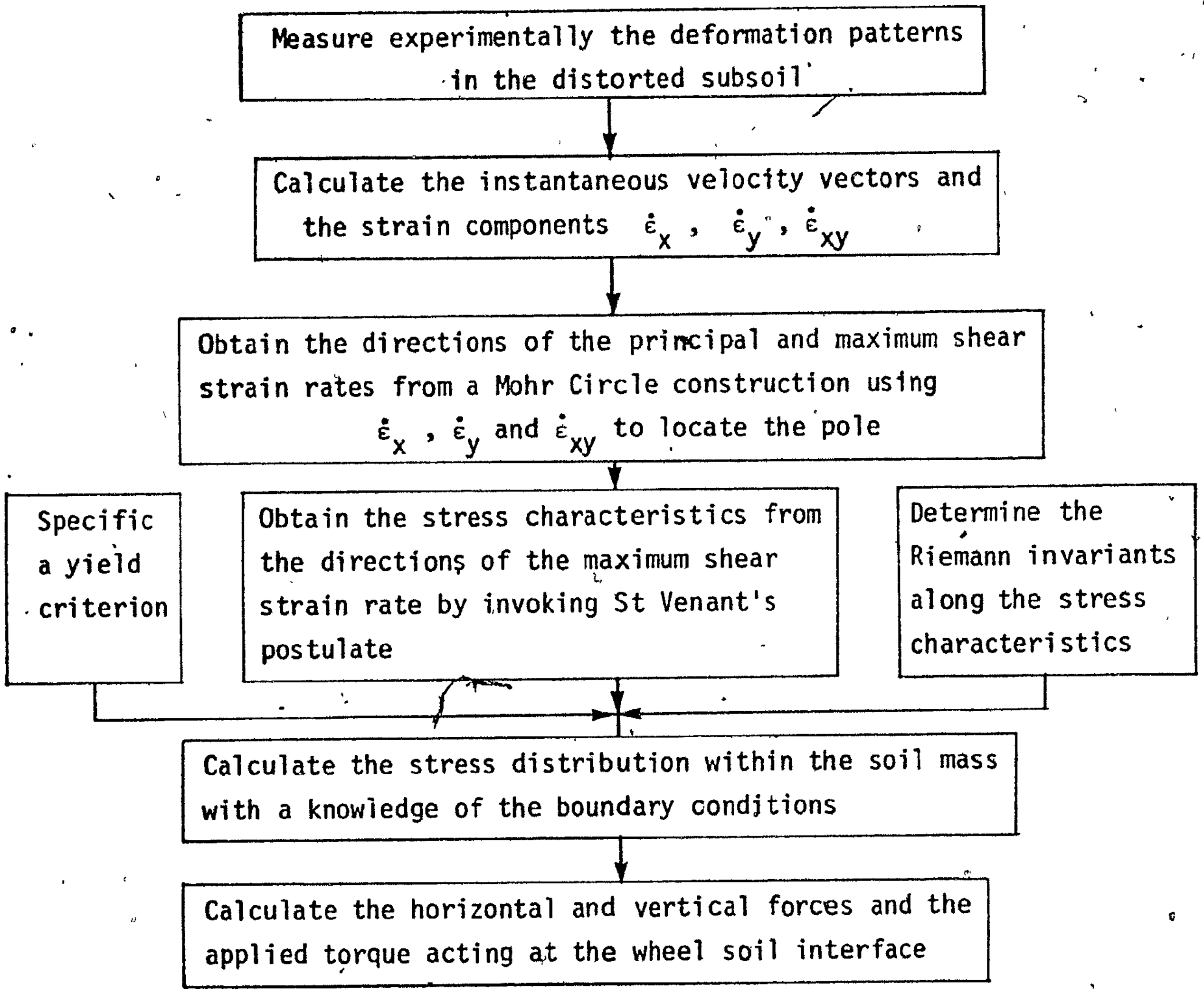

Fig. E-5 Calculation of the stress distribution by the method of characteristics (Williams 1973)

FINITE ELEMENT COMPUTER PROGRAMS

During the course of this study several computer programs were developed to predict the performance of vehicle tractive element and soil behavior beneath it. The programs were grouped under a series named "MAIN" and were based on Zienkiewicz's program (1971). The programs can handle nonlinear material properties, and the different methods used to perform the nonlinear analysis and the type of the problem dictate the particular program to be used.

"MAIN 1" and "MAIN 2" use an incremental iterative method to solve nonlinear problems in clay. "MAIN 1" is a general routine developed to handle wheel-soil interaction problems, and "MAIN 2" is used to handle grouser-soil interaction and soil-cutting problems (Hannah, 1975). The programs were written in the Fortran language for use on the IBM 360/75. A brief outline of the working of a general "MAIN 1" program is given here.

General Outline of Program "MAIN 1"

The program consists of several subroutines, Figure F-1 and a brief description of each subroutine is given below.

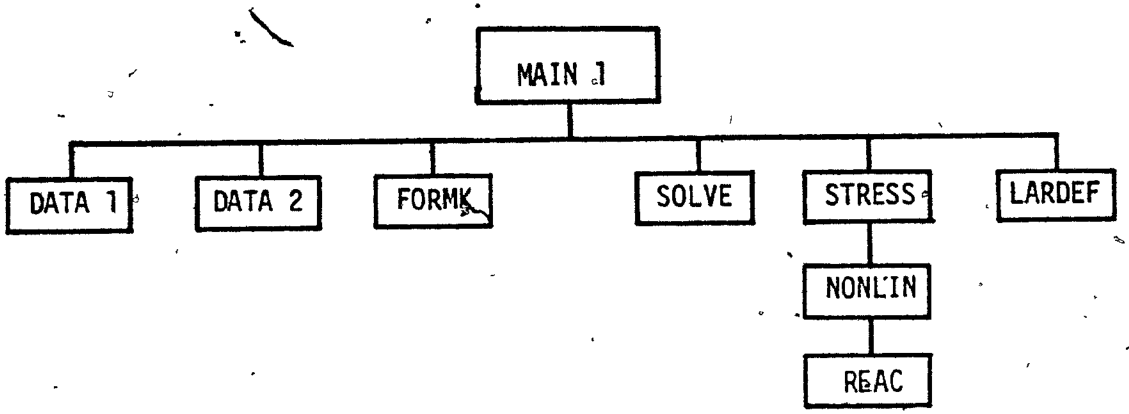

Fig. F-1. Subroutine linkage

Main Program

This is the main routine of the program. It handles all input data and calls several other subroutines. The program reads the data concerning the boundary conditons.

Subroutine "GDATA 1"

This routine reads the basic data concerning problem idealization, which are

1. Junction coordinates and element characteristics.
2. Initial material properties for each element.
3. Number of increments, and number of iterations in every increment required for execution of the problem.

Subroutine "GDATA 2"

This routine incorporates the nonlinear stress-strain data into the program. The stress-strain data derived from laboratory tests are used directly in digital form. Several points on the stress-strain curve are selected as input to this routine in the form of number of pairs.

Subroutine "STIF(N)"

This routine generates the stiffness matrix for each element using the constitutive relations of the material and the geometry of the element. This subroutine has all the necessary data transmitted to it through common storage and passes the element stiffness matrix back to the calling subroutine "FORMK".

Subroutines "FORMK and "MODIFY"

This routine assembles the total stiffness matrix for the entire continuum using the direct stiffness method. The "FORMK" routine also generates the total nodal force vector. The applied nodal forces are added directly, while the total stiffness matrix is modified for the applied displacement conditions using subroutine MODIFY.

Subroutine "SOLVE"

This routine uses the Gaussian elimination method and solves the unknown displacements from the set of stiffness equations generated in "FORMK". These equations are of the form AX=B. The "FORMK" routine stores specified blocks of equations in the core and "SOLVE" solves them one by one. A forward pass is first performed to triangularize the matrix. A back substitution is then followed to solve for the unknowns. The results are stored in matrix A to be printed in the "STRESS" subroutine as displacements.

Subroutine "STRESS"

This subroutine computes the stresses and strains at the center of each element using the nodal displacements obtained from "SOLVE" and the strain-displacement matrix computed by applying "STIFF". The subroutine also computes the principal stresses and principal strains, velocities, deformation energy and power of deformation energy. The stresses, the strains, the strain rates and the power of deformation energy of all the elements connected to a node are summed and divided by the number of elements.

Subroutine "REAC"

The reactions at the nodal points at the wheel-soil interface and on the other boundaries are determined in this subroutine. The reactions obtained for any particular increment are added to the cumulative values obtained in previous increments to obtain total reactions.

Subroutine "LARDEF"

After each incremental wheel travel distance, the element nodal coordinates are updated by adding the nodal displacements to the element nodal coordinates in order to obtain new coordinates for the next increment.

Subroutine "NONLIN"

The nonlinear analysis is performed in this subroutine. Values of E are computed for each element from the nonlinear stress-strain curves depending on the state of strain and confining pressures in each element. The deviator stresses (σ_1-σ_3) and the principal strains, ε_1, are used to conduct the nonlinear analysis. The nonlinear routine can handle several nonlinear curves for any number of different materials by suitably altering the dimension statements.

BIBLIOGRAPHY

Abbott, M.B. (1966). "An Introduction to the Method of Characteristics", American Elsevier, New York.

Andreev, A.A. (1956). "Kinematics of Rolling of Rigid Wheels Forming a Track", Sbor. Trud. Zemled. Mekhan., Vsesoyuz. Lenin Akad. Selkhoz. Mauk., No. 3, p.3.

Bekker, M.G. (1956). "Theory of Land Locomotion - The Mechanics of Vehicle Mobility", University of Michigan Press, Ann Arbor, Michigan.

Bekker, M.G. (1969). "Introduction to Terrain-Vehicle Systems", University of Michigan Press, Ann Arbor, Michigan.

Bernstein, R. (1913). "Problem Zur Experimentellen Motorpflugmechanik. Problems of Experimental Mechanics of Motor Ploughs", Der Motorwagen, p.199.

Chang, C.Y. and Duncan, J.M. (1970). "Analysis of Soil Movement Around a Deep Excavation", J. ASCE, SMFD, Vol. 96, No. 5, pp. 1655.

Chung, T.J. and Lee, J.K. (1975). "Dynamics of Viscoelastoplastic Soil under a Moving Wheel", J. Terramechanics, 12(1), p.15.

Clough, R.W. and Woodward, R.J. (1967). "Analysis of Embankment Stresses and Deformations", J. ASCE, SMFD, Vol. 93, No. SM4.

Desai, C.S. (1972). "Overview, Trends and Projections: Theory and Application of the Finite Element Method in Geotechnical Engineering, State-of-the-Art", Proceedings of the Symposium on the Application of the Finite Element Method in Geotechnical Engineering, Vicksburg, Mississippi.

Desai, C.S. and Abel, J.F. (1972). "Introduction to the Finite Element Method", Van Nostrand Reinhold Company, New York.

Duncan, J.M. and Chang, C.Y. (1970). "Nonlinear Analysis of Stress and Strain in Soils", J. ASCE, SMFD, Vol. 96, No. 5, pp.1629.

Elsamny, M.K. and Ghobarah, A.A. (1972). "Stress Field Under Slipping Rigid Wheel", J. ASCE, SMFD, Vol. , No. 1, p.13.

Freitag, D.R. (1965). "The Design of Off-Road Vehicle Test Beds", Waterways Experiment Station Mobility Index System, Paper presented to the Fifth Meeting, Quadripartite Standing Working Group on Ground Mobility, U.S. Army Engineer Waterways Experiment Station, Vicksburg, Mississippi.

Freitag, D.R. and Smith, M.E. (1966). "Center-line Deflection of Pneumatic Tires Moving in Dry Sand", J. Terramechanics, Vol. 3, No. 1, p.31.

Fung, Y.C. (1965). "Foundation of Solid Mechanics", Prentice Hall, New Jersey.

Girijavallabhan, C.V. and Reese, L.C. (1968). "Finite Element Method Applied to Some Problems in Soil Mechanics", J. ASCE, SMFD, Vol. 94, No. SM2.

Goodman, L.J. (1966). "The Significance of Disturbance and Thixotropy in Mobility Problem", Proc. Second Conf. ISTVS, Quebec.

Green, A.E. and Adkins, J.E. (1970). "Large Elastic Deformations", Clarendon Press, Oxford.

Hanna, A. (1975). "Finite Element Analysis of Soil Cutting and Traction", Ph.D. Thesis, McGill University, Montreal.

Hansen, B. (1965). "A Theory of Plasticity for Ideal Friction Materials", Teknisk Forlag, Copenhagen.

Hencky, H. (1923). "Uber Einige Statisch Bestimmte Falle des Gleichgewichts in Plastischen Korpern", Zeits. Ang. Math. Mech 3, p.241.

Hill, R. (1950). "The Mathematical Theory of Plasticity", Oxford University Press, London.